



**EXPERIMENTAL AND THEORETICAL
BASIS FOR A CLOSED-FORM SPECTRAL
BRDF MODEL**

DISSERTATION

Samuel D. Butler, Major, USAF
AFIT-ENP-DS-15-S-021

**DEPARTMENT OF THE AIR FORCE
AIR UNIVERSITY**

AIR FORCE INSTITUTE OF TECHNOLOGY

Wright-Patterson Air Force Base, Ohio

DISTRIBUTION STATEMENT A
APPROVED FOR PUBLIC RELEASE; DISTRIBUTION UNLIMITED.

The views expressed in this document are those of the author and do not reflect the official policy or position of the United States Air Force, the United States Department of Defense or the United States Government. This material is declared a work of the U.S. Government and is not subject to copyright protection in the United States.

AFIT-ENP-DS-15-S-021

EXPERIMENTAL AND THEORETICAL BASIS FOR A CLOSED-FORM
SPECTRAL BRDF MODEL

DISSERTATION

Presented to the Faculty
Graduate School of Engineering and Management
Air Force Institute of Technology
Air University
Air Education and Training Command
in Partial Fulfillment of the Requirements for the
Degree of Doctor of Philosophy

Samuel D. Butler, BS, MS
Major, USAF

September 2015

DISTRIBUTION STATEMENT A
APPROVED FOR PUBLIC RELEASE; DISTRIBUTION UNLIMITED.

AFIT-ENP-DS-15-S-021

EXPERIMENTAL AND THEORETICAL BASIS FOR A CLOSED-FORM
SPECTRAL BRDF MODEL

DISSERTATION

Samuel D. Butler, BS, MS
Major, USAF

Committee Membership:

Michael A. Marciniak, PhD
Chairman

Kevin C. Gross, PhD
Member

Benjamin F. Akers, PhD
Member

Michael T. Eismann, PhD
Member

Joseph Meola, PhD
Member

ADEDJI B. BADIRU, PhD
Dean, Graduate School of Engineering and Management

Abstract

The microfacet class of BRDF models is frequently used to calculate optical scatter from realistic surfaces using geometric optics, but has the disadvantage of not being able to consider wavelength dependence. This dissertation works toward development of a closed-form approximation to the BRDF that is suitable for hyperspectral remote sensing by presenting measured BRDF data of 12 different materials at four different incident angles and up to seven different wavelengths between 3.39 and 10.6 μm . The data was intended to be fit to various microfacet BRDF models to determine an appropriate form of the wavelength scaling. However, when fitting the microfacet models to measured data, the results indicated a breakdown in the microfacet model itself. To overcome this deficiency, elements of microfacet BRDF models are compared to elements of scalar wave optics BRDF models, which inherently contain a wavelength dependence. This analysis led to a theoretical understanding of how to modify microfacet BRDF models to maintain the simplicity of a closed-form model, while better approximating the underlying physics. These results are expected to enable the development of even more robust closed-form models of the BRDF that can be applied to wavelength-sensitive applications such as hyperspectral remote sensing.

*To my family,
for their support, love, and patience,
and reminders of the joys and discoveries of childhood,
and to my Mom,
who inspired me to have a love of learning,
and live a life of service*

Acknowledgements

I am very thankful for the mentoring I received from my research advisor, Dr. Michael Marciniak. His scholarship and ability to communicate thoughts clearly to me were critical in producing this work. I would also like to thank Dr. Kevin Gross and Dr. Benjamin Akers for their inputs as members of my committee, and for the clarity in which they have taught difficult subjects that have helped me during my time at AFIT. In addition, I appreciate the time and help from Dr. Michael Eismann and Dr. Joseph Meola at the Air Force Research Laboratory, both as committee members and scholars, and in providing critical direction and funding for this research. I would like to acknowledge many long hours put in by Dr. Stephen Nauyoks helping me use the CASI® equipment, analysis of the data, and an understanding of BRDF theory. Additionally, I would like to thank Dr. Michael Benson in helping me keep my sanity, and for his help with the equipment. Finally, I would like to thank Mr. Greg Smith and Mr. Michael Ranft for their valuable assistance as laboratory technicians, as well as Ms. Sara Kraft, Ms. Brittany Barrett, and Ms. Amanda Zehring for their administrative support throughout the Ph.D. process.

Samuel D. Butler

Table of Contents

	Page
Abstract	iv
Acknowledgements	vi
List of Figures	x
List of Tables	xix
List of Symbols	xxiii
List of Acronyms	xxv
I. Introduction	1
1.1 Problem Statement	3
1.2 Dissertation Organization	6
II. Impact of BRDF on Basic HSRS Model	10
2.1 Scene Model	12
Radiance Model	13
MERL BRDF Data in HSRS Scene	15
2.2 Basic Model Results	18
2.3 Spectral Model Results	24
2.4 Summary of Impact	27
III. BRDF Theory Background	29
3.1 Electromagnetism	29
Polarization	31
3.2 Surface Reflection and Fresnel Equations	35
3.3 Self-Emission	37
Polarimetric Self-Emission	38
3.4 Reflectance Functions	39
3.5 BRDF Model Basics	42
Coordinate Variables for Reflection	45
3.6 Microfacet BRDF Models	47
Fresnel Approximations	49
Distribution Functions	50
Geometric Attenuation Terms	54
Directional Volumetric Reflection	56
Pre-factor Terms	57
Common Unpolarized BRDF Models	58

	Page
Unpolarized BRDF Model Remarks	67
Polarimetric BRDF Models	69
3.7 Spectral Dependence of Microfacet BRDFs	77
Investigation of Microfacet Wavelength Scaling	80
MERL Analysis	86
Potential Closed-Form Wavelength Scaling	94
3.8 Scalar Wave Optics BRDF Models	95
Angular Dependence	98
Polarization Factor	100
Original Beckmann-Kirchhoff BRDF Model	101
Modified Beckmann-Kirchhoff BRDF Model	104
IV. Measurement Process	106
4.1 Measuring Polarimetric BRDF	106
DRR Data Analysis	110
DRR Measurement Results	115
4.2 Measuring Unpolarized BRDF	117
4.3 Uncertainty Analysis	120
V. Measurement Results	127
5.1 Samples	127
5.2 Fitting Data to Microfacet BRDF	130
Adaptive Microfacet BRDF Model	135
BRDF Fit with Hyper-Cauchy Distribution	139
Fitting to Other Samples	140
5.3 Wavelength Variation of Raw Data BRDF Width	146
Unknown Microfacet Distribution Function	147
Raw Wavelength-Dependent Data	156
5.4 BRDF Magnitude at Specular Peak	160
5.5 Experimental Data Conclusions	164
VI. Theoretical Results	166
6.1 Comparing Microfacet and Scalar Wave Optics Models	168
Very Rough Surface Comparison	170
Polished Surface Comparison	176
Validity of Microfacet Model	177
Original Beckmann-Kirchhoff Modification	178
BRDF Scaling by $1/\sigma$	179
6.2 Experimental Validation of Results	180
6.3 Summary of Theoretical Results	190

	Page
VII. Conclusion	193
7.1 Summary of Key Results	194
7.2 Summary of Contributions	198
7.3 Future Work	199
Bibliography	203

List of Figures

Figure		Page
1	Illustration of the problem addressed by this dissertation. Items with a blue background are described in the background. Items with a green background are addressed in this dissertation. The item with a yellow background is left for future work.	5
2	Basic BRDF geometry, with incident and outgoing vectors relative to the surface normal $\hat{\mathbf{z}}$	11
3	Basic model of the scene employed by this BRDF study. The atmosphere is treated as a shell with radiation profile of a blackbody at 250 K; the object is assumed to be a graybody at 300 K; the Sun is assumed to be a blackbody at 5800 K.	14
4	BRDF shape from MERL nickel file, scaled to HDRs of 0.1, 0.5, and 0.9, plotted in two slices: (a) In-plane slice in θ_s for $\theta_i = 45^\circ$ and $\Delta\phi = 180^\circ$; (b) Out-of-plane slice in ϕ_s for $\theta_i = \theta_s = 45^\circ$ and $\phi_i = 0^\circ$. The shaded region represents grazing angle data, which is more prone to experimental error.....	17
5	MERL nickel scaled HDR for $\theta_i = 45^\circ$, $\phi_i = 0$ (for any ϕ_o). The shaded region represents grazing angle data, which is more prone to experimental error.	18
6	Ratios of self-emissive, solar, and diffuse downwelling radiances to total observed pupil plane radiance, for $\theta_i = 45^\circ$ and $\Delta\phi = 180^\circ$. The MERL nickel BRDF shape was scaled to result in a maximum HDR of three different values: (a) 0.1, (b) 0.5, and (c) 0.9; all other parameters remained fixed between the three plots. The shaded region represents grazing angle data, which is prone to experimental error.....	20
7	Hemispherical view of the conical region where $L_S/L_p > 0.1$ for a BRDF shape of nickel with an HDR of 0.9. The solid blue line is the incident vector ($\theta_i = 45^\circ$); the dotted blue line represents specular reflection.....	20

8	Contour plot of the difference in brightness temperature between MERL and Lambertian cases for an HDR of 0.9 and two incident angles: (a,b) $\theta_i = 30^\circ$; (c,d) $\theta_i = 45^\circ$. Plots (b) and (d) zoom in on the specular lobe contours. In (a) and (c), contours are in $1^\circ K$ steps; in (b) and (d), contours are in $10^\circ K$ steps. The plots extend only to $\theta_i = 70^\circ$ due to error in the BRDF data at grazing angles.	22
9	Contour plot of the difference in brightness temperature between MERL and Lambertian cases for an HDR of 0.5 and two incident angles: (a,b) $\theta_i = 30^\circ$; (c,d) $\theta_i = 45^\circ$. Plots (b) and (d) zoom in on the specular lobe contours. In (a) and (c), contours are in $1^\circ K$ steps; in (b) and (d), contours are in $10^\circ K$ steps. The plots extend only to $\theta_i = 70^\circ$ due to error in the BRDF data at grazing angles.	23
10	Total pupil plane radiance calculated assuming an object's BRDF is of the shape of nickel in the MERL database, scaled to an HDR of 0.9, as compared to the Lambertian assumption with the same HDR. In all cases, the incident angle is 45° . The outgoing angle varies in each plot: (a) 30° , (b) 35° , (c) 40° , (d) 45° , (e) 50° , and (f) 55° . The Lambertian (red dotted) line in each plot does not change in value, but the y axis changes in scale. The shape of the wavelength variation, as well as the overall value, changes when using BRDF data instead of the Lambertian approximation.	26
11	Microfacet geometry, with incident and outgoing vectors relative to $\hat{\mathbf{z}}$ (overall macro-surface normal), $\hat{\boldsymbol{\omega}}_h$ (specular microsurface orientation), and $\hat{\boldsymbol{\omega}}_d$ (rotated incident vector in this microsurface orientation)	46
12	BRDFs for Infragold from NEF at $1.06 \mu m$, $3.39 \mu m$, and $10.6 \mu m$. The linearly scaled BRDF to $3.39 \mu m$ using Equation (93) (fixed scaling) is also shown	83
13	Relative error of the linearly scaled Infragold BRDF to $3.39 \mu m$ using $1.06 \mu m$ and $10.6 \mu m$ BRDF data using Equation (93) (fixed scaling)	83
14	In plane BRDFs for aluminum from NEF at $1.06 \mu m$, $3.39 \mu m$, and $10.6 \mu m$. The linearly scaled BRDF to $3.39 \mu m$ using Equation (93) (fixed scaling) is also shown	84

Figure		Page
15	Relative error of the linearly scaled aluminum BRDF to 3.39 μm using 1.06 μm and 10.6 μm BRDF data using Equation (93) (fixed scaling)	84
16	BRDF from MERL brass file for $\theta_i = 30^\circ$ and for the red, green, and blue channels	88
17	HDR from MERL brass file for the red, green, and blue channels	89
18	Relative error of MERL brass file when scaling green BRDF to red BRDF, and when scaling green BRDF to blue BRDF, using Equation (92)	89
19	BRDF from MERL gold-paint file for $\theta_i = 30^\circ$ and for the red, green, and blue channels	90
20	HDR from MERL gold-paint file for the red, green, and blue channels	90
21	Relative error of MERL gold-paint file when scaling green BRDF to red BRDF, and when scaling green BRDF to blue BRDF, using Equation (92)	91
22	Relative error of MERL brass file when scaling red/blue BRDF to green BRDF, using Equation (93) (variable scaling)	91
23	Relative error of MERL brass file when scaling red/blue BRDF to green BRDF, using Equation (93) (fixed scaling)	92
24	Relative error of MERL gold-paint file when scaling red/blue BRDF to green BRDF, using Equation (93) (variable scaling)	92
25	Relative error of MERL gold-paint file when scaling red/blue BRDF to green BRDF, using Equation (93) (fixed scaling)	93
26	Diagram of AFIT modified CASI layout, taken from a paper by Vap[69]	108
27	QCL wavelengths available for use in the AFIT CASI®.	109

Figure	Page
28	Mueller matrix results for grit-blasted Ni at $\lambda = 4.4 \mu m$, $\theta_i = 40^\circ$, and $\theta_s = 40^\circ \pm 5^\circ$ 117
29	Grit-blasted Ni sample data at all incident angles, plotted in $\Delta\beta = \beta_s - \beta_i$ space, with error bars. 124
30	Polished Ni sample data at all incident angles, plotted in $\Delta\beta = \beta_s - \beta_i$ space, with error bars. 125
31	Comparison of Polished Ni BRDF measured data (relative to its maximum value at $\theta_i = \theta_s = 50^\circ$) taken completely independently on two separate occasions, for (a) $\theta_i = 20^\circ$, (b) $\theta_i = 30^\circ$, (c) $\theta_i = 40^\circ$, and (d) $\theta_i = 50^\circ$ 126
32	BRDF divided by DHR for grit-blasted Ni measured at $3.39 \mu m$ 131
33	BRDF divided by DHR for grit-blasted Ni measured at $10.6 \mu m$ 131
34	Linear interpolation to calculate grit-blasted Ni BRDF divided by DHR at $\theta_i = 40^\circ$ and $\lambda = 8.0 \mu m$, using measured BRDF data at $\lambda = 3.39 \mu m$ and $\lambda = 10.6 \mu m$, compared to the actual BRDF measured at $\lambda = 8.0 \mu m$ 133
35	Relative error in the linear interpolation to calculate grit-blasted Ni BRDF divided by DHR at $\theta_i = 40^\circ$ and $\lambda = 8.0 \mu m$, using measured BRDF data at $\lambda = 3.39 \mu m$ and $\lambda = 10.6 \mu m$ 133
36	Linear interpolation to calculate shot-blasted Ni BRDF divided by DHR at $\theta_i = 20^\circ$ and $\lambda = 8.0 \mu m$, using measured BRDF data at $\lambda = 3.39 \mu m$ and $\lambda = 10.6 \mu m$, compared to the actual BRDF measured at $\lambda = 8.0 \mu m$ 134
37	Relative error in the linear interpolation to calculate shot-blasted Ni BRDF divided by DHR at $\theta_i = 20^\circ$ and $\lambda = 8.0 \mu m$, using measured BRDF data at $\lambda = 3.39 \mu m$ and $\lambda = 10.6 \mu m$ 134
38	BRDF for grit-blasted Ni measured at $3.39 \mu m$, fitted to Cook-Torrance BRDF, using the default error metric, $g(x) = x$ 136

Figure		Page
39	BRDF for grit-blasted Ni measured at $3.39\ \mu m$, fitted to Cook-Torrance BRDF, using \ln error metric, $g(x) = \ln(x)$	136
40	Comparison of various isotropic microfacet distribution functions. $D_{bm,u}$ and $D_{e,u}$ are unnormalized. D_c is an approximation to D_b (and thus also to D_g).	137
41	Fit of Cook-Torrance BRDF to MERL nickel.binary file at 20° , 40° , and 60° . The Gaussian facet distribution appears to be the improper shape for this BRDF data, suggesting a better result may be obtained through use of a different microfacet distribution function. The lines represent the best fit and the dots represent the BRDF data from Matusik's MERL database[42].	138
42	Fit of modified Cook-Torrance BRDF to MERL Nickel file at 20° , 40° , and 60° . This modified form is identical to Cook-Torrance, except with the Hyper-Cauchy distribution function in place of the Beckmann (Gaussian) distribution function. This modified form is a significantly better fit to the data. The lines represent the best fit and the dots represent the BRDF data from Matusik's MERL database[42].	138
43	BRDF for grit-blasted Ni at $3.39\ \mu m$, fitted to Cook-Torrance BRDF with Hyper-Cauchy distribution in place of the Beckmann distribution, using the default error metric, $g(x) = x$	141
44	BRDF for grit-blasted Ni at $3.39\ \mu m$, fitted to Cook-Torrance BRDF with Hyper-Cauchy distribution in place of the Beckmann distribution, using \ln error metric, $g(x) = \ln(x)$	141
45	BRDF for shot-blasted Ni at $3.39\ \mu m$, fitted to Cook-Torrance BRDF with Hyper-Cauchy distribution in place of the Beckmann distribution, using the \ln error metric, $g(x) = \ln(x)$	142
46	BRDF for shot-blasted Ni at $4.4\ \mu m$, fitted to Cook-Torrance BRDF with Hyper-Cauchy distribution in place of the Beckmann distribution, using \ln error metric, $g(x) = \ln(x)$	142

Figure	Page
47	BRDF for shot-blasted Ni at $5.63\ \mu m$, fitted to Cook-Torrance BRDF with Hyper-Cauchy distribution in place of the Beckmann distribution, using the default error metric, $g(x) = x$ 143
48	BRDF for shot-blasted Ni at $10.6\ \mu m$, fitted to Cook-Torrance BRDF with Hyper-Cauchy distribution in place of the Beckmann distribution, using \ln error metric, $g(x) = \ln(x)$ 143
49	BRDF for rough Al at $3.39\ \mu m$, fitted to Cook-Torrance BRDF, using \ln error metric, $g(x) = \ln(x)$ 144
50	BRDF for polished Al at $3.39\ \mu m$, fitted to Cook-Torrance BRDF with Hyper-Cauchy distribution, using \ln error metric, $g(x) = \ln(x)$ 145
51	BRDF for polished Al at $10.6\ \mu m$, fitted to Cook-Torrance BRDF with Hyper-Cauchy distribution, using \ln error metric, $g(x) = \ln(x)$ 145
52	(a) BRDF divided by DHR for grit-blasted Ni measured at $3.39\ \mu m$, in direction cosine space, over the entire interval, and (b) zoomed in near the peak. The dotted lines in (b) represent the width of the BRDF data for each incident angle. The dark solid line on the right side of the horizontal axis represents the mean value of the width. 150
53	BRDF width versus λ for grit-blasted Ni in (a) linear space (with standard deviation), and (b) log-log space. The dotted lines provide guidelines for integer powers of λ 151
54	BRDF width versus λ for shot-blasted Ni in (a) linear space (with standard deviation), and (b) log-log space. 151
55	BRDF width versus λ for polished Ni in (a) linear space (with standard deviation), and (b) log-log space. 151
56	BRDF width versus λ for polished Al in (a) linear space (with standard deviation), and (b) log-log space. 152
57	BRDF width versus λ for rough Al in (a) linear space (with standard deviation), and (b) log-log space. 152

Figure	Page
58	BRDF width versus λ for Infragold® in (a) linear space (with standard deviation), and (b) log-log space. 152
59	BRDF width versus λ for gray paint ($DE = 0$) in (a) linear space (with standard deviation), and (b) log-log space. 153
60	BRDF width versus λ for gray paint ($DE = 2.2$) in (a) linear space (with standard deviation), and (b) log-log space. 153
61	BRDF width versus λ for gray paint ($DE = 4.1$) in (a) linear space (with standard deviation), and (b) log-log space. 153
62	BRDF width versus λ for specular black paint in (a) linear space (with standard deviation), and (b) log-log space. 154
63	BRDF width versus λ for glass in (a) linear space (with standard deviation), and (b) log-log space. 154
64	BRDF width versus λ for rough silver paint sample in (a) linear space (with standard deviation), and (b) log-log space. 154
65	Raw BRDF data for grit-blasted Ni at $\theta_i = 40^\circ$ and all wavelengths, in (a) semilog space, and (b) linear space, zoomed at the peak. 157
66	Raw BRDF data for polished Ni at $\theta_i = 40^\circ$ and all wavelengths, for (a) all angles, and (b) zoomed at the peak. 159
67	Raw BRDF data for Infragold® at $\theta_i = 40^\circ$ and all wavelengths. 160
68	Grit-blasted nickel BRDF at $3.39 \mu m$ in (a) real space, (b) $\Delta\beta$ space, (c) zoomed at peak (with error bars), (d) scaled by $1/\sigma$, (e) scaled and zoomed at peak. All plots are relative to the peak at $\theta_i = 50^\circ$ and divided by DHR.[8] 161

69	Comparison between peak BRDF values in (a,b,c) direction cosine space and (d,e,f) $1/\sigma$ scaled direction cosine space for: (a,d) shot-blasted nickel; (b,e) polished nickel; (c,f) polished aluminum at $\lambda = 3.39 \mu m$. All plots are relative to the peak at $\theta_i = 50^\circ$, and are divided by DHR to account for variation in reflectance.[8]	163
70	Comparison between peak BRDF values in (a,b,c) direction cosine space and (d,e,f) $1/\sigma$ scaled direction cosine space for: (a,d) shot-blasted nickel; (b,e) polished nickel; (c,f) grit-blasted nickel at $\lambda = 10.6 \mu m$. All plots are relative to the peak at $\theta_i = 50^\circ$, and are divided by DHR to account for variation in reflectance.[8]	163
71	Comparison of the ratio of $2F(\theta_d)/Q(\theta_i, \theta_s)$ and S for Nickel at $\lambda = 3.39 \mu m$ ($\tilde{n} = 4.0605 + 12.497i$)[54] with incident angles of: (a) $\theta_i = 0^\circ$, (b) $\theta_i = 15^\circ$, (c) $\theta_i = 30^\circ$, (d) $\theta_i = 45^\circ$, (e) $\theta_i = 60^\circ$, and (f) $\theta_i = 75^\circ$. [7]	174
72	Comparison of the ratio of $2F(\theta_d)/Q(\theta_i, \theta_s)$ and S for fused silica at $\lambda = 3.39 \mu m$ ($\tilde{n} = 1.4091$)[40] with incident angles of: (a) $\theta_i = 0^\circ$, (b) $\theta_i = 15^\circ$, (c) $\theta_i = 30^\circ$, (d) $\theta_i = 45^\circ$, (e) $\theta_i = 60^\circ$, and (f) $\theta_i = 75^\circ$. [7]	174
73	Surface plot of relative difference R_d for four different indices of refraction: (a-d) $\tilde{n} = 4 + 10i$, (e-h) $\tilde{n} = 1.5 + 1i$, (i-l) $\tilde{n} = 1.4$, (m-p) $\tilde{n} = 1.7 + 5i$, (q-t) $\tilde{n} = 0.25 + 3i$. For each index, four different incident angles are plotted: (a,e,i,m,q) $\theta_i = 15^\circ$; (b,f,j,n,r) $\theta_i = 30^\circ$; (c,g,k,o,s) $\theta_i = 45^\circ$; (d,h,l,p,t) $\theta_i = 60^\circ$. The plots are all symmetric about $\phi_s = 180^\circ$. The dotted black line at $\phi_s = 180^\circ$ on the right side of each plot represents in-plane scatter. In each case, $R_d = 0$ when $\theta_i = \theta_s$ and $\phi_s = 180^\circ$; R_d is generally small when θ_i and θ_s are small.	175
74	BRDF for rough Al at $6.4 \mu m$, fitted to Cook-Torrance BRDF, using \ln error metric, $g(x) = \ln(x)$	183
75	BRDF for rough Al at $6.4 \mu m$, fitted to modified Cook-Torrance BRDF using Q in place of F , using \ln error metric, $g(x) = \ln(x)$	183

Figure		Page
76	BRDF for AFIT Infragold® sample at $5.2 \mu m$, fitted to Cook-Torrance BRDF, using \ln error metric, $g(x) = \ln(x)$	184
77	BRDF for AFIT Infragold® sample at $5.2 \mu m$, fitted to modified Cook-Torrance BRDF using Q in place of F , using \ln error metric, $g(x) = \ln(x)$	184
78	BRDF data, with error bars, for rough Al at $6.4 \mu m$ and $\theta_i = 50^\circ$ compared to both the original Cook-Torrance model fit and the modified Cook-Torrance model fit using Q in place of F	185
79	BRDF data for rough Al at $6.4 \mu m$ and $\theta_i = 50^\circ$ compared to both the original Cook-Torrance model fit and the modified Cook-Torrance model fit using Q in place of F , on semilog plot.	185
80	BRDF data, with error bars, for Infragold® at $5.2 \mu m$ and $\theta_i = 50^\circ$ compared to both the original Cook-Torrance model fit and the modified Cook-Torrance model fit using Q in place of F	186
81	BRDF data, with error bars, for Infragold® at $5.2 \mu m$ and $\theta_i = 50^\circ$ compared to both the original Cook-Torrance model fit and the modified Cook-Torrance model fit using Q in place of F , on semilog plot.	186

List of Tables

Table		Page
2.1	Ratio of Radiance Component to Total Radiance, assuming Lambertian BRDF	18
3.1	Common Unpolarized Microfacet BRDF Models	67
3.2	Summary of Modified Cauchy Distribution fits for NEF Materials	85
4.1	Relative error in reported unpolarized BRDF measurements using the AFIT CASI® system	123
5.1	Summary of BRDF data collected using CASI®	128
5.2	Norm of difference in BRDFs for each material measured. BRDF is scaled by weight functions w given by each column header (“Raw” indicates no scaling.)	162
6.1	Comparison of the norm of the relative difference, d , when fitting BRDF data to the Cook-Torrance model using the \ln error metric, and the relative difference using the Modified Cook-Torrance model (using Q instead of F), for multiple diffuse samples, at all wavelengths measured. The largest relative uncertainty at any single data point for any incident and scattered angle is also reported.	187
6.2	Values of g for Ni samples with known surface statistics. For each incident angle, the value reported is for specular scatter ($\theta_s = \theta_i$).	190

List of Symbols

<i>Symbol</i>	<i>Definition</i>
$\vec{\mathbf{B}}$	Magnetic field
$\vec{\mathbf{D}}$	Macroscopic electric field
D	Microfacet distribution function
$\vec{\mathbf{E}}$	Electric field
E_{SE}	Solar irradiance
E_i	Incident irradiance
F	Fresnel reflectance (unpolarized)
F_{bk}	Geometric factor from BK
F_p	Fresnel reflectance (p polarization)
F_s	Fresnel reflectance (s polarization)
G	Geometric attenuation (shadowing and masking)
$\vec{\mathbf{H}}$	Macroscopic magnetic field
$\vec{\mathbf{J}}$	Free current density
L_B	Blackbody radiance
L_S	Solar radiance
L_d	Diffuse downwelling radiance
L_e	Self-emitted radiance
L_p	Pupil plane radiance
L_{path}	Path radiance

L_s	Scattered radiance
$\overset{\leftrightarrow}{\mathbf{M}}$	Mueller matrix
P	Pre-factor term
Q	Polarization factor
R_d	Relative difference
S	Scaling relationship between F and Q
$\mathbb{R}_a(\beta)$	Right-hand rotation about axis a
T_B	Temperature
V	Directional volumetric scattering
Ω_{SE}	Solid angle subtended by the Sun from Earth
c	Speed of light
f_p	Polished MBK BRDF model
f_r	BRDF
$\overset{\leftrightarrow}{\mathbf{f}}_r$	Polarimetric BRDF
f_{vr}	Very rough MBK BRDF model
f_μ	Microfacet BRDF model
h	Planck's constant
k	Boltzmann's constant
$\vec{\mathbf{k}}$	Wave vector
l_c	Correlation length
m	Beckmann distribution width parameter
n	Index of refraction (real component)

\tilde{n}	Index of refraction (complex)
$\hat{\mathbf{n}}$	Surface normal vector
$\vec{\mathbf{r}}$	Position vector
$\vec{\mathbf{s}}$	Stokes vector
ε	Permittivity
η_r	Radial direction cosine space angle
θ	Depression angle relative to surface normal
θ_d	Depression angle of incident vector in microfacet coordinates
θ_h	Depression angle of half vector in microfacet coordinates
θ_i	Depression angle of incident light
θ_s	Depression angle of scattered light
κ	Index of refraction (imaginary component)
λ	Wavelength of light
μ	Permeability
ρ	DHR
ρ_d	Diffuse model parameter
ρ_f	Free charge density
ρ_H	HDR
ρ_s	Specular model parameter
ρ_v	Volumetric model parameter
σ	Cross section conversion term
σ_g	Microfacet distribution gaussian width parameter

σ_h	Surface height standard deviation
ϕ	Azimuthal angle
ϕ_d	Azimuthal angle of incident vector in microfacet coordinates
ϕ_h	Azimuthal angle of half vector in microfacet coordinates
ϕ_i	Azimuthal angle of incident light
ϕ_s	Azimuthal angle of scattered light
ω	Angular frequency
$\hat{\omega}_d$	Difference angle vector (θ_d, ϕ_d)
$\hat{\omega}_h$	Half angle vector (θ_h, ϕ_h)
$\hat{\omega}_i$	Incident angle vector (θ_i, ϕ_i)
$\hat{\omega}_s$	Scattered angle vector (θ_s, ϕ_s)

List of Acronyms

<i>Acronym</i>	<i>Definition</i>
AFRL	Air Force Research Laboratory
ASF	Angle Spread Function
BK	Beckmann-Kirchhoff
BRDF	Bidirectional Reflectance Distribution Function
CASI	Complete Angle Scatter Instrument
DHR	Directional-Hemispherical Reflectance
DoLP	Degree of Linear Polarization
DoP	Degree of Polarization
DRR	Dual Rotating Retarder
GHS	Generalized Harvey-Shack
HDR	Hemispherical-Directional Reflectance
HSRS	Hyperspectral Remote Sensing
IR	Infrared
LWIR	Long-Wave Infrared (7 - 12 μm)
MBK	Modified Beckmann-Kirchhoff
MERL	Mitsubishi Electric Research Laboratories
MWIR	Mid-Wave Infrared (3 - 7 μm)
NEF	Non-conventional Exploitation Factors
NIST	National Institute of Standards and Technology

pBRDF	Polarimetric Bidirectional Reflectance Distribution Function
QCL	Quantum Cascade Laser
SMS	Schmitt Measurement Systems
SWIR	Short-Wave Infrared (1 - 3 μm)
VNIR	Visible and Near-Infrared (0.4 - 1 μm)

EXPERIMENTAL AND THEORETICAL BASIS FOR A CLOSED-FORM SPECTRAL BRDF MODEL

I. Introduction

Hyperspectral Remote Sensing (HSRS) is an area of interest to the Air Force for its use in material identification. In HSRS, a data cube is captured containing two-dimensional spatial data for several wavelengths, typically spanning the Visible and Short-Wave Infrared (SWIR), Mid-Wave Infrared (MWIR), or Long-Wave Infrared (LWIR) spectrum [19]. In such a collection, one must make an assumption about how light is reflected off materials in the scene.

To date, HSRS has primarily relied upon a diffuse (Lambertian) approximation to scattering that is not representative of all materials [19]. Instead of assuming a Lambertian reflector, a more general approach is described by a Bidirectional Reflectance Distribution Function (BRDF). The BRDF is a 5-dimensional function that defines the reflectance distribution of a surface for any incident solid angle, outgoing solid angle, and wavelength for realistic surfaces expected to be observed in a remotely sensed scene [48]. As the function space is so large and general electromagnetic calculations for realistic surfaces are quite complex, BRDF models have been developed to make measurement possible without sampling the entire 5-dimensional space. These models generally focus on the angular dependence of BRDFs, and do not often account for the wavelength dependence of the BRDF.

In HSRS, it is possible to obtain very fine wavelength spacing, and variations in the BRDF as a function of wavelength may provide important clues for material identification. Since HSRS is often focused on identifying the complex index of re-

fraction (or analogously the complex dielectric constant) of a material in a remotely sensed scene, it is most desirable to develop a model that directly accounts for all wavelength dependences in the scene that are not related to the complex index of refraction, leaving only the wavelength variations relating to the complex index of refraction to make a material identification.

Typical measurements of the BRDF of a sample are made at a relatively small number of wavelengths, then interpolated based on unitless directional reflectance measurements to scale the overall functional shape. (The unitless directional reflectance is the integral of the BRDF over the hemisphere.) In the MWIR/LWIR, one common technique is to linearly interpolate between $3.39\ \mu\text{m}$ and $10.6\ \mu\text{m}$ to obtain estimated BRDF values. However, this linear interpolation in the MWIR and LWIR has not been experimentally verified in the literature. Furthermore, a preliminary analysis based on existing BRDF data that is presented in Chapter III suggests this linear interpolation may not accurately account for BRDF wavelength variation.

Since the linear interpolation is not well quantified in the literature, it is helpful to examine BRDF models to gain insight on what may have a spectral dependence. When examining BRDF models, one popular class of models is the microfacet model, which assumes diffraction and interference effects are negligible. A detailed analysis of these models is discussed in Chapter III. Neglecting volumetric reflection effects (which are not directly modeled by the microfacet theory), this class of models has a known wavelength dependence only in the Fresnel reflection term, directly related to the index of refraction of a material. However, when examining certain BRDF databases that assume a microfacet BRDF model, such as the Non-conventional Exploitation Factors (NEF) database [46], it is known that the size of the specular reflection lobe also changes as a function of wavelength. It is therefore anticipated that experimental investigation of BRDFs in the MWIR and LWIR may result in

uncovering other wavelength dependencies currently unaccounted for, beyond the complex index of refraction. These wavelength dependencies that are unaccounted for in microfacet BRDF models have the potential to be wrongly attributed to the index of refraction.

1.1 Problem Statement

The overarching problem to be solved by research in the area of spectral BRDF variation is to develop a closed-form BRDF approximation that accounts for the wavelength-dependent properties of the BRDF, while accurately describing the BRDF properties of a wide class of materials. A closed-form approximation that is not highly parameterized is desirable because HSRS already faces the monumental task of determining atmospheric properties from a remotely-sensed scene, which is an area of intense and ongoing research.

Solving this entire problem is beyond the scope of this research. The problem can initially be broken down as follows:

- Determine whether BRDF may have a significant impact on HSRS using a basic scene model
- Catalog current closed-form, physics-based BRDF models
- Determine whether current models can be modified in a simple manner to insert a wavelength-dependent term
- If a simple modification is not possible, determine how closed-form geometric optics models relate to more accurate (but more computationally complex) physical optics BRDF models to understand how to arrive at novel closed-form approximations

- Test novel closed-form approximations to the BRDF
- Propose a novel, physics-based, closed-form approximation to the BRDF suitable for HSRS that works at a wide range of wavelengths and for a wide class of materials

The first four items in the list are developed in this work. Additionally, a novel closed-form approximation to the BRDF, motivated by physical optics, is presented for rough surfaces that more accurately describes the BRDF without adding any additional parameters; this approach is generic enough to apply to any BRDF model that uses a Fresnel reflection component. The rough and polished surface spectral variation is developed from theory, and is backed by measured spectral BRDF data, providing the basis for a comprehensive spectral model to be developed in the future.

Figure 1 illustrates the problem addressed by this dissertation. Items in blue are provided as background. Items in green are addressed in this dissertation. The item in yellow is identified for future work.

The initial approach was to proceed down the left column of Figure 1, using existing physically based closed-form BRDF models to fit measured spectral BRDF data to a model, then determine how the model parameters vary with wavelength. However, as will be detailed in Chapter V, BRDF fitting was more problematic than initially expected, with fit error in excess of an order of magnitude for a material spanning four orders of magnitude in dynamic range of the BRDF. This problem could be due to the microfacet distribution function, which is primarily responsible for the overall shape of the BRDF, so the next step was to perform BRDF fitting using a more flexible distribution function. That approach was marginally better, but the fits still differed significantly from measured data by as much as an order of magnitude. The next step was to examine the raw BRDF data and determine whether the width of the specular lobe is varying in a similar manner in all datasets measured,

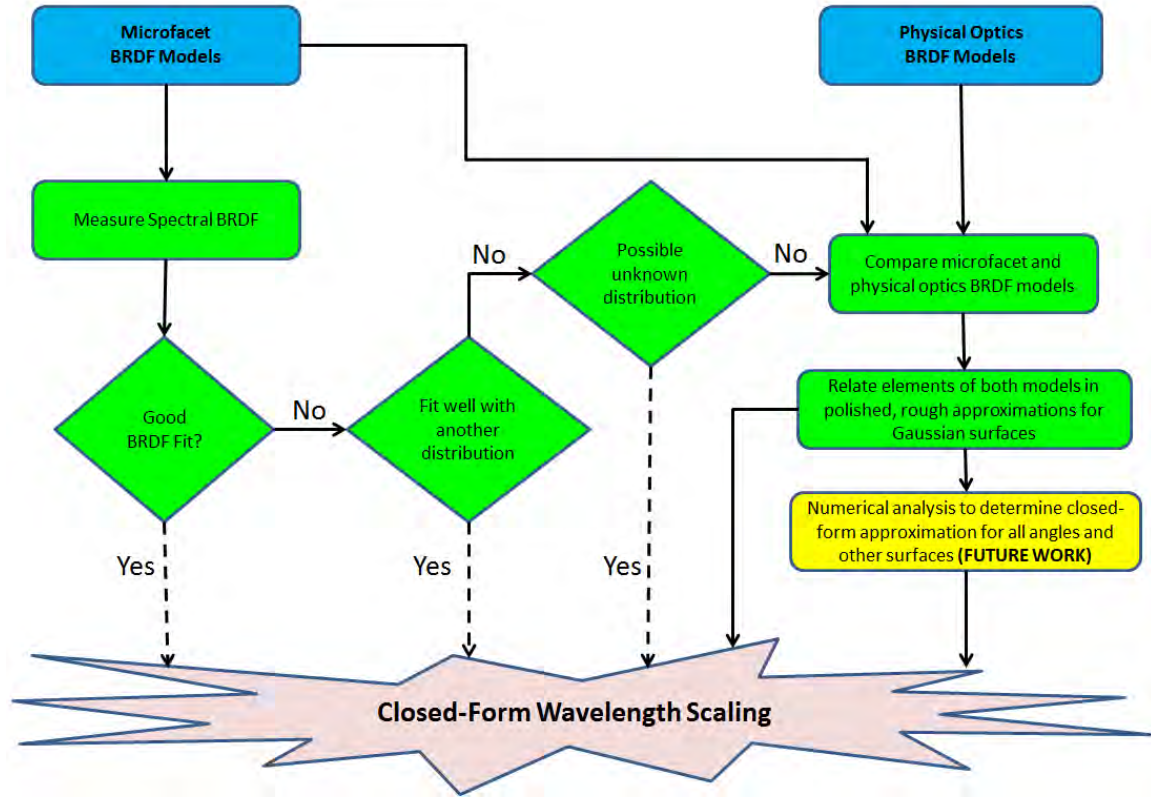


Figure 1. Illustration of the problem addressed by this dissertation. Items with a blue background are described in the background. Items with a green background are addressed in this dissertation. The item with a yellow background is left for future work.

which could indicate there is a possible unknown distribution that could be developed to perform the wavelength scaling. (As will be discussed in Chapter III, the specular lobe is where the greatest error occurs in current microfacet BRDF wavelength scaling techniques, which is why this attribute was chosen for further examination.) This method failed to produce consistent results, indicating a parameter modification to existing models was not straightforward.

Since these methods all failed, it appears there are fundamental flaws with the closed-form microfacet BRDF approximation. Another class of BRDF models, physical optics models, includes diffraction, but results in a model that has no known general closed-form approximation that is valid over the entire hemisphere. For this

reason, direct use of a physical optics model was not considered. However, if these physical optics models could be compared to the microfacet models, which are closed-form, it may be possible to learn what may be improved in the microfacet model to determine how to better approximate the BRDF with a closed-form model. This novel comparison is performed in Chapter VI. This comparison leads to a relationship between the closed-form elements of both types of models in the limits of a polished or very rough surface. These novel theoretical developments are backed by experimental observations developed in the analysis of the measured spectral data, leading to confidence in the closed-form wavelength scaling for these two limiting cases and an understanding of how to expand this relationship to other angles and surfaces. These theoretical results form a basis for the future development of a comprehensive spectral BRDF model.

1.2 Dissertation Organization

Chapter II addresses whether the BRDF may have a noticeable impact on HSRS by assuming a very basic scene and comparing the results of a scene with a Lambertian model to the results of a scene with a BRDF model. Following the development presented in [6], this chapter shows that, in a basic scene model, the BRDF has the potential to affect the calculated brightness temperature of objects in a scene dramatically. Furthermore, the BRDF has potential to affect the spectral results observed.

In Chapter III, BRDF theory is presented in depth. This chapter includes an overview of common microfacet (geometric optics) BRDF models that have been rewritten into a common form that more readily allows for direct comparison, following the development in [5]. A brief expansion into polarimetric BRDF models is then developed, followed by examination of current wavelength-dependent techniques.

The deficiencies in current wavelength-dependent scaling techniques for closed-form microfacet models is then discussed. Finally, this chapter presents background on one of the more complete physical optics-based BRDF models. Although this model has no general closed-form that is easy to compute, it will be instructive later in this dissertation.

Chapter IV next describes the measurement process used to gather wavelength-dependent experimental BRDF data. To uncover the wavelength dependence, BRDF data was collected at multiple wavelengths between $3.39\ \mu\text{m}$ and $10.6\ \mu\text{m}$ using HeNe, CO₂, and Quantum Cascade Lasers (QCLs). These measurements are quite time-consuming to make, but proper BRDF measurements require the high intensity and narrow wavelength band of laser sources at fixed wavelengths because the range of the BRDF function spans several orders of magnitude. This chapter includes a discussion of how to measure polarimetric BRDF, which was the initial approach planned for this work, then presents some results from measurements made on a few samples to determine that unpolarized measurements can be made in a much simpler fashion. That simpler process is then outlined. The chapter concludes with an uncertainty analysis for the measurement process used in this dissertation.

Chapter V then presents results from the measured BRDF data of 12 different samples at up to seven different wavelengths. This chapter addresses the third item discussed in Section 1.1, attempting to add a simple wavelength dependence to the BRDF. Initially, the approach to be taken was to fit these BRDFs to microfacet (geometric optics) models and observe the wavelength scaling that may need to be added to the microfacet models. However, after beginning this process, it became apparent that there were actual deficiencies in the microfacet model itself that needed to be better understood. With this observation, it also became apparent that the microfacet model needed to be examined in more detail to explain the wavelength variation.

From that initial attempt, three key observations are made: there is no straightforward wavelength-dependent addition that can be inserted into current models; there does not appear to be a simple modification to current models that would allow for a simple wavelength-dependent addition; and even at a single wavelength, closed-form BRDF models do not fit a wide class of materials well; it is especially problematic as wavelength increases (since materials become more specular). This chapter concludes by examining the role of the cross section conversion term, which is a part of microfacet models, and which diverges to infinity at grazing angles but plays a key role in microfacet BRDF models to explain a difference in magnitude of the specular peak as a function of angle; this discussion at the end of Chapter V was published in [8]. At the end of this chapter, it becomes apparent that novel theoretical developments are required to make progress on understanding how to properly account for the wavelength dependence of the BRDF.

The BRDF literature tends to pick either microfacet models (for a closed-form model) or scalar wave optics models (for a more physically accurate solution at the expense of much greater computational resources being required). This dissertation uses both models to determine similarities and differences, leading to enhanced physical insight as to what the microfacet model actually represents. Chapter VI presents novel theoretical work to address the fourth item in the problem statement by comparing the microfacet (geometric optics) BRDF models to scalar wave optics BRDF models, following the discussion in [7] and in a journal article submitted to *Optics Express* [10]. This comparison is performed in both the polished and very rough surface limits, and represents the development of a novel theoretical understanding of where each term in the microfacet model derives in a scalar wave optics BRDF approach. Furthermore, the developments in this chapter provide a theoretical explanation for the results observed in Chapter V when examining the experimental BRDF

data. An understanding of the limitations of current microfacet models is thoroughly developed, and for the first time each term in the microfacet BRDF model is directly related to terms in a scalar wave optics BRDF model. Finally, this chapter proposes a novel BRDF model, based upon these theoretical results. This novel BRDF model allows for more accurate BRDF fitting at large incident or scattered angle, while not compromising the BRDF fit at other angles.

Finally, Chapter VII summarizes key results and discusses future work.

II. Impact of BRDF on Basic HSRS Model

In this chapter, the motivation for applying a BRDF to HSRS is developed. A very simple scene model is developed for a notional hyperspectral scene. Then, the radiance and brightness temperature are calculated for a few different BRDF models, and compared to the Lambertian case (which is currently used in many hyperspectral algorithms). The purpose of this chapter is to show the potential impact of the BRDF on HSRS. This work was presented at SPIE Optics and Photonics in 2014[6].

The BRDF defines the ratio of the exiting reflected radiance to the incident irradiance for materials; that is, it describes optical scatter off all surfaces, even if it is not perfectly smooth. Nicodemus formally defined the BRDF as [48]

$$f_r(\hat{\omega}_i, \hat{\omega}_s, \lambda) = \frac{dL_s(\hat{\omega}_i, \hat{\omega}_s, \lambda)}{dE_i(\hat{\omega}_i, \lambda)}.$$

In this notation, λ represents the wavelength of light, $\hat{\omega}_i$ is the incident unit vector, and $\hat{\omega}_s$ is the scattered (outgoing) unit vector, where $\hat{\omega} = [1, \theta, \phi]^T$ is a unit vector pointing from the point of intersection with the material's surface to the incident (or outgoing) direction, with spherical coordinates θ and ϕ (assuming $\hat{\mathbf{z}}$ is normal to the surface); see Figure 2. L_s represents the scattered radiance, and E_i represents the incident irradiance. Since the BRDF is defined by radiometric quantities and not directly from Maxwell's equations, there are several different BRDF models currently in use; these models will be discussed in Chapter III in depth.

Total hemispherical-directional reflectance (HDR) for a specified observer location $\hat{\omega}_s$ and all incident angles $\hat{\omega}_i$ can be obtained from the BRDF as

$$\rho_H(\hat{\omega}_s) = \int_0^{2\pi} \int_0^{\pi/2} f_r(\hat{\omega}_i, \hat{\omega}_s) \cos \theta_i \sin \theta_i d\theta_i d\phi_i. \quad (1)$$

The HDR, which can be computed from the BRDF, is what is typically thought of

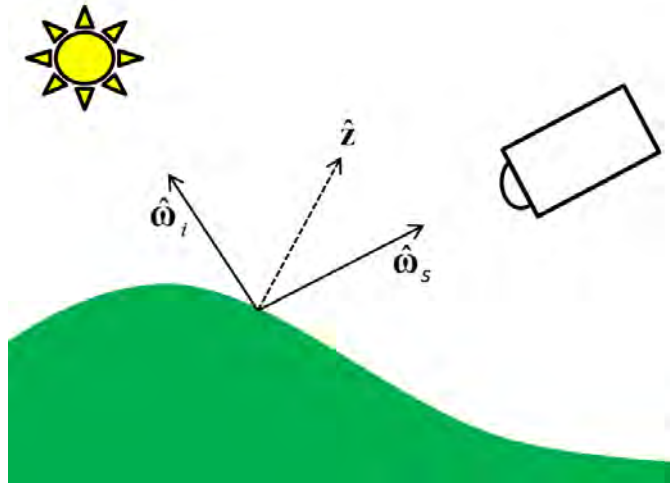


Figure 2. Basic BRDF geometry, with incident and outgoing vectors relative to the surface normal \hat{z}

as reflectance; that is, it is unitless and constrained to be between 0 and 1. However, it may still depend on viewing direction. The BRDF is a *reflectance distribution per solid angle*, possessing units of sr^{-1} and depending on both incident and scattered angles. Since the BRDF is not unitless, its value can be any non-negative number, even if it is larger than 1, as long as the BRDF integrates to a unitless HDR that is between 0 and 1.

This chapter deals with two BRDF models: Lambertian and measured BRDF data from Matusik’s Mitsubishi Electronic Research Laboratories (MERL) database [42]. Although the MERL database consists of visible BRDF data, the datasets provide densely-populated, measured BRDF data for materials with reflectance distributions that could notionally exist in the LWIR. Furthermore, the MERL data is measured over three wavelength bands (red, green, and blue). The primary motivation for using actual measured BRDF data instead of relying on a BRDF model is to ensure observations are not due to errors in the BRDF model, as no universally accepted model currently exists. Furthermore, densely-populated BRDF data measured at multiple wavelengths in the LWIR (or in the MWIR) for the same material is currently

not readily available, as will be discussed in Chapter III.

A simple scene model is developed to analyze geometric effects in the LWIR. Two cases are then analyzed: first, treating the BRDF of an object in the scene as Lambertian; second, treating the BRDF of an object as having the shape of a material in the MERL database. For each case, the BRDF is scaled to an HDR of 0.1, 0.5, and 0.9; thus, there are a total of six simulations. The relative contributions of solar, diffuse downwelling, and self-emissive radiation to the overall scene are then analyzed. Results suggest non-negligible solar radiation at certain observer geometries may occur even in the LWIR when using a BRDF model in place of the Lambertian assumption.

Next, this model is extended to obtain the pupil plane radiance at three different wavelengths, using three different measured BRDFs of the same material from the MERL database. In this model, the BRDFs were assigned to represent a notional material at $8\text{ }\mu\text{m}$, $10\text{ }\mu\text{m}$, and $12\text{ }\mu\text{m}$. The wavelength-dependent result was analyzed for a fixed incident geometry and fixed maximum HDR of 0.9 at all wavelengths, at a few different observer geometries. Results from this model indicate that the shape of the resulting pupil plane radiance as a function of wavelength changes, not just the overall magnitude. These results suggest there is value in pursuing further research into incorporating BRDF models in the LWIR.

2.1 Scene Model

In this section, the two main components of the scene model will be discussed: pupil plane radiance calculation and incorporating the MERL BRDF into the scene.

Radiance Model.

The pupil plane radiance at the observer can be expressed under this simple model as

$$L_p(\hat{\omega}_i, \hat{\omega}_s, \lambda) = L_S(\hat{\omega}_i, \hat{\omega}_s, \lambda) + L_e(\hat{\omega}_s, \lambda) + L_d(\hat{\omega}_s, \lambda) + L_{path}(\lambda), \quad (2)$$

where L_p is the pupil plane radiance, L_S is the solar radiance upon reflection off the object, L_e is the radiance due to self-emission of the object, L_d is the radiance due to diffuse downwelling atmospheric emission reflected off the object, and L_{path} is the path radiance. Since this chapter is dealing primarily with a comparison between the Lambertian approximation and a more directional BRDF, L_{path} was neglected since it does not depend on geometry, BRDF, or HDR; it would essentially add the same constant offset to each wavelength in both the directional BRDF and Lambertian cases.

The radiance model used in this chapter is a simple model that assumes the atmosphere is a spherical shell above the observer—that is, it produces the diffuse downwelling contribution L_d to the pupil plane radiance related to blackbody radiation. Atmospheric transmission is not modeled; it is again assumed to be a constant. See Figure 3 for a graphical representation of this basic model.

Under such a simple atmospheric model, the terms L_S , L_e , and L_d can be expanded in a straightforward manner. Let $L_B(T, \lambda)$ represent the blackbody radiance of an object at a given temperature T . The remaining radiances are specified as follows:

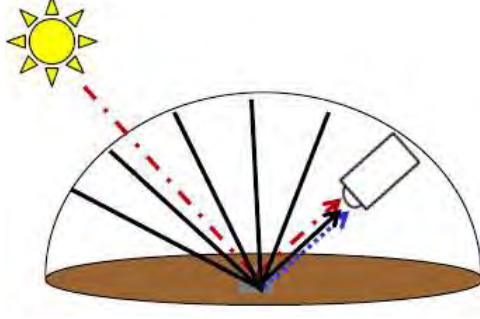


Figure 3. Basic model of the scene employed by this BRDF study. The atmosphere is treated as a shell with radiation profile of a blackbody at 250 K; the object is assumed to be a graybody at 300 K; the Sun is assumed to be a blackbody at 5800 K.

$$\begin{aligned}
 L_S(\hat{\omega}_i, \hat{\omega}_s, \lambda) &= E_{SE}(\theta_i, \lambda) f_r(\hat{\omega}_i, \hat{\omega}_s, \lambda) \\
 &= [\Omega_{SE} L_B(T_S, \lambda) \cos \theta_i] f_r(\hat{\omega}_i, \hat{\omega}_s, \lambda) \\
 L_e(\hat{\omega}_s, \lambda) &= [1 - \rho_H(\hat{\omega}_s)] L_B(T_o, \lambda) \\
 L_d(\hat{\omega}_s, \lambda) &= \rho_H(\hat{\omega}_s) L_B(T_a, \lambda),
 \end{aligned} \tag{3}$$

where E_{SE} is the solar irradiance incident upon the object and Ω_{SE} is the mean solid angle subtended by the Sun from Earth, approximated from the mean distance from the Earth to the Sun and the radius of the Sun. For this model, $T_S = 5800 \text{ K}$ was assumed for the approximate solar blackbody temperature. The surface is assumed to lie flat on the ground, and is assumed to be isotropic. In this case, there is an ambiguity in ϕ : this dissertation adopts the convention that $\phi_i = 0$ to resolve this ambiguity. (The Sun's azimuthal orientation defines the $\phi = 0$ location). The Sun's depression angle is represented by θ_i , which is measured relative to the surface normal of the object. The object is assumed to be at $T_o = 300 \text{ K}$ and the atmospheric downwelling radiation is approximated as a blackbody at $T_a = 250 \text{ K}$. This simple model is a good starting point to eliminate all variables except those related directly to BRDF; such an analysis is beneficial as a first step prior to the more time-consuming application of a complex atmospheric model.

MERL BRDF Data in HSRS Scene.

In the modeling equations presented in the previous section, the BRDF of the object is used directly in calculation of L_S ; it is also used indirectly via the HDR in calculation of L_e and L_d . In this chapter, two BRDF shapes are analyzed. For the first BRDF shape, a single-parameter Lambertian BRDF is analyzed, using the following equation:

$$f_r(\hat{\omega}_i, \hat{\omega}_s, \lambda) = \frac{\rho_d}{\pi} \quad (4)$$

where ρ_d is a parameter equal to the HDR; this was set to 0.1, 0.5, or 0.9 to analyze three different reflectances. This scaling would be analogous to considering three different notional materials in a scene that all had the same general BRDF shape, but a different overall reflectance, and thus a different overall magnitude to the BRDF. For a Lambertian BRDF, the reflectance does not vary with incident angle, although this is not generally true for most BRDF models. The Lambertian BRDF is chosen because it is commonly assumed in HSRS[19].

The second BRDF shape used was from nickel in Matusik’s MERL database[42]. The MERL database was chosen so the actual shape of a BRDF would be used instead of a modeled shape, as the question of which BRDF model to use is still an area of active research in computer graphics and scene generation[1, 13, 18, 33, 45, 71, 72]; in fact, even when restricting data to the MERL database, there is no universally best model, as determined in a study by Ngan[47]. (This will be further discussed in Chapter III.) In the MERL database, there is no equation governing the BRDF model. Instead, isotropic BRDF data were obtained for 100 different materials by illuminating a sphere, allowing collection for several incident and reflected angles simultaneously. The red, green, and blue channels of a camera were used to collect the data[42]. These data were densely sampled in both $\hat{\omega}_i$ and $\hat{\omega}_s$, and stored in

Rusinkiewicz microfacet coordinates[56]; this coordinate system is discussed more in Chapter III.

A detailed uncertainty analysis was not presented for the MERL data. However, as will be discussed in detail when performing an error analysis on my BRDF measurements in Chapter IV, the BRDF data is most difficult to measure accurately at two locations: the peak, and grazing angles. For the measurements presented later in this work, BRDF data is not measured at grazing angles, but Matusik does make grazing angle measurements without being careful to account for potential grazing angle inaccuracies. For this reason, steep BRDF data (that is, θ_i or θ_s near 90°) is unreliable due to increased noise in the data collection method. As a reminder of this, all plots showing $\theta > 70^\circ$ are shaded gray in that region. Since it is expected that materials become more specular in the LWIR than in the visible portion of the spectrum, these results are expected to be more significant in the LWIR; thus, using this visible BRDF data serves as a reasonable preliminary analysis. As was shown in [25] and will be shown in Chapter V, more carefully measured BRDF data can result in values that are in excess of the maximum BRDF value used in this initial study, showing the peak values used here are not unreasonable. The MERL dataset is being used here to motivate a more detailed examination of BRDF spectral dependence, but it is not used to draw conclusions on what the form of the spectral dependence is.

C++ and MATLAB® wrappers were written to read the MERL binary files and provide a convenient interface for analyzing these data. These wrappers were based on code included with the MERL database[42]. Additionally, the code created for this work performs trilinear interpolation between data points in the MERL binary file, as well as object-oriented encapsulation, error checking, HDR integration routines, and a MEX interface between MATLAB® and C++.

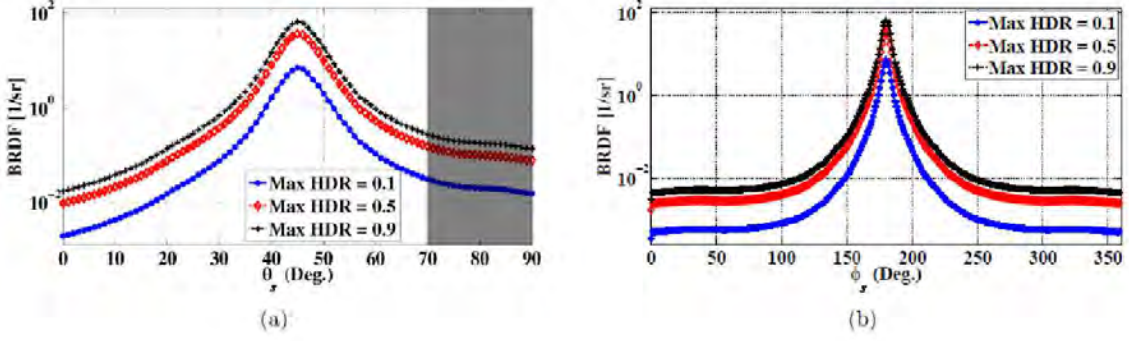


Figure 4. BRDF shape from MERL nickel file, scaled to HDRs of 0.1, 0.5, and 0.9, plotted in two slices: (a) In-plane slice in θ_s for $\theta_i = 45^\circ$ and $\Delta\phi = 180^\circ$; (b) Out-of-plane slice in ϕ_s for $\theta_i = \theta_s = 45^\circ$ and $\phi_i = 0^\circ$. The shaded region represents grazing angle data, which is more prone to experimental error.

For this analysis, the MERL nickel material’s channel 0 (red channel) data was used to provide the notional shape of a glossy BRDF at $\lambda = 8\,\mu m$. The BRDF was scaled to a maximum HDR of 0.1, 0.5, or 0.9 to compare three different reflectances to the Lambertian case while still ensuring conservation of energy for all Sun and observer geometries. Unlike the Lambertian case, the reflectance (HDR) does vary with θ_s (although it does not vary with ϕ_s since the material is assumed to be isotropic; that is, azimuthally symmetric). The scaled BRDFs are plotted in Figure 4, and resulting HDRs are plotted in Figure 5. Notice the HDR approaches 0 at steep angles instead of approaching 1; this is due to the experimental error in the MERL database at steep angles (as noted previously); in general, the HDR remains roughly constant for angles where the data is more reliable, for this particular BRDF shape.

The magnitude of the specular peak of this BRDF does not appear to be unrealistic for a notional material in the LWIR. It is not unusual for materials to contain relatively large BRDF values (exceeding $100\,sr^{-1}$). In fact, Harkiss showed that the peak value of the BRDF of bare aluminum at $\lambda = 10.6\,\mu m$ ranges from 10^3 to $10^5\,1/sr$, depending upon viewing geometry, while possessing an HDR of about 0.9[25]. Thus, the shape of the densely-populated BRDF from the MERL database, although measured in

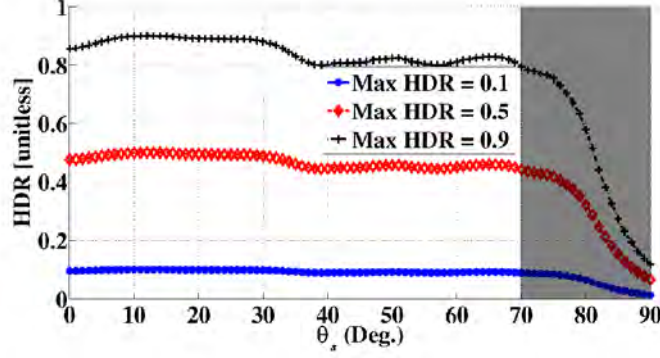


Figure 5. MERL nickel scaled HDR for $\theta_i = 45^\circ$, $\phi_i = 0$ (for any ϕ_o). The shaded region represents grazing angle data, which is more prone to experimental error.

red, green, and blue channels, is not an anomaly when used to represent a notional material in the LWIR.

2.2 Basic Model Results

In the previous section, all components of a simple scene model at a single wavelength were discussed. These equations, together with the MERL BRDF data, were analyzed at $\lambda = 8 \mu m$ in this section.

For the Lambertian cases ($\rho_d = 0.1$, 0.5 , and 0.9), the results do not vary with observation angle since the Lambertian BRDF does not vary with observation angle. As the reflectance varies, the relative importance of the emissive and diffuse downwelling components varies (and thus both components should be kept in a LWIR model), but the solar component is never more than a few percent of the total observed radiance.

Table 2.1. Ratio of Radiance Component to Total Radiance, assuming Lambertian BRDF

	$\rho_d = 0.1$	$\rho_d = 0.5$	$\rho_d = 0.9$
L_S/L_P	0.0018	0.0128	0.0392
L_e/L_P	0.9659	0.7588	0.2590
L_d/L_P	0.0323	0.2284	0.7017

These results are summarized in Table 2.1. This observed behavior is in line with the common assumption that solar reflection is unimportant in the LWIR.

When the previously discussed MERL BRDF model representing a notional glossy BRDF with a reflectance of 0.1, 0.5, or 0.9 is analyzed using the same process, the results are substantially different; the relative contribution of each component now becomes dependent upon viewing geometry. These results are plotted in Figure 6. Although for many observer geometries the solar reflection may be negligible, as one approaches the specular lobe of a material, the solar reflection becomes non-negligible even at $\lambda = 8\mu m$; in fact, the solar reflection may become the most significant component of the observed total pupil plane radiance. This result challenges an assumption that is made within some communities such as HSRS, where in the LWIR band solar radiation is assumed to have negligible impact[19].

Another way to visualize these data is to pick a solar position and a threshold value (such as 10%), and create a 3-D plot of all points within the hemisphere where the solar reflection is at least 10% of the total observed radiance (that is, plot all points on the hemisphere where $L_S/L_p > T$, where T is a threshold value). For a threshold of 10% with the MERL nickel BRDF scaled to an HDR of 0.9, the results are plotted in Figure 7. As shown in that figure, there is a non-negligible portion of the hemisphere where the solar specular reflection is at least 10% of the total pupil plane radiance; however, this region does not constitute a majority of the hemispherical region for this material. Thus, the effect of solar reflection is highly directionally dependent. It may appear in a relatively significant fraction of the hemisphere, but it is not a significant factor everywhere in the hemisphere. Thus, care should be taken to identify when the Sun-object-sensor geometry has a significant influence on the observed radiance.

It is also useful to visualize the effect on pupil plane radiance in an absolute sense,

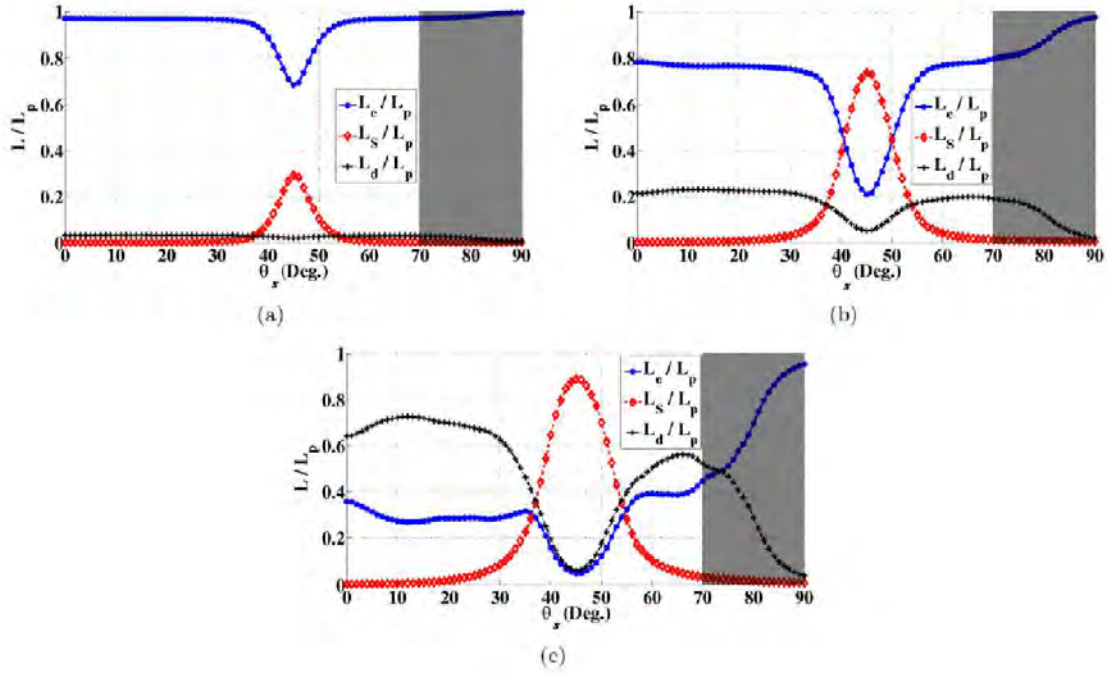


Figure 6. Ratios of self-emissive, solar, and diffuse downwelling radiances to total observed pupil plane radiance, for $\theta_i = 45^\circ$ and $\Delta\phi = 180^\circ$. The MERL nickel BRDF shape was scaled to result in a maximum HDR of three different values: (a) 0.1, (b) 0.5, and (c) 0.9; all other parameters remained fixed between the three plots. The shaded region represents grazing angle data, which is prone to experimental error.

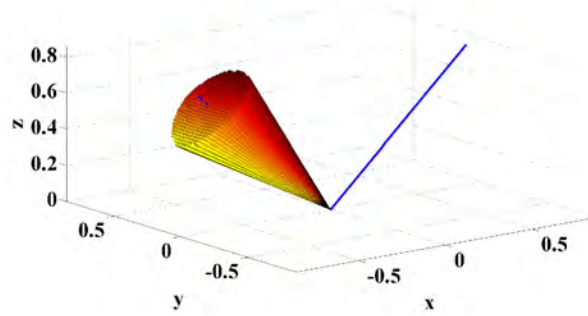


Figure 7. Hemispherical view of the conical region where $L_S/L_p > 0.1$ for a BRDF shape of nickel with an HDR of 0.9. The solid blue line is the incident vector ($\theta_i = 45^\circ$); the dotted blue line represents specular reflection.

not just with a threshold, in three dimensions. Since the pupil plane radiance changes by orders of magnitude depending upon whether one is in or out of the specular lobe, the data are more readable when presented in terms of brightness temperature. The brightness temperature T_B is simply the temperature that a blackbody would need to be at if it were to emit the observed pupil plane radiance; that is, it is the blackbody equation solved for temperature, for a given wavelength ($8 \mu m$ in this case) and radiance. The equation for brightness temperature is as follows:[19]

$$T_B(L_p, \lambda) = \frac{hc}{k\lambda} \left[\ln \left(1 + \frac{2hc^2}{L_p\lambda^5} \right) \right]^{-1}, \quad (5)$$

where k is Boltzmann's constant, h is Planck's constant, and c is the speed of light in a vacuum.

Figures 8 and 9 are contour plots of the difference in brightness temperatures between the MERL and Lambertian cases; i.e., $T_B(L_{p,MERL}) - T_B(L_{p,Lamb})$ at $8 \mu m$. In Figure 8, the maximum HDR is 0.9; in Figure 9, the maximum HDR is 0.5. The incident angle θ_i is 30° in plots (a) and (b) in Figures 8 and 9; in (c) and (d), the incident angle is 45° . Each contour line represents a brightness temperature difference of $1 K$ in (a) and (c), and $10 K$ in (b) and (d). In each case, significant differences in brightness temperature are observed, representing substantial differences in observed pupil plane radiance. The difference is more dramatic with a maximum HDR of 0.9 (Figure 8), as is to be expected; that case will be analyzed first. By comparing Figure 8(b) and (d), one can observe that as θ_i decreases, the specular lobe width increases but its overall magnitude decreases; this is due to the projected area $\cos \theta_i$ effect in Equation (3) as well as the BRDF. The maximum brightness temperature difference in Figure 8 is in excess of $120 K$ for $\theta_i = 45^\circ$. The difference in brightness temperature also is negative at some points, indicating the brightness temperature with the Lambertian BRDF model exceeds the brightness temperature with the MERL BRDF

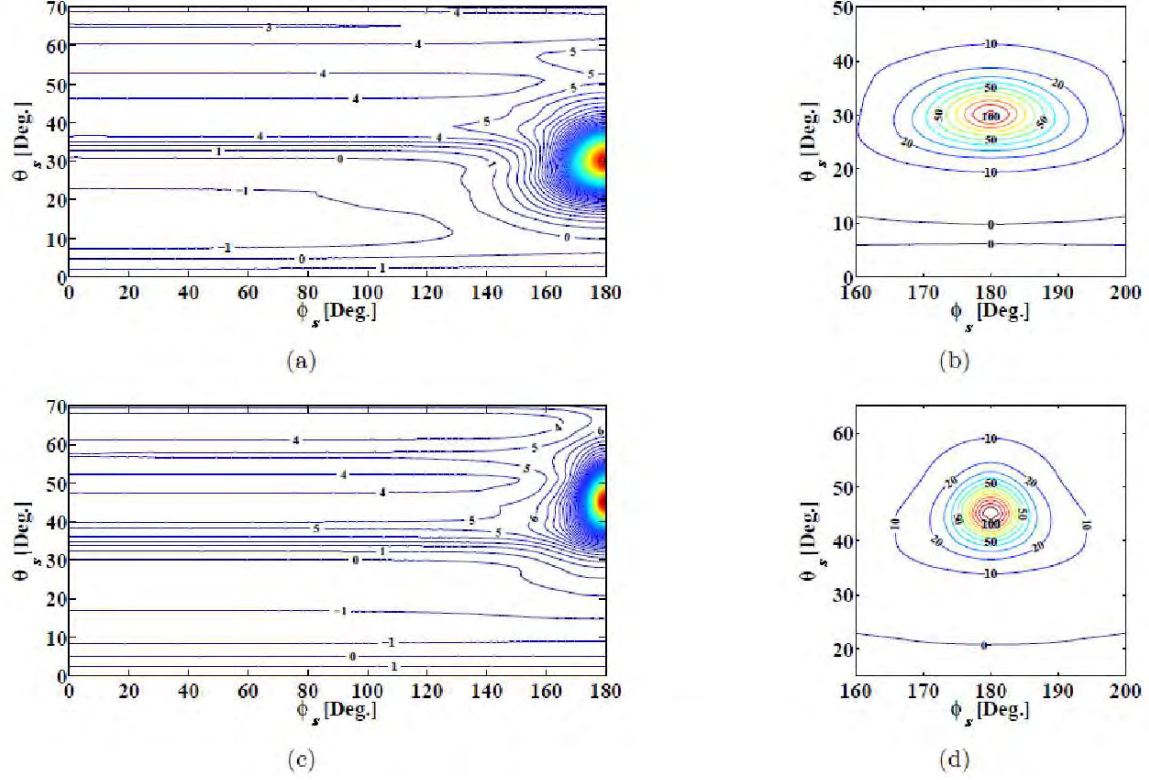


Figure 8. Contour plot of the difference in brightness temperature between MERL and Lambertian cases for an HDR of 0.9 and two incident angles: (a,b) $\theta_i = 30^\circ$; (c,d) $\theta_i = 45^\circ$. Plots (b) and (d) zoom in on the specular lobe contours. In (a) and (c), contours are in $1^\circ K$ steps; in (b) and (d), contours are in $10^\circ K$ steps. The plots extend only to $\theta_i = 70^\circ$ due to error in the BRDF data at grazing angles.

at some angles. Focusing now on Figure 9, it is clear that the general shape of the brightness temperature difference has not changed, but the overall magnitude has changed.

The results of this analysis are noteworthy. Although the Lambertian case agrees with conventional wisdom, there is frequently an assumption in the community that one can always neglect solar reflection in the LWIR, regardless of geometry; these data do not validate that result if one is at or near the specular lobe of a material in the scene, which is dependent upon not only the solar and sensor geometry but also the object's geometry in the scene. Such a result is unsurprising in the VNIR/SWIR, but this finding shows that solar reflection, and thus object BRDF, may be important

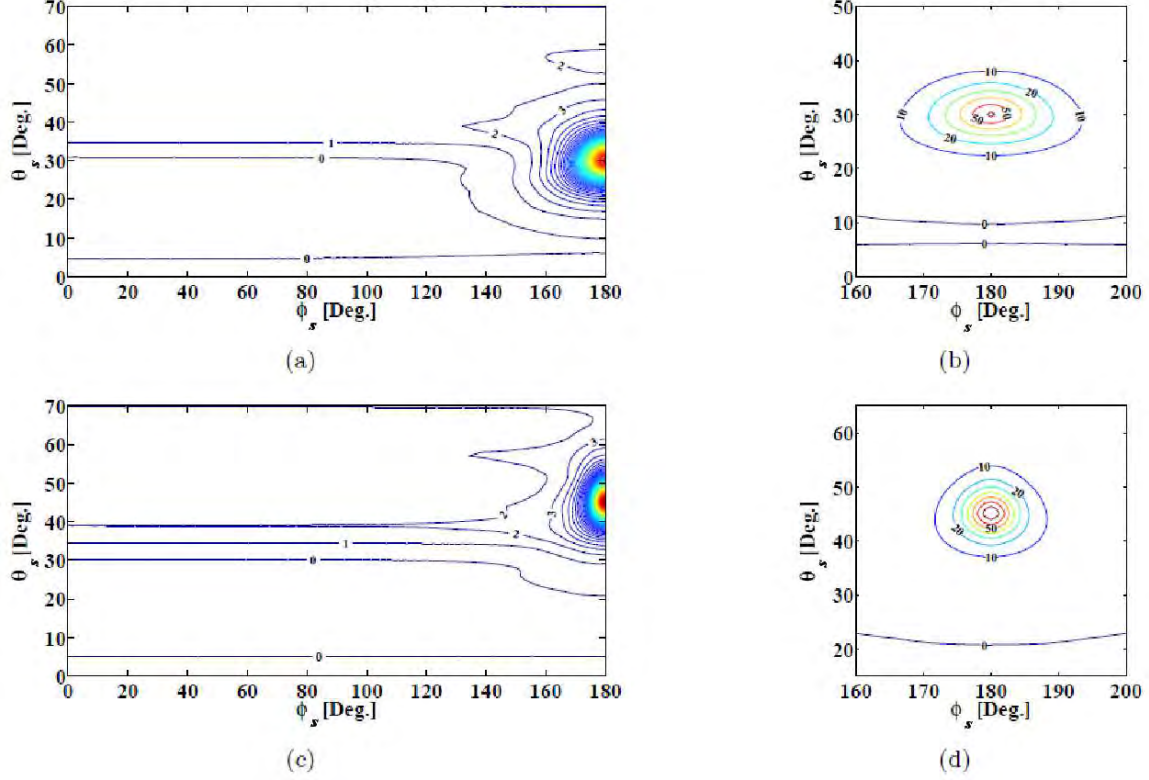


Figure 9. Contour plot of the difference in brightness temperature between MERL and Lambertian cases for an HDR of 0.5 and two incident angles: (a,b) $\theta_i = 30^\circ$; (c,d) $\theta_i = 45^\circ$. Plots (b) and (d) zoom in on the specular lobe contours. In (a) and (c), contours are in $1^\circ K$ steps; in (b) and (d), contours are in $10^\circ K$ steps. The plots extend only to $\theta_i = 70^\circ$ due to error in the BRDF data at grazing angles.

even in the LWIR for certain applications. Furthermore, a highly reflective surface ($\text{HDR} = 0.9$) may exhibit brightness temperature differences of 5 K even off specular. Finally, these results suggest a mechanism to identify whether solar radiation is a factor. If brightness temperatures are significantly higher than the expected value of an object in a scene, it may be possible that solar reflection off a glossy object is partially responsible for the observed brightness temperature.

It is anticipated that, for constant HDR, a more specular BRDF would result in brightness temperature differences that are higher in magnitude, but are localized to a smaller area of the scene. Similarly, a less specular BRDF would likely result in smaller brightness temperature differences, but these differences would be less localized. On

the other hand, as was observed in this analysis, variation in HDR for constant BRDF shape would affect the magnitude of the brightness temperature differences. Additionally, although the MERL data does not support a grazing angle analysis due to difficulty in recording accurate experimental data at grazing angles for BRDF and HDR, it is expected that the brightness temperature would differ significantly from Lambertian at grazing angles due to the phenomenon that materials become more reflective at very steep observed angles.

2.3 Spectral Model Results

In the previous section, the impacts of a BRDF based upon Sun-object-sensor viewing geometry were analyzed for a single wavelength. In this section, a fixed Sun-object-viewer geometry is chosen and a notional wavelength variation of the BRDF is assigned; the results are then contrasted with the case of a Lambertian reflector to determine whether there is a significant spectral difference, even when the overall reflectance of a material is held constant with wavelength. The maximum HDR is held constant at 0.9 for all results in this section. For an HDR of 0.5, or for a different incident angle, the effects would change in magnitude and spatial extent in an analogous manner to the variations observed in the previous section.

To gain an understanding of the potential for spectral BRDF to affect measurements, it is necessary to obtain the BRDF variation with wavelength; such variation is not well-documented in the literature in the LWIR. The reason for the relative lack of spectral BRDF data in the LWIR is due to the difficulty in measuring BRDF due to the presence of relatively little signal away from the specular peak of the BRDF.

Due to this scarcity of BRDF data at multiple wavelengths in the LWIR, the MERL data was again used to provide the notional shape of a BRDF. MERL nickel red channel data was mapped to $\lambda = 12 \mu m$, green channel data was mapped to $\lambda = 10$

μm , and blue channel data was mapped to $\lambda = 8 \mu m$. This wavelength spacing is approximately the same in ratio as the center of the red ($\approx 650 \text{ nm}$), green ($\approx 550 \text{ nm}$), and blue ($\approx 450 \text{ nm}$) wavelengths for a typical camera such as the one used to collect the MERL data. Although such a mapping does not necessarily apply to nickel in the LWIR, it is used to represent the notional BRDF of an unknown material; as noted previously, the BRDF shape for nickel is not unrealistic for materials in the LWIR. Nickel also has the advantage of not being transmissive. Thus, Nickel can be assumed to be a surface reflector; all energy not reflected by the surface can be assumed to be absorbed and thus in thermal equilibrium, emitted. Therefore, the model described by Equations (2) and (3) can be applied.

As before, two different cases were analyzed: Lambertian and MERL BRDF. In this experiment, the maximum HDR for each wavelength was set to 0.9. The results were generated for $\theta_i = 45^\circ$ and $\Delta\phi = 180^\circ$, with $\theta_s = 30^\circ$ to 55° in 5° increments; see Figure 10.

From these results, two key observations are noted. First, the overall magnitude changes substantially when approaching specular reflection, consistent with the observation in the previous section. Second, and perhaps more importantly, the relative difference in pupil plane radiance for each wavelength also changes significantly in shape. Near the specular peak, the observed pupil plane radiance decreases with wavelength (as in plots c, d, and e), whereas in the Lambertian approximation the observed pupil plane radiance increases somewhat with wavelength. As the observer departs from the specular lobe (as in plot a), the variation with wavelength more closely resembles the Lambertian approximation. This effect of the BRDF on the resulting pupil plane radiance underscores the potential importance of using a BRDF model for areas where relative difference between wavelength data are important, as is the case in HSRS.

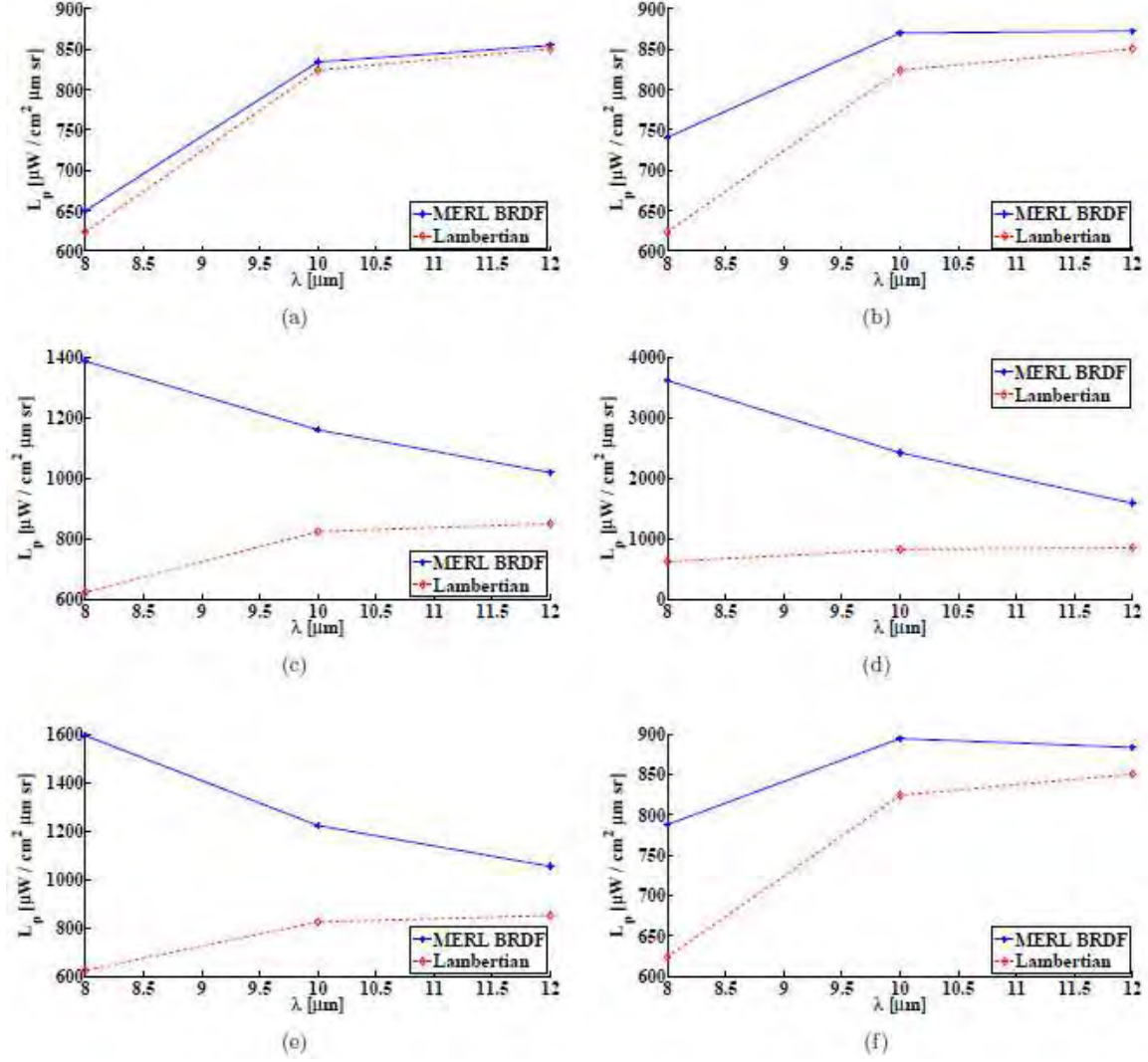


Figure 10. Total pupil plane radiance calculated assuming an object's BRDF is of the shape of nickel in the MERL database, scaled to an HDR of 0.9, as compared to the Lambertian assumption with the same HDR. In all cases, the incident angle is 45°. The outgoing angle varies in each plot: (a) 30°, (b) 35°, (c) 40°, (d) 45°, (e) 50°, and (f) 55°. The Lambertian (red dotted) line in each plot does not change in value, but the y axis changes in scale. The shape of the wavelength variation, as well as the overall value, changes when using BRDF data instead of the Lambertian approximation.

2.4 Summary of Impact

In this chapter, a simple scene model was developed for pupil plane radiance. This model included solar reflection in addition to self-emission and diffuse downwelling radiance. Two different BRDF models were analyzed: Lambertian and MERL nickel-shaped. These models were used to begin to understand the geometric and wavelength-dependent impacts of BRDF on LWIR pupil plane radiance data.

First, the effects were analyzed with varying HDR and various viewing geometries. For a single MERL BRDF, three different HDRs were considered: 0.1, 0.5, and 0.9. Results validated neglecting solar reflection for a Lambertian material. However, when a glossy material such as a notional BRDF shape based on data from the MERL database was introduced in the same model, for certain angles, the solar reflection became a significant factor even in the LWIR. For an HDR of 0.5 or 0.9, the result is a significantly different brightness temperature in the specular region, with the width of this region increasing with small θ_i or higher HDR. These results directly challenge the notion that solar reflection is unimportant in the LWIR, which is often assumed to simplify the processing of LWIR HSRS data [19].

Second, the effects were analyzed for a constant HDR of 0.9, with three different channels of experimentally-measured MERL BRDF data mapped to 8 μm , 10 μm , and 12 μm . These results showed differences in not just magnitude, but also shape, as a function of wavelength and viewing geometry.

This chapter serves as motivation for why the BRDF could impact analysis in domains such as HSRS. Although quantitative conclusions should not be drawn from the MERL data due to its method of collection, this preliminary analysis qualitatively suggests it may be possible to improve upon the results of HSRS by replacing the Lambertian model assumption with a spectral BRDF model. Since HSRS in a realistic scene is already tasked with the difficult non-linear problem of accounting for

atmospheric effects, a closed-form approximation to the BRDF with only a few parameters is highly desirable. Additionally, since HSRS is typically utilized to identify a material in the scene based on the variation in the material's index of refraction as a function of wavelength, the closed-form BRDF model approximation should account for other potential wavelength effects. Chapter III begins to address this problem in more detail by providing thorough background on existing BRDF theory.

III. BRDF Theory Background

In this chapter, BRDF theory for the microfacet model is developed, starting from basic electromagnetism theory, then assuming geometric optics and using statistics to develop the basic models. Then, polarimetric BRDF models are briefly discussed. Some issues with microfacet BRDF models that motivate closer investigation into a closed-form approximation for the BRDF are presented. Finally, scalar wave optics BRDF models, which are significantly more complex than microfacet models, are also be introduced.

3.1 Electromagnetism

One of the greatest successes of theoretical physics was demonstrating light behaves as an electromagnetic wave; thus, Maxwell's Equations directly apply to propagation of light and interactions of light with a surface. Maxwell's equations with the constitutive relations specify the electric and magnetic field, and are as follows:[34]

$$\begin{aligned}
 \nabla \cdot \vec{\mathbf{D}} &= \rho_f & \nabla \times \vec{\mathbf{E}} + \frac{\partial \vec{\mathbf{B}}}{\partial t} &= 0 \\
 \nabla \cdot \vec{\mathbf{B}} &= 0 & \nabla \times \vec{\mathbf{H}} &= \vec{\mathbf{J}} + \frac{\partial \vec{\mathbf{D}}}{\partial t} \\
 \vec{\mathbf{D}} &= \varepsilon \vec{\mathbf{E}} & \vec{\mathbf{B}} &= \mu \vec{\mathbf{H}}
 \end{aligned} \tag{6}$$

In the above expression, $\vec{\mathbf{D}}$ is the macroscopic (displacement) electric field, $\vec{\mathbf{E}}$ is the microscopic electric field, $\vec{\mathbf{B}}$ is the microscopic magnetic field, $\vec{\mathbf{H}}$ is the macroscopic magnetic field, $\vec{\mathbf{J}}$ is the free current density, and ρ_f is the free charge density. When describing propagation through a material in SI units, a permittivity ε and a permeability μ are used as material parameters; for isotropic materials, these are scalar values. If one assumes plane wave solutions of the form $\exp(-i\omega t)$, then by Fourier series superposition, the Helmholtz wave equation results:[34]

$$(\nabla^2 + \mu\epsilon\omega^2)\vec{\mathbf{E}} = 0 \quad (7)$$

From the Helmholtz equation, it is possible to define the wave vector $\vec{\mathbf{k}}$, with direction $\hat{\mathbf{n}}$ and magnitude $k = \omega\sqrt{\mu\epsilon}$. The speed of light through the material is then given by $v = \omega/k$. For free space (vacuum) propagation, the result is the speed of light c ; for general media, the speed is no larger than c . The general expression for the electric field strength for free space propagation, up to an overall phase factor which is generally not noticeable at optical frequencies, is as follows:[34]

$$\vec{\mathbf{E}}(\vec{\mathbf{r}}, t) = \vec{\mathbf{E}}_0 e^{-i(\vec{\mathbf{k}} \cdot \vec{\mathbf{r}} - \omega t)} \quad (8)$$

Note that electromagnetism conventionally assumes that the user takes the real part when associating a complex quantity with a field, as in the equation above. Assuming isotropic media, Maxwell's Equations directly show light propagates in one direction, with the electric field $\vec{\mathbf{E}}$ perpendicular to that direction of propagation and the magnetic field perpendicular to both the direction of propagation and the $\vec{\mathbf{E}}$ field. $\vec{\mathbf{E}}_0$ represents the magnitude and direction of the electric field, known as the polarization, discussed in more depth shortly.

One common way to describe material parameters is by relating the parameters μ and ϵ to the free space parameters μ_0 and ϵ_0 :[34]

$$n = \sqrt{\frac{\mu\epsilon}{\mu_0\epsilon_0}} \quad (9)$$

For free space, it is clear that $n = 1$; for the large class of non-magnetic materials, $\mu \approx \mu_0$ and n relates the permittivity of the material to the permittivity of free space. When considering an absorptive medium, it is possible to add an imaginary component to the permittivity ϵ (which results in exponential decay in the material);

the complex index of refraction is still of the same form but now has a real part n and imaginary part κ ; κ is non-negative and is 0 for wavelengths without absorption. The complex index of refraction is thus $\tilde{n} = n + i\kappa$. At optical frequencies, since most materials are non-magnetic, materials are frequently described by this complex index of refraction rather than by the permittivity of free space directly.

This research is primarily concerned with the interaction of light (and thus the interaction of electromagnetic waves) where one boundary can be approximated as free space (i.e., air or vacuum, $\tilde{n} \approx 1$) and the other boundary is an isotropic material. Prior to discussing this interaction, however, it is necessary to resolve an ambiguity in the electric field direction; this is described by the polarization state of light.

Polarization.

$\vec{\mathbf{E}}$ is restricted by Maxwell's equations to be perpendicular to the direction of propagation for isotropic materials, but there is an ambiguity still present in the direction of $\vec{\mathbf{E}}$, which is confined to a plane but is not unique; this effect is described by the polarization state, introduced in Equation (8) by $\vec{\mathbf{E}}_0$. (Alternatively, one could claim the ambiguity is in the magnetic field's direction, but conventionally the polarization state describes the direction of the $\vec{\mathbf{E}}$ field.)

In general, the polarization of the electric field is confined by Maxwell's equations to be elliptical[34]. To describe this elliptical distribution of the electric field, it is typically decomposed into one of two popular bases: linear or circular. To simplify notation, this section assumes the direction of propagation is $\hat{\mathbf{z}}$.

A linear coordinate system describes the electric field as being oriented in either the $\hat{\mathbf{x}}_1$ direction (one coordinate axis) or the $\hat{\mathbf{x}}_2$ direction (the other coordinate axis). This linear coordinate system picks two vectors spanning the x-y space (i.e., the space not in the direction of propagation). A common choice is to choose the $\hat{\mathbf{x}}$

and $\hat{\mathbf{y}}$ directions, although other choices are possible (in fact, the Stokes vector to be discussed later uses the x-y coordinate system along with the $\pm 45^\circ$ coordinate system). These coordinate systems are typically chosen to be orthonormal. Assuming the $\hat{\mathbf{x}}$ - $\hat{\mathbf{y}}$ coordinate system is chosen, this coordinate system is described by defining $\vec{\mathbf{E}}_0$ from Equation (8) as [34]

$$\vec{\mathbf{E}}_0 = E_x e^{i\delta_x} \hat{\mathbf{x}} \pm i E_y e^{i\delta_y} \hat{\mathbf{y}} \quad (10)$$

If $\delta_x = \delta_y$ (i.e., the waves have the same relative phase), the wave is linearly polarized, with magnitude $E_0 = \sqrt{E_x^2 + E_y^2}$. If the phase is different, then in general elliptical polarization occurs.

A special case occurs if $E_x = E_y$ and $\delta_x - \delta_y = \pm\pi/2$. In this case, one can define new coordinate system $\hat{\mathbf{e}}_+$ and $\hat{\mathbf{e}}_-$ as [34]

$$\hat{\mathbf{e}}_{\pm} = \frac{1}{\sqrt{2}}(\hat{\mathbf{e}}_+ \pm i\hat{\mathbf{e}}_-) \quad (11)$$

This forms an alternate orthonormal coordinate system known as circular coordinates, with $\vec{\mathbf{E}}_0$ from Equation (8) defined as [34]

$$\vec{\mathbf{E}}_0 = E_+ e^{i\delta_+} \hat{\mathbf{e}}_+ + E_- e^{i\delta_-} \hat{\mathbf{e}}_- \quad (12)$$

The Stokes vector $\vec{\mathbf{s}}$ is a convenient descriptor of the polarization state of an electromagnetic wave using all of the coordinate systems described above. This is a 4-component vector defined as follows:[34]

$$\vec{s} = \begin{bmatrix} s_0 \\ s_1 \\ s_2 \\ s_3 \end{bmatrix} = \begin{bmatrix} E_x^2 + E_y^2 \\ E_x^2 - E_y^2 \\ 2E_x E_y \cos(\delta_y - \delta_x) \\ 2E_x E_y \sin(\delta_y - \delta_x) \end{bmatrix} = \begin{bmatrix} E_+^2 + E_-^2 \\ 2E_+ E_- \cos(\delta_- - \delta_+) \\ 2E_+ E_- \sin(\delta_- - \delta_+) \\ E_+^2 - E_-^2 \end{bmatrix} \quad (13)$$

From this equation, it is clear $\sqrt{s_0}$ indicates the intensity of the total field. In polarization analysis, frequently this term is factored out to produce a normalized Stokes vector with $s_0 = 1$. (This normalization is not the same definition as mathematically normalizing a vector, but rather it is an intensity normalization particular to the Stokes vector.) The s_1 term indicates the predominance of horizontal polarization to vertical polarization. If s_1 is positive, the polarization is more horizontal than vertical; if negative, the polarization is more vertical than horizontal; if zero, there are equal parts horizontal and vertical polarization. If a normalized Stokes vector has $s_1 = \pm 1$, the light is completely polarized horizontally (for $+1$) or vertically (for -1). The s_2 term does not have an obvious expression from the above bases, but it shows the predominance of 45° linear polarization to -45° linear polarization, as can be seen by putting the equation for $\vec{\mathbf{E}}_0$ in the $\pm 45^\circ$ coordinate system. The s_3 term is easiest to understand in the circular coordinate system, representing the predominance of right hand circular polarization (E_+) to left hand circular polarization (E_-). [34, 59]

The Stokes vector is a 4-component vector depending upon only three quantities (E_x , E_y , and $\delta_y - \delta_x$). For fully polarized light, an additional constraint on the Stokes vector is that [59]

$$s_0^2 = s_1^2 + s_2^2 + s_3^2 \quad (14)$$

In general, the Stokes vector can describe partially polarized light, so s_0^2 is only required to be greater than or equal to the sum of the other components (i.e., $s_0^2 \geq$

$s_1^2 + s_2^2 + s_3^2$). In fact, if the light is completely unpolarized, the normalized Stokes vector is $\vec{s}_u = [1, 0, 0, 0]^T$. This leads to one of the primary advantages of using the Stokes vector characterization—the Stokes vector provides a metric for the Degree of Polarization (*DoP*): [59]

$$DoP = \frac{\sqrt{s_1^2 + s_2^2 + s_3^2}}{s_0} \leq 1 \quad (15)$$

If $DoP = 1$, the light is fully polarized; if $DoP = 0$, the light is fully unpolarized. The DoP can never be negative since s_0 is never negative.

Frequently in nature, materials are found to not circularly polarize light (which passive 3-D TVs take advantage of to display two different images from the same screen); thus, another metric commonly used in remote sensing is the Degree of Linear Polarization (*DoLP*), which drops the s_3 component from the calculation:[59]

$$DoLP = \frac{\sqrt{s_1^2 + s_2^2}}{s_0} \leq 1 \quad (16)$$

Again, $DoLP = 1$ represents fully linearly polarized light and $DoLP = 0$ represents light which is not at all linearly polarized. A caution is in order, though: light which is not linearly polarized can still be circularly polarized if $s_3 \neq 0$; this metric indicates only the degree of linear polarization, not the degree of total polarization. For natural scenes, the DoP and $DoLP$ are approximately equal, but this is not the case for some man-made materials[59].

The Mueller matrix is a 4x4 matrix representing the transformation of a Stokes vector through an optical component (such as a polarizer). This matrix is often normalized so there is some overall constant transmission term multiplying the entire matrix, and the upper left entry is thus set to 1 (as it relates total incident intensity to total scattered intensity). To determine the resulting Stokes vector given an incident

Stokes vector and a Mueller matrix, simply perform a matrix-vector multiplication: $\vec{s}_{out} = \overset{\leftrightarrow}{\mathbf{M}} \vec{s}_{inc}$. As an example of a Mueller matrix, consider an ideal horizontal polarizer:[59]

$$\overset{\leftrightarrow}{\mathbf{M}}_h = \frac{1}{2} \begin{bmatrix} 1 & 1 & 0 & 0 \\ 1 & 1 & 0 & 0 \\ 0 & 0 & 0 & 0 \\ 0 & 0 & 0 & 0 \end{bmatrix} \quad (17)$$

If the incident light is completely horizontally polarized (i.e., if $\vec{s}_{inc} = s_0[1, 1, 0, 0]^T$), there is no change in the resulting vector; otherwise, the incident light is attenuated and result in $\vec{s}_{out} = f s_0[1, 1, 0, 0]^T$, where f is a fraction less than 1 depending upon how horizontally polarized the incident light was. If the light is vertically polarized ($\vec{s}_{inc} = s_0[1, -1, 0, 0]^T$), the result is $\vec{0}$. A non-ideal horizontal polarizer may have some overall scaling factor less than 1 multiplying $\overset{\leftrightarrow}{\mathbf{M}}_h$, or may have matrix entries slightly different from the above form, depending upon whether the non-ideal behavior was due to overall attenuation or due to incomplete polarization of the light.

Occasionally, the Stokes vector is expressed as a 3-component vector (assuming $s_3 \approx 0$), and measurement of the Stokes vector for natural scenes is frequently implemented as only a 3-component measurement. Also, Mueller matrices may sometimes be expressed as 3x3 matrices instead of 4x4 matrices for this reason [59].

3.2 Surface Reflection and Fresnel Equations

Now that polarization states have been described in detail, electromagnetic reflection can be described. Consider light incident upon a surface; assume the surface normal is pointing in the $\hat{\mathbf{z}}$ direction. The plane of incidence is defined as the plane containing both the point of intersection and the direction of propagation, which is

no longer constrained to be in the $\hat{\mathbf{z}}$ direction, but the coordinate system is chosen such that the direction of propagation lies in the $\hat{\mathbf{x}} - \hat{\mathbf{z}}$ plane. In this orientation, the electric field can oscillate in one of two directions: E_{xz} , which is called in-plane (or parallel) oscillation and is frequently called p polarization (German: parallel), or E_y , which is called out-of-plane (or perpendicular) oscillation and is frequently called s polarization (German: senkrecht).

Three rays of light exist at a material boundary: incident (i), reflected (r), and transmitted (t). From Maxwell's equations, boundary conditions for conservation of momentum can be used to relate these three waves: the tangential components of $\vec{\mathbf{E}}$ and $\vec{\mathbf{H}}$ are continuous, and the normal components of $\vec{\mathbf{B}}$ and $\vec{\mathbf{D}}$ are continuous.

From these boundary conditions, three well-known results can be derived: the law of reflection, Snell's Law and the Fresnel equations[34]. The law of specular reflection states $\theta_r = \theta_i$ and $\phi_r = \phi_i + \pi$, or in other words, angle of incidence equals angle of reflection. (The additive π factor arises from spherical coordinates used in this chapter, as the beam is traveling in the opposite direction but at the same angle θ relative to the surface normal.) This result does not depend upon incident polarization state. Snell's Law also does not depend upon incident polarization state, and is expressed as follows (recall this dissertation assumes $n_i \approx 1$):

$$\sin \theta_i = n \sin \theta_t \tag{18}$$

When reflecting off a surface, the boundary conditions produce an inherent polarization effect even if the incident light is unpolarized. This effect differs depending on angle of incidence relative to the surface normal ($\hat{\mathbf{z}}$), and based on whether the incident polarization of the electric field is in the plane of incidence (p polarization) or perpendicular to the plane of incidence (s polarization). The Fresnel equations for reflection quantify this effect; again assuming propagation through air can be approx-

imated as a vacuum ($\tilde{n}_i = n_{air} \approx 1$), these equations are dependent on only incident angle with respect to surface normal and the reflecting material's complex index of refraction \tilde{n} as follows:[34, 59]

$$r_p(\theta) = \frac{\tilde{n} \cos \theta - \sqrt{1 - (\frac{\sin \theta}{\tilde{n}})^2}}{\tilde{n} \cos \theta + \sqrt{1 - (\frac{\sin \theta}{\tilde{n}})^2}} \quad (19)$$

$$r_s(\theta) = \frac{\cos \theta - \sqrt{\tilde{n}^2 - \sin^2 \theta}}{\cos \theta + \sqrt{\tilde{n}^2 - \sin^2 \theta}} \quad (20)$$

The r_p and r_s components are reflection of the electric field, not intensity. The intensity of each component is the magnitude squared of each field reflection:

$$\begin{aligned} F_p(\theta) &= |r_p(\theta)|^2 \\ F_s(\theta) &= |r_s(\theta)|^2 \end{aligned} \quad (21)$$

If the incident light is unpolarized, these amplitudes are combined as follows:

$$F(\theta) = \frac{F_p(\theta) + F_s(\theta)}{2} \quad (22)$$

3.3 Self-Emission

An important factor related to reflection is a material's self-emission ε . By conservation of energy, the relationship $\alpha + \tau + \rho = 1$ must hold; that is, all of the energy must be absorbed (α), transmitted (τ), or reflected (ρ). Kirchhoff's Law states that the self-emission ε must be equal to absorption α to maintain thermal equilibrium; that is, in thermal equilibrium, the amount of energy absorbed must be equal to the amount of energy emitted. If a material is opaque, $\tau = 0$ and the following result is obtained: $\varepsilon = 1 - \rho$. In general, as is observed in Section 3.4, this reflectance can be directional; thus, the emissivity can also be directional.

Although Kirchhoff's Law states emitted and absorbed energy is equal, materials do not necessarily absorb and radiate at the same wavelength. Some materials can be approximated as blackbodies in their radiation profile; this wavelength distribution depends on temperature of the object and is given by Planck's Law, originally proposed by Max Planck in 1900 as derived from quantum theory. Its form in terms of spectral radiance is as follows:[50]

$$L_B(\lambda, T) = \frac{2hc^2}{\lambda^5} \frac{1}{e^{hc/\lambda kT} - 1} \quad (23)$$

where h is Planck's constant, k is Boltzmann's constant, c is the speed of light in a vacuum, T represents the temperature of the radiating body, and as before λ represents wavelength. Many materials are well-approximated as a graybody over a small region of interest in the electromagnetic spectrum. For a graybody, the shape of the blackbody radiation curve is the same but the overall emission is multiplied by a constant emissivity ϵ_g , which is between 0 and 1.

Polarimetric Self-Emission.

When incorporating polarimetric effects of the BRDF in self-emission, some modification is required to obtain the Stokes vector representation. Recall the Stokes vector is a 4-element vector. The magnitude information is represented by the first entry (s_0) in the Stokes vector, and the other entries represent relative contributions of the difference of the polarization state in different coordinate systems. For this reason, the polarimetric extension is not as simple as taking $1 - \rho$, since ρ is a 4x4 Mueller matrix when including polarimetric effects.

Blackbody radiation is unpolarized, meaning its representation in Stokes vector notation is $[1, 0, 0, 0]^T$. Taking the dot product of this unpolarized Stokes vector extracts the first column of the BRDF only. As shown by Resnick *et al.*, the emissivity

of the surface is given as follows:[55]

$$\vec{\varepsilon} = \begin{bmatrix} 1 - \rho_{00}(\hat{\omega}_s) \\ -\rho_{10}(\hat{\omega}_s) \\ -\rho_{20}(\hat{\omega}_s) \\ -\rho_{30}(\hat{\omega}_s) \end{bmatrix} = \vec{s}_B - \overset{\leftrightarrow}{\rho}(\hat{\omega}_s)\vec{s}_B \quad (24)$$

where \vec{s}_B is the normalized Stokes vector for a blackbody (which is unpolarized radiation: $\vec{s}_B = [1, 0, 0, 0]^T$). In the above equation, $\rho_{xy}(\hat{\omega}_s)$ represents the Mueller matrix for the HDR, given by the integral expression in Equation (28) with the indexed pBRDF element in place of the scalar BRDF. Since blackbody radiation is unpolarized, only the first column of the BRDF is required to obtain the self-emission term (00, 10, 20, or 30). Mathematically, this represents light which is scaled to the correct total emissivity, but is of opposite polarization. That is, if incident unpolarized light at an angle θ_i is completely horizontally polarized upon reflection ($s_1 = 1$), then the self-emitted light at that angle θ_i is completely vertically polarized ($s_1 = -1$). The overall magnitude of the self-emitted light is the same, as $s_0 = 1 - \rho_{00}(\hat{\omega}_s) = \rho(\hat{\omega}_s)$. (Recall the 00 entry of any Mueller matrix is the same as the unpolarized result.)

3.4 Reflectance Functions

Solving Maxwell's equations for realistic surfaces is a very time-consuming process requiring knowledge of several material parameters, which can become unwieldy in remote sensing or scene generation. For this reason, simplified approximations of the result for typical materials have been developed. The BRDF was defined by Nicodemus *et al.* in a NIST standard as [48]

$$f_r(\hat{\omega}_i, \hat{\omega}_s, \lambda) = \frac{dL_s(\hat{\omega}_i, \hat{\omega}_s, \lambda)}{dE_i(\hat{\omega}_i, \lambda)} \quad (25)$$

Since the BRDF relates incident irradiance E_i to scattered radiance L_s , it carries units of sr^{-1} . Its range is on the interval $[0, \infty)$, although with additional constraints to be discussed shortly. Initially, wavelength dependence (λ) is neglected in the BRDF model discussion; this wavelength dependence is revisited after the BRDF for fixed wavelength is examined in detail. The term “scattered” vector is preferred by the author to the term “reflected” vector here. The term “reflected” is not used here for two reasons. First, due to surface roughness, the angle of incidence θ_i is not required to equal the scattered angle θ_s relative to the macrosurface normal. Additionally, the scattered radiation may consist of more than just reflected radiation, as volumetric scattering may also exist.

Throughout this dissertation, $\hat{\omega}_i$ represents the normalized incident vector relative to the overall surface normal and $\hat{\omega}_s$ represents the normalized scattered vector relative to the surface normal (see Figure 2). In both cases, the unit vector $\hat{\omega}$ is defined as a unit vector in spherical coordinates, with the origin set at the point of intersection with the surface and the $\hat{\mathbf{z}}$ direction is defined by the surface normal; this results in a normalized spherical coordinate vector as follows:

$$\hat{\omega} = \begin{bmatrix} 1 \\ \theta \\ \phi \end{bmatrix} \quad (26)$$

Due to Helmholtz reciprocity of Maxwell’s Equations, the BRDF of a material should obey the following property:

$$f_r(\hat{\omega}_i, \hat{\omega}_s) = f_r(\hat{\omega}_s, \hat{\omega}_i) \quad (27)$$

To be physically accurate, the BRDF of a material also must obey conservation of energy; that is, for any incident solid angle $\hat{\omega}_i$, the integrated BRDF over all scattered

solid angles $\hat{\omega}_s$ must be in the range $[0, 1]$. This integrated BRDF is known as the Directional-Hemispherical Reflectance (DHR), which is unitless and is calculated as follows:

$$\rho(\hat{\omega}_i) = \int_{\Omega/2} f_r(\hat{\omega}_i, \hat{\omega}_s) d\hat{\omega}_s = \int_0^{2\pi} \int_0^{\pi/2} f_r(\hat{\omega}_i, \hat{\omega}_s) \cos \theta_s \sin \theta_s d\theta_s d\phi_s \quad (28)$$

The expansion of $d\hat{\omega}_s$ includes a $\sin \theta_s$ term from standard spherical coordinate integration over θ_s and ϕ_s . The extra $\cos \theta_s$ arises from the projected area effect of the integration; that is, at an angle other than nadir ($\theta_s = 0$), the same total energy in the reflection is spread over a larger area, resulting in less energy per unit area.

Similarly, for any scattered solid angle $\hat{\omega}_s$, the integrated BRDF over all incident solid angles $\hat{\omega}_i$ must also be in the range $[0, 1]$. This is known as the Hemispherical-Directional Reflectance (HDR), which is also unitless and equal to the DHR:

$$\rho_{hdr}(\hat{\omega}_s) = \int_0^{2\pi} \int_0^{\pi/2} f_r(\hat{\omega}_i, \hat{\omega}_s) \cos \theta_i \sin \theta_i d\theta_i d\phi_i = \rho(\hat{\omega}_s) \quad (29)$$

Although HDR and DHR are the same value for each solid angle, there is a subtle difference—the DHR is a function of incident angle and the HDR is a function of scattered angle. Despite this difference, frequently HDR and DHR are used interchangeably in literature.

These conditions are true for actual material BRDFs; however, these conditions are not guaranteed to apply for all BRDF models that are discussed in this document. Many BRDF models were developed by the computer graphics community for efficient scene rendering, where radiometric accuracy can be sacrificed to some extent in exchange for a faster algorithm as long as the result still looks reasonably close. Additionally, a BRDF function may at times be nearly symmetric and conserve energy

for careful choices of the model parameters, but may not guarantee symmetry or conservation of energy if the user chooses parameters that do not make sense. Therefore, care must be taken when using BRDF models to ensure these conditions are still met after fitting parameters to a particular model. Finally, some BRDF models approach ∞ as θ_i or θ_s approaches 90° ; when that is the case, that value is not allowed in a model, as there is no surface reflection at $\theta = 90^\circ$ anyway.

3.5 BRDF Model Basics

BRDF models are an area of active research, as popular BRDF models in use by both the physics and computer graphics communities are known to have some materials for which they are well suited, while there are other materials for which the models fail; see, for example, a study by Ngan in 2005 on 100 materials with densely-measured BRDF data[47].

For a perfectly specular BRDF, there is a single parameter ρ (total reflectance). Its representation in spherical coordinates uses the Dirac delta function and is as follows:

$$f_r(\hat{\omega}_i, \hat{\omega}_s) = \rho \delta(\theta_i - \theta_s) \delta(\phi_i + \pi - \phi_s) \quad (30)$$

In words, this BRDF function quantifies the common knowledge statement that angle of incidence equals angle of reflection. If a surface were perfectly flat, the BRDF would be perfectly specular, having this form. Its value is 0 everywhere except at the mirrored angle of incidence, where its value is infinite, with its DHR equal to ρ .

Another simple idealized BRDF model is the Lambertian BRDF, which assumes constant reflectance in all directions regardless of incident or scattered angle. It is parameterized by a single variable, ρ , representing the total reflectance. This BRDF would be notionally valid for a very rough surface, or for a highly volumetric scatterer.

(That said, there is no NIST standard for a nearly-Lambertian surface in the IR; no material is truly Lambertian in the IR, although it can be a decent approximation for some materials.) The Lambertian BRDF is defined as

$$f_r = \frac{\rho}{\pi} \quad (31)$$

These idealized BRDF models do not describe most materials. There are two primary classes of physics-based BRDF models that are examined in this work: microfacet models and scalar wave optics models. Polarimetric (vector) wave optics models are not discussed in this dissertation. Polarimetric microfacet BRDF models are described briefly in this chapter since the concept is of some importance to the discussion in Chapter IV, but it is not a focus of this dissertation. Microfacet BRDF models assume geometric optics and result in a simple, closed-form model to the BRDF, and are more commonly applied to domains that are already resource-constrained. (For example, in HSRS, atmospheric correction requires significant computational effort already [19], so limited computational resources are available to compute the BRDF.) Scalar wave optics models are significantly more cumbersome to use and do not generally possess a simple closed-form model for all angles or all surfaces. These models are typically used for predicting actual surface parameters from the BRDF, rather than for simply estimating the reflectance profile. This is due to the significant additional computational complexity when using a scalar wave optics approach to the BRDF.

This section of the background deals primarily with common microfacet BRDF models, as the microfacet model is more appealing to apply to HSRS due to its relative ease of use. In fact, the initial approach in this dissertation was to measure the BRDF of materials as a function of wavelength, then determine a modification to the microfacet model to account for the wavelength dependence. However, as is shown in Chapter V, this method was found to not work when fitting to measured

BRDF data. A more detailed examination of the relationship between microfacet and scalar wave optics BRDFs are then developed in Chapter VI. Therefore, after presenting microfacet BRDF models, common scalar wave optics BRDF models are presented at the end of this chapter.

Other classes of BRDF models exist, but are primarily of interest in computer graphics, as they are not derived from physical or geometric optics. For a good overview of other popular BRDF models, see [45, 17]. According to Montes, there are three main classes of BRDF models: empirical, theoretical, and experimental[45, 17]. Empirical BRDFs are primarily of use to the Computer Graphics community, and are largely not be discussed in this dissertation (except a brief mention of the popular Phong and Blinn-Phong models). Experimental BRDFs are functions based on theoretical BRDFs, but tweaked somewhat to better fit a certain category of BRDF data; they are not applicable to a wide range of models, however, and the tweaks are typically not physically driven, so this class is also not be discussed in-depth. Theoretical BRDFs are of most interest in this dissertation, as these models have a physical basis from which they are derived. The largest group of theoretical models are microfacet models that neglect diffraction and interference.

In any BRDF model, reflection off a material can come from two different sources: surface reflection and volumetric scatter. In the literature, volumetric scatter is sometimes called diffuse reflection, since it tends to be less directional. In this dissertation, diffuse is reserved to be synonymous with Lambertian. In general, the volumetric BRDF contribution may be directional, or it may be diffuse, so some models include up to three distinct terms, with the volumetric component split into a perfectly diffuse portion and a directional volumetric portion. Mathematically, the form of a BRDF is[5]

$$f_r(\hat{\omega}_i, \hat{\omega}_s) = \rho_s S(\hat{\omega}_i, \hat{\omega}_s) + \left[\rho_v V(\hat{\omega}_i, \hat{\omega}_s) + \frac{\rho_d}{\pi} \right] \quad (32)$$

Here, S is the surface reflection, V is the directional volumetric scatter, and ρ_d/π is the diffuse volumetric scatter; ρ_s , ρ_v , and ρ_d are fitting parameters. Since setting $\theta = 0$ as the macrosurface normal direction for an isotropic material results in an ambiguity in ϕ , there is added flexibility in definition of a reference point for the azimuthal angle ϕ for isotropic materials. One convention, which is adopted throughout this document, is to set $\phi_i = 0$. Microfacet models are the primary type of BRDF model that are considered in this research, and are discussed in greater detail shortly. First, it is helpful to discuss a different coordinate system that is of use in describing microfacet BRDFs.

Coordinate Variables for Reflection.

When dealing with the microfacet model for the BRDF, it is convenient to work in both the macrosurface coordinate system discussed above, as well as a microsurface coordinate system. Although the relationships between the microsurface and macrosurface have been in use for decades, this coordinate system was formally defined by Rusinkiewicz[56] in 1998, defining a half vector $\hat{\omega}_h$ and difference vector $\hat{\omega}_d$ as

$$\hat{\omega}_h = \frac{\hat{\omega}_i + \hat{\omega}_s}{\|\hat{\omega}_i + \hat{\omega}_s\|}, \quad \hat{\omega}_d = \mathbb{R}_y(-\theta_h) \mathbb{R}_z(-\phi_h) \hat{\omega}_i. \quad (33)$$

In the above equation, $\mathbb{R}_a(\beta)$ is a right-handed rotation about axis a by an angle β . The difference vector is thus obtained by derotating the incident vector in the ϕ direction, then derotating the difference vector in the θ direction.

Physically, the half vector $\hat{\omega}_h$ can be interpreted as the microfacet orientation which produces specular reflection for a given incident and scattered direction. In

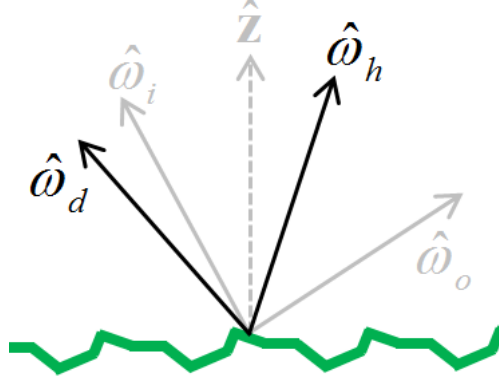


Figure 11. Microfacet geometry, with incident and outgoing vectors relative to $\hat{\mathbf{z}}$ (overall macro-surface normal), $\hat{\omega}_h$ (specular microsurface orientation), and $\hat{\omega}_d$ (rotated incident vector in this microsurface orientation)

other words, the variable θ_h represents the angular difference between the macro-surface normal and the microsurface normal for specular reflection. In Rusinkiewicz coordinates, the isotropic condition results in symmetry about ϕ_h . The difference vector $\hat{\omega}_d$ is the incident vector, rotated to be in the microfacet's coordinate system[56]. This becomes important when calculating Fresnel reflectance, which is dependent upon the angle of incidence relative to the microsurface normal, θ_d ; see Figure 11.

In addition to the above formal definitions, if the ϕ_h and ϕ_d variables are not needed (which is frequently the case in isotropic, unpolarized, microfacet BRDF models), the angular dependence may be calculated using the well-known equations found in many microfacet BRDF papers: [19, 33, 43, 52, 53, 57, 65, 70]

$$\theta_d = \frac{1}{2} \cos^{-1} [\cos \theta_i \cos \theta_s + \sin \theta_i \sin \theta_s \cos(\phi_i - \phi_s)] \quad (34)$$

$$\theta_h = \cos^{-1} \left[\frac{\cos \theta_i + \cos \theta_s}{2 \cos \theta_d} \right] \quad (35)$$

For most BRDF models, it is convenient to work in both Rusinkiewicz coordinates and macrosurface coordinates. Terms depending on microsurface orientation

(such as Fresnel reflection and microfacet distribution) are most naturally expressed in Rusinkiewicz coordinates, while other terms such as geometric attenuation or volumetric reflection are more naturally expressed in macrosurface coordinates.

3.6 Microfacet BRDF Models

In [5], many popular microfacet BRDF models were written in a common form and summarized, as well as showing the potential to enhance BRDF fitting by altering the distribution function of a microfacet BRDF model. This section discusses the BRDF models presented in [5] in more depth, as well as expanding the discussion to polarimetric BRDFs. The potential BRDF fitting enhancement presented in [5] are discussed in Chapter V, when BRDF fitting is addressed.

One of the most popular classes of BRDF models is the microfacet model. In a microfacet model, wave optics is ignored, and thus all terms are additive and non-negative. It is assumed that surface reflection is due only to specular reflection of microfacets oriented in the specular direction relative to the source and observer (i.e., the $\hat{\omega}_h$ direction). The microfacet model assumption does not specify any detail about the form of the volumetric reflection, but it does specify the form for the surface reflection S , as follows:

$$S(\hat{\omega}_i, \hat{\omega}_s) = D(\hat{\omega}_h)F(\hat{\omega}_d)G(\hat{\omega}_i, \hat{\omega}_s)\sigma(\theta_i, \theta_s) \quad (36)$$

The function D represents the microsurface normal distribution. If one assumes the microsurface normals are uniformly distributed about the macrosurface normal $\hat{\mathbf{z}}$ (e.g., it is isotropic), the distribution is dependent only on θ_h . (For an anisotropic surface, there may additionally be a ϕ_h dependence.) As discussed by Trowbridge, the facet distribution function (excluding normalization) for isotropic surfaces should obey the following properties for $\theta_h \in [0, \pi/2]$: finite, nonnegative, single-valued,

and continuous [66]. When properly normalized, the facet distribution should also integrate to 1 over the hemisphere.

The function F was previously defined in Equation (22) and represents Fresnel reflection with unpolarized incident light, which is parameterized by the complex index of refraction $\tilde{n} = n + i\kappa$. It is dependent only on $\hat{\omega}_d$ in Rusinkiewicz coordinates, since $\hat{\omega}_d$ is the incident vector in the specular microsurface's orientation. In fact, since Fresnel reflection is dependent only upon depression angle with respect to the microsurface normal $\hat{\omega}_h$, this function depends only upon θ_d . The function G represents the geometric attenuation term, also known as shadowing and obscuration, which may in general depend upon any of the angles.

As pointed out by multiple authors[16, 21, 33, 53], when converting from scattering cross section to BRDF, there is a conversion term denoted here as σ and defined as

$$\sigma(\theta_i, \theta_s) = \frac{1}{4 \cos \theta_i \cos \theta_s}. \quad (37)$$

The $1/\cos \theta_s$ comes from what is known in the community as the cosine corrected BRDF [62]. The remaining $\cos \theta_i$ term arises from scattering cross section typically being defined for spherical scattering particles rather than flat surfaces, for which the projected area must be considered. Physically, considering Huygens wavelet theory, all points on the wavefront are emitting spherical waves effectively from point sources which have no area. Microfacet models compute BRDF as intensity per incident flux for a spherical wave, then converts to BRDF for a flat surface via σ . The cross section conversion term is not in units of area because the BRDF models only angular dependencies, but the angular terms in the conversion from a spherical scattering surface to a flat scattering surface are present in this cross section conversion term.

In some references, it is asserted there should also be a $1/\cos \theta_h$ term present[33, 71], but Shell and Hyde both state it is a negligible factor[61, 33]. In this work, the

$1/\cos\theta_h$ term is included as part of the distribution function normalization instead of part of σ .

When combined with Equation (32) and restricted to isotropic surfaces, microfacet BRDFs may be expressed as [5]

$$f_r(\hat{\omega}_i, \hat{\omega}_s) = \rho_s P \sigma(\theta_i, \theta_s) D(\theta_h) F(\theta_d) G(\hat{\omega}_i, \hat{\omega}_s) + \rho_v V(\hat{\omega}_i, \hat{\omega}_s) + \frac{\rho_d}{\pi} \quad (38)$$

The additional term $P(\hat{\omega}_i, \hat{\omega}_s)$ is called a pre-factor term; it represents terms that exist in microfacet BRDF models that are specific to one particular model, and are not found in other microfacet BRDF models.

Fresnel Approximations.

The Fresnel equations discussed previously are fairly complex for some applications, and require two parameters (n and κ). Some BRDF models use a Fresnel approximation instead of using Equation (22). A common approximation to the unpolarized Fresnel curve is given by Schlick and has the following form, with a single real parameter R_0 : [58]

$$F_{Sch}(\theta_d) = R_0 + (1 - R_0)(1 - \cos\theta_d)^5 \quad (39)$$

This parameterization is common in the computer graphics community due to its speed, simplicity, and having one fewer parameter. It is less useful for this physics-based research since it does not easily generalize to the polarimetric BRDFs to be discussed later. Thus, it is not used in any of the BRDF models presented in this dissertation, although it could be substituted in place of the more complex Fresnel equation if appropriate for a certain application.

Another Fresnel approximation is used in the Sandford-Robertson BRDF model,

which is a single parameter approximation given as[57, 13, 35]

$$\begin{aligned} F(\theta) \approx F_s(\theta) &= [g_s(\theta)] \left[\frac{1}{G_s} \right] \\ &= \left[\frac{1}{1 + b^2 \tan^2 \theta} \right] \left[\frac{(1 - b)^2(1 + b)}{1 - b^2 + 2b^2 \ln b} \right] \end{aligned} \quad (40)$$

In the above equation, the first term in brackets is $g_s(\theta)$ and the second term in brackets (which is independent of θ but still depends upon the Sandford-Robertson parameter b) is $1/G_s$, the normalization term for $g_s(\theta)$.

Distribution Functions.

Distribution functions can be broken into two categories: isotropic and anisotropic. For isotropic functions, the distribution function depends only on θ_h ; anisotropic distribution functions additionally depend on ϕ_h . Trowbridge states requirements on a facet normal distribution that require it to be integrable and non-negative[66]. If the facet normal distribution is thought of as a probability distribution function, the integral over the entire hemisphere of a properly normalized distribution function is 1; this normalization has been used where possible. Recall in Section 3.6, it was noted that Hyde and Shell indicated the correct normalization of a microfacet BRDF includes a $1/\cos \theta_h$ term as well as the σ term[33, 61]. I have chosen to include that term in these distribution functions, so in some cases where the term was not already included, my normalization has an extra power of $1/\cos \theta_h$. In this dissertation, unless otherwise noted, the following equation holds (if fit parameters are assumed positive):

$$\int_0^{2\pi} \int_0^{\pi/2} D(\theta_h) \cos \theta_h \sin \theta_h d\theta_h d\phi_h = 1 \quad (41)$$

The cosine lobe distribution is parameterized by k ; its form is as follows:[51, 3, 1]

$$D_c(\theta_h) = \frac{k+2}{2\pi} (\cos \theta_h)^k \quad (42)$$

The Beckmann distribution is a Gaussian distribution used by many microfacet models. Its origin is in a study on electromagnetic reflection performed in 1963. The Beckmann distribution is parameterized by a single variable m and has the following form:[2, 14]

$$D_b(\theta_h) = \frac{1}{\pi m^2 \cos^4 \theta_h} \exp \left[- \left(\frac{\tan \theta_h}{m} \right)^2 \right] \quad (43)$$

In some BRDF models, such as Torrance-Sparrow[65, 59, 45] and Ward-Duer[70, 18], an approximation to the Beckmann distribution is used for small θ_h , as follows: $\tan \theta_h \approx \theta_h$. In the case of Ward-Duer, the normalization is also approximated as 1; this is accounted for in the pre-factor section.

A slightly modified form of the Beckmann distribution is used by Priest [53]. His Gaussian distribution is equivalent to setting $m = \sigma_g \sqrt{2}$ in the Beckmann distribution. For this reason, the summary table presented later in Table 3.1 still refers to this distribution function as $D_b(\theta_h)$. Its form is as follows:

$$D_g(\theta_h) = \frac{1}{2\pi\sigma_g^2 \cos^4 \theta_h} \exp \left[- \frac{\tan^2 \theta_h}{2\sigma_g^2} \right] \quad (44)$$

Wellems presents a two-parameter Hyper-Cauchy distribution that introduces an extra parameter q to the Cauchy distribution. When $q = 3/2$ in this Hyper-Cauchy function, the Cauchy distribution results. The other parameter, s , controls the width of the distribution function. This Hyper-Cauchy distribution has the following form:[71]

$$D_h(\theta_h) = \frac{(q-1)(s\sqrt{2})^{2q-2}}{\pi(\cos^4 \theta_h)((s\sqrt{2})^2 + \tan^2 \theta_h)^q} \quad (45)$$

The Modified Beard-Maxwell BRDF is perhaps the most popular BRDF that sometimes uses a single-parameter Cauchy distribution, although the form used is slightly different from the Hyper-Cauchy distribution. Note that this distribution function is not normalized over the hemisphere as the previous distribution functions were, so a subscript u has been added. This modified Cauchy distribution is as follows:[19, 22, 61]

$$D_{bm,u}(\theta_h) = \frac{B}{(\cos \theta_h)(s^2 + \tan^2 \theta_h)} \quad (46)$$

In the original Beard-Maxwell formulation, this distribution was not used directly, but was estimated from measured bi-static data[16, 43]; this is still used sometimes in place of the Cauchy distribution function (such as in the popular NEF database). Instead of using a parameterized Cauchy distribution function, the BRDF value is measured for each half-vector orientation θ_h from 0° to 90° , at $\theta_d = 0$. This is termed the bi-static scan in the literature. The empirically-driven distribution function ρ_{fs} is then scaled as follows:[72, 16]

$$D_s(\theta_h) = \frac{4\rho_{fs}(\theta_h, 0) \cos^2 \theta_h}{F(0)} \quad (47)$$

The Sandford-Robertson BRDF uses an single-parameter elliptical distribution function originally derived by Trowbridge and Reitz in 1975:[66, 57, 13, 35]

$$D_{e,u}(\theta_h) = \frac{1}{c^2 \cos^2 \theta_h + \sin^2 \theta_h} \quad (48)$$

Unlike most other distributions presented here, this distribution is not normalized; the normalization contained in the Sandford-Robertson BRDF depends on θ_i . Since it is not explicitly a function of only θ_h , I do not include it here, and I include a u subscript as a reminder this is an unnormalized distribution. The normalization N_e

is included in the pre-factor subsection, below.

Although this research is primarily concerned with isotropic BRDF models, a model may be made anisotropic by modifying the distribution function to depend upon ϕ_h as well as θ_h . This was accomplished in the Ward BRDF for the Beckmann distribution[70], and in the Ashikhman-Shirely BRDF for the cosine lobe distribution[1]. In both cases, the single parameter model becomes a 2-parameter model with an additional angular dependence of the form $k_x \cos^2 \phi_h + k_y \sin^2 \phi_h$; if $k_x = k_y$, the dependence on ϕ_h is eliminated and the distribution functions reduce to the isotropic form stated above.

The anisotropic form of the Beckmann distribution is as follows:[70]

$$D_{b,a}(\hat{\omega}_h) = \frac{1}{\pi m_x m_y \cos^4 \theta_h} \exp \left[-\tan^2 \theta_h \left(\frac{\cos^2 \phi_h}{m_x^2} + \frac{\sin^2 \phi_h}{m_y^2} \right) \right] \quad (49)$$

The normalization presented here differs slightly from Ward's since he neglected the $1/\cos^4 \theta_h$ term in the Beckmann distribution and included a factor of 1/4 that I put in $\sigma(\hat{\omega}_i, \hat{\omega}_s)$. If $m_x = m_y = m$, the Beckmann distribution $D_b(\theta_h)$ is obtained.

The anisotropic form of the cosine lobe distribution is as follows:[1]

$$D_{c,a}(\hat{\omega}_h) = \frac{\sqrt{k_x + 2}\sqrt{k_y + 2}}{2\pi} (\cos \theta_h)^{k_x \cos^2 \phi_h + k_y \sin^2 \phi_h} \quad (50)$$

Note that I have shifted k_x and k_y parameters by 1 relative to Ashikhman *et al.* to account for dividing by the extra $1/\cos \theta_h$ normalization term that Hyde and Shell said should be present. Ashikhman defines the distribution function $d(\theta_h)$ without the extra $1/\cos \theta_h$ term that Hyde and Shell state should be present in microfacet BRDF models[33, 61], and which I have included with the distribution function in this dissertation. If one were to add the $1/\cos \theta_h$ normalization to the definition provided by Ashikhman, the above distribution function is obtained:

$$\begin{aligned}
\frac{\sqrt{k_u+1}\sqrt{k_v+1}}{2\pi \cos \theta_h} (\cos \theta_h)^{k_u \cos^2 \phi_h + k_v \sin^2 \phi_h} &= \frac{\sqrt{k_u+1}\sqrt{k_v+1}}{2\pi} (\cos \theta_h)^{k_u \cos^2 \phi_h + k_v \sin^2 \phi_h - 1} \\
&= \frac{\sqrt{k_u+1}\sqrt{k_v+1}}{2\pi} (\cos \theta_h)^{k_u \cos^2 \phi_h + k_v \sin^2 \phi_h - \cos^2 \phi_h - \sin^2 \phi_h} \\
&= \frac{\sqrt{k_u+1}\sqrt{k_v+1}}{2\pi} (\cos \theta_h)^{(k_u-1) \cos^2 \phi_h + (k_v-1) \sin^2 \phi_h} \\
&= \frac{\sqrt{k_x+2}\sqrt{k_y+2}}{2\pi} (\cos \theta_h)^{k_x \cos^2 \phi_h + k_y \sin^2 \phi_h}
\end{aligned} \tag{51}$$

In the last line, $k_x = k_u - 1$ and $k_y = k_v - 1$ have been substituted into the original form used by Ashikhman to put the function in the form obtained in Equation (50). When written in this form with the $1/\cos \theta_h$ correction, if $k_x = k_y = k$, the cosine lobe distribution $D_c(\theta_h)$ results, as expected.

Geometric Attenuation Terms.

The Torrance-Sparrow BRDF model, which was perhaps the first microfacet BRDF model, used the following geometric attenuation term:[65]

$$G_T(\psi_p, \theta_p) = 1 - \frac{1 - \sqrt{1 - A(\psi_p, \theta_p)}}{A(\psi_p, \theta_p)} \tag{52}$$

The factor $A(\psi_p, \theta_p)$ in the geometric attenuation term is defined as follows:

$$A(\psi_p, \theta_p) = \frac{\sin^2 \psi_p - \cos^2 \frac{\theta_p - \psi_p}{2}}{\cos^2 \frac{\theta_p - \psi_p}{2} - \cos(\theta_p - \psi_p) \sin^2 \theta_p} \tag{53}$$

The inputted variables ψ_p and θ_p are the in-plane projected angles of the incident and outgoing vector respectively, and are related to the incident and outgoing vectors as follows:

$$\psi_p = \tan^{-1} \left[\cos \left(\pi - \sin^{-1} \left[\frac{\sin \theta_s \sin \phi_s \sin \theta_d}{\sin 2\theta_d \sin \theta_h} \right] \right) \tan \theta_i \right] \quad (54)$$

$$\theta_p = \psi_p + 2\theta_h \quad (55)$$

A common geometric function was proposed by Blinn[3] and first widely used in the Cook-Torrance BRDF:[14]

$$G_c(\hat{\omega}_i, \hat{\omega}_s) = \min \left[1, \frac{2 \cos \theta_h \cos \theta_s}{\cos \theta_d}, \frac{2 \cos \theta_h \cos \theta_i}{\cos \theta_d} \right] \quad (56)$$

This geometric function is a simplification of the Torrance-Sparrow geometric function. The first term in this equation obviously represents no geometric attenuation; the second term represents geometric attenuation due to the outgoing angle or microfacet normal being steep relative to the surface normal (frequently called obscuration); the third term represents geometric attenuation due to the incident angle or microfacet normal being steep relative to the surface normal (frequently called shadowing).

The Modified Beard-Maxwell BRDF uses the following geometric function to model effects due to shadowing and obscuration, containing two fitting parameters that are determined for each material (Ω and τ), as follows:[19, 44]

$$G_{bm}(\theta_h, \theta_d) = \frac{1 + \frac{\theta_h}{\Omega} e^{-2\theta_d/\tau}}{1 + \frac{\theta_h}{\Omega}} \quad (57)$$

Interestingly, this Beard-Maxwell geometric attenuation term is calculated solely in microsurface coordinates, and not macrosurface coordinates. In the original Beard-Maxwell paper in 1973, this geometric function had an additional term depending on ϕ_n , which is a term derived from geometry;[43, 16] however, that term is dropped in

the Modified Beard-Maxwell form. Crockett asserts its contribution is negligible [16].

A rigorous analysis of the geometric attenuation function in the context of an unpolarized microfacet BRDF model was developed, assuming geometric optics, in [32]. Heitz explains the necessity for a geometric attenuation term so that a microfacet BRDF model conserves energy. The necessity for a geometric attenuation term to conserve energy stems from the cross section conversion term σ given in Equation (37) approaching ∞ as θ_i or θ_s approaches 90° . Heitz presents integral tests to determine whether a BRDF conserves energy, and presents a method to derive a geometric attenuation function that is dependent upon the microfacet distribution function. From a geometric optics approach, this understanding makes sense. However, at the scale of a microfacet, geometric optics may not be the best model. A different approach based on a novel comparison between the microfacet BRDF and scalar wave optics diffraction BRDF is developed in this dissertation in Chapter VI, which no longer requires the cross section conversion term σ , eliminating the necessity of a geometric attenuation term.

Directional Volumetric Reflection.

Two models make use of a directional volumetric contribution to the overall BRDF. The Modified Beard-Maxwell model uses the following directional volumetric term:[43, 16, 19, 44, 61]

$$V_{bm}(\theta_i, \theta_s) = \frac{2}{\cos \theta_i + \cos \theta_s} \quad (58)$$

The Sandford-Robertson BRDF has an interesting form of the directional volumetric term, relating to the Fresnel reflection approximation $F_s(\theta)$ as follows:[57, 13]

$$V_s(\theta_i, \theta_s) = \frac{F_s(\theta_i)F_s(\theta_s)}{\pi} \quad (59)$$

Pre-factor Terms.

This section includes terms that were not categorized in the above sections, but are still present in the microfacet BRDF models. Unlike the previous terms, the pre-factor terms are often unique to only one specific model, and thus should not be varied when creating specialized BRDF models. In some cases (such as Ashikhman-Shirley), this includes terms due to using a different microfacet normalization, and terms not found in other BRDF models that did not clearly belong in another category. It also includes terms that may contain part of the cross section conversion σ but not the entire form.

The Ashikhman-Shirley BRDF[1] contains the following pre-factor terms:

$$P_a(\hat{\omega}_i, \hat{\omega}_s) = \frac{k+1}{4(k+2)} \left(\frac{1}{\cos \theta_d \max[\cos \theta_i, \cos \theta_s]} \right) \quad (60)$$

The terms involving the cosine lobe parameter k are simply due to a difference in normalization of the cosine lobe distribution and are unimportant. The term $4 \max[\cos \theta_i, \cos \theta_s]$ could be thought of as a portion of σ , but is not exactly the same form. The term $1/\cos \theta_d$ is unique to this BRDF and may be a geometric attenuation but it was not entirely clear how it relates to terms in other BRDF models, so this was left as a pre-factor term.

The Ward-Duer BRDF[70, 18] uses an approximation to the Beckmann distribution, and does not contain the microfacet distribution normalization. Thus, the pre-factor term exists to cancel the normalization performed by the Beckmann distribution:

$$P_w(\theta_h) = \cos^4 \theta_h \quad (61)$$

The Sandford-Robertson BRDF has the most complex pre-factor form. This is due

to the BRDF's reliance upon Kirchoff's Law for geometric attenuation, which is not generalizable as a closed-form expression. This term is dependent upon an analytically integrable expression for both the surface and the directional volumetric components of the BRDF. Additionally, the normalization of the microfacet distribution function and part of the cross section conversion σ are also present. Its form is as follows (where ε_0 and c are parameters of the Sandford-Robertson BRDF):

$$P_s(\hat{\omega}_i, \hat{\omega}_s) = \frac{N_e(\theta_i)}{4\pi \cos \theta_s} [1 - \rho_v F_s(\theta_i) - \varepsilon_0 F_s(\theta_i)] \quad (62)$$

The microfacet normalization $N_e(\theta_i)$ above is as follows:[57, 13, 35]

$$N_e(\theta_i) = \frac{1}{H(\theta_i)} = \frac{2c^2}{(1 - c^2) \cos \theta_i + \frac{2c^2 + (1 - c^2)^2 \cos^2 \theta_i}{\sqrt{(1 - c^2)^2 \cos^2 \theta_i + 4c^2}}} \quad (63)$$

The Cook-Torrance BRDF, when transformed to this generalized microfacet notation, also contains a pre-factor term of 4. This is unimportant as it simply scales the parameter ρ_s by a fixed overall factor not dependent upon any variables; scaling the parameter ρ_s by 1/4 compensates for this pre-factor.

Common Unpolarized BRDF Models.

In this section, several common BRDF models are related to the general form of a microfacet BRDF developed in Equation (38). By putting these models in the expected form of a microfacet BRDF (where possible), it is easier to understand what assumptions are made by each model, as well as determining what modifications may be performed to enhance the fidelity of a BRDF model.

Many different models are presented in this section, but have been rewritten to fit the common form of a microfacet distribution function presented earlier in this chapter. By writing the models in a common form, the similarities and differences

between the models are more readily apparent. At the end of the section, a summary table is presented to show how these models are similar and how they are different. From the summary table, it is observed that the Cook-Torrance BRDF model is of particular importance, since it is not an overly complex microfacet BRDF model, yet still contains the major components of a microfacet BRDF model. In addition, later in the chapter it is shown that current spectral BRDF extensions of the microfacet model do not adequately describe the BRDF near the specular peak. Since the specular lobe is primarily influenced by the microfacet distribution function, it is instructive to devote particular attention to the choice of microfacet distribution functions between the models. For this reason, the BRDF models are grouped in order of distribution function in this section. Not all microfacet BRDF models are listed here, but many of the more popular models are presented.

Phong.

One of the earliest BRDFs that is still popular today in computer graphics is the Phong BRDF. It can be expressed as follows (where the normalization is altered slightly from the original form):[51]

$$f_r(\hat{\omega}_i, \hat{\omega}_s) = \frac{\rho_s}{2\pi}(k+2)(\hat{\omega}_i \cdot \hat{\omega}_s)^k + \frac{\rho_d}{\pi} \quad (64)$$

Since $\hat{\omega}_i \cdot \hat{\omega}_s = \cos \alpha$, where α is the angle between $\hat{\omega}_i$ and $\hat{\omega}_s$, this BRDF cannot be considered a microfacet model at all, as it does not include a Fresnel term and it does not include a surface normal distribution (i.e., $\alpha \neq \theta_h$). Thus, the Phong BRDF model is not a geometric optics-based model, and is not used in this dissertation. It is included here for completeness due to its popularity, and because it led to development of the Blinn-Phong BRDF model, which can be loosely interpreted as a microfacet model.

Blinn-Phong.

Blinn made a slight modification to the Phong BRDF, noticing it was better to relate the BRDF dependence to the half vector. The Blinn-Phong BRDF is as follows:[3]

$$f_r(\hat{\omega}_i, \hat{\omega}_s) = \rho_s D_c(\theta_h) + \frac{\rho_d}{\pi} \quad (65)$$

This modification by Blinn could allow one to loosely interpret Blinn-Phong as a microfacet model, using the cosine lobe surface normal distribution given in Equation (42). That said, it does not include a Fresnel term and thus is only loosely a microfacet model.

Ashikhman-Shirley.

In 2000, Ashikhman and Shirley developed a BRDF model based on the cosine lobe distribution[1]. Although the model presented was for anisotropic surfaces, it can be easily reduced to isotropic form by setting the author's parameter $n_u = n_v = k$. This yields a form of the BRDF as follows:[1, 47]

$$f_r(\hat{\omega}_i, \hat{\omega}_s) = \rho_s \left(\frac{k+1}{4(k+2)} \right) \left(\frac{D_c(\theta_h) F(\theta_d)}{\cos \theta_d \max[\cos \theta_i, \cos \theta_s]} \right) \quad (66)$$

Ashikhman mentions one may add a constant diffuse offset to this BRDF, but that this could lead to energy conservation issues when used in conjunction with the Fresnel formula. He also provides an approximate scaling of a volumetric term, but it is based on the Schlick approximation to the Fresnel equation and does not contain any other angular dependence other than forcing conservation of energy, so it is excluded here. Ngan's study of BRDF models also neglected this diffuse volumetric term given by Ashikhman, instead using a Lambertian term[47]. The terms in parentheses

depending upon k are due to a slightly different normalization in Ashikhman-Shirley as opposed to the normalization used for the cosine lobe distribution (as was discussed in the distribution function section); the result would be a different fitting parameter ρ_s but the overall best fit quality would not be affected since the angular dependence was not altered. Out of the models using the cosine lobe distribution, the Ashikhman-Shirley model most closely resembles what one would expect a microfacet model to look like based on the underlying physics, having many major elements present for surface reflection. However, it is worth noting it lacks the $\sigma(\theta_i, \theta_s)$ dependence.

Priest Microfacet Model.

The Priest Microfacet Model was the basis upon which the well-known Priest-Germer polarimetric BRDF model was built. Its form is as follows:[53]

$$f_r(\hat{\omega}_i, \hat{\omega}_s) = \rho_s \sigma(\theta_i, \theta_s) D_g(\theta_h) F(\theta_d) \quad (67)$$

This model does not account for volumetric or diffuse scattering, but has all major elements of geometric optical surface reflection. In this model, a Gaussian (Beckmann) distribution is assumed for surface normal orientation. There is no geometric attenuation term, but the geometric scaling due to conversion from cross section to BRDF is present.

Ward-Duer.

In 1992, Ward created a novel anisotropic BRDF model which reduced to an isotropic form by setting his $\alpha_x = \alpha_y = m$. This BRDF model originally included a term proportional to $\sqrt{\sigma(\theta_i, \theta_s)}$ instead of $\sigma(\theta_i, \theta_s)$. This $\sqrt{\sigma}$ dependence was fixed by Duer to form the Ward-Duer model, and was shown by Ngan to be more accurate than the Ward model[47]. The Ward-Duer model is as follows:[18]

$$f_r(\hat{\omega}_i, \hat{\omega}_s) = \rho_s \sigma(\theta_i, \theta_s) D_b(\theta_h) \cos^4(\theta_h) + \frac{\rho_d}{\pi} \quad (68)$$

The Ward-Duer BRDF model uses the Beckmann distribution, but it uses a different normalization which is only accurate if $\theta_h \lesssim 0.2 \text{ rad}$ [70]. This model also ignores Fresnel effects, and does not include any geometric obscuration.

Torrance-Sparrow.

Torrance-Sparrow was one of the first microfacet BRDF models created. It was formulated to represent off-nadir reflection, and thus represents the ratio of the BRDF off-nadir to the BRDF at nadir; i.e., $f_r(\hat{\omega}_i, \hat{\omega}_s)/f_r(\hat{\omega}_i, \hat{\omega}_{i'})$ where, using the notation of Equation (26), $\hat{\omega}_{i'} = [1, \theta_i, \pi]^T$ is the specular reflection from the macrosurface normal. Solving for the BRDF off-specular, its form is as follows:[65]

$$f_r(\hat{\omega}_i, \hat{\omega}_s) = \left(\frac{\rho_s \frac{G_T(\psi_p, \theta_p)}{\cos \theta_s} \exp(-c^2 \theta_h^2) F(\theta_d) + \cos \theta_i}{\rho_s \frac{F(\theta_i)}{\cos \theta_i} + \cos \theta_i} \right) f_r(\hat{\omega}_i, \hat{\omega}_{i'}) \quad (69)$$

This model was groundbreaking in the literature, and is cited by many models developed after its time. It included such notions as Fresnel scaling by the difference angle, and included a distribution function: $\exp(-c^2 \theta_h^2)$. This distribution function, for small θ_h , is approximately the same as the unnormalized Beckmann distribution in Equation (43) if $c = 1/m$ (since $\tan \theta_h \approx \theta_h$ and $\cos \theta_h \approx 1$). For this reason, the Torrance-Sparrow distribution function is not listed separately, even though his approach appears to be novel for his time. The geometric attenuation term was discussed previously.

The additional $\cos \theta_i$ term in the numerator could be thought of as a volumetric term in the model, as it does not include any surface reflectance scaling. The denominator of the equation is purely for normalization. In fact, the equation could be

rewritten in a more symmetric form using basic algebra as follows:

$$f_r(\hat{\omega}_i, \hat{\omega}_s) = \left(\frac{\rho_s \exp(-c^2 \theta_h^2) F(\theta_d) G_T(\psi_p, \theta_p) \cos \theta_i + \cos^2 \theta_i \cos \theta_s}{\rho_s F(\theta_i) \cos \theta_s + \cos^2 \theta_i \cos \theta_s} \right) f_r(\hat{\omega}_i, \hat{\omega}_i') \quad (70)$$

In this form, it is clear that other than the microsurface distribution, the denominator is the numerator if $\theta_h = 0$; that is, the specular reflection case where the half vector aligns with the macrosurface normal. In this case, the geometric attenuation factor $G_T = 1$, and $\theta_d = \theta_i$ since the microfacet orientation is identical to the macrosurface normal. That said, it is also clear that the Torrance-Sparrow BRDF does not obey symmetry (that is, the result is different if $\hat{\omega}_i$ and $\hat{\omega}_s$ are swapped).

Alternate Torrance-Sparrow Form.

A slight modification of the Torrance-Sparrow BRDF form above is sometimes given as follows:[59, 45]

$$f_r(\hat{\omega}_i, \hat{\omega}_s) = \rho_s \sigma(\theta_i, \theta_s) G_T(\psi_p, \theta_p) \exp(-c^2 \theta_h^2) F(\theta_d) + \frac{\rho_d}{\pi} \quad (71)$$

The parameters in this rewritten form are not the same as the parameters in the original form. In this form, the distribution function and all other major elements are the same, but its form appears closer to that of standard microfacet BRDFs, and it is not dependent upon knowledge of the specular BRDF value. The second term in the above rewritten form often appears as $a/d\omega_i$ in the literature, but it is more clearly written as a Lambertian term[45]. The primary components of this alternate Torrance-Sparrow form remain the same, although the $\sigma(\theta_i, \theta_s)$ dependence is also included. Since this is only a minor variation of the Torrance-Sparrow BRDF, it is not given a different name.

Cook-Torrance.

The Cook-Torrance BRDF was introduced in 1982 as one of the first modern microfacet BRDFs, establishing a common distribution function (based on the Beckmann distribution) and a symmetric form. This was one of the first popular BRDFs to use a simple geometric attenuation term that numerically approximates the Torrance-Sparrow geometric attenuation. Its form is as follows:[14]

$$f_r(\hat{\omega}_i, \hat{\omega}_s) = 4\rho_s\sigma(\theta_i, \theta_s)D_b(\theta_h)F(\theta_d)G_c(\hat{\omega}_i, \hat{\omega}_s) + \frac{\rho_d}{\pi} \quad (72)$$

The factor of 4 arises from writing the BRDF in the form of my $\sigma(\theta_i, \theta_s)$ function; it would be compensated by a constant scaling of the fit parameter ρ_s and is thus not important. The only missing component is a directional volumetric contribution to the BRDF. In this light, it is perhaps not surprising that Ngan found this Cook-Torrance BRDF to perform relatively well for a wide variety of materials as compared to other BRDF models included in his study[47].

Sandford-Robertson.

The Sandford-Robertson BRDF was developed in 1985 to handle infrared properties of aircraft paints[57]. The original paper can be difficult to obtain, but descriptions of the original model can also be found in polarimetric extensions by Conant[13] and Jafolla[35]. Although loosely a microfacet model, its primary concern was to force conservation of energy through employment of Kirchhoff's Law.

Recall the Sandford-Robertson BRDF used an approximation to Fresnel $F_s(\theta)$, and an unnormalized elliptical distribution function given by $D_{e,u}(\theta_h)$, as discussed previously. Using these equations, its form is as follows:

$$\begin{aligned}
f_r(\hat{\omega}_i, \hat{\omega}_s) &= f_s(\hat{\omega}_i, \hat{\omega}_s) + f_v(\theta_i, \theta_s) \\
&= \frac{N_e(\theta_i)D_{e,u}(\theta_h)}{4\pi \cos \theta_s} [1 - \rho_v F_s(\theta_i) - \varepsilon_0 F_s(\theta_i)] + \rho_v V_s(\theta_i, \theta_s)
\end{aligned} \tag{73}$$

Sandford-Robertson normalized the distribution function in θ_i space rather than θ_h space, so the normalization was kept separate here as $N_e(\theta_i)$, given in the Equation (63) of the pre-factor section above.

This BRDF is somewhat unique in that it uses a Fresnel approximation for the volumetric component of the BRDF as well as the surface reflection component of the BRDF. Conservation of energy is assured by using Kirchhoff's Law, represented by the term in brackets, rather than through a direct geometric attenuation term. Also, the Fresnel approximation in terms of θ_d is never computed directly. For surface reflection, the Fresnel approximation is implicitly called through the Kirchhoff term, but in $(\hat{\omega}_i, \hat{\omega}_s)$ macrosurface coordinates instead of $(\hat{\omega}_h, \hat{\omega}_d)$ microsurface coordinates. Also, although part of the $\sigma(\theta_i, \theta_s)$ term is present, it is missing a dependence on $\cos \theta_i$. The normalization term $N_e(\theta_i)$ does have a $\cos \theta_i$ term that could be factored out to provide this $1/\cos \theta_i$ dependence, but the paper states this is for distribution normalization, and thus is separate from the cross section conversion $\sigma(\theta_i, \theta_s)$. Finally, note that it is not obvious whether the Sandford-Robertson BRDF is symmetric with respect to $\hat{\omega}_i, \hat{\omega}_s$ input coordinates due to this normalization with respect to θ_i .

The Sandford-Robertson BRDF model depends on four parameters: b (within $F_s(\theta)$), ρ_v , ε_0 , and c (within the distribution function). A nice property of Sandford-Robertson is that there are well-defined constraints on these values to obtain a physical BRDF [13]. Recall that $1/G_s$ is defined in Equation (40); the constraints are then given as follows:

- $0 \leq b < 1$ to maintain the Fresnel approximation
- $0 \leq c < 1$ to maintain an elliptical distribution

- $0 \leq \varepsilon_0 \leq G_s$ to ensure directional emittance never exceeds 1
- $0 \leq \rho_v \leq G_s - \varepsilon_0$ to ensure conservation of energy

Modified Beard-Maxwell.

The Beard-Maxwell BRDF model was originally developed in 1973 to model paints[43]. However, it is not used much today in its unmodified form. The Modified Beard Maxwell model is far more popular, in part due to an extensive library of parameters contained in the NEF database to be discussed later. Comprehensive discussions of the Beard-Maxwell model can be found in an AFRL Technical Report by Crockett[16] and a dissertation by Shell[61].

The Modified Beard-Maxwell model has the following form:[19, 44]

$$f_r(\hat{\omega}_i, \hat{\omega}_s) = \rho_s \sigma(\theta_i, \theta_r) D_{bm}(\theta_h) G_{bm}(\theta_h, \theta_d) F(\theta_d) + \rho_v V_{bm}(\theta_i, \theta_s) + \rho_d \quad (74)$$

As written above, this model uses the Cauchy distribution for the surface normals, and contains a simple directional volumetric scattering term. It also has a separate diffuse volumetric scattering term that was not specified in the original Beard-Maxwell model. As discussed when cataloging distribution functions above, sometimes the bi-static scan distribution $D_s(\theta_h)$ is used instead of the modified Cauchy distribution $D_{bm}(\theta_h)$ above.

Recently, it appears the NEF database has been updated to include a more complex form of the volumetric term, and parameters have been rearranged (as of version 10). That latest version is not discussed in this document, as there is little information on that version available at this time. However, be aware that later versions of the NEF Database may not use the Modified Beard-Maxwell form described above.

Table 3.1. Common Unpolarized Microfacet BRDF Models

Model	P	D($\hat{\omega}_h$)	G	V	$\rho_d?$	$\sigma?$	F?	# Prm
Phong	1	$(\hat{\omega}_i \cdot \hat{\omega}_s)^k$	n/a	n/a	Y	n	n	3
Blinn-Phong	1	$D_c(\theta_h)$	n/a	n/a	Y	n	n	3
Ash.-Shir.	P_a	$D_c(\theta_h)$	n/a	n/a	Y	n	Y	5
Priest	1	$D_b(\theta_h)$	n/a	n/a	Y	Y	Y	5
Ward-Duer	P_w	$\approx D_b(\theta_h)$	n/a	n/a	Y	Y	Y	5
Torr.-Spar.	*	$\approx D_b(\theta_h)$	G_T	n/a	Y	n	Y	5
Alt Torr.-Spar.	1	$\approx D_b(\theta_h)$	G_T	n/a	Y	Y	Y	5
Cook-Torr.	4	$D_b(\theta_h)$	G_c	n/a	Y	Y	Y	5
Wellems	1	$D_h(\theta_h)$	G_T	n/a	Y	Y	Y	6
Beard-Maxwell	1	$D_{bm,u}(\theta_h)^\dagger$	G_{bm}	V_{bm}	Y	Y	Y	$\geq 8^\dagger$
Sand.-Rob.	P_s	$D_{e,u}(\theta_h)$	Kirchhoff	V_s	n	n	**	4

[†] In place of the Cauchy distribution, Beard-Maxwell can use the bi-static scan, which adds several more parameters $\rho_{fs}(\theta_h)$ to specify $D_s(\theta_h)$ empirically

* The original 1967 Torrance-Sparrow BRDF does not have a convenient form for the pre-factor, as it was designed to relate in-plane BRDF to the specular peak via a ratio.

** Sandford-Robertson uses a Fresnel approximation $F_s(\theta)$, but it is used indirectly in the reflective component via Kirchhoff's law, and is not in microsurface coordinates

Unpolarized BRDF Model Remarks.

As can be seen when putting these BRDF models in a common form, there are many shared elements. The most common choice for surface normal distribution is the Beckmann (Gaussian) distribution. This includes: Priest, Ward-Duer, Torrance-Sparrow, and Cook-Torrance BRDF models. Another reasonable choice is the cosine lobe distribution, which is used by Blinn-Phong and Ashikhman-Shirley distributions. Finally, the Sandford-Robertson BRDF uses an elliptical distribution, and uses Kirchhoff's law to enforce geometric attenuation. The results are summarized in Table 3.1[5].

Within these models, the Ward-Duer model has no apparent theoretical advantage in accuracy over the Cook-Torrance model. Similarly, the Torrance-Sparrow model uses an approximation for the distribution function that makes its use suspect at large θ_h angles that occur in some view geometries. The Cook-Torrance BRDF is

also nearly identical to the Priest Microfacet Model, except with a geometric scaling term and Lambertian component. For this reason, it is expected that the Cook-Torrance BRDF to perform the best out of these Beckmann models analyzed in this section. Similarly, it is expected that the Ashikhman-Shirley (modified to include a Lambertian term) to perform best out of models with the cosine lobe distribution due to inclusion of Fresnel scaling. Ngan’s assessment agrees with these conclusions when he states the best models he analyzed were Ashikhman-Shirley, Cook-Torrance, and He-Torrance[47]. Note that Ngan did not compare Sandford-Robertson, Modified Beard-Maxwell, or Torrance-Sparrow in his analysis; he did additionally include He-Torrance and Lafortune models. The He-Torrance model is not a geometric optics microfacet model and includes an infinite series sum[31]; the Lafortune model is similar to the Blinn-Phong model with an added parameter representing the number of specular lobes[39, 45].

By putting these microfacet BRDFs into a uniform format, some observations can be made. For example, consider the Ashikhman-Shirley BRDF model. The geometric scaling and additional dependence on θ_d outside of Fresnel may suggest that replacing those terms with a different model’s geometric scaling may achieve better performance. Also, a volumetric and Lambertian scattering term may also be incorporated in the BRDF to improve performance.

One could also attempt to create a flexible microfacet BRDF function from this compilation of BRDFs, using the general form in Equation (38). The distribution function, geometric function, and volumetric function could be chosen for a particular application and compared with other choices to determine the ideal form of a BRDF for each material separately. For example, if one were to modify the Cook-Torrance BRDF model to include a directional volumetric component based on the Modified Beard-Maxwell model, one could use a notional BRDF of the following form:

$$f_r(\hat{\omega}_i, \hat{\omega}_s) = \rho_s \sigma(\theta_i, \theta_s) D_b(\theta_h) F(\theta_d) G_c(\hat{\omega}_i, \hat{\omega}_s) + \frac{2\rho_v}{\cos \theta_i + \cos \theta_s} + \frac{\rho_d}{\pi} \quad (75)$$

When making such combinations, care must be taken to ensure fit parameters are obtained that do not violate conservation of energy, by ensuring the DHR is restricted to the range $[0, 1]$ for all $\hat{\omega}_i$ in the hemisphere.

For a particular material, one could also attempt to fit to the cosine lobe distribution instead of the Beckmann distribution by replacing $D_b(\theta_h)$ with $D_c(\theta_h)$ and comparing results, choosing the distribution function best suited to the material. Fitting to anisotropic versions of these distribution functions could also be used, depending on material properties. This flexible microfacet BRDF model is used in Chapter V.

Polarimetric BRDF Models.

When incorporating polarization effects to a BRDF, the primary modification to the general BRDF form is that the Fresnel equation is no longer a scalar value, but is in general a 4x4 Mueller matrix which is referred to as $\overset{\leftrightarrow}{\mathbf{F}}(\hat{\omega}_i, \hat{\omega}_s)$. The resulting polarimetric BRDF (pBRDF) is also a 4x4 Mueller BRDF matrix must be multiplied by the incident Stokes vector, $\overset{\leftrightarrow}{\mathbf{f}}_r(\hat{\omega}_i, \hat{\omega}_s)$.

In microfacet coordinates, the Mueller matrix for Fresnel reflection of the incident beam is [59]

$$\overset{\leftrightarrow}{\mathbf{F}}_h(\theta_d) = \frac{1}{2} \begin{bmatrix} F_s + F_p & F_s - F_p & 0 & 0 \\ F_s - F_p & F_s + F_p & 0 & 0 \\ 0 & 0 & 2 \operatorname{Re}[r_s r_p^*] & 2 \operatorname{Im}[r_s r_p^*] \\ 0 & 0 & -2 \operatorname{Im}[r_s r_p^*] & 2 \operatorname{Re}[r_s r_p^*] \end{bmatrix} \quad (76)$$

The subscript h is a reminder that this equation is for Fresnel reflection *in the microfacet (half vector) coordinate system*, not in the macrosurface coordinates. In

macrosurface coordinates, the expression for Fresnel reflection is

$$\overset{\leftrightarrow}{\mathbf{F}}(\hat{\boldsymbol{\omega}}_i, \hat{\boldsymbol{\omega}}_s) = \mathbb{R}_z(\phi_h + \pi) \mathbb{R}_y(\theta_h) \overset{\leftrightarrow}{\mathbf{F}}_h(\theta_d) \mathbb{R}_y(-\theta_h) \mathbb{R}_z(-\phi_h) \quad (77)$$

where $\mathbb{R}_a(\theta)$ is a right-handed rotation about the a axis by an amount θ , as before, but the rotation must be done in terms of Stokes vector rotation, as the Stokes vector is a 4-dimensional constrained vector (not an orthogonal basis). A rotation in Mueller matrix coordinates is not easily defined in general (for arbitrary axis of rotation). It is simpler to find $\overset{\leftrightarrow}{\mathbf{F}}$ by rotating the electric field vectors directly (using the Jones matrix), then converting those results to the Mueller matrix form. Since Fresnel reflection does not contain any depolarizing element, this calculation can be performed exactly using the Jones calculus[52, 53].

Recall that, for isotropic media, the electric field is perpendicular to the direction of propagation, but can be s polarized (perpendicular to the plane of incidence) or p polarized (parallel to the plane of incidence). In this two-dimensional space, the following equation defines the Jones matrix relationship between incident and scattered electric fields due to Fresnel reflection $\overset{\leftrightarrow}{\mathbf{F}}_j$: [52, 53]

$$\begin{aligned} \vec{\mathbf{E}}_{j,o} &= \begin{bmatrix} E_{s,o} \\ E_{p,o} \end{bmatrix} = \overset{\leftrightarrow}{\mathbf{F}}_j(\hat{\boldsymbol{\omega}}_i, \hat{\boldsymbol{\omega}}_s) \vec{\mathbf{E}}_{j,i} \\ &= \mathbb{R}(\eta_o) \overset{\leftrightarrow}{\mathbf{F}}_j(\theta_d) \mathbb{R}(-\eta_i) \vec{\mathbf{E}}_{j,i} \\ &= \begin{bmatrix} \cos \eta_o & \sin \eta_o \\ -\sin \eta_o & \cos \eta_o \end{bmatrix} \begin{bmatrix} r_s(\theta_d) & 0 \\ 0 & r_p(\theta_d) \end{bmatrix} \begin{bmatrix} \cos \eta_i & -\sin \eta_i \\ \sin \eta_i & \cos \eta_i \end{bmatrix} \begin{bmatrix} E_{s,i} \\ E_{p,i} \end{bmatrix} \end{aligned} \quad (78)$$

As shown above, a rotation into $\hat{\boldsymbol{\omega}}_h$ space is used to diagonalize the Fresnel reflection, and a rotation to $\hat{\boldsymbol{\omega}}_s$ space is used to transform Fresnel reflection into scattered

coordinates. Note that the Fresnel terms used are the *complex* Fresnel reflection terms for the electric field reflection (r_p and r_s), so the Fresnel matrix is complex. This matrix multiplication can be simplified to the following form:

$$\begin{aligned} \overset{\leftrightarrow}{\mathbf{F}}_j(\hat{\omega}_i, \hat{\omega}_s) &= \begin{bmatrix} F_{ss} & F_{ps} \\ F_{sp} & F_{pp} \end{bmatrix} \\ F_{ss} &= r_s(\theta_d) \cos \eta_i \cos \eta_o + r_p(\theta_d) \sin \eta_i \sin \eta_o \\ F_{ps} &= -r_s(\theta_d) \cos \eta_o \sin \eta_i + r_p(\theta_d) \cos \eta_i \sin \eta_o \\ F_{sp} &= r_p(\theta_d) \cos \eta_o \sin \eta_i - r_s(\theta_d) \cos \eta_i \sin \eta_o \\ F_{pp} &= r_p(\theta_d) \cos \eta_i \cos \eta_o + r_s(\theta_d) \sin \eta_i \sin \eta_o \end{aligned} \tag{79}$$

The variables η_i and η_o relate to the transformation to half-vector and difference vector coordinates from incidence angle and scattered angle coordinates. Let $\hat{\mathbf{s}}_i$ be a unit vector in the direction of the s polarization state of the incident beam and let $\hat{\mathbf{s}}_o$ be a unit vector in the direction of the s polarization state of the scattered beam. Then, these values are given by Priest and Germer as[52, 53]

$$\begin{aligned} \cos \eta_i &= \hat{\mathbf{s}}_i \cdot \left(\frac{\hat{\omega}_i \times \hat{\omega}_h}{\|\hat{\omega}_i \times \hat{\omega}_h\|} \right) \\ &= \frac{\hat{\omega}_i \times \hat{\mathbf{z}}}{\|\hat{\omega}_i \times \hat{\mathbf{z}}\|} \cdot \frac{\hat{\omega}_i \times \hat{\omega}_h}{\|\hat{\omega}_i \times \hat{\omega}_h\|} \\ &= \frac{\hat{\omega}_h \cdot \hat{\mathbf{z}} - (\hat{\omega}_i \cdot \hat{\mathbf{z}})(\hat{\omega}_i \cdot \hat{\omega}_h)}{\|\hat{\omega}_i \times \hat{\mathbf{z}}\| \|\hat{\omega}_i \times \hat{\omega}_h\|} \\ &= \frac{\cos \theta_h - \cos \theta_i \cos \theta_d}{\sin \theta_i \sin \theta_d} \end{aligned} \tag{80}$$

$$\begin{aligned}
\cos \eta_o &= \hat{\mathbf{s}}_o \cdot \left(\frac{\hat{\boldsymbol{\omega}}_s \times \hat{\boldsymbol{\omega}}_h}{\|\hat{\boldsymbol{\omega}}_s \times \hat{\boldsymbol{\omega}}_h\|} \right) \\
&= \frac{\hat{\boldsymbol{\omega}}_s \times \hat{\mathbf{z}}}{\|\hat{\boldsymbol{\omega}}_s \times \hat{\mathbf{z}}\|} \cdot \frac{\hat{\boldsymbol{\omega}}_s \times \hat{\boldsymbol{\omega}}_h}{\|\hat{\boldsymbol{\omega}}_s \times \hat{\boldsymbol{\omega}}_h\|} \\
&= \frac{\hat{\boldsymbol{\omega}}_h \cdot \hat{\mathbf{z}} - (\hat{\boldsymbol{\omega}}_s \cdot \hat{\mathbf{z}})(\hat{\boldsymbol{\omega}}_s \cdot \hat{\boldsymbol{\omega}}_h)}{\|\hat{\boldsymbol{\omega}}_s \times \hat{\mathbf{z}}\| \|\hat{\boldsymbol{\omega}}_s \times \hat{\boldsymbol{\omega}}_h\|} \\
&= \frac{\cos \theta_h - \cos \theta_s \cos \theta_d}{\sin \theta_s \sin \theta_d}
\end{aligned} \tag{81}$$

The 2x2 complex matrix $\overset{\leftrightarrow}{\mathbf{F}}_j(\hat{\boldsymbol{\omega}}_i, \hat{\boldsymbol{\omega}}_s)$ is then transformed to a Mueller matrix, given as [4, 36, 21, 53]

$$\begin{aligned}
F_{00} &= |F_{ss}|^2 + |F_{sp}|^2 + |F_{ps}|^2 + |F_{pp}|^2 \\
F_{01} &= |F_{ss}|^2 + |F_{sp}|^2 - |F_{ps}|^2 - |F_{pp}|^2 \\
F_{02} &= F_{ss}F_{ps}^* + F_{ss}^*F_{ps} + F_{sp}F_{pp}^* + F_{sp}^*F_{pp} \\
F_{03} &= i(F_{ps}F_{ss}^* - F_{ps}^*F_{ss}) + i(F_{pp}F_{sp}^* - F_{pp}^*F_{sp}) \\
F_{10} &= |F_{ss}|^2 - |F_{sp}|^2 + |F_{ps}|^2 - |F_{pp}|^2 \\
F_{11} &= |F_{ss}|^2 - |F_{sp}|^2 - |F_{ps}|^2 + |F_{pp}|^2 \\
F_{12} &= F_{ss}F_{ps}^* + F_{ss}^*F_{ps} - F_{sp}F_{pp}^* - F_{sp}^*F_{pp} \\
F_{13} &= i(F_{ps}F_{ss}^* - F_{ps}^*F_{ss}) - i(F_{pp}F_{sp}^* - F_{pp}^*F_{sp}) \\
F_{20} &= F_{ss}F_{sp}^* + F_{ss}^*F_{sp} + F_{ps}F_{pp}^* + F_{ps}^*F_{pp} \\
F_{21} &= F_{ss}F_{sp}^* + F_{ss}^*F_{sp} - F_{ps}F_{pp}^* - F_{ps}^*F_{pp} \\
F_{22} &= F_{ss}F_{pp}^* + F_{ss}^*F_{pp} + F_{ps}F_{sp}^* + F_{ps}^*F_{sp} \\
F_{23} &= i(F_{ps}F_{sp}^* - F_{ps}^*F_{sp}) - i(F_{ss}F_{pp}^* - F_{ss}^*F_{pp}) \\
F_{30} &= i(F_{ss}F_{sp}^* - F_{ss}^*F_{sp}) + i(F_{ps}F_{pp}^* - F_{ps}^*F_{pp}) \\
F_{31} &= i(F_{ss}F_{sp}^* - F_{ss}^*F_{sp}) - i(F_{ps}F_{pp}^* - F_{ps}^*F_{pp}) \\
F_{32} &= i(F_{ss}F_{pp}^* - F_{ss}^*F_{pp}) + i(F_{ps}F_{sp}^* - F_{ps}^*F_{sp}) \\
F_{33} &= F_{ss}F_{pp}^* + F_{ss}^*F_{pp} - F_{ps}F_{sp}^* - F_{ps}^*F_{sp}
\end{aligned} \tag{82}$$

$$\overset{\leftrightarrow}{\mathbf{F}}(\hat{\boldsymbol{\omega}}_i, \hat{\boldsymbol{\omega}}_s) = \frac{1}{2} \begin{bmatrix} F_{00} & F_{01} & F_{02} & F_{03} \\ F_{10} & F_{11} & F_{12} & F_{13} \\ F_{20} & F_{21} & F_{22} & F_{23} \\ F_{30} & F_{31} & F_{32} & F_{33} \end{bmatrix} \quad (83)$$

A couple of special cases are worth noting. First, if in-plane data is taken, there is symmetry in the Fresnel coefficients. Only the following coefficients are non-zero and are related: $F_{00} = F_{11}$, $F_{01} = F_{10}$, $F_{22} = F_{33}$, and $F_{23} = -F_{32}$ (all other coefficients are zero since $\eta_i = \eta_o = 0$). Second, if the index of refraction is real, then regardless of orientation of the incident and scattered vectors the $\overset{\leftrightarrow}{\mathbf{F}}_j$ Jones matrix form of the Fresnel expression is also real. This means there is no phase change in the material, and thus the circular polarization state is unchanged (i.e., $F_{3x} = F_{x3} = 0$ for all $x \neq 3$)[52]. These properties may hold for a BRDF, but are not necessarily valid since the BRDF can also have a volumetric reflection component that alters this surface reflection polarization behavior. However, if a material is primarily a surface reflector, it is expected that these properties approximately hold for the BRDF as well. In fact, a metric measuring how closely these properties hold could possibly be used as a measure of how volume-reflecting a material is relative to the surface-reflecting properties.

This Fresnel Mueller matrix handles the surface reflection's polarization effects. Other modifications are also required for the volumetric components (directional and diffuse) to put them in matrix form, although typically the diffuse volumetric component is assumed to be depolarizing [59]. This depolarizing volumetric Mueller matrix is referred to as $\overset{\leftrightarrow}{\mathbf{M}}_d$, and defined as

$$\overset{\leftrightarrow}{\mathbf{M}}_d = \begin{bmatrix} 1 & 0 & 0 & 0 \\ 0 & 0 & 0 & 0 \\ 0 & 0 & 0 & 0 \\ 0 & 0 & 0 & 0 \end{bmatrix} \quad (84)$$

Thus, the polarimetric expression for a microfacet BRDF is as follows:

$$\overset{\leftrightarrow}{\mathbf{f}}_r(\hat{\omega}_i, \hat{\omega}_s) = \rho_s \sigma(\theta_i, \theta_s) G(\hat{\omega}_i, \hat{\omega}_s) D(\theta_h) \overset{\leftrightarrow}{\mathbf{F}}(\hat{\omega}_i, \hat{\omega}_s) + \rho_v V(\hat{\omega}_i, \hat{\omega}_s) \overset{\leftrightarrow}{\mathbf{M}}_v + \frac{\rho_d}{\pi} \overset{\leftrightarrow}{\mathbf{M}}_d \quad (85)$$

In this formulation, $f_{r,00}(\hat{\omega}_i, \hat{\omega}_s) = f_r(\hat{\omega}_i, \hat{\omega}_s)$; i.e., the first entry in the matrix is the unpolarized BRDF. It is possible for $V(\hat{\omega}_i, \hat{\omega}_s)$ to have a polarimetric component, which is represented by the arbitrary definition of $\overset{\leftrightarrow}{\mathbf{M}}_v$; this could be the Fresnel Mueller matrix $\overset{\leftrightarrow}{\mathbf{F}}(\theta_d)$, the diffuse (depolarizing) Mueller matrix $\overset{\leftrightarrow}{\mathbf{M}}_d$, or a Mueller matrix unique to the model.

Priest-Germer.

The Priest-Germer pBRDF polarizes the Priest Microfacet Model BRDF discussed in Section 3.6. By replacing the Fresnel term in the Priest Microfacet Model with the Fresnel Mueller Matrix, the Priest-Germer pBRDF is obtained as follows:[52, 53]

$$\overset{\leftrightarrow}{\mathbf{f}}_r(\hat{\omega}_i, \hat{\omega}_s) = \rho_s \sigma(\theta_i, \theta_s) D_g(\theta_h) \overset{\leftrightarrow}{\mathbf{F}}(\hat{\omega}_i, \hat{\omega}_s) \quad (86)$$

As can be seen, its form is identical to the previous form, except the polarimetric Fresnel Mueller Matrix discussed above is used in place of the Fresnel equation for unpolarized light.

Hyde.

The Hyde pBRDF was derived using a Method of Moments electromagnetic calculation to develop a fully polarimetric model. Functionally, using the results of Hyde's Method of Moments calculation, his pBRDF extended the Priest-Germer pBRDF by adding the geometric factor that was derived by Blinn and used in the Cook-Torrance BRDF. This model is given as[33]

$$\overset{\leftrightarrow}{\mathbf{f}}_r(\hat{\boldsymbol{\omega}}_i, \hat{\boldsymbol{\omega}}_s) = \rho_s \sigma(\theta_i, \theta_s) D_g(\theta_h) G_c(\hat{\boldsymbol{\omega}}_i, \hat{\boldsymbol{\omega}}_s) \overset{\leftrightarrow}{\mathbf{F}}(\hat{\boldsymbol{\omega}}_i, \hat{\boldsymbol{\omega}}_s). \quad (87)$$

The Hyde pBRDF model includes a slightly different form of the distribution $D_g(\theta_h)$, with two parameters: σ_h and ℓ . The rationale for this choice is because Hyde reasoned the surface is more correctly described by a probability distribution not just in surface height, but also in correlation length, given as

$$\sigma_g = \frac{\sigma_h \sqrt{2}}{\ell}, \quad (88)$$

where σ_h is the Gaussian width of the probability distribution function describing the surface height and ℓ is the Gaussian width of the probability distribution function describing the correlation length of the surface. With this substitution the Hyde pBRDF Gaussian distribution reduces to Equation (44) (and thus also to the Beckmann distribution). This substitution is noted again in Chapter VI.

A diffuse component was also generated by the Hyde pBRDF but is not included above; if one wanted to add a generic diffuse component, it would simply be of the form given in Equation (85) as a depolarizing Lambertian component.

Conant-Iannarilli.

The Conant-Iannarilli pBRDF polarizes the Sandford-Robertson BRDF discussed in Section 3.6. Since the Sandford-Robertson BRDF does not explicitly use the Fresnel equation but instead uses an approximation, a different approach was used to polarize this model. To do so, the model first estimates \tilde{n} from the Fresnel approximation $F_s(\theta_d)$ (which depends on a single parameter b), then assigns the Mueller matrix formulation above to the fractional portion of the BRDF produced by the specular term in the original Sandford-Robertson BRDF. The volumetric component of the Sandford-Robertson BRDF is assumed to be depolarizing (i.e., it is multiplied by $\overset{\leftrightarrow}{\mathbf{M}}_d$).

The Conant-Iannarilli pBRDF form is as follows:[13]

$$\overset{\leftrightarrow}{\mathbf{f}}_r(\hat{\omega}_i, \hat{\omega}_s) = \frac{f_s(\hat{\omega}_i, \hat{\omega}_s)}{f_s(\hat{\omega}_i, \hat{\omega}_s) + f_v(\theta_i, \theta_s)} \overset{\leftrightarrow}{\mathbf{F}}(\hat{\omega}_i, \hat{\omega}_s) + f_v(\theta_i, \theta_s) \overset{\leftrightarrow}{\mathbf{M}}_d \quad (89)$$

where $f_s(\hat{\omega}_i, \hat{\omega}_s)$ and $f_v(\theta_i, \theta_s)$ are given by the unpolarized Sandford-Robertson model in Equation (73).

Other Polarimetric Models.

It is trivial to polarize nearly all other unpolarized microfacet models discussed (as long as Fresnel reflection is modeled) by replacing the Fresnel reflection with $\overset{\leftrightarrow}{\mathbf{F}}(\hat{\omega}_i, \hat{\omega}_s)$, and the diffuse component with the depolarizing $\overset{\leftrightarrow}{\mathbf{M}}_d$ matrix. For example, one could generate a polarimetric Cook-Torrance model as follows:

$$\overset{\leftrightarrow}{\mathbf{f}}_r(\hat{\omega}_i, \hat{\omega}_s) = \rho_s \sigma(\theta_i, \theta_s) D_b(\theta_h) G_c(\hat{\omega}_i, \hat{\omega}_s) \overset{\leftrightarrow}{\mathbf{F}}(\theta_d) + \frac{\rho_d}{\pi} \overset{\leftrightarrow}{\mathbf{M}}_d \quad (90)$$

3.7 Spectral Dependence of Microfacet BRDFs

Up to this point, the possibility of a spectral dependence in the microfacet model has been largely ignored. However, there are some existing techniques for inserting the wavelength dependence in microfacet models in a manner that is easy to use; these techniques are discussed in this section. After introducing these techniques, a brief analysis is presented that indicates there is still room for improvement.

From a modeling standpoint, looking at the generic form of an unpolarized microfacet model in Equation (38) and inserting wavelength dependence, the following result is expected:

$$f_r(\hat{\omega}_i, \hat{\omega}_s, \lambda) = \rho_s G(\hat{\omega}_i, \hat{\omega}_s) D(\theta_h) F(\theta_d, \tilde{n}(\lambda)) \sigma(\theta_i, \theta_s) + \rho_v V(\hat{\omega}_i, \hat{\omega}_s, \lambda) + \frac{\rho_d(\lambda)}{\pi} \quad (91)$$

In the microfacet model, where physical optics is ignored, ideally surface reflection should not depend on wavelength except via the Fresnel term (where \tilde{n} is known to vary with wavelength). If one had a material with measured \tilde{n} (both real and imaginary parts), and measured the BRDF of such a material, the only variation with wavelength for surface reflection should be directly analogous to the variation in Fresnel reflectance for a given pair of incident and scattered angles if the microfacet model strictly holds.

If the microfacet BRDF models do not strictly hold (as is expected since physical optics is neglected) but still has approximate accuracy, it may be possible to reinterpret the microfacet distribution function $D(\theta_h)$ as instead being a scattering distribution function, which could then vary with wavelength. As λ increases, for the same surface normal distribution the scattering distribution function is expected to appear more flat, and thus it is expected that the BRDF, in general, becomes more

specular. For a surface reflector, the width of the specular lobe is due to the microfacet distribution, and not due to the geometric scaling or Fresnel components (which simply scale the overall height, but do not change relative width significantly). There was no experimental evidence found in the current literature to indicate how BRDF functions scale with small changes in wavelength in the MWIR and LWIR; one of the intended major contributions of my work is to fill that void. BRDF measurements tend to be at 3.39 and 10.6 μm in the MWIR and LWIR, with other methods to estimate the BRDF being used in between. These common techniques in the literature for approximating BRDF at an unknown wavelength are summarized here.

Crockett mentions three approaches in his description of the Modified Beard-Maxwell microfacet BRDF model, two of which are general enough to apply to any BRDF model. The first approach he mentions is to simply scale the BRDF measured at the closest wavelength λ_0 by the DHR at both λ_0 and the target wavelength λ , as follows:[16]

$$f_r(\hat{\omega}_i, \hat{\omega}_s, \lambda) = \frac{\rho(\hat{\omega}_i, \lambda)}{\rho(\hat{\omega}_i, \lambda_0)} f_r(\hat{\omega}_i, \hat{\omega}_s, \lambda_0) \quad (92)$$

A second approach, stated by Crockett and also used by Montanaro (and the NEF database, which uses the Modified Beard-Maxwell BRDF model), is to linearly interpolate between two known BRDF wavelengths λ_j and λ_k and the reflectance $\rho(\hat{\omega}_i, \lambda)$, as follows:[16, 44]

$$f_r(\hat{\omega}_i, \hat{\omega}_s, \lambda) = \rho(\hat{\omega}_i', \lambda) \left[\left(\frac{\lambda_j - \lambda}{\lambda_j - \lambda_k} \right) \frac{f_r(\hat{\omega}_i, \hat{\omega}_s, \lambda_k)}{\rho(\hat{\omega}_i', \lambda_k)} + \left(\frac{\lambda - \lambda_k}{\lambda_j - \lambda_k} \right) \frac{f_r(\hat{\omega}_i, \hat{\omega}_s, \lambda_j)}{\rho(\hat{\omega}_i', \lambda_j)} \right] \quad (93)$$

Montanaro states that early materials in the NEF used a fixed DHR value at $\theta'_i = 10^\circ$, but later materials use a fixed DHR value at $\theta'_i = 20^\circ$ ($\phi'_i = 0$), which

performs better [44]. For sake of a preliminary investigation, consider two separate cases: $\theta'_i = 20^\circ$ (which is called *fixed* linear interpolation), and $\theta'_i = \theta_i$ (which is called *variable* linear interpolation); the latter seems to make more intuitive sense, but appears to not be used in the NEF database.

One of the advantages of the Sandford-Robertson BRDF is that it allows for scaling with respect to wavelength based on the DHR. Knowledge of DHR specifies the parameter ε_0 in Sandford-Robertson, and thus that parameter varies as a function of λ in a way that is easy to measure in the laboratory. The volumetric parameter ρ_v also varies as a function of wavelength, but other parameters are assumed constant [57, 13, 35]. That said, experimental evidence in the MWIR or LWIR to confirm or deny the Sandford-Robertson wavelength variation was not found.

Crockett proposed a third approach, which was to interpolate the BRDF parameters in Beard-Maxwell[16]. He proposes a solution related to Beard-Maxwell's bi-static scan function. Shell also mentioned Crockett's scaling of BRDF parameters in his Ph.D. dissertation[61]. To accomplish this, one must measure the BRDF at multiple wavelengths, then fit to a microfacet model. The NEF only measures two wavelengths in the MWIR and LWIR, so the NEF dataset does not form a good basis upon which to perform this analysis. Extending this approach to other BRDF models for surface-reflecting materials was the initial approach taken for this dissertation; however, in Chapter V, flaws in this approach are noted, requiring a shift to pioneering a method to compare microfacet BRDFs with scalar wave optics BRDFs, which are based on physical optics and therefore should have an inherent wavelength dependence. This connection is developed in Chapter VI. Despite these noted flaws in the microfacet model, the addition of experimentally measured BRDF data in the MWIR and LWIR for multiple samples represents a significant contribution in this dissertation that did not previously exist.

Investigation of Microfacet Wavelength Scaling.

This section examines some existing BRDF data in the literature to suggest possible additional wavelength dependence of BRDFs not currently captured by the microfacet BRDF models. In particular, two common sources of BRDF data are examined: the MERL database and the NEF database. The results suggest there should be a wavelength dependence in at least the microfacet distribution function.

Two different approaches were taken to quantify the error in wavelength scaling techniques given in Equations (92) and (93). The first approach was based on data in the NEF database, and the second approach was based on data in the MERL database. The general procedure was to compute the relative error of scaling the BRDF at one wavelength to the BRDF at another wavelength. In both approaches, the following definition of relative error was used:

$$\epsilon(\hat{\omega}_i, \hat{\omega}_s) = \frac{f_r(\hat{\omega}_i, \hat{\omega}_s) - s(\hat{\omega}_i, \hat{\omega}_s)}{f_r(\hat{\omega}_i, \hat{\omega}_s)} \quad (94)$$

where $f_r(\hat{\omega}_i, \hat{\omega}_s)$ represents the actual BRDF value and $s(\hat{\omega}_i, \hat{\omega}_s)$ represents the interpolated BRDF value. Thus, the reported error at each incident and scattered angle is relative to the actual BRDF value at that same incident and scattered angle. The magnitude indicates amount of relative error; if ϵ is positive, the actual BRDF value exceeds the interpolated BRDF; if ϵ is negative, the interpolated BRDF value exceeds the actual BRDF.

Common Sources of BRDF Data.

There are several sources of measured BRDF data, but the two that are perhaps most prevalent are Matusik's Mitsubishi Electric Research Laboratory (MERL) database[42] and the Non-conventional Exploitation Factors (NEF) Database[72]. The MERL database contains densely measured BRDF data for 100 materials, with

three channels for each material (red, green, and blue). Data is stored in Rusinkiewicz coordinates[56]. The MERL database’s primary advantage is that the raw BRDF data is available without any model fitting error for several materials.

On the other hand, the NEF Database contains a library of over 400 materials, many with DHRs measured from 400 nm to 12 μm . BRDF data for these materials is measured at up to five wavelengths: 0.325, 0.6328, 1.06, 3.39, and 10.6 μm [72]. Unlike the MERL database, the NEF database only stores fit parameters for the Modified Beard Maxwell model; it does not contain the actual BRDF measurement data. However, this database measures the BRDF in the IR, and uses laser illumination to obtain a much higher precision BRDF measurement not possible using Matusik’s method.

A free online database posted by Cornell contains a few materials with BRDFs measured from 400 nm to 700 nm with 10 nm spacing, using a spherical reflection surface and a monochrometer [15, 41]. Corresponding index of refraction measurements (for Fresnel scaling), DHR (for linear interpolation), and error bounds were not included, so it is difficult to decouple the Fresnel effect from other BRDF effects for this data and discern the accuracy of the measurements. It is also not possible to confirm or reject the linear wavelength scaling suggested by Crockett[16] and Montanaro[44] using this data due to the absence of DHR calculations. Due to these limitations, this dataset was not examined in this dissertation.

NEF Analysis.

The analysis in this section is, in part, contained in a paper presented at the SPIE Defense, Sensing, and Security Conference 2015; see [7]. To investigate the MWIR and LWIR behavior of the BRDF, the NEF database was used[46]. Recall that in the IR, the BRDF for the NEF database is measured at 1.06 μm , 3.39 μm , and 10.6

μm ; this data is then fit to a modified Beard-Maxwell model similar to the model discussed in Section 3.5, but with the bi-static scan distribution function in place of the Cauchy distribution function. (The NEF database includes parameters specifying the shape of the bi-static scan.) To determine the accuracy of wavelength scaling, the BRDF values at $1.06 \mu m$ and $10.6 \mu m$ were used to predict the BRDF value at $3.39 \mu m$. A MATLAB® script from Dr. Joseph Meola (AFRL Sensors Directorate) was used to obtain the BRDF values from the NEF database for a specified material and geometry. For all materials analyzed, the input angle was chosen to be $\theta_i = 30^\circ$ and $\phi_i = 0$. The output angle was chosen to be in-plane forward scatter ($\phi_s = 180^\circ$) for 1° increments of θ_s .

This process was performed for Infragold® (NEF Material ID 0494UUUSTD), which is a fairly diffuse material in the IR commonly used for calibration. The BRDF for all three IR wavelengths, and for a linear interpolation to $3.39 \mu m$ from $1.06 \mu m$ and $10.6 \mu m$ using Equation (93) with fixed scaling, is shown in Figure 12 for $\theta_i = 30^\circ$. The relative error of the linear interpolation using Equation (94) is shown in Figure 13. For this very diffuse material without much variation at the three measured wavelengths, the relative error is within 10% at all points, and is generally within 5% at most points.

To determine the behavior for a more specular material, the process was repeated for aluminum (NEF Material ID 0539UUUALM). The BRDFs are plotted in Figure 14 (note the logarithmic scale), with the relative error plotted in Figure 15. For aluminum with an incident angle of $\theta_i = 30^\circ$, it is clear the results are not good at all. The relative error of linear interpolation in predicting the BRDF at $3.39 \mu m$ is nearly always above 100%, and is frequently above 300%. This result suggests that the linear scaling may also fail significantly at points between $3.39 \mu m$ and $10.6 \mu m$, justifying further investigation of the BRDF variation as a function of wavelength.

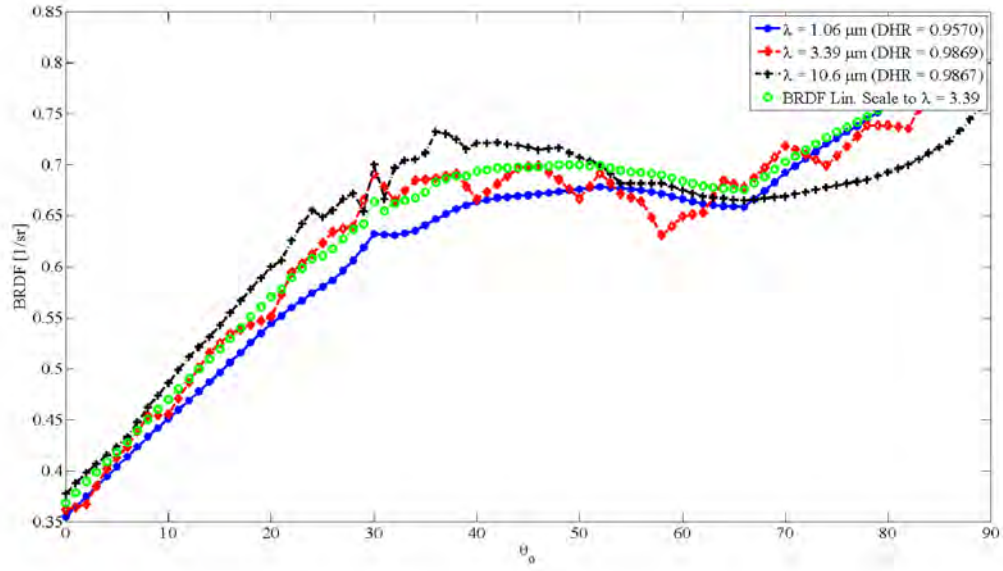


Figure 12. BRDFs for Infragold from NEF at $1.06 \mu m$, $3.39 \mu m$, and $10.6 \mu m$. The linearly scaled BRDF to $3.39 \mu m$ using Equation (93) (fixed scaling) is also shown

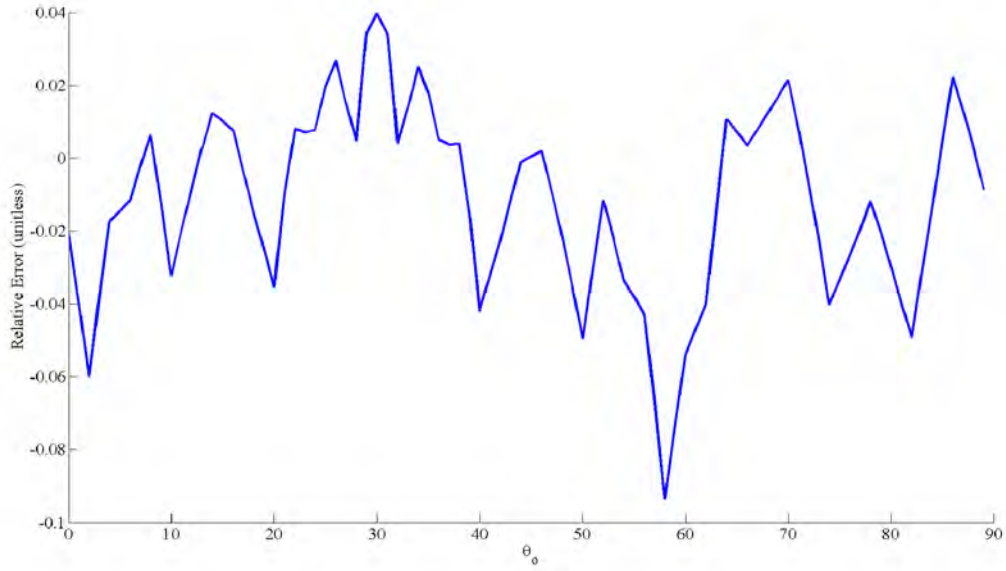


Figure 13. Relative error of the linearly scaled Infragold BRDF to $3.39 \mu m$ using $1.06 \mu m$ and $10.6 \mu m$ BRDF data using Equation (93) (fixed scaling)

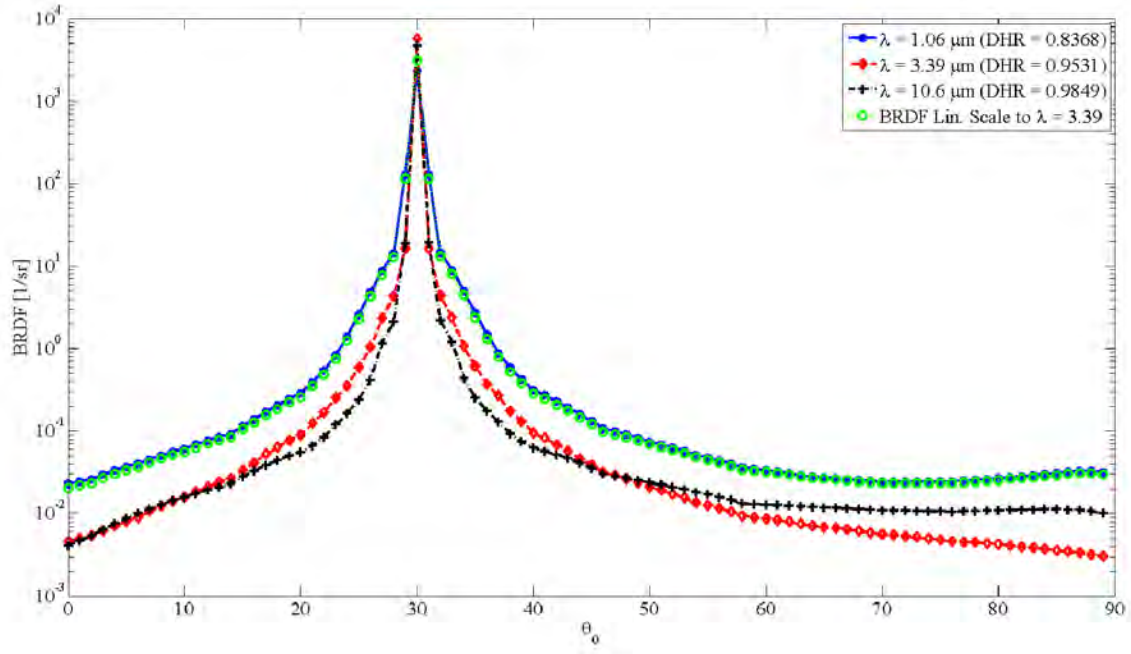


Figure 14. In plane BRDFs for aluminum from NEF at $1.06 \mu m$, $3.39 \mu m$, and $10.6 \mu m$. The linearly scaled BRDF to $3.39 \mu m$ using Equation (93) (fixed scaling) is also shown

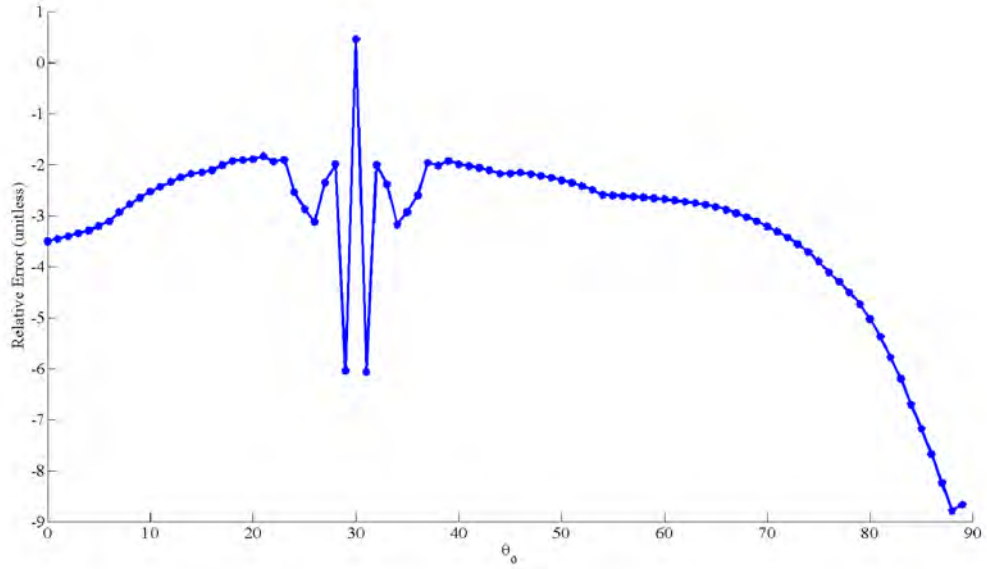


Figure 15. Relative error of the linearly scaled aluminum BRDF to $3.39 \mu m$ using $1.06 \mu m$ and $10.6 \mu m$ BRDF data using Equation (93) (fixed scaling)

Table 3.2. Summary of Modified Cauchy Distribution fits for NEF Materials

Material ID	λ (μm)	B	s	R^2
0886UUUPNT	3.39	0.1141	0.2051	0.9966
	10.6	0.0924	0.1239	0.9999
0404UUUWOD	3.39	0.0595	0.1413	0.9844
	10.6	0.0392	0.0898	0.9775

R^2 represents quality of fit (closer to 1 is better)

Another preliminary analysis of NEF data was performed. As mentioned earlier, the NEF data uses a bi-static scan for the microfacet normal distribution function, although Modified Beard-Maxwell sometimes uses a modified Cauchy distribution $D_{bm}(\theta_h)$ given by Equation (46) instead. To observe whether there exists a potential wavelength dependence of the microfacet surface normal distribution parameter, a least squares fit of the bi-static scan data to the modified Cauchy distribution was performed for the same material at 3.39 μm and 10.6 μm .

First, this analysis was performed on the NEF material ID 0886UUUPNT (white, weathered paint on aluminum). This material was chosen because the bi-static scan fit well to the modified Cauchy distribution at both 3.39 μm and 10.6 μm . This analysis was then repeated again for NEF material ID 0404UUUWOD (weathered bare pine lumber). The fitting results are presented in Table 3.2.

As can be seen in the table, the amplitude B does not appear to change significantly for either wavelength; however, the specular lobe width parameter s reduces to about 60% of its value at 10.6 μm . This suggests that one area where a significant wavelength scaling may appear is in the distribution function. Although the microfacet orientation is not changing with wavelength, the longer wavelengths are sampling a larger area of the surface for a single wave, and thus are closer to the global surface normal orientation. Therefore, one key area to observe changes in wavelength while conducting this spectral BRDF analysis is the microfacet distribution function $D(\theta_h)$.

Additionally, by observing model parameters in the NEF database, it became obvious that the NEF data at times violates fundamental microfacet model assumptions to obtain the best fit. Since the modified Beard-Maxwell model is a microfacet distribution that ignores diffraction and interference effects, all terms in the model should theoretically be non-negative. However, the NEF contains negative entries for volumetric scattering parameters at $10.6\ \mu m$ for both of the above materials (0886UU-UPNT and 0404UUWOD). This does not fit with a geometric optics (microfacet) interpretation of the BRDF.

Unfortunately, with the NEF database, it is not possible to discern how much of the error is due to fitting to the chosen modified Beard-Maxwell BRDF model and how much of the error is due to actual measured BRDF variation, as the measured data was not included with the database. Additionally, the complex index of refraction is not known independently as a function of wavelength (except as it was fit to the BRDF model as a fitting parameter), so it is not possible to determine how much of this variation is due to Fresnel variation with different microfacet normal angles θ_d .

MERL Analysis.

The second technique used to investigate BRDF changes with wavelength from existing data was from the MERL database. Recall the MERL database contains densely measured red, green, and blue channel BRDF data. Although the red, green, and blue data is broadband, the wavelength spacing is much closer than with the NEF IR data. Thus, the MERL data has two primary advantages over the NEF dataset for a preliminary analysis: wavelength spacing between known BRDF values is relatively close, and the data is not fit to any model. Its primary disadvantages are: wavelength collection is broadband, wavelength ranges are in the visible spectrum, and the complex index of refraction for each material is unknown. Thus, the MERL

database is a reasonable complement to the NEF database for a preliminary analysis but cannot be used for the direct analysis required by this research.

The simple HDR scaling in Equation (92) was investigated using materials from the MERL database with an incident angle of $\theta_i = 30^\circ$ (recall by convention for all isotropic materials $\phi_i = 0$). A MATLAB® and C++ wrapper was created to read in MERL data and calculate the DHR from the MERL data, and a trilinear interpolation routine was used to interpolate between data points. Then, the HDR scaling for each scattered angle in Equation (92) was computed. The BRDF values for all channels of brass are plotted in Figure 16 (note the scale is logarithmic), and the HDR values for brass are plotted in Figure 17.

Then, the scalar interpolation routine was used twice. First, Equation (92) was used to estimate the scaled red BRDF based on the green BRDF and the scaled HDR from green to red, resulting in an estimate for the red BRDF. Then, the same equation was used to estimate the scaled blue BRDF based on the green BRDF and the scaled HDR from green to blue, resulting in an estimate for the blue BRDF. The results are plotted in Figure 18 for in-plane data, using the relative error of the estimated BRDF to the actual BRDF at each scattered angle.

As can be seen from Figure 18, even ignoring the specular peak, the relative error for brass is still fairly high, as much as 30% in either direction. The DHR scales correctly (ie, the error is about equal in the positive and negative direction), but changes to the shape of the BRDF do not occur by the overall scaling.

This process was then repeated for a relatively Lambertian surface, the "gold-paint.binary" file in the MERL database. The BRDFs for the red, green, and blue channels are plotted in Figure 19 (note the scale is not logarithmic), HDR in Figure 20, and relative error in scaling with Equation (92) is shown in Figure 21. The relative error for the green to red conversion is generally about 10%, while the relative error

for the green to blue conversion is about double. These results also show substantial relative error, suggesting that this scaling may not result in accurate values for the BRDF. The error does not follow a similar pattern as with the previous brass analysis, suggesting the error may not be systemic. This suggests a different technique may be better suited for wavelength scaling.

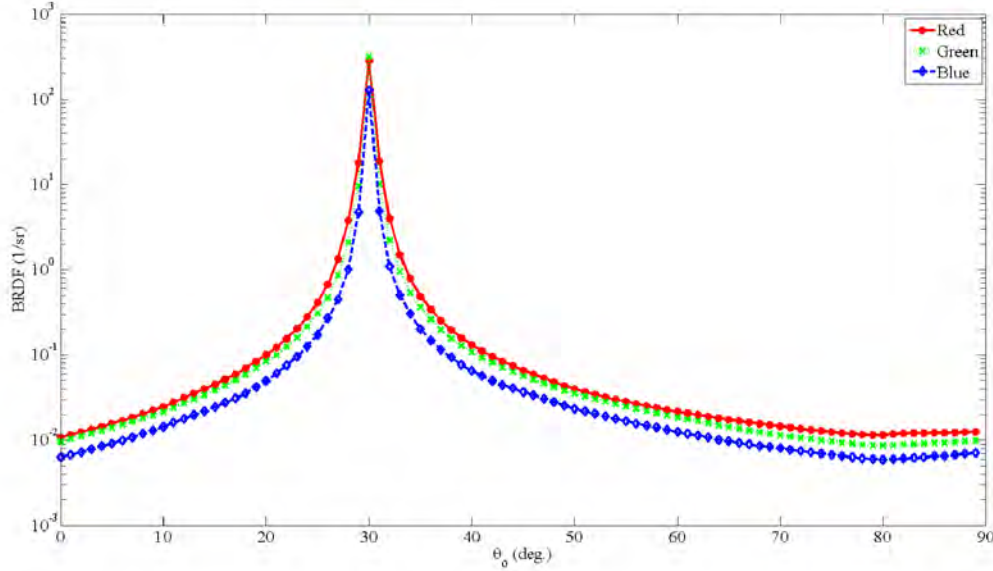


Figure 16. BRDF from MERL brass file for $\theta_i = 30^\circ$ and for the red, green, and blue channels

Examining the linear scaling of BRDF is somewhat more difficult using MERL data, as the MERL data is broadband over the red, green, and blue channels. To perform a preliminary investigation, it was necessary to assign wavelength values to each channel. A typical CCD camera spectral response curve has a peak in the red, green, and blue channels, but the peak is broadband, not at a narrow wavelength. Since camera specifications used to take the MERL data were not provided, notional values of 610 nm, 540 nm, and 460 nm are assigned to the red, green, and blue channels. Then the red and blue channel BRDF data is used as truth data, attempting to obtain the green BRDF using Equation (93). The relative error between the actual

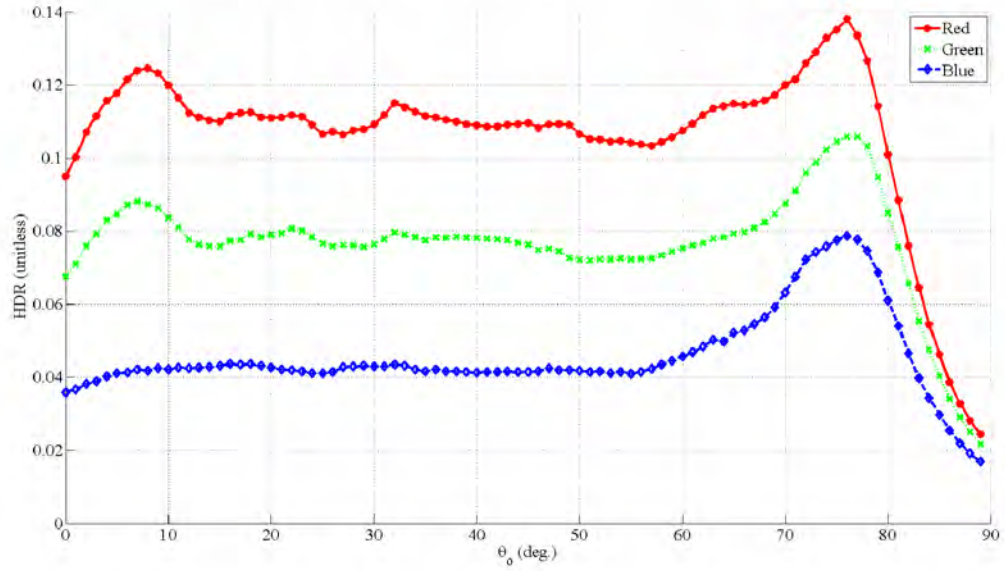


Figure 17. HDR from MERL brass file for the red, green, and blue channels

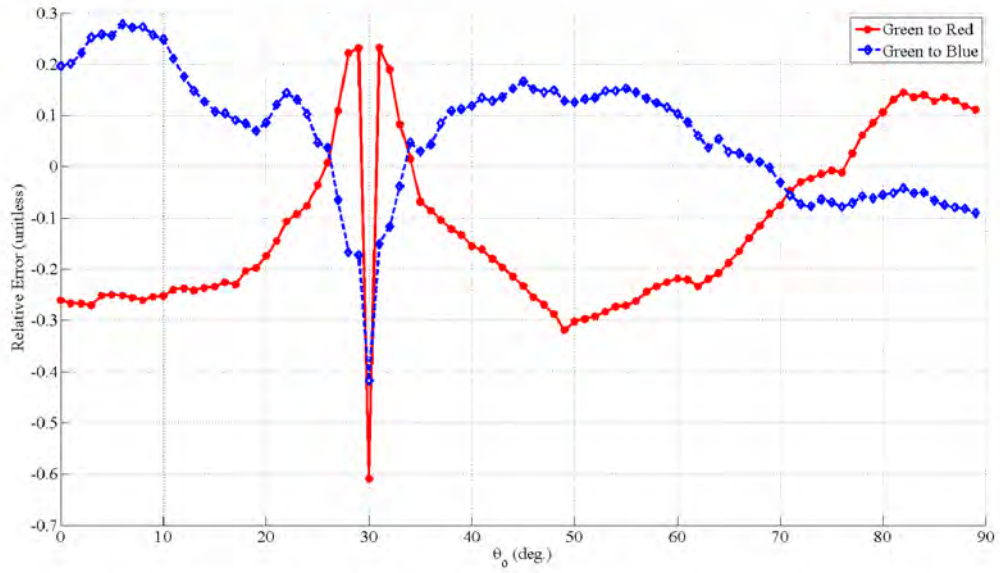


Figure 18. Relative error of MERL brass file when scaling green BRDF to red BRDF, and when scaling green BRDF to blue BRDF, using Equation (92)

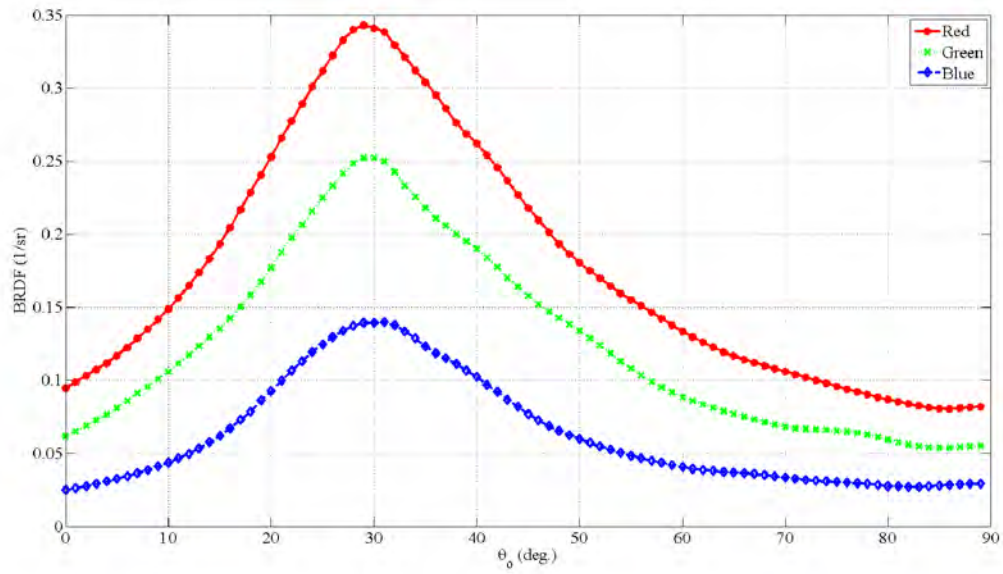


Figure 19. BRDF from MERL gold-paint file for $\theta_i = 30^\circ$ and for the red, green, and blue channels

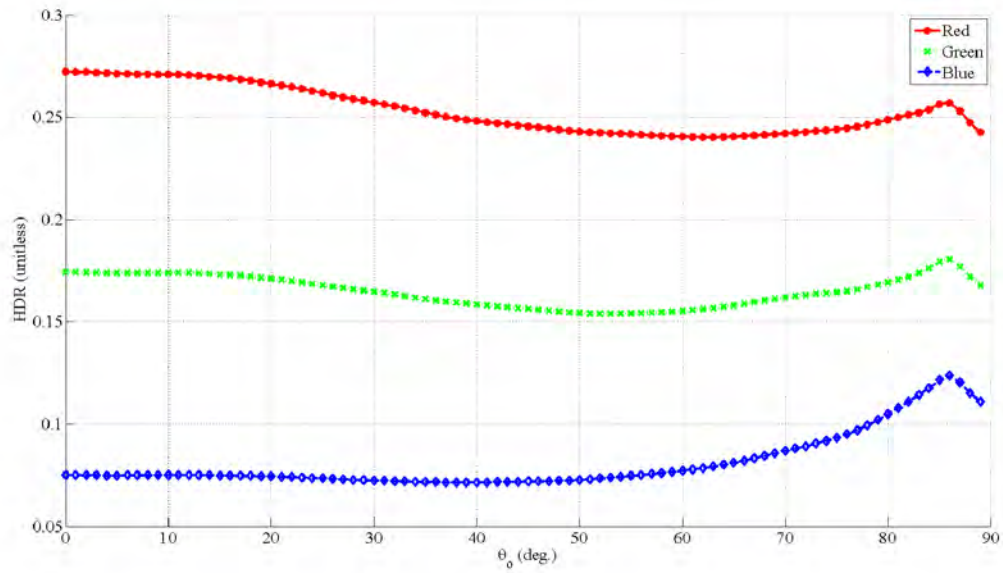


Figure 20. HDR from MERL gold-paint file for the red, green, and blue channels

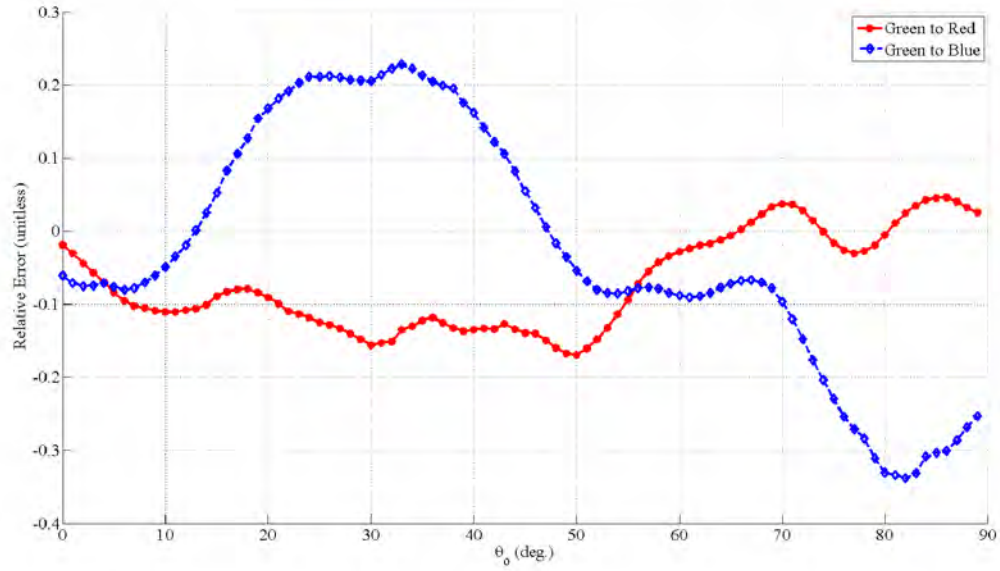


Figure 21. Relative error of MERL gold-paint file when scaling green BRDF to red BRDF, and when scaling green BRDF to blue BRDF, using Equation (92)

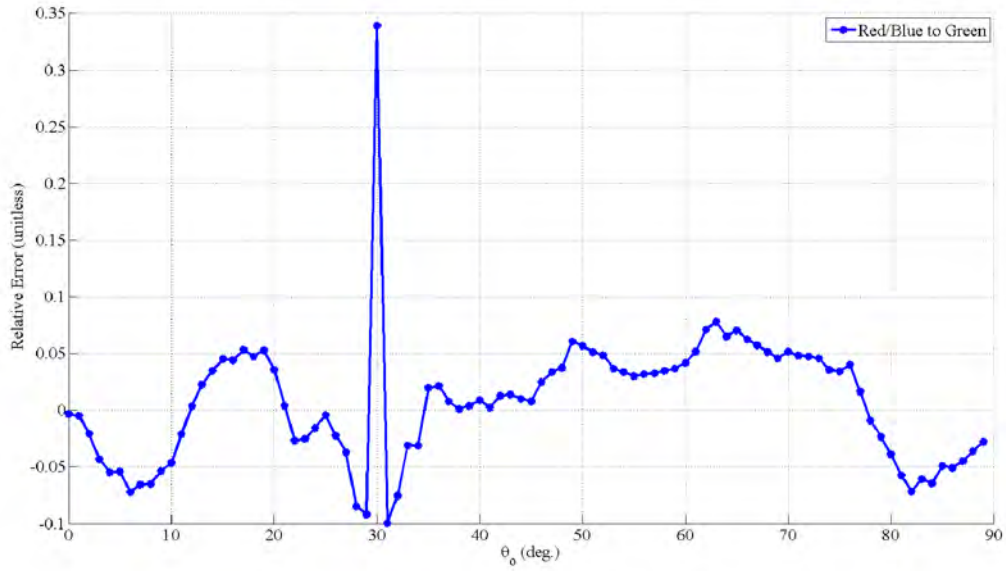


Figure 22. Relative error of MERL brass file when scaling red/blue BRDF to green BRDF, using Equation (93) (variable scaling)

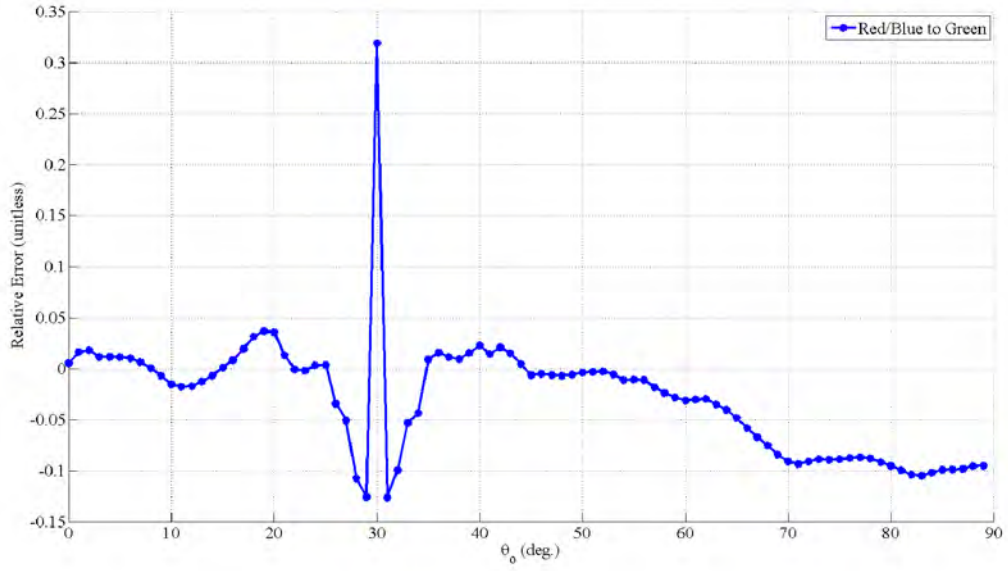


Figure 23. Relative error of MERL brass file when scaling red/blue BRDF to green BRDF, using Equation (93) (fixed scaling)

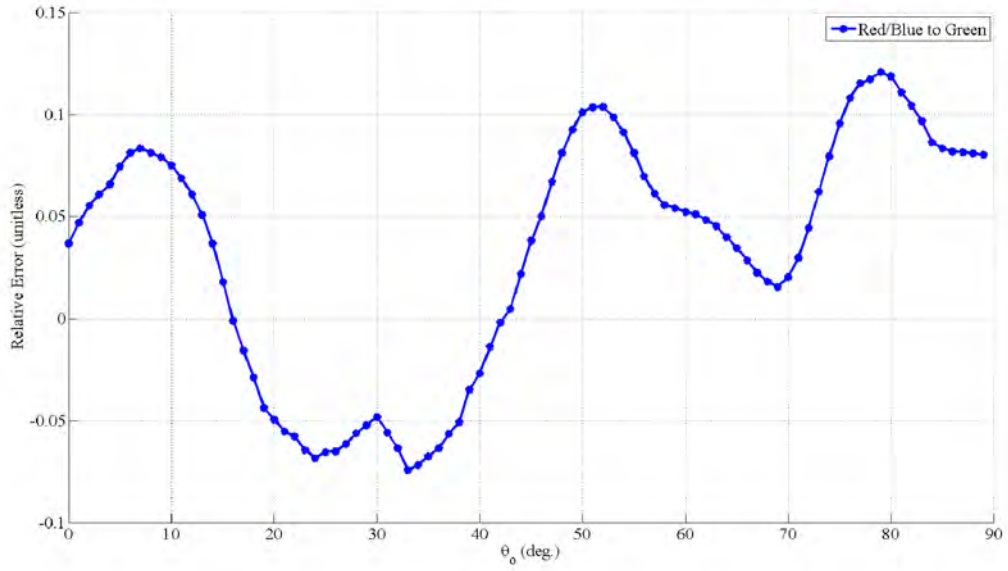


Figure 24. Relative error of MERL gold-paint file when scaling red/blue BRDF to green BRDF, using Equation (93) (variable scaling)

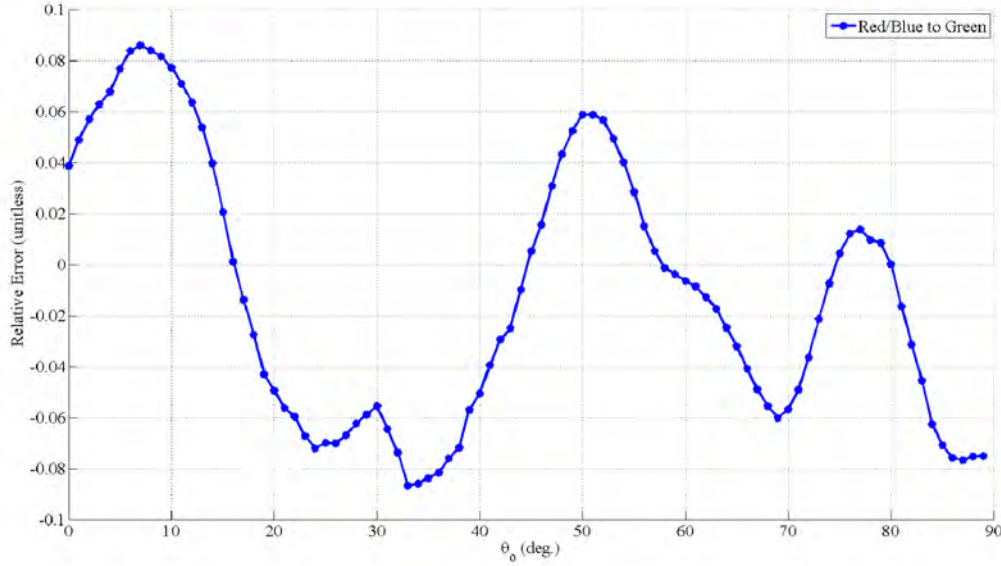


Figure 25. Relative error of MERL gold-paint file when scaling red/blue BRDF to green BRDF, using Equation (93) (fixed scaling)

BRDF and the linear estimate of the BRDF is then plotted in Figures 22 and 23 for brass (relative and fixed scaling). For gold-paint results, see Figures 24 and 25.

In both cases, the error is reduced when using linear scaling by having finely-measured BRDF data, but it is still present. For a more specular material such as brass, there is still significant error around the specular lobe regardless of whether fixed or variable linear scaling is used; relative error at the specular lobe is especially concerning, as the specular lobe can be several orders of magnitude higher in BRDF value, and thus results in a significantly large absolute error. In general, for both materials, the relative error is still $\pm 10\%$ for either fixed or variable scaling even if the specular point is ignored. The error also tends to be higher (in absolute value) at around specular reflection, suggesting the shape of the specular lobe may not scale linearly. This result is for a relatively dense measurement of BRDF in 100 nm increments, where the two known BRDFs are separated by only 200 nm in wavelength; in the MWIR and LWIR, this error is expected to be amplified due to the extremely large

separation in wavelength between the 3.39 μm and 10.6 μm BRDF measurements typical in this region.

Potential Closed-Form Wavelength Scaling.

From this investigation, it appears a more accurate nonlinear wavelength scaling may be desirable. In [64], a proposed BRDF distribution function scaling based on a modified form of the Ward-Duer BRDF was specified. In this proposed scaling, the Gaussian width parameter σ_g was revised to scale with wavelength, with this scaling given as

$$\sigma_g = \frac{\sigma_0}{\lambda} \quad (95)$$

where σ_0 is an actual surface roughness. The results agreed with DHR measurements that were made for that paper, but since DHR is an integrated BRDF, this did not show whether the BRDF is accurately modeled by this scaling factor. However, this paper suggested a possible modification that is indicative of what was originally thought to be a viable closed-form approximation to the BRDF.

These observations from my MERL and NEF preliminary analysis, along with the suggested modification by Su, motivated measurement of the BRDF of a handful of materials at multiple wavelengths in the MWIR and LWIR, to be discussed in Chapters IV and V. These observations motivated devoting particular attention to changes in the specular lobe. Measurements could then be fitted to a BRDF model, and the λ dependence of the width parameter could then be extracted and added to the model. After attempting that approach, it was determined that there are fundamental flaws with microfacet models. Therefore, prior to concluding this chapter, the background for scalar wave optics BRDF models is presented, as it is important for theoretical developments presented in Chapter VI.

3.8 Scalar Wave Optics BRDF Models

Another class of BRDF models is scalar (non-polarimetric) BRDF models based on wave optics; that is, models that include diffraction and interference. The primary advantage of this class of models is that a more complete description of the BRDF is present, since diffraction is included in the derivation of the model. However, a key drawback of these models is that, for an arbitrary surface, the models quickly become computationally cumbersome and generally do not result in a closed-form model. Scalar wave optics models are, therefore, not directly useful for a resource-constrained problem like HSRS. However, as is observed later in the dissertation, analysis of the wavelength scaling of experimental BRDF data uncovered a shortcoming in the microfacet BRDF model that can be explained using scalar wave optics models. Portions of this section were taken from the background in [10].

Several different physical optics models have been developed, deriving from the Kirchhoff tangent plane approximation (for a wide variety of surfaces at paraxial angles), small perturbation approximation (for optically smooth surfaces at all angles), and other unifying methods (which attempt to join the two); for a survey of over 30 of these models, see Elfouhaily [20]. More recently, a method for estimating surface statistics using the tangent plane approximation and assuming a Gaussian distribution of surface properties was developed in [12]. Although this method did not include out-of-plane scatter and assumed s -polarized incident light, its success in predicting surface statistics lends credence to using a physical optics model based on the tangent plane approximation.

The Beckmann-Kirchhoff (BK) scattering model was formulated in 1963 [2]. Similar to [12], the BK model uses the tangent plane approximation and assumes a Gaussian distribution of surface properties. However, the original BK theory was formulated prior to formal definition of the BRDF in 1977 [48]. This BK model was

modified when the linear systems diffraction BRDF theory was generalized to all incident and scattered angles, as well as for a variety of surfaces, by Krywonos [38]. Linear systems diffraction BRDF theory was originally formulated for paraxial reflection in the Harvey-Shack BRDF model, then was extended to arbitrary angles in the Generalized Harvey-Shack (GHS) BRDF model [30, 29, 38]. The GHS BRDF model developed by Krywonos does not possess a known closed-form solution in general. It was derived from a linear systems (Fourier theory) approach to scalar wave optics to calculate scattering off a surface. GHS theory is more physically rigorous, but is more computationally intensive and unfortunately, this method fails to distinguish between scattering due to surface reflection versus scattering due to volumetric effects. In both cases, the surface is treated as adding an overall phase offset, regardless of whether the scatter is due to the surface or due to impurities in the material. Krywonos also proposed MBK BRDF theory that forms the basis of comparison for this dissertation, and which is equal to his GHS theory in the limit of either a polished or very rough surface [30, 37]. GHS theory has been used to accurately predict surface statistics in studies by Stover [63] and Schröder [60].

The GHS model is quite complex in its general form, and thus not suitable for remote sensing applications. In calculating the BRDF using GHS, it is necessary to define the reflecting surface, then perform a Fourier transform for each incident and scattered angle pair, and to compute a relevant surface roughness that involves a double integral expression that does not, in general, evaluate in closed-form. Another numerical double integration is required to ensure conservation of energy [37, 7]. Since hyperspectral remote sensing is already tasked with the difficult objective of backing out atmospheric parameters from an observed scene, adding such computational complexity to describe optical scatter would not be an easy task. This is why the microfacet model was initially examined instead of a linear systems model. However,

in Chapter V, experimental measurements performed for this work show that microfacet models do not capture fundamental spectral changes in the form of the BRDF. Therefore, it is important to introduce the GHS BRDF here, and then compare it to the microfacet model in Chapter VI.

The GHS BRDF is derived as an extension to Harvey-Shack theory. It is based on the Rayleigh-Sommerfeld diffraction integral, which is derived from Maxwell's Equations presented in Equation (6) for a homogeneous, isotropic media. Under these conditions, the vector field components are separable, resulting in the scalar form of the Helmholtz equation. By applying the physical optics approximation to a diffracting scenario, the Rayleigh-Sommerfeld equation results, commonly found in Fourier optics texts such as Goodman: [24, 37]

$$U(\hat{x}, \hat{y}, \hat{z}) = \int_{-\infty}^{\infty} \int_{-\infty}^{\infty} U_o(\hat{x}', \hat{y}'; 0) \left(\frac{1}{2\pi\hat{\ell}} - i \right) \frac{\hat{z} \exp(i2\pi\hat{\ell})}{\hat{\ell}} d\hat{x}' d\hat{y}', \quad (96)$$

where U_o represents the electromagnetic field at the diffracting plane ($z = 0$), and $\hat{\ell}$ is given as

$$\hat{\ell}^2 = (\hat{x} - \hat{x}')^2 + (\hat{y} - \hat{y}')^2 + \hat{z}^2, \quad (97)$$

where $(x', y', 0)$ is a Cartesian point in the diffracting plane, assumed to be illuminated by a plane wave, and (x, y, z) is the Cartesian point at which the field is to be computed. In these prior two equations, the hat represents length relative to the wavelength of light (for example, $\hat{x} = x/\lambda$). The Rayleigh-Sommerfeld equation can be thought of as a mathematical expression of the Huygens wavelet principle, where the spherical waves emitted by the diffracting plane at $(x', y', 0)$ are integrated together to describe the resulting wave at the observation point (x, y, z) .

In 1976, Harvey and Shack [26] developed a theory based on scalar wave optics.

The term U_o is essentially treated as a phase screen that induces a phase shift due to the surface scatter rather than due to an optic. To define the phase induced by the surface, this theory defined a surface transfer function, and the Fourier transform of this surface transfer function resulted in a scattered radiance distribution known as the angle spread function (ASF) that is related to the BRDF. The ASF is analogous to the modulation transfer function in traditional linear systems scalar wave optics texts such as [24]. However, this original Harvey-Shack theory was derived using the paraxial approximation rather than the Rayleigh-Sommerfeld integral expression above, and did not conserve energy. These problems were fixed somewhat by development of a modified Harvey-Shack theory, but still was not accurate for all surfaces and angles.

In 2006, Krywonos [37] extended this theory to arbitrary incident and scattered angles via the GHS model. Then, the GHS model is compared to the Modified Beckmann-Kirchhoff (MBK) model, which is a modification to the original Beckmann-Kirchhoff (BK) optical scatter model that was proposed by Krywonos in [37, 38, 30]. This MBK model is equal to the GHS model for surfaces that obey Gaussian statistics, and for incident and scattered angles that are not large. It should be noted that GHS theory, unlike microfacet theory, treats both surface and volumetric scatter as adding a phase function to the electromagnetic field; GHS does not distinguish between surface scatter and volumetric scatter. This could potentially lead to problems in identification of materials such as paints, where the scatter contains both surface and volumetric elements. Prior to developing these theories in more depth, some common terms are presented here that appear in both GHS and MBK theory.

Angular Dependence.

In GHS and MBK theory, the BRDF is calculated in direction cosine space (α, β) instead of spherical space (θ, ϕ) . (γ is also included in direction cosine space, but is

related to α and β via the relationship $\gamma^2 = 1 - \alpha^2 - \beta^2$. Similarly, r is present in spherical coordinates, but the radial direction is normalized to a value of 1.) Direction cosine space is related to the wave vector \vec{k} but retains only the angular dependence of that vector; it is defined as

$$\begin{aligned}\Delta\alpha &= \alpha_s - \alpha_i = \lambda\nu_y = \sin\theta_s \sin(\phi_s - \pi) \\ \Delta\beta &= \beta_s - \beta_i = \lambda\nu_x = \sin\theta_s \cos(\phi_s - \pi) - \sin\theta_i,\end{aligned}\tag{98}$$

where, as before, the subscript s refers to scattered angles and the subscript i refers to incident angles. The extra π terms arise from a difference in defining the $\phi = 0$ location in the microfacet model as compared to the linear systems model. For in-plane forward scatter, $\phi_s = \pi$ in all models as presented in this dissertation (backscatter is $\phi_s = 0$); however, in-plane forward scatter data is represented by $\phi_s = 0$ in some linear systems papers [29, 38]. For isotropic samples, the angular dependence simplifies to

$$\eta_r^2 = (\Delta\alpha)^2 + (\Delta\beta)^2 = \sin^2\theta_i + \sin^2\theta_s + 2\sin\theta_i \sin\theta_s \cos\phi_s = \left(\frac{\lambda\nu_{xy}}{2\pi}\right)^2, \tag{99}$$

where ν_r is the notation used by Beckmann in the original formulation of Beckmann-Kirchhoff theory [2]. η_r represents the angular extent in direction cosine space. (For an isotropic surface, angular extent in α or β is treated similarly by computing the Euclidian distance.) $\nu_{xy} = k\eta_r$ simply scales direction cosine space by the magnitude of the wave vector, k . In the literature prior to this work, the connection between linear systems direction cosine space given above and the microfacet coordinate system defined by Equations (34) and (35) was not examined; this connection is developed in Chapter VI.

Polarization Factor.

Another significant difference between scalar wave optics theory and linear systems theory is the use of the polarization factor Q instead of the standard Fresnel equation F . Q is a perturbation of Fresnel reflectance, which was defined in Equation (22). In deriving the Fresnel equation, an infinitely smooth surface is assumed. The derivation of the polarization factor, Q , perturbs that solution for a rougher surface. It is significantly more complex than F , but still possesses a closed-form solution given most clearly by Stover in [62] by the following five equations:

$$Q_{ss} = \left| \frac{(\tilde{n}^2 - 1) \cos(\phi_s - \pi)}{(\cos \theta_i + \sqrt{\tilde{n}^2 - \sin^2 \theta_i})(\cos \theta_s + \sqrt{\tilde{n}^2 - \sin^2 \theta_s})} \right|^2 \quad (100)$$

$$Q_{sp} = \left| \frac{(\tilde{n}^2 - 1) \sqrt{\tilde{n}^2 - \sin^2 \theta_s} \sin(\phi_s - \pi)}{(\cos \theta_i + \sqrt{\tilde{n}^2 - \sin^2 \theta_i})(\tilde{n}^2 \cos \theta_s + \sqrt{\tilde{n}^2 - \sin^2 \theta_s})} \right|^2 \quad (101)$$

$$Q_{ps} = \left| \frac{(\tilde{n}^2 - 1) \sqrt{\tilde{n}^2 - \sin^2 \theta_i} \sin(\phi_s - \pi)}{(\tilde{n}^2 \cos \theta_i + \sqrt{\tilde{n}^2 - \sin^2 \theta_i})(\cos \theta_s + \sqrt{\tilde{n}^2 - \sin^2 \theta_s})} \right|^2 \quad (102)$$

$$Q_{pp} = \left| \frac{(\tilde{n}^2 - 1) \left(\sqrt{\tilde{n}^2 - \sin^2 \theta_i} \sqrt{\tilde{n}^2 - \sin^2 \theta_s} \cos(\phi_s - \pi) - \tilde{n}^2 \sin \theta_i \sin \theta_s \right)}{(\tilde{n}^2 \cos \theta_i + \sqrt{\tilde{n}^2 - \sin^2 \theta_i})(\tilde{n}^2 \cos \theta_s + \sqrt{\tilde{n}^2 - \sin^2 \theta_s})} \right|^2 \quad (103)$$

$$Q = Q_{ss} + Q_{sp} + Q_{ps} + Q_{pp} \quad (104)$$

The factors of π appearing here again are due to a difference in defining the $\phi = 0$ location. (In this work, $\phi = 0$ represents backscatter, as is consistent with the previous section defining microfacet models; however, in the derivation of Q , $\phi = 0$ represents forward scatter.) For s -polarized light incident on a surface, $Q_s = Q_{ss} + Q_{sp}$. For p -polarized light incident on a surface, $Q_p = Q_{ps} + Q_{pp}$. For unpolarized light incident on a surface, $Q = Q_s + Q_p$. If $\theta_i = \theta_s$ and $\phi_s = 180^\circ$, the equations reduce to the standard Fresnel equations for s and p polarization given in Equation (21). Additionally, for in-plane scattering, $Q_{sp} = Q_{ps} = 0$.

In [62], Stover provides a few cases in which the Q term may be simplified, but does not provide a general approximation for Q relative to F . Stover notes that the Q_{ss} term is directly related to the Fresnel s polarization term F_s . He also provides an approximate reduction for all terms that only applies for highly reflective materials. Prior to this work, it was not clear how this Q term related to the microfacet model, or to the Fresnel equation. In Chapter VI, a relationship is developed, providing another key element in being able to translate between microfacet and scalar wave optics models, and forming one of the key contributions of this dissertation.

Now that the basic terms common to the MBK and GHS models have been described, the basis for the original Beckmann-Kirchhoff optical scatter model is presented. After describing the derivation of the BK model, the GHS and MBK model relationships are discussed in further detail.

Original Beckmann-Kirchhoff BRDF Model.

BK theory was developed in 1963 [2], prior to standardized definition of the BRDF by Nicodemus in 1977 [48]. For this reason, its development is more clearly presented in [37]; highlights of that description are presented here.

BK theory makes use of the Helmholtz integral expression to estimate the electric field at a scattered point P . To make use of the Helmholtz integral, boundary conditions must be specified; the tangent plane approximation is used to estimate these boundary conditions as [2, 37]

$$\begin{aligned} E(S) &= (1 + R)E_{inc} \\ \left(\frac{\partial E}{\partial n}\right)_S &= (1 - R)E_{inc}(\vec{\mathbf{k}} \cdot \vec{\mathbf{n}}), \end{aligned} \tag{105}$$

where $\vec{\mathbf{n}}$ is the surface normal, R is the local reflection coefficient, $E(S)$ is the electric field at the surface point S , and E_{inc} is the incident electric field. Recall from the

basic electromagnetism theory developed at the beginning of this chapter that \vec{k} is the wave vector.

Beckmann then derives a scattering coefficient that relates the electric field scattered off a realistic surface (E_s) to the electric field scattered off a polished surface (E_o), given as [2, 37]

$$\rho_{bk} = E_s/E_o \quad (106)$$

From scatter off a polished surface, a geometric term F_{bk} is derived, given as [2, 37]

$$F_{bk}^2 = \left(\frac{1 + (\cos \theta_i \cos \theta_s + \sin \theta_i \sin \theta_s \cos \phi_s)}{\cos \theta_i (\cos \theta_i + \cos \theta_s)} \right)^2. \quad (107)$$

This term arises from calculation of the electric field for a perfectly reflecting surface, and assuming the Fraunhofer approximation. However, since BK theory predates the definition of the BRDF, its role in computing the BRDF was not well-established in the literature; this connection is developed in Chapter VI.

Beckmann then derived an expression for $\langle \rho_{bk} \rho_{bk}^* \rangle$, where $*$ represents complex conjugate and $\langle \cdot \rangle$ represents the mean value, given as [2, 37]

$$\langle \rho_{bk} \rho_{bk}^* \rangle = D\{\rho_{bk}\} + \langle \rho_{bk} \rangle \langle \rho_{bk}^* \rangle. \quad (108)$$

In this expression, $D\{\rho_{bk}\}$ represents the diffusely scattered portion of the BRDF.

Beckmann then performs a series of statistical calculations to estimate $D\{\rho_{bk}\}$ for a realistic surface by assuming the surface statistics are governed by a Gaussian distribution function and computing $\langle \rho_{bk} \rho_{bk}^* \rangle - \langle \rho_{bk} \rangle \langle \rho_{bk}^* \rangle$; the result is [2, 37]

$$D\{\rho_{bk}\} = \frac{\pi l_c^2 F_{bk}^2 \exp(-g)}{A} \sum_{m=1}^{\infty} \frac{g^m}{m!m} \exp\left(-\frac{\nu_{xy}^2 l_c^2}{4m}\right), \quad (109)$$

where l_c is the correlation length, and g is given as

$$g(\theta_i, \theta_s) = \left(\frac{2\pi\sigma_s}{\lambda} \right)^2 (\cos \theta_i + \cos \theta_s)^2. \quad (110)$$

σ_s represents the standard deviation of the surface height.

This expression is not useful when g is sufficiently large, as the series sum would not converge rapidly. In that case, the surface is very rough ($g \propto \sigma_s/\lambda$). Consider Equation (108). For a very rough surface, an assumption is made that the specular beam intensity is negligible, and thus $\langle \rho_{bk} \rangle \approx 0$. From this result, Beckmann showed $D\{\rho_{bk}\}$ is given as [2, 37]

$$D\{\rho_{bk}\} \approx \langle \rho_{bk} \rho_{bk}^* \rangle = \frac{2\pi F_{bk}^2}{A} \int_0^\infty J_0(\nu_{xy}\tau) \exp \left[-g \left(1 - \exp \left(\frac{\tau^2}{l_c^2} \right) \right) \right] \tau d\tau, \quad (111)$$

where it is assumed that the surface height function $h(x, y)$ is stationary, so that the probability density depends only on the Euclidian distance τ between two points on the surface. The exponential term arises from the characteristic function of the Gaussian surface statistics, and J_0 represents the Bessel J function of order 0. Since $g \gg 1$, this integral can be evaluated because it is only nonzero for $\tau \approx 0$, which enables a Taylor series expansion of $\exp(\tau^2/l_c^2)$ function. Keeping only the first two terms of the Taylor series expansion, the integral is then evaluated, resulting in [2, 37]

$$D\{\rho_{bk}\} = \frac{\pi F_{bk}^2 l_c^2}{Ag} \exp \left[-\frac{\nu_{xy}^2 l_c^2}{4g} \right] \quad (112)$$

Unfortunately, the relationship between $D\{\rho_{bk}\}$ in the BK model and the BRDF was not well established, since this Beckmann scattering theory predates the formal definition of the BRDF, and it is clear that F_{bk}^2 does not obey Helmholtz reciprocity. Krywonos resolved the first issue by modifying the BK theory, as is discussed next. The second issue, relating to F_{bk}^2 not obeying Helmholtz reciprocity and not having a

clearly defined purpose in the context of BRDF theory, is addressed in Chapter VI.

Modified Beckmann-Kirchhoff BRDF Model.

The BK scattering model described in the last section was formulated in 1963 [2], prior to the formal definition of the BRDF by Nicodemus in 1977 [48], and should not be confused as a BRDF model for this reason. This BK model was modified when the linear systems diffraction BRDF theory was generalized to all incident and scattered angles, as well as for a variety of surfaces, by Krywonos [38, 29, 30].

The MBK formulation presented in Equation (113) is the angle spread function (ASF) f_a , which is related to the radiance L ; the ASF is equal to the BRDF if $F = 1$ (total Fresnel reflectance). Assuming the surface statistics follow a Gaussian autocovariance, and taking into account the $1/\lambda^2$ term present in MBK as shown in [37], the ASF is calculated as

$$f_a = \frac{\pi K l_c^2}{\lambda^2} \exp(-g) \sum_{m=1}^{\infty} \frac{g^m}{m!m} \exp\left(-\frac{\nu_{xy}^2 l_c^2}{4m}\right), \quad (113)$$

where K is a renormalization term that ensures conservation of energy, l_c is the correlation length of the surface, and g is given by Equation (110). Similar to BK theory, these modifications can additionally be applied to the very rough surface ($g \gg 1$) case. This expression is given in Chapter VI, where the MBK analysis is most relevant in this dissertation.

When written in terms of scattered radiance L_s , K is defined as [30, 37, 38]

$$K(\beta_i) = \frac{\int_{-\infty}^{\infty} \int_{-\infty}^{\infty} L_s(\alpha_s, \beta_s - \beta_i) d\beta_s d\alpha_s}{\int_{-1}^1 \int_{-\sqrt{1-\alpha_s^2}}^{\sqrt{1-\alpha_s^2}} L_s(\alpha_s, \beta_s - \beta_i) d\beta_s d\alpha_s}. \quad (114)$$

$L_s \geq 0$ everywhere, so $K \geq 1$ for all incident angles. Physically, K is a unitless quantity that ensures energy is not lost to evanescent waves by redistributing energy

that may fall outside the unit circle of real space defined by the direction cosines. For some BRDF applications, this term can be problematic to compute because it depends on knowing the surface distribution shape, and involves computation of a double integral expression that does not possess an analytic solution for most surface distributions.

As can be seen from this definition of the MBK model, it is not clear how to relate this to the microfacet model. One of the contributions of this dissertation toward development of a basis for a wavelength-dependent, closed-form BRDF model is providing a mechanism to translate between this scalar wave optics BRDF model and the microfacet BRDF model. This contribution is detailed in Chapter VI.

IV. Measurement Process

In this chapter, BRDF measurement theory and equipment are discussed. The procedure to measure BRDF data in this dissertation is then be described in detail. Finally, an uncertainty analysis is performed.

4.1 Measuring Polarimetric BRDF

Unlike measuring HDR or using ellipsometry to estimate the complex index of refraction, for some materials there is too little signal outside the specular lobe to measure BRDF by simply illuminating over multiple wavelengths and sending the results to a spectrometer. Instead, a narrow band of radiation is desirable to measure a larger dynamic range of the BRDF. As discussed in Chapter III, BRDF values may vary by several orders of magnitude, in the range $[0, \infty)$. Consider, for example, a specular BRDF sample. Such a measurement could be easily performed at the specular peak, but to obtain the shape of the specular lobe and to obtain enough signal in the wings of the BRDF is a difficult task not encountered when measuring HDR or \tilde{n} . Thus, measuring BRDF requires a more careful measurement. For accurate BRDF measurements in the IR, laser illumination is typically used because it is highly directional illumination over a very narrow spectral band.

To measure BRDF, AFIT has a modified Complete Angle Scatter Instrument (CASI®) from Schmitt Measurement Systems (SMS), a division of Schmitt Industries, Inc. To manage the difficulties of measuring BRDF outlined above, this system uses a chopper and lock-in amplifier. This process reduces the effects of self-emission on the measured signal, as the incident laser beam is chopped at a known frequency while the self-emissive component from the sample is not. Furthermore, the signal is amplified at multiple possible gain levels (depending on wavelength and detector),

allowing for measurement of a signal over several orders of magnitude. Additionally, a filter wheel with a known neutral density value (determined from experimental measurement at each wavelength in which it was used) controls the incident irradiance on the sample.

The basic CASI® system uses a sample holder mounted at the center of a goniometer. The sample may then be illuminated by laser light at a certain wavelength and incident angle, while the goniometer arm scans the detector to obtain in-plane data ($\phi_s = 0^\circ$ or $\phi_s = 180^\circ$). Out-of-plane data ($\phi_s \neq 0$ and $\phi_s \neq 180^\circ$) may also be collected by tipping the sample, although this work was focused only on collecting in-plane BRDF data.

AFIT modified this system to be a Dual Rotating Retarder (DRR) polarimetric CASI® system, as shown in Figure 26. In the DRR configuration, the CASI® system supports a generating polarizer prior to illuminating the source, and an analyzing polarizer at the detector (after illuminating the source). Similarly, a generating waveplate and analyzing waveplate may be placed prior to the sample and prior to the detector. This allows for the full Mueller matrix to be obtained.[23] By rotating the analyzing retarder at 5x the frequency of the generating retarder, and rotating the generating retarder through 180° rotation, a Fourier decomposition can be used to obtain the entire 4x4 Mueller matrix, including circular polarization[23]. Vap showed through condition number analysis and experiment that, for imperfect equipment found in the DRR CASI® system, it is ideal to use an angular rotation of 37.5° for the analyzing retarder and 7.5° for the generating retarder if more than 18 measurements are used. (The W-matrix method, an alternate way to compute the fully polarimetric BRDF, may also be used, as will be described in detail later; Vap showed that for the W-matrix method, if fewer than 18 measurements are used, an analyzing retarder rotation of 34° and a generating retarder rotation of 26° is the best rota-

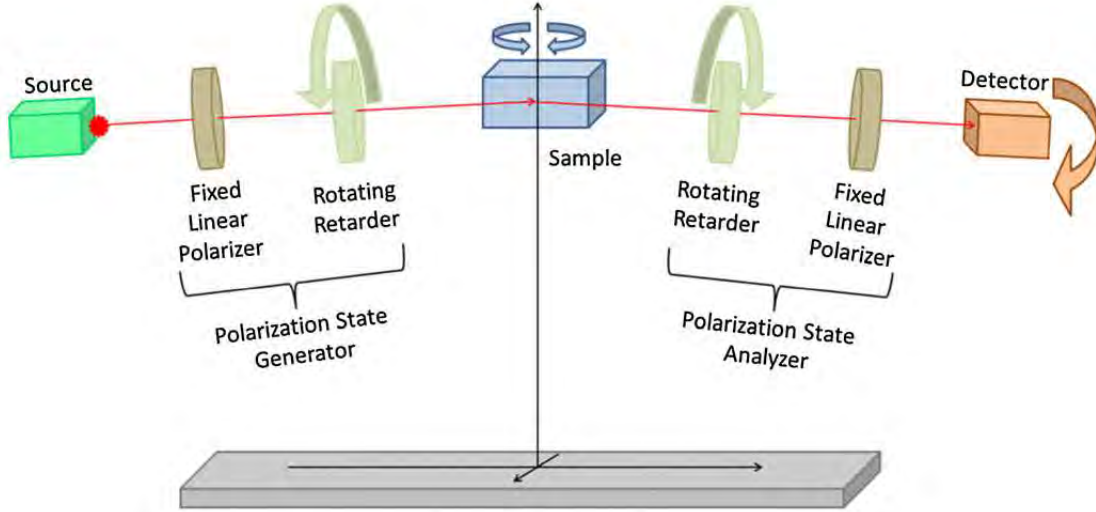


Figure 26. Diagram of AFIT modified CASI layout, taken from a paper by Vap[69]

tion ratio to apply.) Although in theory 16 measurements are required to determine the full Mueller matrix, in general it is preferable to over-determine the system and perform a least squares analysis to reduce experimental uncertainty; thus, in general the ideal ratio to use is 37.5° for the analyzing retarder and 7.5° for the generating retarder[69].

The AFIT CASI® comes with a HeNe laser at $3.39 \mu m$ and a CO₂ laser at $10.6 \mu m$; it has further been modified to use Quantum Cascade Lasers (QCLs), providing tunable output within the MWIR and LWIR, from 4.3 to $9.7 \mu m$. For details, see [68]; a figure illustrating wavelength range is reproduced in Figure 27. The QCLs are tunable to within 0.2% of the desired wavelength value[67]. In this dissertation, obtaining BRDF data with the QCL that is in the $8.06 - 9.71 \mu m$ band was found to be too difficult, primarily due to challenges in laser alignment to prepare for the BRDF measurement. (Note that the QCL in that wavelength band is pulsed, with a weak average power output, which is why laser alignment was found to be difficult. All other QCLs were used in continuous wavelength mode.)

When switching laser wavelengths (even for the same QCL), laser realignment and

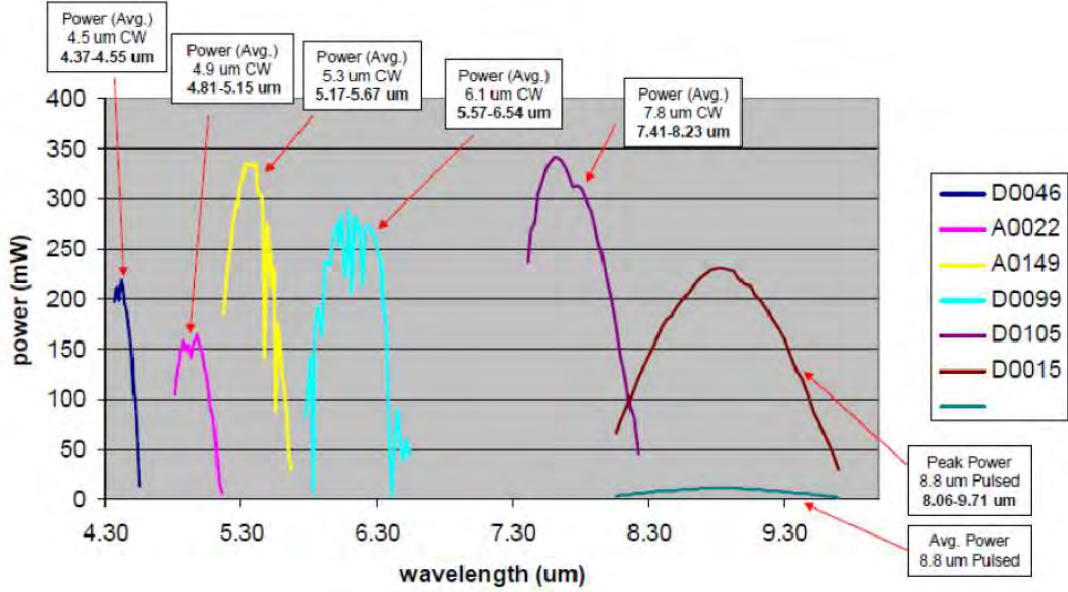


Figure 27. QCL wavelengths available for use in the AFIT CASI®.

calibration is performed. After aligning the laser with the detector, a trial run with no sample is conducted to ensure the identity Mueller matrix is obtained. This result quantifies the error in each element of the measurement and validates measurement.

Typical usage of this system for the full 4x4 Mueller matrix has shown that 50 scans of the entire in-plane data are typically desired to obtain the full Mueller matrix[69]. These additional scans beyond the minimum required are necessary to compensate for alignment errors and imperfections in the polarizers and wave plates, using a Fourier analysis with error compensation as described by Goldstein[23], to be discussed in more depth below. Additionally, this process was repeated at least three times per incident angle to average out noise in the data. Finally, multiple incident angles were collected to account for variation in $\hat{\omega}_i$.

For the MWIR, a Teledyne-Judson InSb detector is used; for the LWIR, a Teledyne-Judson HgCdTe (MCT) detector is used. Both detectors were cooled to 77 K using liquid nitrogen. Polarizers and waveplates are also chosen based upon wavelength of the laser source. For lasers in the LWIR that would otherwise saturate the detector,

a filter wheel was used to ensure the signal stayed in the linear regime of the detector. A variable aperture with four different diameters (300 μm , 1.100 mm, 4.075 mm, and 13.85 mm) is located 0.5 m from the sample. These aperture sizes correspond to angular step sizes of 0.011° , 0.042° , 0.156° , and 0.529° , respectively. The optic behind the variable aperture is used to focus light onto the detector. The CASI® system selects the aperture based on how close it is to the specular lobe. The focusing optic at the detector is positioned 50 ± 0.5 cm away from the sample.

A typical measurement of a single material may take several days for the full 4x4 Mueller matrix, not including calibration or realignment. More specular materials tend to take longer, as they tend to have lower BRDF values at off-specular positions, which comprise most of the measurement space.

DRR Data Analysis.

To obtain the Mueller matrix from the DRR polarimetric setup described above, two primary approaches are used: Fourier analysis and W matrix method. These methods are detailed in [23]. Each method will be discussed in turn.

W Matrix Method.

In the W matrix method, the Mueller matrix is restructured as a 16-element vector of unknowns. As long as waveplate and polarizer orientations are chosen such that each measurement is linearly independent, it is possible to measure the full Mueller matrix with at least 16 data points. (A 5:1 ratio between the generating and analyzing waveplate rotations is not required, as will be the case for the equations derived by Goldstein relating the Fourier method to the Mueller matrix, to be discussed later.) Generally, more than 16 data points are collected and a least squares pseudoinverse is used to obtain the Mueller matrix using well-established linear algebra techniques[23].

For the W matrix method, it is necessary to account for imperfections in the equipment and alignment process. The Mueller matrix for an imperfect linear horizontal polarizer with transmission τ and diattenuation D is

$$\overset{\leftrightarrow}{\mathbf{P}} = \frac{\tau}{2} \begin{bmatrix} 1 & D & 0 & 0 \\ D & 1 & 0 & 0 \\ 0 & 0 & \sqrt{1-D^2} & 0 \\ 0 & 0 & 0 & \sqrt{1-D^2} \end{bmatrix} \quad (115)$$

The Mueller matrix of a waveplate oriented horizontally with retardance δ in addition to transmissivity τ and diattenuation D is

$$\overset{\leftrightarrow}{\mathbf{V}} = \tau \begin{bmatrix} 1 & D & 0 & 0 \\ D & 1 & 0 & 0 \\ 0 & 0 & \sqrt{1-D^2} \cos \delta & \sqrt{1-D^2} \sin \delta \\ 0 & 0 & -\sqrt{1-D^2} \sin \delta & \sqrt{1-D^2} \cos \delta \end{bmatrix} \quad (116)$$

These Mueller matrices assume horizontal alignment, but they can be rotated to any arbitrary alignment. Additionally, a rotation matrix could be used to represent misalignment errors. The Mueller matrix of a rotation about the optic axis is

$$\overset{\leftrightarrow}{\mathbf{R}}(\theta) = \begin{bmatrix} 1 & 0 & 0 & 0 \\ 0 & \cos 2\theta & \sin 2\theta & 0 \\ 0 & -\sin 2\theta & \cos 2\theta & 0 \\ 0 & 0 & 0 & 1 \end{bmatrix} \quad (117)$$

To account for misalignment of a polarizer by an angle α , the proper equation is as follows:

$$\overset{\leftrightarrow}{\mathbf{P}}_e(\alpha) = \overset{\leftrightarrow}{\mathbf{R}}(-\alpha) \overset{\leftrightarrow}{\mathbf{P}} \overset{\leftrightarrow}{\mathbf{R}}(\alpha) \quad (118)$$

Misalignment of a waveplate is handled analogously.

The ideal experimental setup of the DRR system is mathematically expressed as follows:

$$\begin{aligned}\vec{s}_m &= \overset{\leftrightarrow}{\mathbf{P}}_a \overset{\leftrightarrow}{\mathbf{V}}_a(\theta_a) \overset{\leftrightarrow}{\mathbf{M}} \overset{\leftrightarrow}{\mathbf{V}}_g(\theta_g) \overset{\leftrightarrow}{\mathbf{P}}_g \vec{s}_i \\ &= \overset{\leftrightarrow}{\mathbf{A}} \overset{\leftrightarrow}{\mathbf{M}} \vec{s}\end{aligned}\tag{119}$$

For measurement at the detector, only the s_0 component of the Stokes vector \vec{s}_m is measured. The subscript a refers to the analyzer (after the sample) and the subscript g refers to the generator (before the sample); the Mueller matrix $\overset{\leftrightarrow}{\mathbf{M}}$ is the matrix of the sample (the unknowns). The angles θ_a and θ_g indicate rotations of the analyzing waveplate and generating waveplate, respectively.

Let $\vec{\mathbf{m}}$ represent the unknown Mueller matrix $\overset{\leftrightarrow}{\mathbf{M}}$, but as a vector in column major order. Since only the first row of the analyzer matrix $\overset{\leftrightarrow}{\mathbf{A}} = \overset{\leftrightarrow}{\mathbf{P}}_a \overset{\leftrightarrow}{\mathbf{V}}_a$ can possibly be measured, Goldstein shows it is possible to construct a detected w_i vector for the i th measurement from $\overset{\leftrightarrow}{\mathbf{A}}$ and generated vector incident on the sample \vec{s} as [23]

$$\vec{w}_i = [a_{11}s_1, a_{11}s_2, a_{11}s_3, a_{11}s_4, a_{21}s_1, \dots, a_{44}s_4]^T\tag{120}$$

Then, $s_{m,i} = \vec{w}_i \cdot \vec{\mathbf{m}}$. Since there are 16 unknowns, this measurement must be completed at least 16 times; if more than 16 linearly independent measurements are made, the pseudoinverse is used to perform least squares regression.

Fourier Analysis Method.

The other method commonly used to calculate the Mueller matrix in a DRR system is the Fourier method. Using a generating waveplate rotation of θ and an analyzing waveplate rotation of 5θ , a vector of measurements s_m is obtained. (The 5:1 ratio is not strictly required to use the Fourier method, but the equations developed by

Goldstein that are presented here relating the measurements to the Fourier coefficients do require a 5:1 ratio.) Goldstein shows that, assuming ideal components, the Mueller matrix can be formed from Fourier coefficients of the series. He defines the Fourier series somewhat differently from standard conventional definitions, as follows:[23]

$$\frac{I}{I_0} = \frac{a_0}{4} + \frac{1}{4} \sum_{k=1}^{\infty} a_{2k} \cos(2k\theta) + b_{2k} \sin(2k\theta) \quad (121)$$

where I is the measured intensity and I_0 is the incident intensity. BRDF may be used in place of intensity because the two are directly related. Recall that BRDF is defined as exiting radiance divided by incident irradiance. Radiance is defined as power per area, per solid angle; integrating the radiance over the area results in the intensity. Since the area scattered by the sample does not change for a fixed incident angle, the BRDF may be used in place of the intensity.

The expression given in Equation (121) is in contrast to a more traditional Fourier series expansion a'_k and b'_k , given as

$$\frac{I}{I_0} = \frac{a'_0}{2} + \sum_{k'=1}^{\infty} a'_{k'} \cos(k'\theta) + b'_{k'} \sin(k'\theta) \quad (122)$$

By comparing Equations (121) and (122), one can obtain the relationship between Goldstein's Fourier decomposition and a traditional Fourier decomposition:

$$\begin{aligned} 2a_0 &= a'_0 \\ 4a_k &= a'_{2k'}, k > 0 \\ 4b_k &= b'_{2k'} \end{aligned} \quad (123)$$

This comparison allows one to use traditional Fourier techniques (such as the Fast Fourier Transform) to extract the Fourier coefficients, then translate those Fourier coefficients to Goldstein's notation. The Mueller matrix entries are then given by the

following equation, where Goldstein's notation for the coefficients is being used:[23]

$$\begin{aligned}
m_{00} &= a_0 - a_2 + a_8 - a_{10} + a_{12} \\
m_{01} &= 2a_2 - 2a_8 - 2a_{12} \\
m_{02} &= 2b_2 + 2b_8 - 2b_{12} \\
m_{03} &= b_1 - 2b_{11} \\
m_{10} &= -2a_8 + 2a_{10} - 2a_{12} \\
m_{11} &= 4a_8 + 4a_{12} \\
m_{12} &= -4b_8 + 4b_{12} \\
m_{13} &= -2b_9 + 2b_{11} \\
m_{20} &= -2b_8 + 2b_{10} - 2b_{12} \\
m_{21} &= 4b_8 + 4b_{12} \\
m_{22} &= 4a_8 - 4a_{12} \\
m_{23} &= 2a_9 - 2a_{11} \\
m_{30} &= b_3 - b_5 + b_7 \\
m_{31} &= -2b_3 - 2b_7 \\
m_{32} &= -2a_3 + 2a_7 \\
m_{33} &= a_6 - a_4
\end{aligned} \tag{124}$$

In reality, experimental defects such as misalignment, diattenuation, and birefringence in the waveplate alter its properties. That said, one benefit of the Fourier method is that a mechanism is provided to approximate all of these values from measurement with no sample present. The equations become significantly more complex, spanning several pages and are not reproduced here; see [23], pages 364-367, for the equations. From these equations, misalignment errors for the two waveplates and the analyzing polarizers are calculated relative to the generating polarizer. Additionally,

waveplate retardances for both waveplates are estimated. The Mueller matrix entries are then calculated with these correction terms. When including the correction terms, the Fourier decomposition is required up to the 24th term (a_{12} and b_{12} in Goldstein's notation); for this reason, discrete Fourier transform theory indicates at least 50 measurements are required to avoid Nyquist aliasing[49]. While this may seem more cumbersome than the W matrix method, recall that this method gives not only the Mueller matrix, but also the estimated errors in alignment, without rearranging the generator and analyzer components. For this reason, the Fourier decomposition is preferable to the W matrix for this application.

DRR Measurement Results.

Although most of the measurement results will be presented in the next chapter, the DRR results motivate the procedure chosen for this BRDF study, so DRR results are discussed here. The DRR method was used initially on a few samples to determine the fully polarimetric characteristics of some of the surface reflecting samples.

First, the DRR was measured at $\lambda = 4.4 \mu m$ with no sample, obtaining

$$M_{ident} = \begin{bmatrix} 1.0000 & -0.0080 & 0.0020 & -0.0066 \\ -0.0002 & 0.9940 & -0.0062 & -0.0051 \\ -0.0018 & 0.0167 & 0.9971 & 0.0582 \\ 0.0023 & -0.0123 & 0.0386 & 0.9781 \end{bmatrix}. \quad (125)$$

The identity matrix is the expected result, as there was no sample. The difference from the identity matrix gives an error estimate for each of the components in the pBRDF measurements presented in this section.

Then, the grit-blasted Ni sample, shot-blasted Ni sample, polished Ni sample, and polished Al sample at $\theta_i = 40^\circ$ and $\theta_s = 40^\circ$ were measured; resulting Mueller

matrices are

$$M_{Ni,grit} = \begin{bmatrix} 1.0000 & -0.0040 & -0.0464 & -0.0064 \\ -0.0229 & 0.9786 & -0.0042 & -0.0165 \\ -0.0215 & -0.0046 & 0.9840 & -0.0143 \\ -0.0019 & -0.0047 & 0.1012 & 0.9563 \end{bmatrix}, \quad (126)$$

$$M_{Ni,shot} = \begin{bmatrix} 1.0000 & -0.0226 & -0.0409 & 0.0314 \\ -0.0250 & 0.9106 & 0.0234 & -0.0422 \\ -0.0092 & 0.0120 & 0.8892 & 0.0025 \\ -0.0206 & -0.0623 & 0.0783 & 0.7939 \end{bmatrix}, \quad (127)$$

$$M_{Ni,pol} = \begin{bmatrix} 1.0000 & 0.0415 & -0.0490 & -0.0101 \\ -0.0011 & 0.9958 & -0.0077 & -0.0164 \\ -0.0160 & -0.0125 & 1.0017 & 0.0111 \\ 0.0052 & -0.0210 & 0.0876 & 0.9763 \end{bmatrix}, \quad (128)$$

$$M_{Al,pol} = \begin{bmatrix} 1.0000 & 0.0584 & -0.0345 & -0.0202 \\ 0.0140 & 0.9933 & -0.0134 & -0.0186 \\ -0.0305 & -0.0208 & 0.9940 & 0.0338 \\ 0.0143 & -0.0329 & 0.0621 & 0.9773 \end{bmatrix}. \quad (129)$$

These measurements show that the Mueller matrices are block diagonal for $\theta_i = 40^\circ$ and $\theta_s = 40^\circ$, which is where the BRDF reaches its highest measured value for all of these samples since none of them are extremely diffuse; only one entry that is not block diagonal is in excess of 5%, and only for one entry in the shot-blasted Ni material, which could be due to measurement error. The theory behind the pBRDF data for in-plane BRDF measurements in [33] only shows the BRDF is block diagonal, so a block diagonal form will be assumed instead of a diagonal form.

To determine whether this changes when moving off specular, the Mueller matrix for the grit-blasted Ni sample was measured at $\theta_i = 40^\circ$ and $\theta_s = 40^\circ \pm 5^\circ$; see Figure 28. As can be seen from that plot, the resulting Mueller matrix values do not change significantly with scattering angle for this sample.

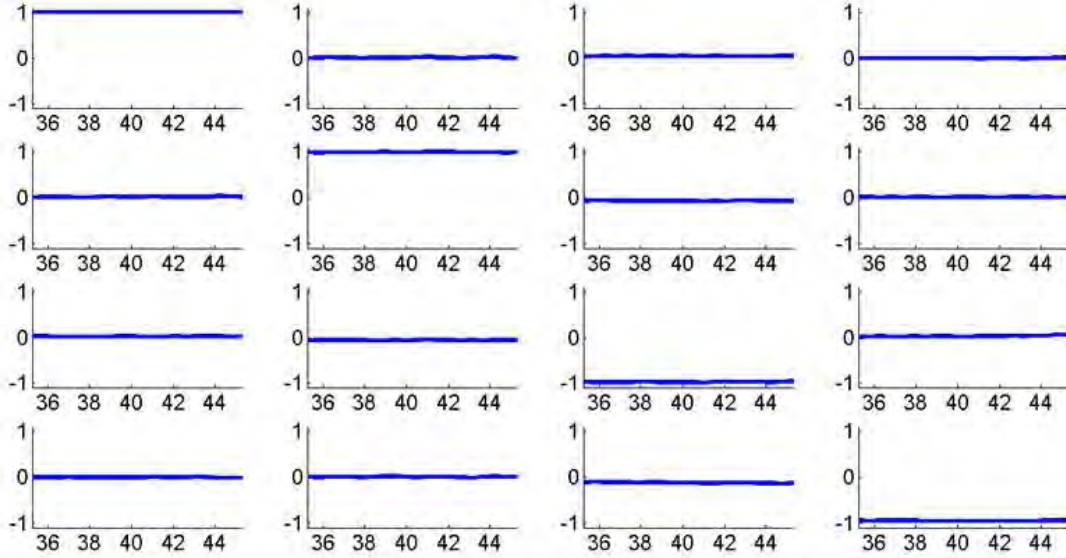


Figure 28. Mueller matrix results for grit-blasted Ni at $\lambda = 4.4 \mu\text{m}$, $\theta_i = 40^\circ$, and $\theta_s = 40^\circ \pm 5^\circ$.

As noted previously, pBRDF theory in [33] asserts a block diagonal form in the general case, which appears to be backed by these pBRDF measurements. Thus, a block diagonal form is assumed in this dissertation.

4.2 Measuring Unpolarized BRDF

From the results obtained by measuring the Mueller matrix using DRR, the cross polarization terms were determined to be negligible; that is, the Mueller matrices $\overset{\leftrightarrow}{\mathbf{M}}_s$ for the samples were determined to be of the form

$$\overset{\leftrightarrow}{\mathbf{M}}_s = \begin{bmatrix} m_{00} & m_{01} & 0 & 0 \\ m_{10} & m_{11} & 0 & 0 \\ 0 & 0 & m_{22} & m_{23} \\ 0 & 0 & m_{32} & m_{33} \end{bmatrix}. \quad (130)$$

Since the DRR results above show the Mueller matrix is block diagonal for these samples and in-plane BRDF measurements, it is possible to greatly reduce the measurement space required to obtain an unpolarized BRDF, as well as simplifying the setup process at each wavelength.

To take advantage of this knowledge and to greatly reduce the measurement time required to compute the unpolarized BRDF, only a generating waveplate and generating polarizer are used. The generating polarizer is placed after the generating waveplate. The generating polarizer is set to horizontal (p , or $+$) and vertical (s , or $-$) polarization states only. The generating waveplate before the polarizer serves the function of rotating the Stokes vector leaving the waveplate, $\vec{\mathbf{s}}_{wp}$, to be in the state

$$\vec{\mathbf{s}}_{wp} = \begin{bmatrix} 1 \\ 0 \\ s_2 \\ s_3 \end{bmatrix}, \quad (131)$$

where s_2 and s_3 are of relative unimportance, as these terms will be extinguished by the polarizer prior to reaching the sample. The generating waveplate thus serves the function of rotating the polarization state of the laser such that there is equal power in the s and p polarization states, as is represented by the 0 entry in the second element of the Stokes vector.

The p or s polarization is selected by varying the polarizer in the horizontal or vertical position, respectively. If BRDF data is taken for both p ($+$) and s ($-$)

polarizations incident on the sample, then the incident Stokes vector \vec{s}_{\pm} is

$$\vec{s}_{\pm} = \frac{1}{2} \begin{bmatrix} 1 \\ \pm 1 \\ 0 \\ 0 \end{bmatrix}. \quad (132)$$

That is, the incident Stokes vector is in either p or s polarization, with equal power incident on the sample independent of polarization. The factor of $1/2$ comes from the $1/2$ in front of the Mueller matrix for a polarizer in Equation (17), but is the same regardless of whether s or p polarization is incident.

Upon reflection of this Stokes vector off the sample Mueller matrix, the Stokes vector $\vec{s}_{\pm,det}$ at the detector is given by

$$\vec{s}_{\pm,det} = \overset{\leftrightarrow}{\mathbf{M}}_s \vec{s}_{\pm} = \frac{1}{2} \begin{bmatrix} m_{00} \pm m_{10} \\ x \\ y \\ z \end{bmatrix}, \quad (133)$$

where x , y , and z values are unimportant because a detector only measures s_0 , as was discussed in detail when Stokes vectors were introduced in Chapter III.

By measuring the BRDF once for p polarization (obtaining a BRDF f_p) and repeating again for s polarization (obtaining a BRDF f_s), at each angle the following linear system is obtained:

$$\frac{1}{2} \begin{bmatrix} 1 & 1 \\ 1 & -1 \end{bmatrix} \begin{bmatrix} m_{00} \\ m_{10} \end{bmatrix} = \begin{bmatrix} f_p \\ f_s \end{bmatrix}. \quad (134)$$

This matrix is easily solved for the unpolarized BRDF f_r given by the m_{00} component by the simple relationship

$$f_r = f_p + f_s \quad (135)$$

The error in this incident Stokes vector is on the order of the extinction ratio of the polarizer, which varies with wavelength but is less than 1% at all wavelengths and thus is not a dominant source of error, as will be seen in the analysis later in this chapter.

To be able to properly account for temporal variations and ensure repeatability of the measurement, each polarization state (s and p) was measured three times for each incident and scattered angle; this result was averaged prior to summing the s and p BRDFs to obtain the unpolarized BRDF.

4.3 Uncertainty Analysis

In this section, an uncertainty analysis for BRDF measured with the CASI® system using the revised measurement process described above is presented. Following the error analysis for BRDF calculations as detailed by Cady in [11], as well as in Stover's popular text in [62], the error in this BRDF measurement method is calculated.

As Stover states, the primary sources of error for BRDF measurement are aperture misalignment, aperture size uncertainty, detector nonlinearity, and (at grazing angles in particular) scattering error. His Equation 7.30 (based on a simplification of Cady's analysis) is given as

$$\left(\frac{\Delta BRDF}{BRDF}\right)^2 = \left(\frac{m}{\theta}\right)^2 \left(\cos^{-1} \left(\frac{R \cos \theta}{\sqrt{\Delta y^2 + R^2}} \right) - \theta \right)^2 + 2(NL)^2 + \left(\frac{2\Delta r}{r}\right)^2 + \left(\frac{\Delta \theta_s \sin \theta_s}{\cos \theta_s}\right)^2 \quad (136)$$

where the first term is aperture misalignment error; m is the slope of the BRDF on a

log plot, $\theta = \theta_s - \theta_i$ is the angular distance away from specular, R is the distance from the sample to the aperture, and Δy is the aperture misalignment in the out-of-plane direction. The second term represents detector nonlinearity, NL . The third term represents uncertainty in the aperture size; Δr is the uncertainty in the radius of the aperture, and r is the radius of the aperture. The last term represents uncertainty in the scattered angle $\Delta\theta_s$.

Additionally, this method combines horizontal (H) and vertical (V) polarization states to approximate the unpolarized BRDF. Since the dominant error terms are independent of incident polarization, this increases the uncertainty in our measurements by $\sqrt{2}$; that is, $\sqrt{(\Delta BRDF_H)^2 + (\Delta BRDF_V)^2} \approx \sqrt{2}(\Delta BRDF)$, with $\Delta BRDF$ given per Equation (136).

Recall that Teledyne-Judson InSb and HgCdTe detectors, liquid nitrogen-cooled to 77 K , were used. Care must be taken to ensure the detector response remains linear. To do so, the incident beam was attenuated until a linear response was obtained. Total signal was measured with the largest aperture, attenuated using neutral density filters, and repeated until the drop in total power was linear when adding another neutral density filter.

For the CASI® system error analysis, the following parameters were used:

- $m = 2$, as this is a typical value for the slope of the BRDF on a log plot for the data collected. Stover states this is typically a value between 1 and 3 for most BRDF measurements.
- $R = 50 \pm 0.5\text{ cm}$, as the measured distance from the sample holder to the aperture. (SMS nominally states $R = 50\text{ cm}$ for CASI®, which was measured and verified.)
- $\Delta y = 30\text{ }\mu\text{m}$. The smallest step size for moving the aperture in the y direction

is $2.5 \mu m$, but when running the aperture centering routine, the CASI® moves the smallest aperture in the y direction by $30 \mu m$ at a time and interpolates to predict where the beam center is located. To be conservative in this error estimate, the beam centering routine's step size, not the minimum step size, was used for this value.

- $NL = 0.02$, as an upper bound on the detector nonlinearity error. As stated before, steps were taken to ensure the measurement was within the linear regime of the detector.
- $\Delta r/r = 0.03$ for the smallest aperture ($300 \mu m$ diameter). Although not measured, conversations with the CASI® manufacturer indicated the diameter may be off in the least significant ($1 \mu m$) digit. This aperture is used for measurement of specular samples within $\pm 0.38^\circ$ of the specular direction. For distances further than 0.38° from specular, $\Delta r/r = 0.02$ is used since larger diameter apertures (1.100 mm, 4.075 mm, and 13.85 mm) have a smaller *relative* uncertainty in aperture size.
- $\Delta\theta_s = 0.5^\circ$, as was measured using a protractor with markings every 1° . $\Delta\theta_s$ represents the uncertainty in the absolute position of the aperture arm. This uncertainty arises from the $\cos\theta_s$ term in the BRDF. Stover states this error term is most important for grazing angles (e.g., $\theta_s \geq 80^\circ$). In this dissertation, BRDF data are measured at a maximum angle of $\theta_s = 65^\circ$, so the error due to this term was far less significant. This absolute position uncertainty quantifies the uncertainty in the sample rotation stage (since θ_s is measured relative to the surface normal) and in the overall receiver arm offset. This term is not to be confused with $\Delta r/r$ and Δy , which quantify uncertainty in *relative* positioning of the aperture arm compared to the specular direction. CASI® is able to scan

at very fine resolution in relative position, as quantified by the numbers above.

Stover's analysis (and Cady's more thorough analysis) diverges at $\theta = 0$, but close to specular, the errors at various points are summarized in Table 4.1. Recall $\theta = \theta_s - \theta_i$. In Table 4.1, $\theta = 0.011^\circ$ represents one data point off specular with the smallest step size used for any of the measurements in this dissertation. The next five entries represent the error at other points close to specular reflection. The final row is the error at $\theta_s = 65^\circ$, the steepest angle measured in this dissertation.

Table 4.1. Relative error in reported unpolarized BRDF measurements using the AFIT CASI® system

$\theta = \theta_s - \theta_i$	$\theta_i = 20^\circ$	$\theta_i = 30^\circ$	$\theta_i = 40^\circ$	$\theta_i = 50^\circ$
0.011°	0.1668	0.1669	0.1671	0.1764
0.022°	0.1039	0.1041	0.1043	0.1049
0.05°	0.0981	0.0982	0.0985	0.0991
0.1°	0.0981	0.0982	0.0985	0.0991
0.5°	0.0750	0.0752	0.0756	0.0764
1°	0.0750	0.0752	0.0756	0.0764
$\theta_s = 65^\circ$	0.0794	0.0794	0.0794	0.0794

The final step in calculating the uncertainty in the data is to add in temporal uncertainty. This temporal uncertainty is calculated from the standard deviation of the three measurements made at each incident angle and incident polarization, and varies from one measurement to the next. Typically, the relative uncertainty due to this temporal variation is largest near the noise floor, which varies with wavelength and laser power, but was generally around 10^{-4} sr^{-1} . To obtain the final uncertainty, the temporal uncertainty is added to the measurement uncertainty in quadrature.

To illustrate the uncertainty for a typical BRDF measurement, consider Figure 29. This figure is an enlarged version of Figure 68(c), to be discussed in more detail in Chapter V. Here, that figure is enlarged to show more clearly that the data is significantly different. In many of the figures of raw BRDF data that are presented in Chapter V, error bars are not included because the plots become difficult to read.

In this chapter, plots with error bars are included to provide a visual reference for the uncertainty numbers computed in the above analysis.

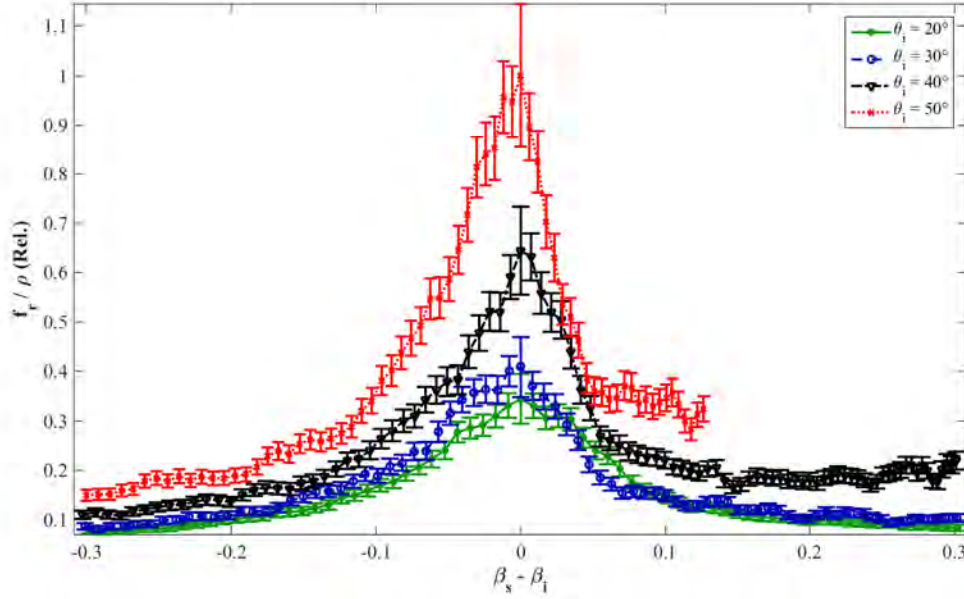


Figure 29. Grit-blasted Ni sample data at all incident angles, plotted in $\Delta\beta = \beta_s - \beta_i$ space, with error bars.

Likewise, in Figure 30, a similar plot is presented. This plot is an enlarged version of Figure 69(b) that is discussed in Chapter V; here, it is presented in an enlarged form to show the error bars. For these more specular samples, measurements were taken at smaller angular spacing, resulting in increased error immediately around specular; however, the error rapidly decreases when moving off specular.

To address repeatability of the overall process, a polished nickel sample with NIST-certified surface roughness of $0.071 \mu m$ was measured at a wavelength of $3.39 \mu m$ on two separate occasions at four different incident angles; see Figure 31. In this figure, the data is shown relative to its maximum measured value, which occurs at $\theta_i = \theta_s = 50^\circ$; data is plotted within 4° of the specular lobe. Before each measurement, a complete setup of the CASI® system was performed. In each case, the complete setup required laser alignment, detector alignment, waveplate alignment, polarizer

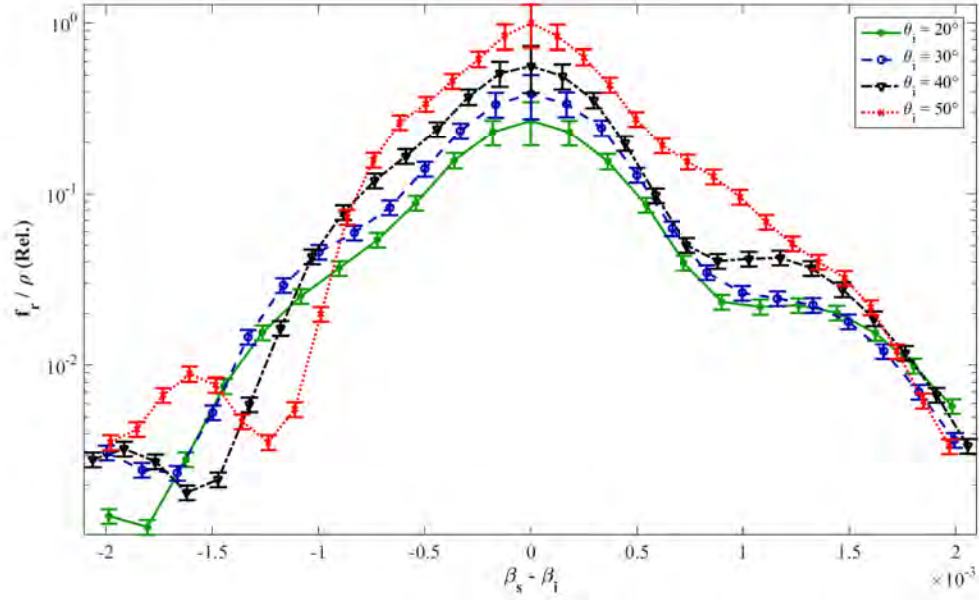


Figure 30. Polished Ni sample data at all incident angles, plotted in $\Delta\beta = \beta_s - \beta_i$ space, with error bars.

alignment, sample alignment, and so forth. The specular peak maintains quite similar shape in both completely independent measurements, and the wings of the BRDF data also match quite well. Minor differences are accounted for by the laser beam striking a slightly different position on the sample (thus resulting in small shifts in the location of the diffractive peaks visible in the BRDF that are a property of the surface of the sample as an artifact of machining).

In summary, this chapter examined the experimental methods that are used for BRDF data presented in the chapters that follow. The DRR measurement technique is detailed, with some results of DRR measurements presented for a few samples. These results suggested a much less time-consuming technique could be used for this study. An uncertainty analysis was performed on this simpler measurement technique for the AFIT CASI® scatterometer. This uncertainty analysis showed that the relative uncertainty 0.5° away from specular is under 8%, and that the relative uncertainty 0.011° away from specular (smallest step size measured) is under 18%. The next

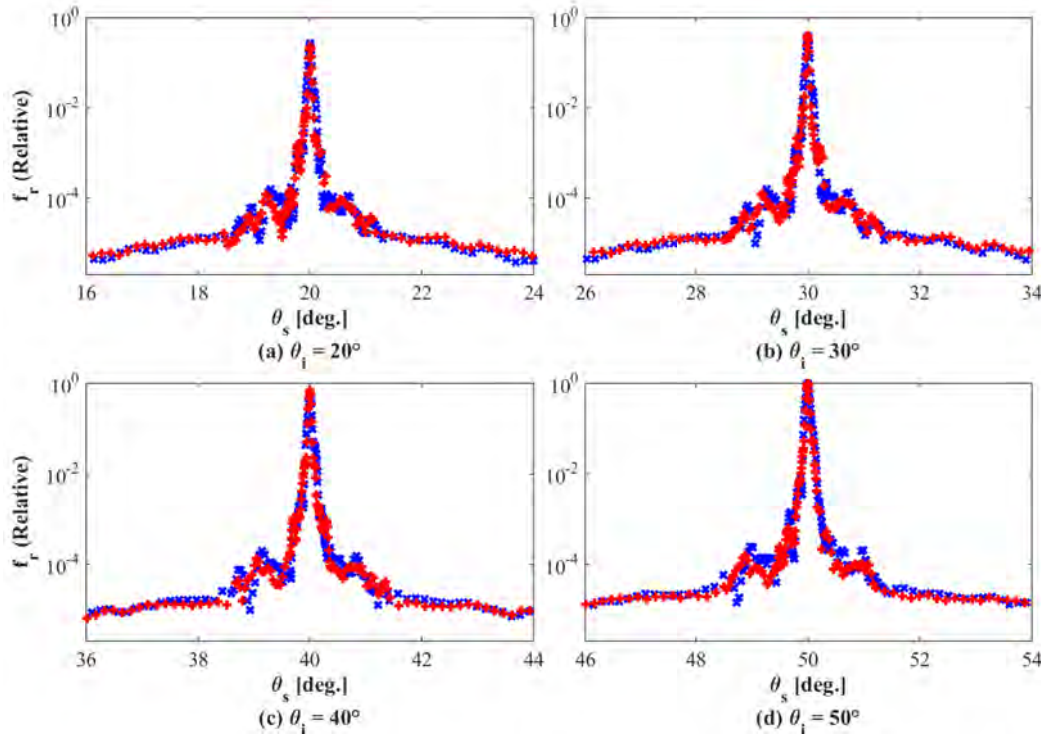


Figure 31. Comparison of Polished Ni BRDF measured data (relative to its maximum value at $\theta_i = \theta_s = 50^\circ$) taken completely independently on two separate occasions, for (a) $\theta_i = 20^\circ$, (b) $\theta_i = 30^\circ$, (c) $\theta_i = 40^\circ$, and (d) $\theta_i = 50^\circ$.

chapter combines the background and measurement to examine the BRDF of several materials, both independently as compared to the microfacet model, and to study how the BRDF becomes more specular with increasing wavelength.

V. Measurement Results

In this chapter, measurement results are discussed. These results showed that modifying the distribution function by inserting a wavelength dependence that is a constant power of λ was not accurate. Thus, at the conclusion of the results discussed in this chapter, it will be necessary to perform novel theoretical work in Chapter VI to better understand how the microfacet models vary with wavelength. Portions of this presentation are also found in [9].

A brief overview of the samples that are measured is presented first. Then, results of fitting some of the BRDF data to the microfacet model are presented. The width at the $\exp(-1)$ point in the raw data is analyzed at each measured wavelength. (This is similar to using the half width at half maximum, but is instead calculated at $\exp(-1) = 37\%$ of the maximum value instead of at 50% of the maximum value.) The width analysis showed that fitting to microfacet BRDF models does not appear to be a matter of simply finding the proper distribution function, but instead there appear to be flaws in the microfacet model itself that are particularly noticeable in the intermediate region, where surface roughness is on the order of the wavelength of light. Finally, as described in [8], the role of the cross section conversion term in aligning BRDF height is examined.

5.1 Samples

A set consisting of 12 samples was obtained to make BRDF data measurements, although due to time and sample availability, not all of the samples were measured at each wavelength. BRDF data were collected for a total of 67 different combinations of sample and wavelength, as summarized in Table 5.1. In total, 276 different BRDF measurements were made for each incident angle, sample, and wavelength.

Each measurement consisted of six scans, three for p polarization that were averaged together and three for s polarization that were averaged together, using the procedure discussed in Chapter IV for making unpolarized BRDF measurements. A total of 1,656 CASI® scans were required to take the BRDF data. In addition, there were significant steps taken for alignment and setup in accordance with SMS CASI® operating procedures that were performed for each wavelength and for each material.

Table 5.1. Summary of BRDF data collected using CASI®

Material	λ (μm)	3.39	4.4	5.2	5.63	6.4	8.0	10.6
Aluminum, polished		✓	-	-	-	-	✓	✓
Aluminum, rough		✓	-	✓+	✓+	✓	✓	✓
Infragold®		✓	-	✓+	✓	✓	✓	✓
Nickel, grit-blasted		✓	✓	✓+	✓+	✓	✓	✓
Nickel, polished		✓	✓	✓+	✓	✓	✓	✓
Nickel, shot-blasted		✓	✓	✓	✓	✓	✓	✓
Paint, Gray (DE = 0)		✓	✓	-	-	-	✓	✓
Paint, Gray (DE = 2.2)		✓	✓	✓+	✓+	✓	✓	✓
Paint, Gray (DE = 4.1)		✓	✓	-	-	-	✓	✓
Paint, Silver (Rough)		✓	-	-	-	-	✓	✓
Vehicle Paint, Black		✓-	✓	✓	✓+	✓	✓	✓
Vehicle Windshield Glass		✓	-	✓	✓	✓	✓	✓

- No BRDF data collected for this sample at this wavelength

✓- BRDF data collected for $\theta_i = \{20^\circ, 40^\circ, 50^\circ\}$

✓ BRDF data collected for $\theta_i = \{20^\circ, 30^\circ, 40^\circ, 50^\circ\}$

✓+ BRDF data collected for $\theta_i = \{10^\circ, 20^\circ, 30^\circ, 40^\circ, 50^\circ\}$

The grit-blasted Ni sample had a NIST-traceable certification of an average surface height of $4.29 \mu m$. The shot-blasted Ni sample had a NIST-traceable certification of an average surface height of $2.5 \mu m$. The polished Ni sample had a NIST-traceable certification of an average surface height of $0.071 \mu m$, and was the most highly polished sample measured in this dataset. Although the surface heights are NIST-traceable for these samples, the correlation length was not known. The measured glass sample was anti-shatter glass, consisting of two tempered glass plates with a material in the

middle to prevent shatter; thus, this form of glass was expected to reflect off the front, back, and middle of the material; this issue made alignment of the glass sample somewhat difficult. The Infragold® sample appeared to be the roughest surface-reflecting sample, with the rough Al sample also expected to be very diffuse. The rough silver paint sample appeared to be the roughest sample overall (but was expected to have both surface-reflecting and volume-reflecting elements); this material had roughness features larger than the laser beam size, which also complicated alignment. The three gray paint samples vary in amount of weathering, represented by the DE value, but otherwise are identical samples.

In general, data was collected at $\theta_i = \{20^\circ, 30^\circ, 40^\circ, 50^\circ\}$. For black vehicle paint at $3.39 \mu m$, data is not present at 30° because later analysis found an error writing out the data files at this wavelength. This issue was not present for other data files. For some of the samples and wavelengths, as shown in Table 5.1, data at 10° was additionally collected. In chronological order, the wavelength data was collected at 4.4, 3.39, 10.6, 8.0, 6.4, 5.63, and $5.2 \mu m$. Not all of the samples were available at the beginning of the data collection at $4.4 \mu m$, so some materials did not have data collected at this wavelength. Furthermore, after the $8.0 \mu m$ data was taken, a reduced sample set was selected to enable collection of more wavelengths. This involved measuring only one polished metal sample, one gray paint sample, and excluding the diffuse rough silver paint sample from the measurement, as it is more time-consuming to align and the BRDF did not show significant wavelength variation for this sample. The collection of this wavelength-dependent BRDF data in the MWIR and LWIR, along with analysis described in this chapter, is one of this dissertation's major contributions toward advancing BRDF research.

5.2 Fitting Data to Microfacet BRDF

In this section, some of the measured BRDF data is presented in standard spherical coordinates to illustrate representative data that were taken. After commenting on some observations with this subset of data, all of the wavelength-dependent features of all of the samples are presented, since wavelength dependence of the BRDF is the focus of the research for this dissertation. For all data presented, the data is normalized by the DHR to remove effects due to overall reflectance of the material; that is, the plots are f_r/ρ , where the DHR ρ is defined by Equation (28). The DHR was calculated from the measured BRDF data.

Figures 32 and 33 show the results for the grit-blasted Ni sample at 3.39 and 10.6 μm , respectively. Recall that this sample was obtained from a set that included a NIST-traceable average surface height roughness of 4.29 μm , or on the order of the wavelengths used to interrogate the sample. At wavelengths of both 3.39 and 10.6 μm , the material has a definite specular peak, despite appearing rough in the visible spectrum, due to IR wavelengths being longer. Furthermore, comparing the two figures directly shows that the BRDF peaks are consistently about an order of magnitude higher at 10.6 μm than at 3.39 μm . Thus, BRDF of the grit-blasted Ni sample is varying substantially with wavelength. This wavelength variation illustrates the problem explored in this work using experimental data measured with the sophisticated CASI® system, in that the BRDF is varying substantially with wavelength in a manner that is not inherently captured by the microfacet geometric optics approximation.

As mentioned in Chapter III, a technique for adding the wavelength dependence to the microfacet model is to assume the variation is linear, and interpolate between two points. This was performed for the grit-blasted Ni sample to validate the results obtained in Chapter III with this work's BRDF measurements. Using Equation (93),

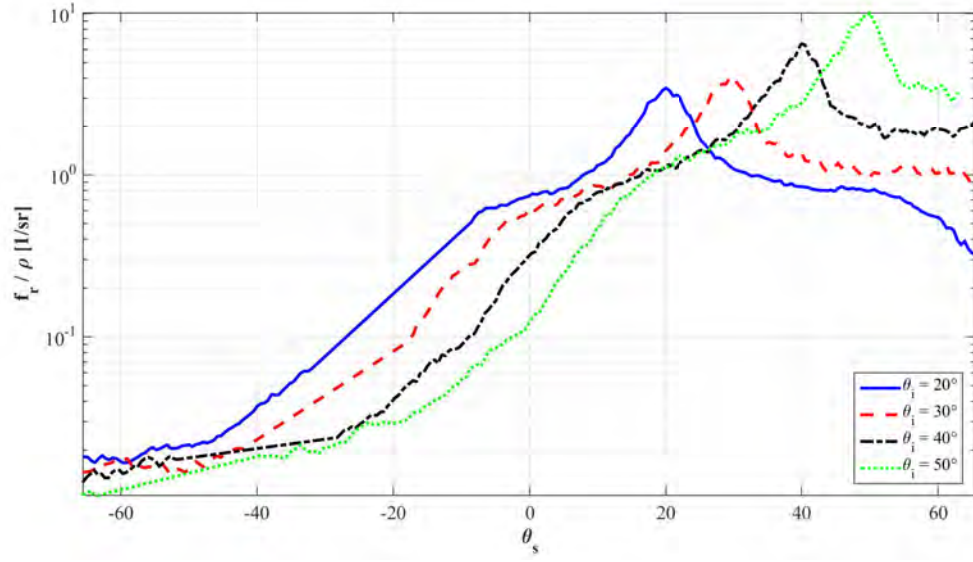


Figure 32. BRDF divided by DHR for grit-blasted Ni measured at $3.39 \mu m$.

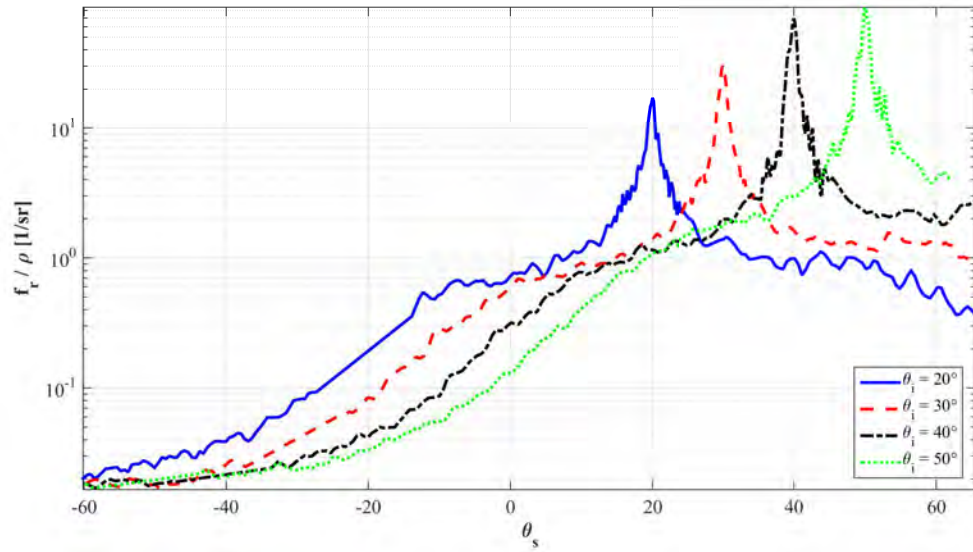


Figure 33. BRDF divided by DHR for grit-blasted Ni measured at $10.6 \mu m$.

the measured BRDF data for grit-blasted Ni at $3.39 \mu m$ and at $10.6 \mu m$ were used to predict the BRDF data at $8.0 \mu m$; see Figure 34 for the BRDF data, and Figure 35 for the relative error. As was observed in Chapter III with the NEF data, the relative error changes most significantly near the specular peak, validating the observation that linear interpolation does not accurately capture the wavelength dependence of the specular peak. This trend was observed at other incident angles, and for other materials that exhibited significant variation with wavelength; see Figures 36 and 37 for an example using the shot-blasted Ni sample at $\theta_i = 20^\circ$. The specular peak is also where much of the energy is being directed in the hemisphere, so errors around the specular peak are particularly problematic.

The initial approach to solving this problem was to take data, fit existing microfacet models (as detailed in Chapter III) to this data, using a variety of different microfacet distribution functions, and modify the model based on experimental data to include a wavelength scaling. To illustrate this effect, consider for example the Cook-Torrance BRDF model discussed in Chapter III. This model uses the Beckmann (Gaussian) distribution function for the microfacet statistics. This data was fitted to the grit-blasted Ni sample plots using all incident angle data, MATLAB® 2014b `lsqcurvefit` built-in function for nonlinear curve fitting, and using two different error metrics $g(x)$; that is, the built-in `lsqcurvefit` function is used to calculate

$$\min_{\vec{p}} ||g[f_r(\hat{\omega}_i, \hat{\omega}_s, \vec{p})] - g[f_m(\hat{\omega}_i, \hat{\omega}_s)]||_2, \quad (137)$$

where f_r is the modeled data with input parameters \vec{p} for the particular BRDF model, f_m is the measured BRDF data, and $g(x)$ is the metric function. Two different metric functions were chosen: $g(x) = x$ (default metric function), which is a standard nonlinear curve fit, and $g(x) = \ln(x)$, which is a logarithmic fit due to the BRDF varying by several orders of magnitude.

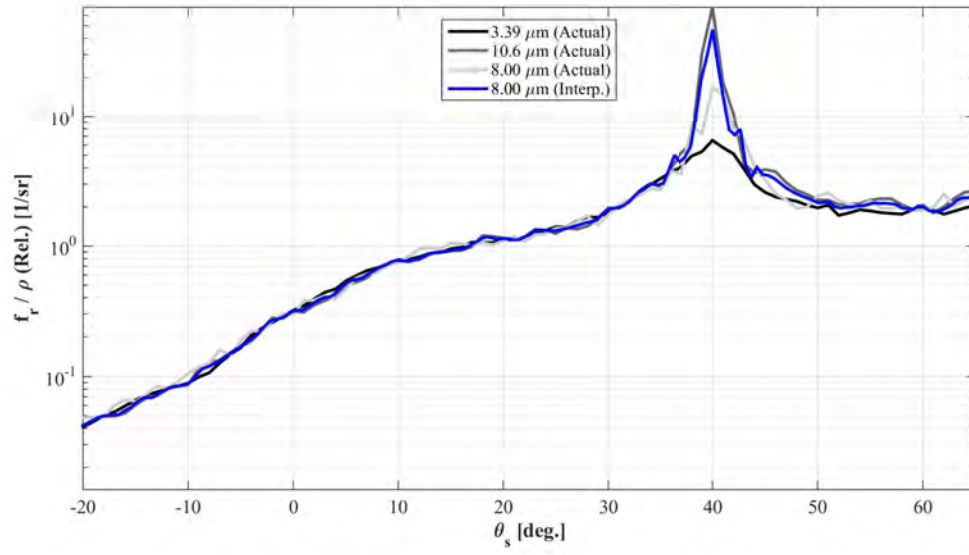


Figure 34. Linear interpolation to calculate grit-blasted Ni BRDF divided by DHR at $\theta_i = 40^\circ$ and $\lambda = 8.0 \mu m$, using measured BRDF data at $\lambda = 3.39 \mu m$ and $\lambda = 10.6 \mu m$, compared to the actual BRDF measured at $\lambda = 8.0 \mu m$.

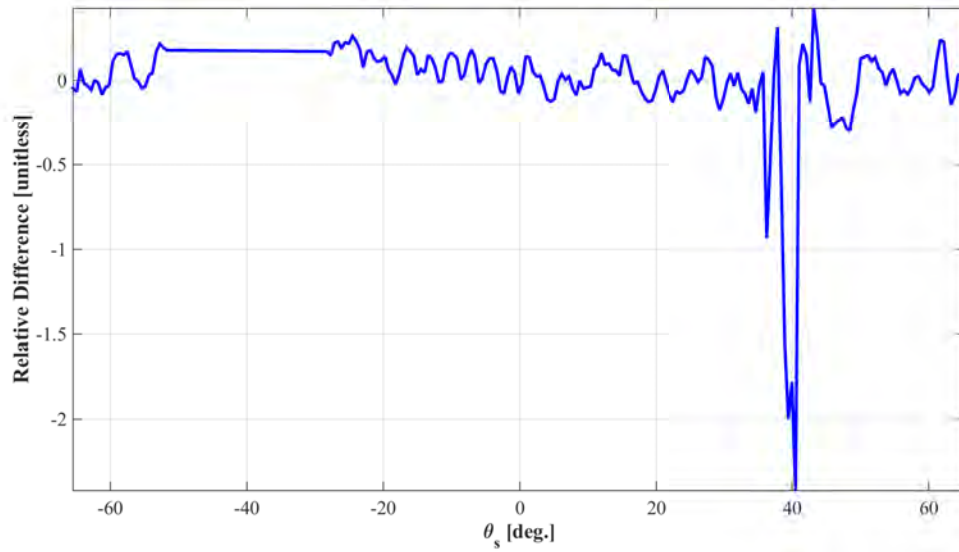


Figure 35. Relative error in the linear interpolation to calculate grit-blasted Ni BRDF divided by DHR at $\theta_i = 40^\circ$ and $\lambda = 8.0 \mu m$, using measured BRDF data at $\lambda = 3.39 \mu m$ and $\lambda = 10.6 \mu m$.

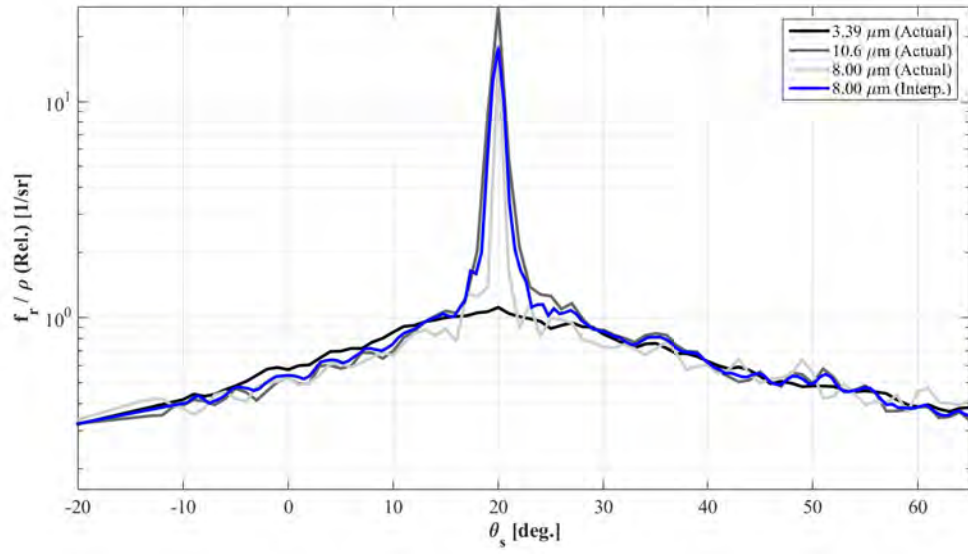


Figure 36. Linear interpolation to calculate shot-blasted Ni BRDF divided by DHR at $\theta_i = 20^\circ$ and $\lambda = 8.0 \mu m$, using measured BRDF data at $\lambda = 3.39 \mu m$ and $\lambda = 10.6 \mu m$, compared to the actual BRDF measured at $\lambda = 8.0 \mu m$.

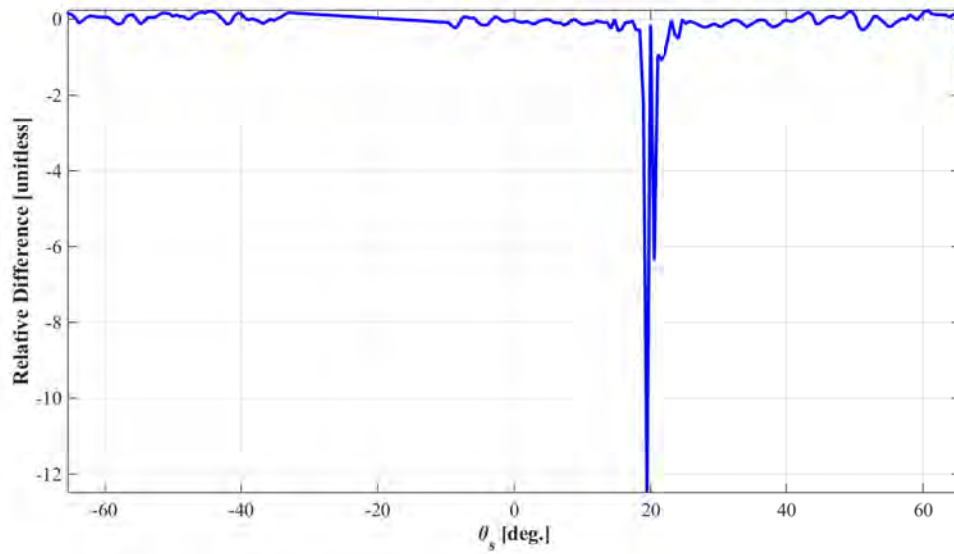


Figure 37. Relative error in the linear interpolation to calculate shot-blasted Ni BRDF divided by DHR at $\theta_i = 20^\circ$ and $\lambda = 8.0 \mu m$, using measured BRDF data at $\lambda = 3.39 \mu m$ and $\lambda = 10.6 \mu m$.

For the grit-blasted nickel BRDF sample at $\lambda = 3.39 \mu m$, results for fitting to the Cook-Torrance BRDF are plotted in Figure 38 for the default metric, and in Figure 39 using the \ln metric. For the default fitting metric, one can see the peak is fit somewhat by the Cook-Torrance model, although the overall shape of the Gaussian distribution does not match the overall shape of the data. Using the \ln metric fits the data off specular reasonably well, but results in a bad fit near the specular peak. Note that in both plots, there is an occultation zone in the measured data, where data points were not collected; this is due to the receiver arm blocking the incident laser beam, and is centered at $-\theta_i$.

One observation that can be made from this result is that perhaps an improper BRDF model was chosen. From Figure 38 in particular, it is clear that the Gaussian shape of the Beckmann microfacet distribution does not match the shape of the measured BRDF data. Perhaps if a better microfacet distribution function were used, the quality of the fit could be improved. This topic is explored next.

Adaptive Microfacet BRDF Model.

As outlined in [5], which is based largely on the microfacet BRDF overview described in Chapter III, several different microfacet BRDF models are of the same basic form. These models differ primarily in which basic physical components (Fresnel reflection, cross section conversion, choice of distribution function, etc.) of a geometric BRDF are included. In [5], and using data from the MERL database[42], BRDF fitting can be significantly improved upon by using the Hyper-Cauchy distribution function in the Cook-Torrance BRDF model instead of the default Beckmann distribution function. These results are described briefly here, prior to returning to the problem of fitting this measured BRDF data.

As long as a normalized distribution function is chosen, one could make sim-

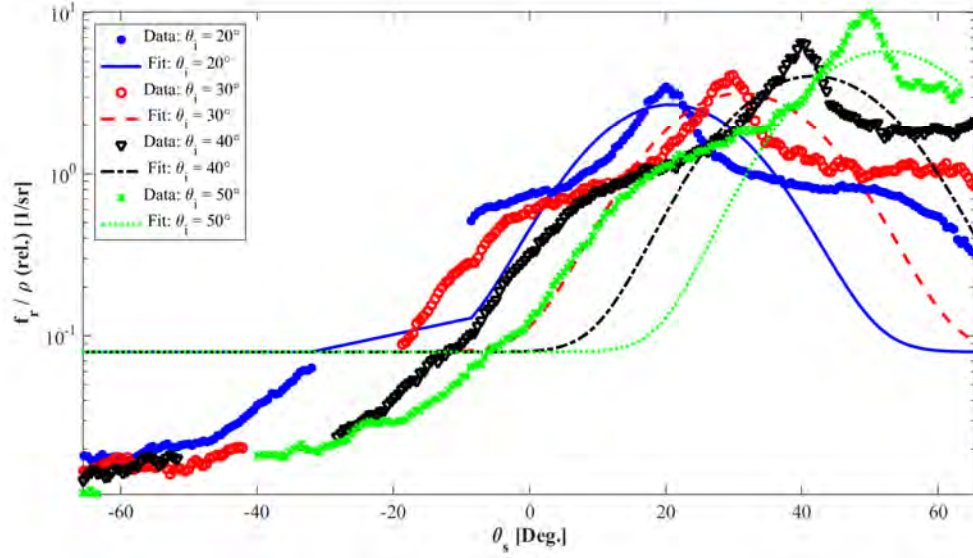


Figure 38. BRDF for grit-blasted Ni measured at $3.39 \mu m$, fitted to Cook-Torrance BRDF, using the default error metric, $g(x) = x$.

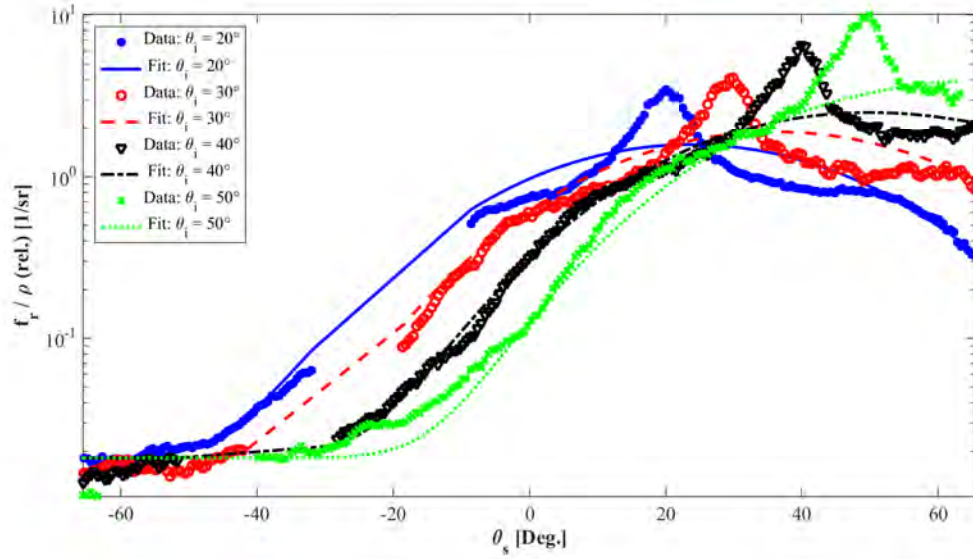


Figure 39. BRDF for grit-blasted Ni measured at $3.39 \mu m$, fitted to Cook-Torrance BRDF, using \ln error metric, $g(x) = \ln(x)$.

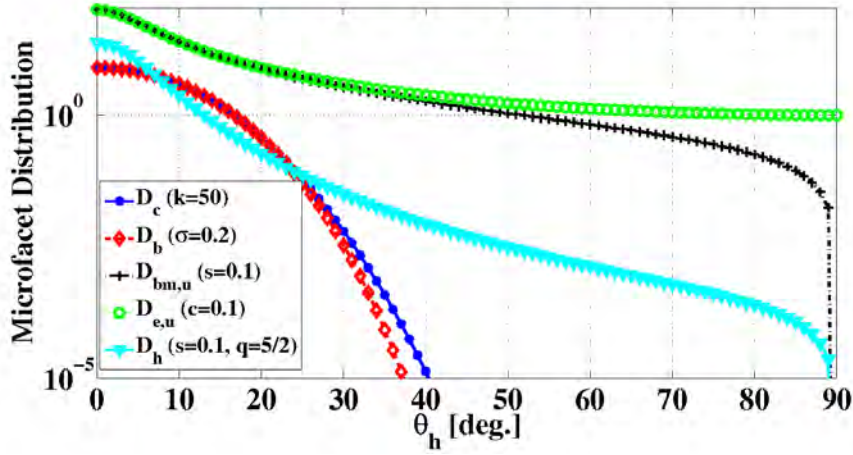


Figure 40. Comparison of various isotropic microfacet distribution functions. $D_{bm,u}$ and $D_{e,u}$ are unnormalized. D_c is an approximation to D_b (and thus also to D_g).

ple changes to existing models based on the summary presented in Chapter III and discussed in [5]. For example, one could create a new BRDF using the normalized two-parameter Hyper-Cauchy microfacet distribution in place of the normalized Beckmann distribution, but otherwise using the Cook-Torrance model elements from Table 3.1:

$$f_r(\hat{\omega}_i, \hat{\omega}_s) = \rho_s D_h(\theta_h) G_c(\hat{\omega}_i, \hat{\omega}_s) \sigma(\theta_i, \theta_s) F(\theta_d) + \frac{\rho_d}{\pi} \quad (138)$$

This additional flexibility enables a material-driven choice of distribution function without sacrificing the desirable benefits in models such as Cook-Torrance, and without generating an entirely new model.

Consider the isotropic distribution functions defined in Chapter III; these functions are plotted in Figure 40. By comparing these shapes to a measured BRDF, one can determine whether its specular lobe is shaped more like that of the Beckmann/Cosine distribution, the Hyper-Cauchy distribution, or the elliptical (Sandford-Robertson) distribution. Other desirable model characteristics, such as Fresnel, geometric attenuation, and cross section conversion, can then be added to the experimentally-

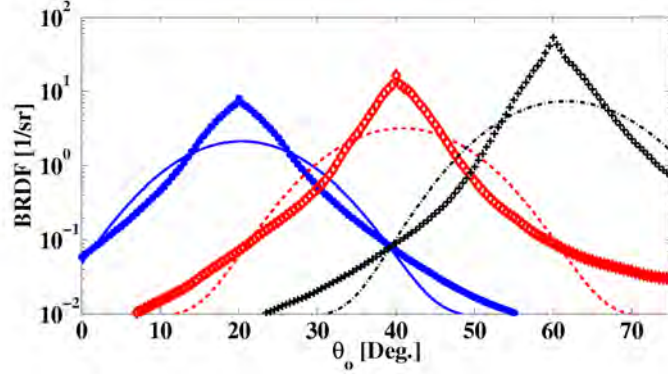


Figure 41. Fit of Cook-Torrance BRDF to MERL nickel.binary file at 20°, 40°, and 60°. The Gaussian facet distribution appears to be the improper shape for this BRDF data, suggesting a better result may be obtained through use of a different microfacet distribution function. The lines represent the best fit and the dots represent the BRDF data from Matusik’s MERL database[42].

determined distribution function choice to provide a data-driven BRDF model.

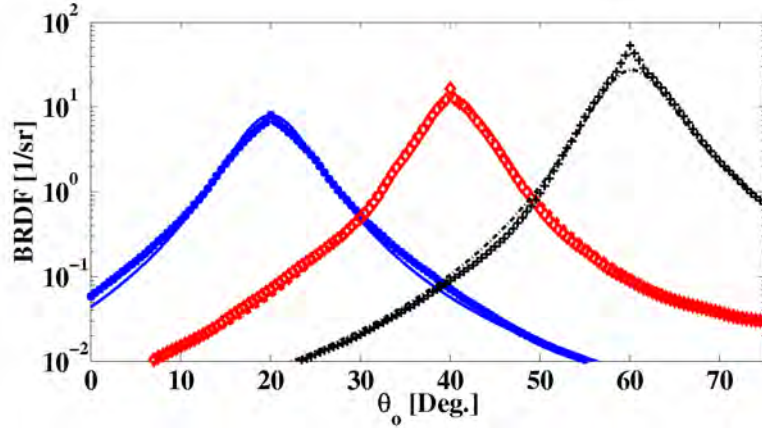


Figure 42. Fit of modified Cook-Torrance BRDF to MERL Nickel file at 20°, 40°, and 60°. This modified form is identical to Cook-Torrance, except with the Hyper-Cauchy distribution function in place of the Beckmann (Gaussian) distribution function. This modified form is a significantly better fit to the data. The lines represent the best fit and the dots represent the BRDF data from Matusik’s MERL database[42].

As an example of the power of expressing the BRDFs in this common language and switching the distribution function used in a model, consider the BRDF for nickel as contained in Matusik’s MERL database nickel.binary file, freely available online[42]. Ngan performed a study fitting the MERL data to some popular BRDF models; in his analysis, Cook-Torrance and He-Torrance (not a microfacet model) were tied for

the best fit to the MERL nickel data, although the fit was not great—it had an error of 11.4% with both models [47]. Nonetheless, this result suggests a reasonable first attempt at fitting this BRDF data to a microfacet model would use the Cook-Torrance BRDF.

Considering only the red channel nickel data, the BRDF is plotted at three incident angles, with Cook-Torrance parameters fitted to the natural logarithm of the BRDF; see Figure 41. (In this analysis, $n = 2.1$ and $\kappa = 3.8$ were used for the index of refraction of nickel at 650 nm according to Rakic *et al.*[54], and were not varied as fitting parameters.) From this figure, it is clear that Cook-Torrance’s Beckmann distribution function is not appropriate for this BRDF data; the Gaussian is concave down over a substantial region where the measured BRDF data is concave up. No amount of varying fit parameters or changing the fitting function’s metric will fix this issue; therefore, it may be assumed that the model’s Beckmann distribution function is not suitable for fitting this data.

Having identified this problem, a new distribution function could be considered to replace the Beckmann distribution in the Cook-Torrance BRDF. By studying the BRDF data in Figure 41 as compared to Figure 40, the Hyper-Cauchy distribution seems to be a better choice, as it is concave down over a much smaller region and concave up over a majority of the microfacet distribution. By simply replacing the Cook-Torrance BRDF’s Beckmann (Gaussian) distribution with the Hyper-Cauchy distribution function from Willems, a far better result is obtained; see Figure 42.

BRDF Fit with Hyper-Cauchy Distribution.

This same procedure could be used to attempt to find a better fit for the Cook-Torrance BRDF to the IR BRDF data measured in this dissertation, using the Hyper-Cauchy distribution function in place of the Beckmann distribution function. This

was attempted with the default metric in Figure 43, and using the \ln metric in Figure 44. In this case, unlike with the MERL data, the change in distribution function did not appear to solve the fit problem, although it still resulted in a somewhat better fit. However, there are still model deficiencies, either in the wings (for the default error metric) or near the peak (for the \ln error metric).

Fitting to Other Samples.

Comparing Figure 45 (shot-blasted Ni at $3.39\ \mu m$) to Figure 44 (grit-blasted Ni at $3.39\ \mu m$), the BRDF is not as strongly peaked at $3.39\ \mu m$. Since the shot-blasted Ni sample is somewhat more diffuse, the Cook-Torrance BRDF with the Hyper-Cauchy distribution function appears to fit this data quite well. However, when moving to higher wavelengths, the BRDF becomes more sharply peaked and the fitting routine for the same BRDF model results in far less accurate fits, as can be seen by examining the shot-blasted Ni sample at 3.39 , 4.4 , 5.63 , and $10.6\ \mu m$; see Figures 45-48.

Considering a different material that is more diffuse, the rough aluminum sample at $3.39\ \mu m$ is now examined. The BRDF data, fitted to the Cook-Torrance BRDF model (with the Beckmann distribution and the \ln error metric) is plotted in Figure 49. The BRDF fit is much closer for this sample. The BRDF for the rough Al sample does not vary much with wavelength, and thus the microfacet model fits relatively well at all wavelengths measured.

Moving on to the polished Al sample, the Cook-Torrance BRDF with the Hyper-Cauchy distribution function appears to give the best fit. Indeed, at $3.39\ \mu m$, the fit is reasonable; see Figure 50. However, when moving to $10.6\ \mu m$, for the same material, the BRDF fit with the same distribution function and fit metric is no longer good; see Figure 51. This does not make sense if the distribution function represents a distribution of microfacets. The BRDF data for polished Al at 4.4 and $8.0\ \mu m$ is

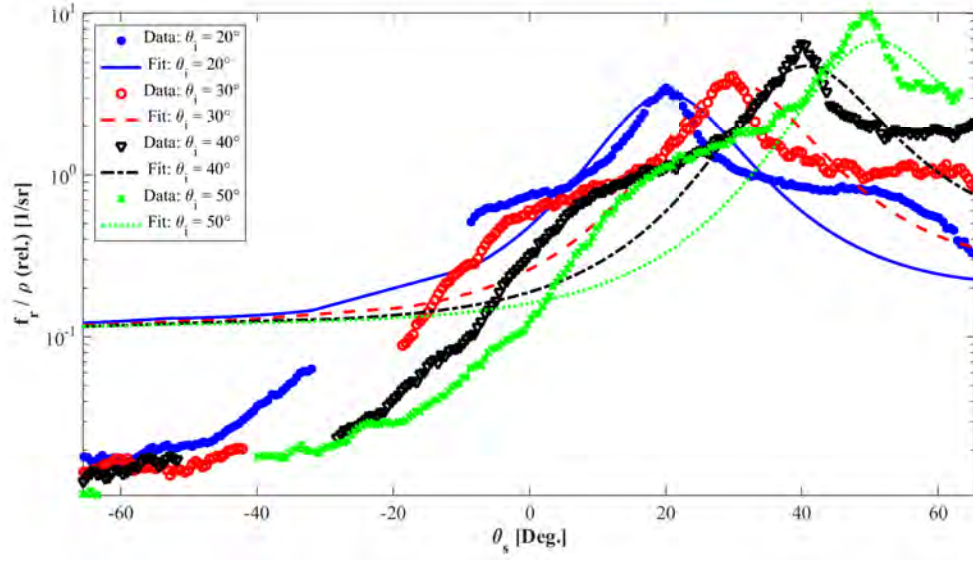


Figure 43. BRDF for grit-blasted Ni at $3.39 \mu m$, fitted to Cook-Torrance BRDF with Hyper-Cauchy distribution in place of the Beckmann distribution, using the default error metric, $g(x) = x$.

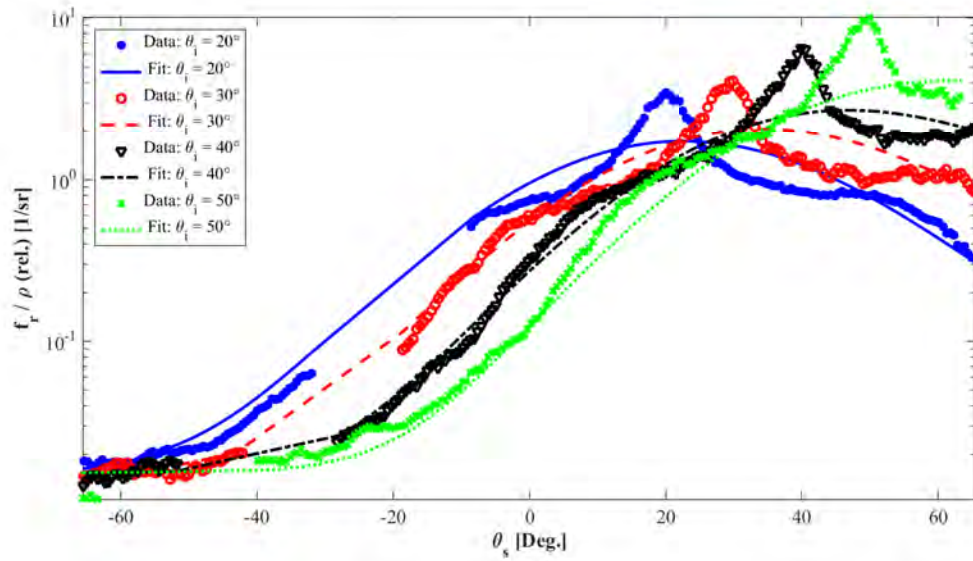


Figure 44. BRDF for grit-blasted Ni at $3.39 \mu m$, fitted to Cook-Torrance BRDF with Hyper-Cauchy distribution in place of the Beckmann distribution, using \ln error metric, $g(x) = \ln(x)$.

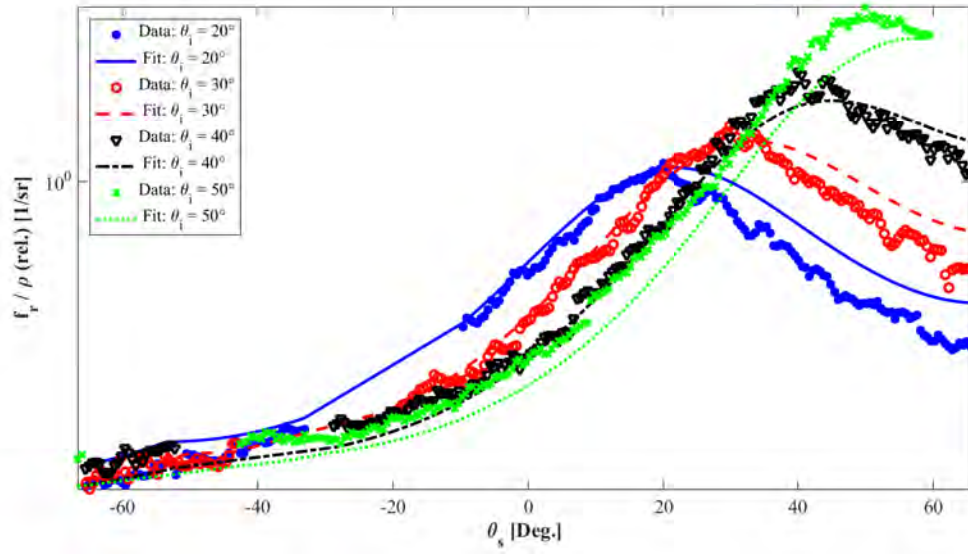


Figure 45. BRDF for shot-blasted Ni at $3.39 \mu m$, fitted to Cook-Torrance BRDF with Hyper-Cauchy distribution in place of the Beckmann distribution, using the \ln error metric, $g(x) = \ln(x)$.

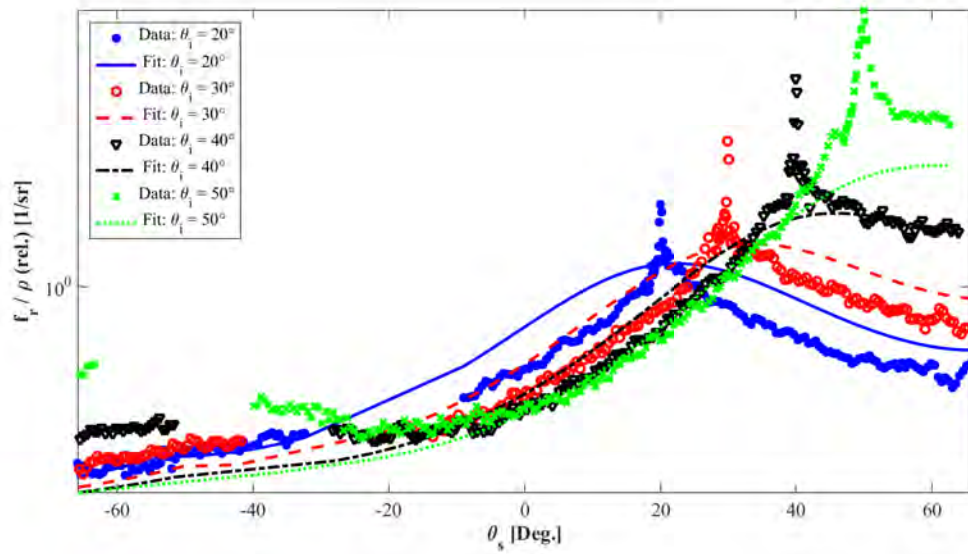


Figure 46. BRDF for shot-blasted Ni at $4.4 \mu m$, fitted to Cook-Torrance BRDF with Hyper-Cauchy distribution in place of the Beckmann distribution, using \ln error metric, $g(x) = \ln(x)$.

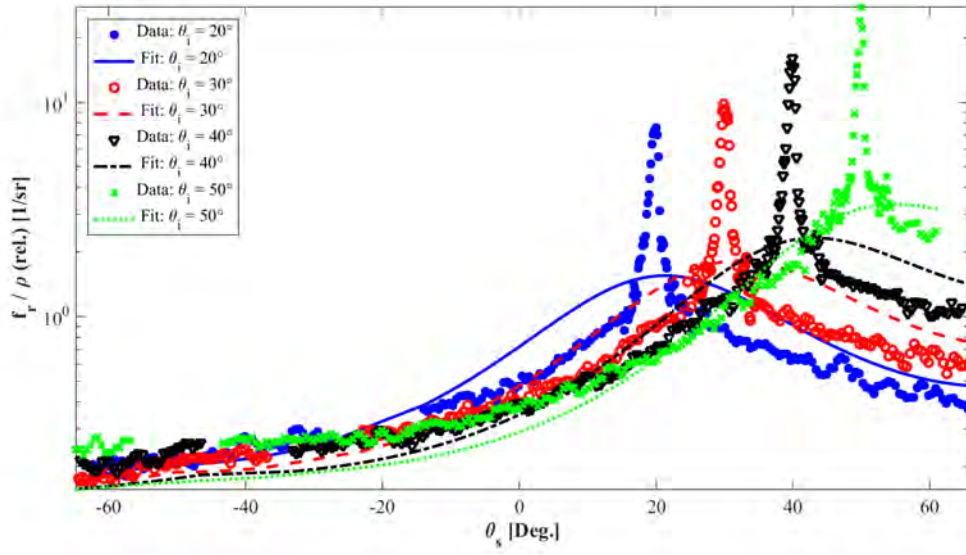


Figure 47. BRDF for shot-blasted Ni at $5.63 \mu m$, fitted to Cook-Torrance BRDF with Hyper-Cauchy distribution in place of the Beckmann distribution, using the default error metric, $g(x) = x$.

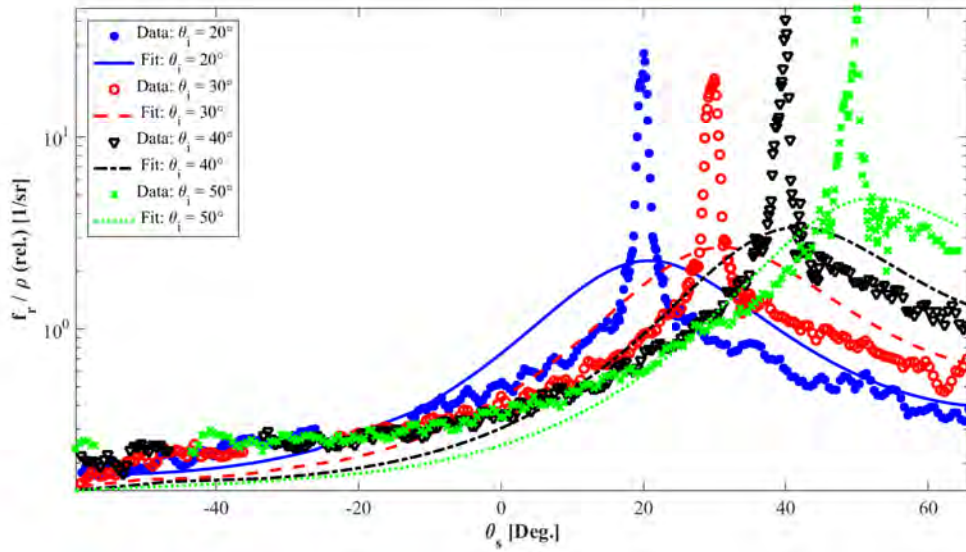


Figure 48. BRDF for shot-blasted Ni at $10.6 \mu m$, fitted to Cook-Torrance BRDF with Hyper-Cauchy distribution in place of the Beckmann distribution, using \ln error metric, $g(x) = \ln(x)$.

in between these two extremes, showing the fit is becoming worse with increasing wavelength. This observation suggests that more than just a wavelength dependence is affecting the microfacet distribution function. This trend was also noticed for the polished Ni sample, although for the polished Ni sample the BRDF model was not a good fit in the wings even at $3.39 \mu m$.

These materials are all surface-reflecting materials, and discrepancies exist for multiple materials and multiple roughnesses. These trends were also noticed when fitting other materials not shown in this section. In general, the more diffuse a material was, the better it would fit to the standard Cook-Torrance model. In between rough and specular, the Cook-Torrance model replaced with a Hyper-Cauchy distribution function would improve on the fit quality, although even then it would not always result in a great fit. As the BRDF became even more specular, the overall fit would become worse. This observation will be explained theoretically when a comparison of microfacet models to scalar wave optics models is made in Chapter VI.

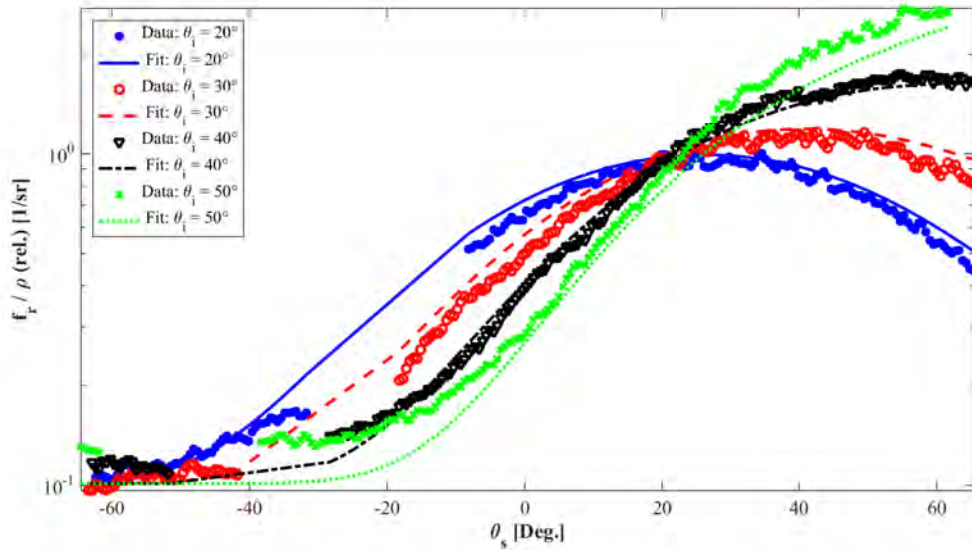


Figure 49. BRDF for rough Al at $3.39 \mu m$, fitted to Cook-Torrance BRDF, using \ln error metric, $g(x) = \ln(x)$.

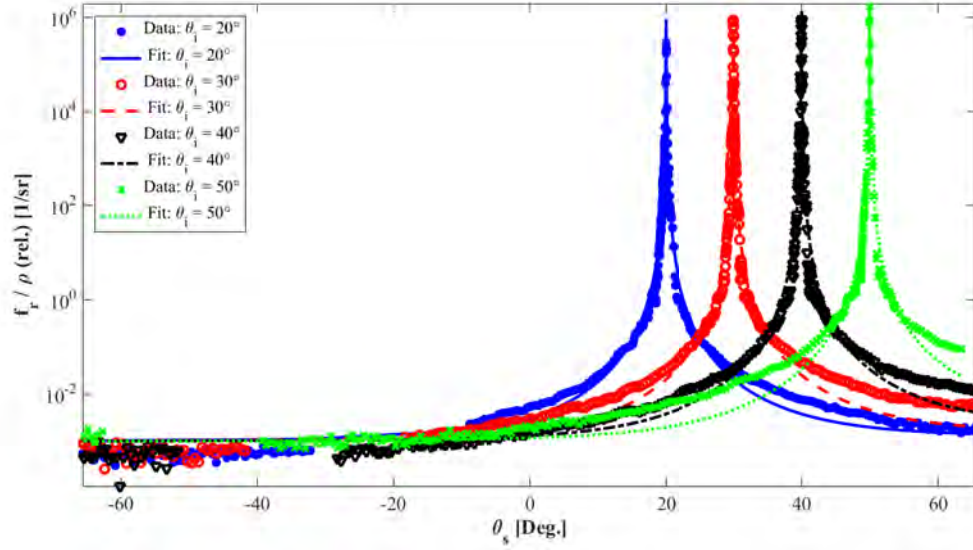


Figure 50. BRDF for polished Al at $3.39 \mu\text{m}$, fitted to Cook-Torrance BRDF with Hyper-Cauchy distribution, using \ln error metric, $g(x) = \ln(x)$.

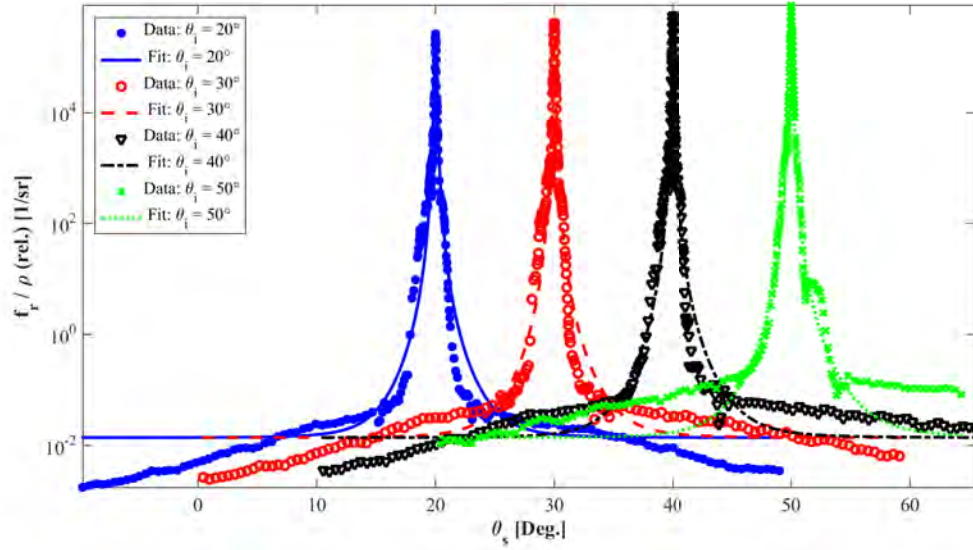


Figure 51. BRDF for polished Al at $10.6 \mu\text{m}$, fitted to Cook-Torrance BRDF with Hyper-Cauchy distribution, using \ln error metric, $g(x) = \ln(x)$.

Although only the Beckmann and Hyper-Cauchy distribution functions are shown here, the Beard-Maxwell model uses a modified Cauchy distribution (and thus is a simplification of the Hyper-Cauchy distribution), and the elliptical distribution function can be approximated by appropriate choice of the second parameter q in the Hyper-Cauchy distribution. The bi-static scan used in the NEF was not tested, since bi-static scan data was not taken for these samples and greatly increases the number of parameters required to specify the BRDF. These fundamental flaws in the microfacet BRDF models led to a shift in the approach to this dissertation, as the underlying model appears to be flawed. Thus, the focus of the research into BRDF models changed from adding a wavelength scaling to the microfacet BRDF models to proposing a scalar wave optics-based modification to the microfacet BRDF models; progress in this area is discussed in Chapter VI. However, the deficiencies noted here for the fitting process do not preclude an analysis of the wavelength-dependent nature of the raw BRDF data that was taken. That raw data analysis is performed in the next section, for all materials measured.

5.3 Wavelength Variation of Raw Data BRDF Width

As discussed in Chapter III, and validated in Figures 35 and 37 using the data measured for this dissertation, the specular lobe was expected to exhibit the strongest non-linear wavelength dependence. At longer wavelengths, the magnitude of the measured BRDF is higher; physically, the surface roughness appears smoother relative to a wavelength. (DHR may also vary with wavelength, but the BRDF data presented in this dissertation is divided by the DHR to account for this material property, as it is not an inherent property of the BRDF in general but depends upon the particular material comprising a sample.)

At this point, there are two possible resolutions to this problem that are examined

in this dissertation. First, consider the microfacet model. This model assumes the main influence on the BRDF (at least for more specular data) is driven by the microfacet distribution function. There is a concern that perhaps there exists a microfacet distribution function that is not analyzed in the previous sections. This concern is addressed first, but it is observed that there does not even appear to be an unknown microfacet distribution function that would fit the data well.

Second, there is the possibility that the microfacet BRDF model's form is fundamentally flawed, particularly at longer wavelengths (where a surface is not as rough relative to a wavelength, and is expected to be more specular). The natural follow-on questions are:

- What appears to be wrong with the microfacet model?
- What does the wavelength-dependent data suggest as a potential fix for the microfacet model?
- When is the microfacet model valid?

The first two questions are addressed qualitatively in this chapter, after attempting to determine whether the microfacet model can be utilized with an unknown distribution function. The last question is addressed in a theoretical analysis of the microfacet model performed in Chapter VI, along with quantifying relationships between the microfacet model and a scalar wave optics model to more rigorously understand the difference in two limiting cases.

Unknown Microfacet Distribution Function.

To quantify whether the BRDF width spectral dependence makes sense in the context of a microfacet model, it is instructive to examine the point at which the BRDF has decreased to e^{-1} of its maximum value. There is a complicating issue

with simply performing this analysis on the raw data. The width parameter in the microfacet distribution function is the width at *normal* incidence. Normal incidence is difficult to measure directly with the CASI®, as the detector arm blocks the incident beam. Thus, prior to analyzing the width of the measured data, a brief detour to scattering theory is taken to describe how the width of the BRDF at normal incidence is estimated from the BRDF data measured. After this brief explanation from theory, results are presented from measured BRDF data at different wavelengths.

As mentioned in Chapter III, scalar wave optics models that include diffraction use direction cosine space to represent BRDF data. The horizontal axis of the BRDF plot in this space is given by Equations (98) and (99). (For in-plane data, recall $\phi_s = \{0^\circ, 180^\circ\}$.) Alternatively, it is possible to transform to a new space where θ ranges from -90° to 90° , and represent in-plane BRDF data in the retroreflective quadrant as $\theta < 0$, and forward scatter as $\theta > 0$. In this space, the in-plane data in direction cosine space is given by $\Delta\beta$, defined as [26, 27, 29, 30, 38, 28]

$$\Delta\beta = \beta_s - \beta_i = \sin \theta_s - \sin \theta_i. \quad (139)$$

This technique of plotting the BRDF data in $\Delta\beta$ space has been used by Harvey to relate measured BRDF data at different incident angles, and show the BRDF data at different incident angles theoretically become identical under this transformation (excluding a difference in overall magnitude) [26, 28]. Therefore, this transformation is used here to estimate the width of the BRDF at normal incidence for the different measured θ_i values. The difference in height in the BRDF at different incident angles are not important in understanding distribution width since it results in a different overall scaling, which does not change the location where the BRDF has decreased by e^{-1} from its maximum value.

To illustrate how this BRDF width analysis process is implemented, consider the

BRDF data for the grit-blasted Ni sample at $3.39\ \mu m$, as shown in standard angular coordinates at the beginning of this chapter in Figure 32. By performing the change in coordinate system defined by Equation (139) for each incident angle and finding the point at which the BRDF has decreased to e^{-1} of its maximum value, the BRDF data for each incident angle is aligned, other than having a variable height. Figure 52(a) depicts the BRDF data from Figure 32 translated to direction cosine space while Figure 52(b) shows this data on a linear plot, which emphasizes the specular peak, and shows the BRDF width as calculated from the four different incident angles at e^{-1} of the maximum height. As discussed previously, an overall height scaling does not affect the e^{-1} location of the BRDF width. This process is performed on both sides of the specular peak, where possible, to increase the number of data points in the average. (For some of the BRDF data for rougher surfaces, the value on one side of the peak does not decrease by e^{-1} ; in this case, that direction is not included.) The standard deviation is also calculated from this averaging process.

This process is conducted at each wavelength for which there is measured wavelength data, resulting in the data plotted in Figure 53. For all BRDF width figures presented in this section, including Figure 53, (a) shows the BRDF width and standard deviation is plotted in linear space, along with reference powers of λ ; (b) shows the BRDF width (without error bars) with reference powers of λ in log-log space, since the λ dependence would be linear on a log-log plot if it were a constant power of λ . For the grit-blasted Ni sample, the BRDF is not varying linearly in power of λ . For this sample, the NIST-certified surface height was $4.29\ \mu m$, which may explain why the variation with λ is most significant near that wavelength in the BRDF data. This result validates the observation in the prior section that the BRDF distribution width does not vary in a straightforward manner with respect to λ ; for this sample at MWIR and LWIR wavelengths, the problem is not limited to finding a different

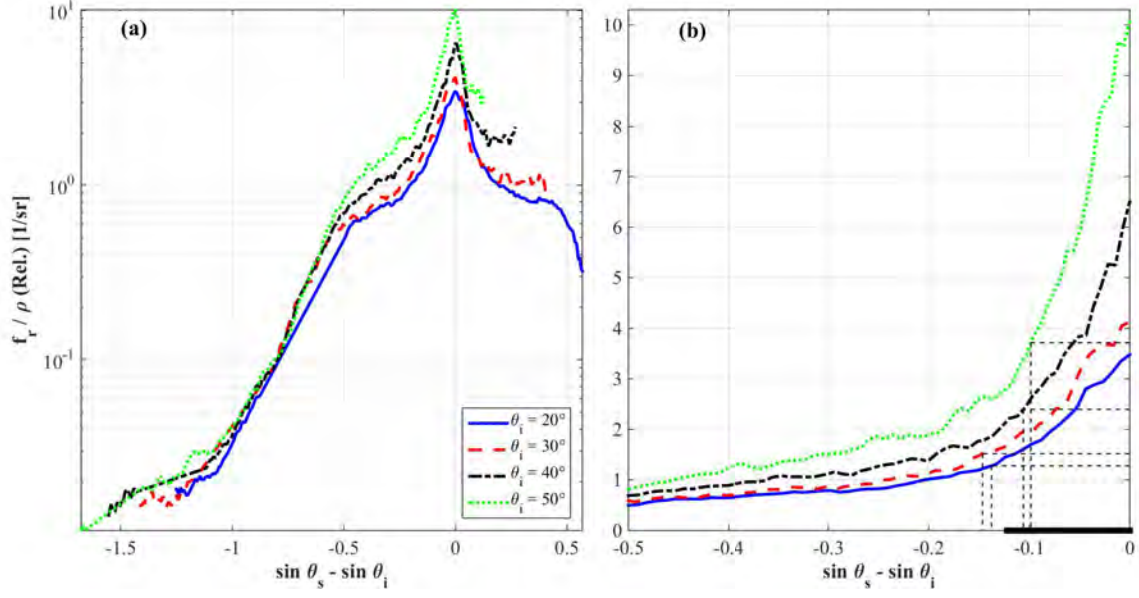


Figure 52. (a) BRDF divided by DHR for grit-blasted Ni measured at $3.39 \mu\text{m}$, in direction cosine space, over the entire interval, and (b) zoomed in near the peak. The dotted lines in (b) represent the width of the BRDF data for each incident angle. The dark solid line on the right side of the horizontal axis represents the mean value of the width.

microfacet distribution function or a better fitting metric.

To determine whether the above trend was peculiar to the grit-blasted Ni sample or was a general property present over multiple samples, each measured sample was plotted using this method. Figures 53-58 show the result for the surface-reflecting samples that were measured, and Figures 59-64 show the result for the samples that were expected to have both surface-reflecting and volumetric components to the BRDF.

Considering the surface-reflecting Ni samples in Figures 53-55 first, it is apparent that there is significant change in the rougher surfaces when the wavelength is on the order of the surface height roughness. However, the polished Ni sample behaves quite strangely, as it appears to be *increasing* slowly in width as a function of wavelength. Looking at the remaining surface-reflecting samples in Figures 56-58, these BRDFs all appear to not vary in width as a function of wavelength. (For the polished Al sample, there might possibly be a slight increase in width at $10.6 \mu\text{m}$ compared to

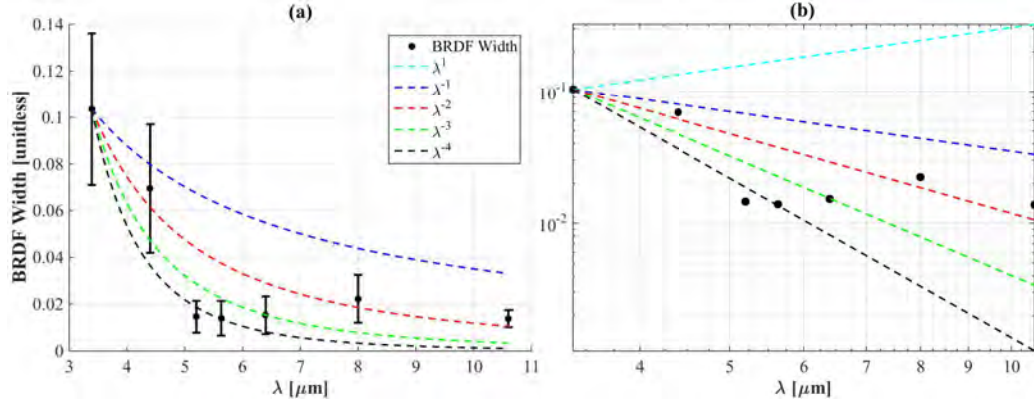


Figure 53. BRDF width versus λ for grit-blasted Ni in (a) linear space (with standard deviation), and (b) log-log space. The dotted lines provide guidelines for integer powers of λ .

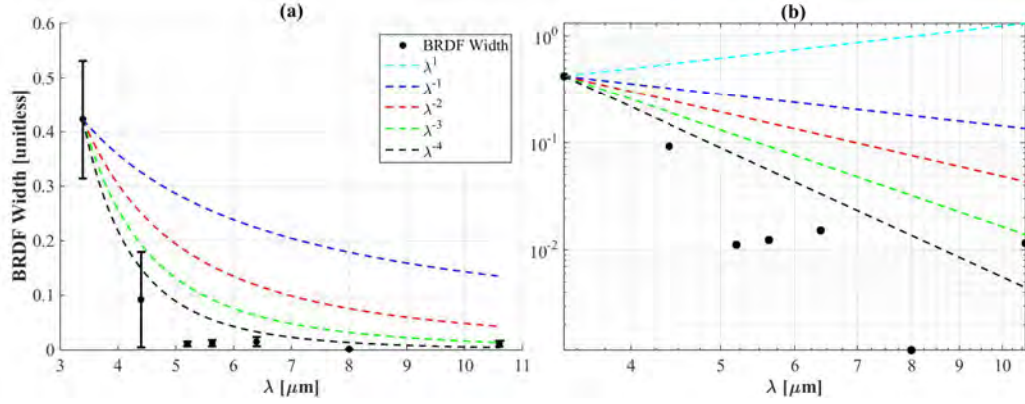


Figure 54. BRDF width versus λ for shot-blasted Ni in (a) linear space (with standard deviation), and (b) log-log space.

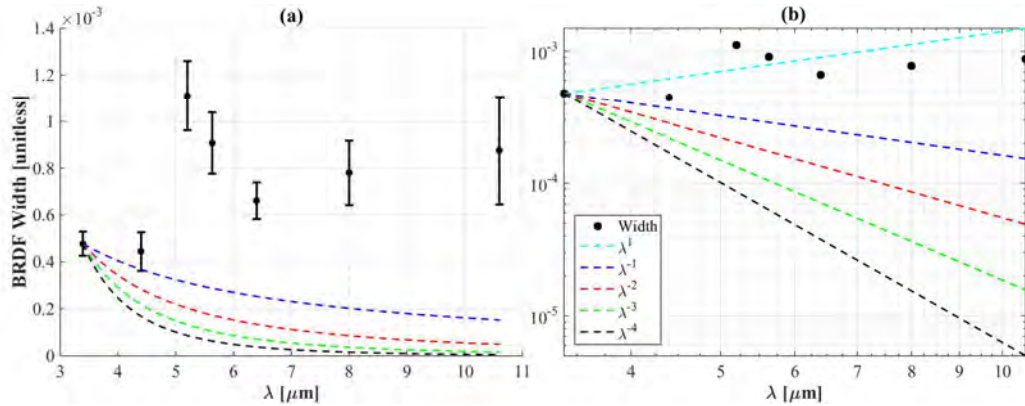


Figure 55. BRDF width versus λ for polished Ni in (a) linear space (with standard deviation), and (b) log-log space.

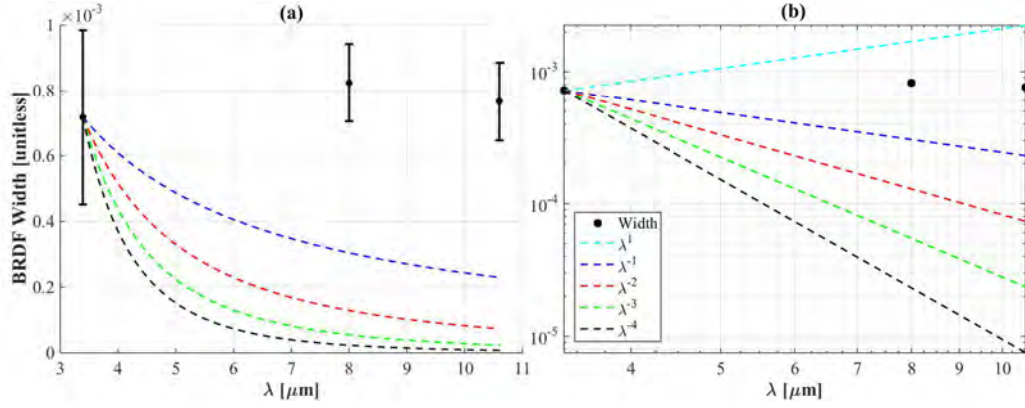


Figure 56. BRDF width versus λ for polished Al in (a) linear space (with standard deviation), and (b) log-log space.

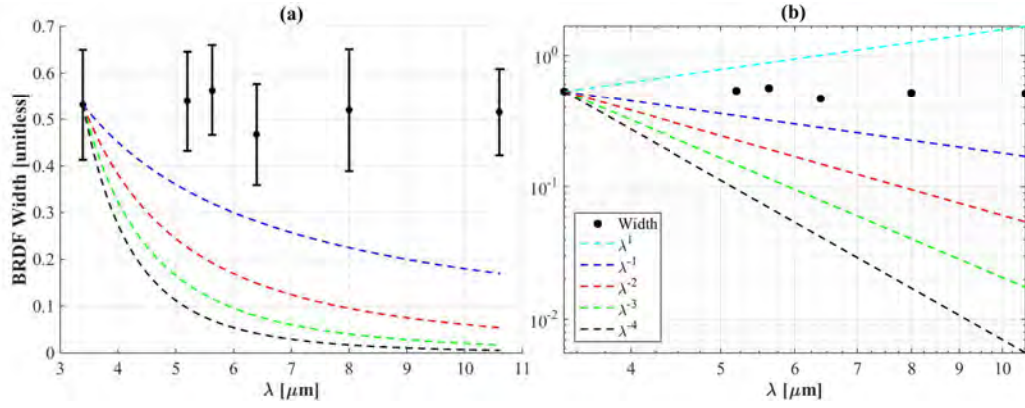


Figure 57. BRDF width versus λ for rough Al in (a) linear space (with standard deviation), and (b) log-log space.

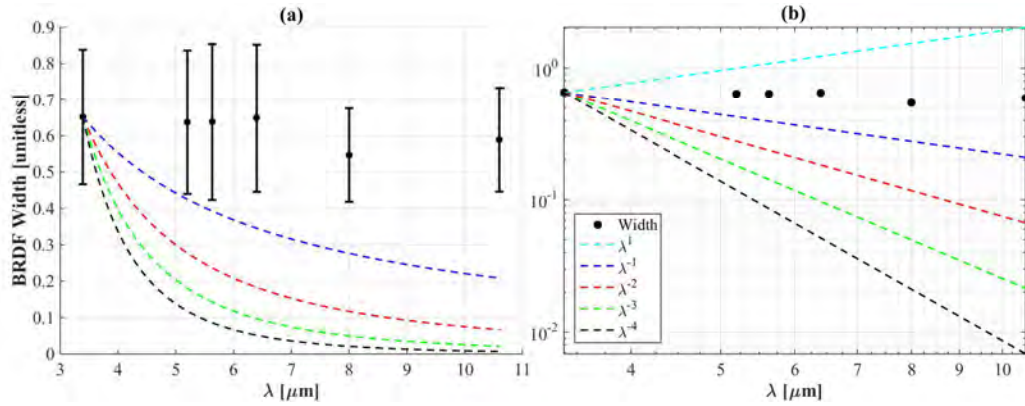


Figure 58. BRDF width versus λ for Infragold® in (a) linear space (with standard deviation), and (b) log-log space.

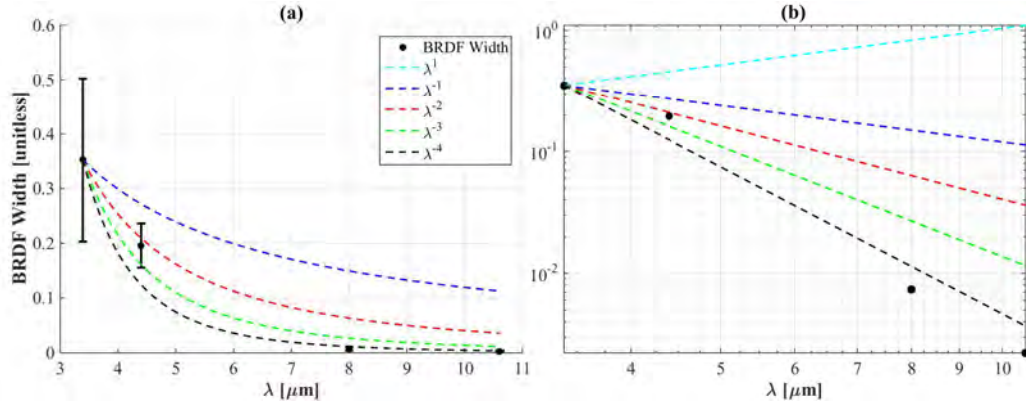


Figure 59. BRDF width versus λ for gray paint ($DE = 0$) in (a) linear space (with standard deviation), and (b) log-log space.

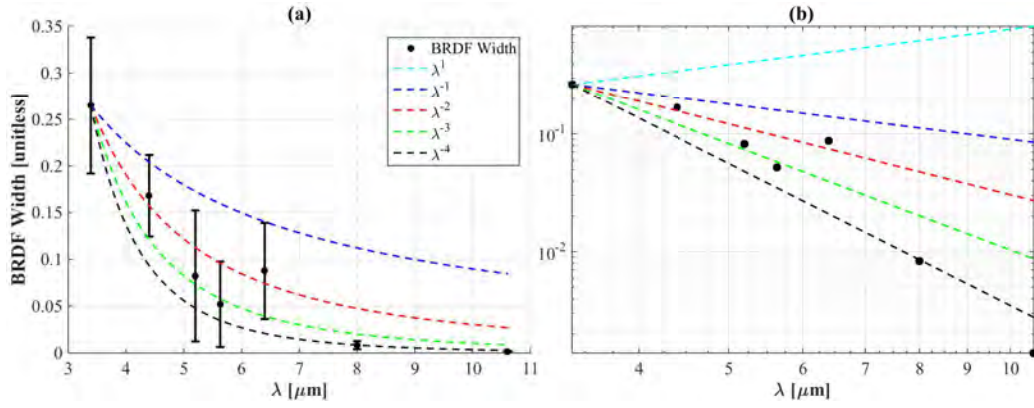


Figure 60. BRDF width versus λ for gray paint ($DE = 2.2$) in (a) linear space (with standard deviation), and (b) log-log space.

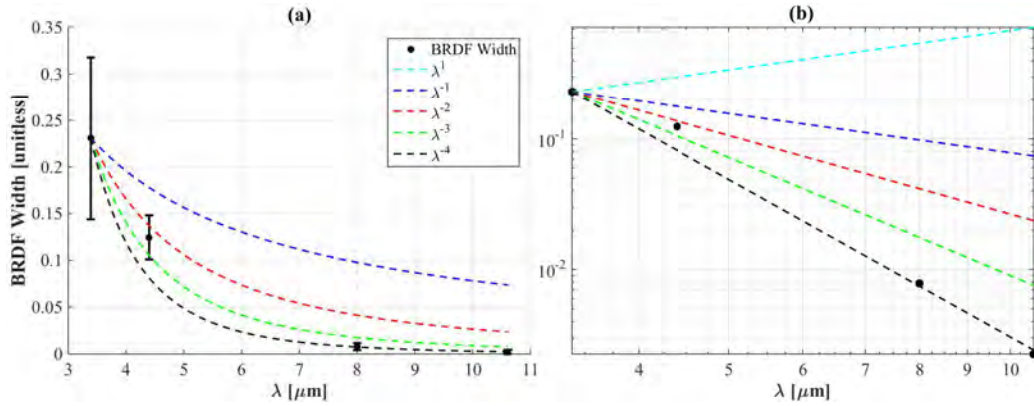


Figure 61. BRDF width versus λ for gray paint ($DE = 4.1$) in (a) linear space (with standard deviation), and (b) log-log space.

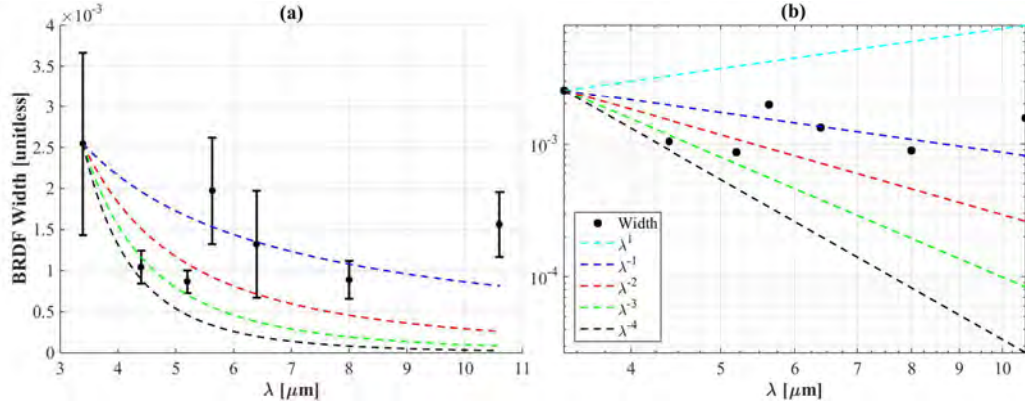


Figure 62. BRDF width versus λ for specular black paint in (a) linear space (with standard deviation), and (b) log-log space.

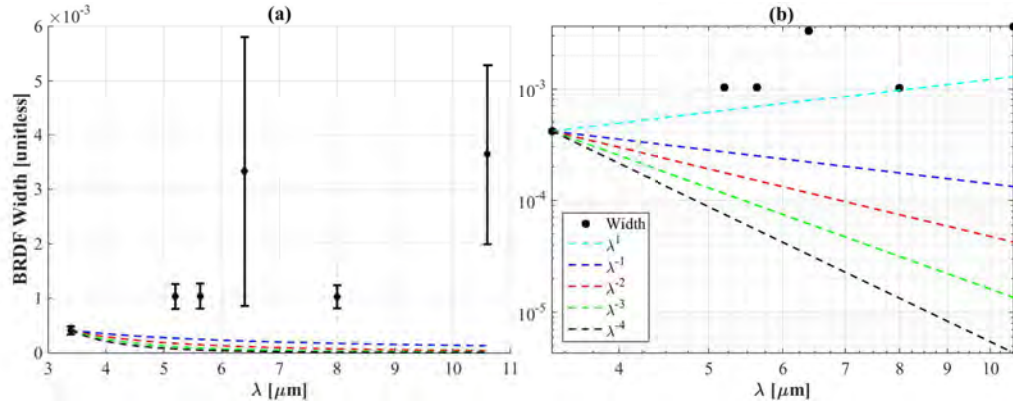


Figure 63. BRDF width versus λ for glass in (a) linear space (with standard deviation), and (b) log-log space.

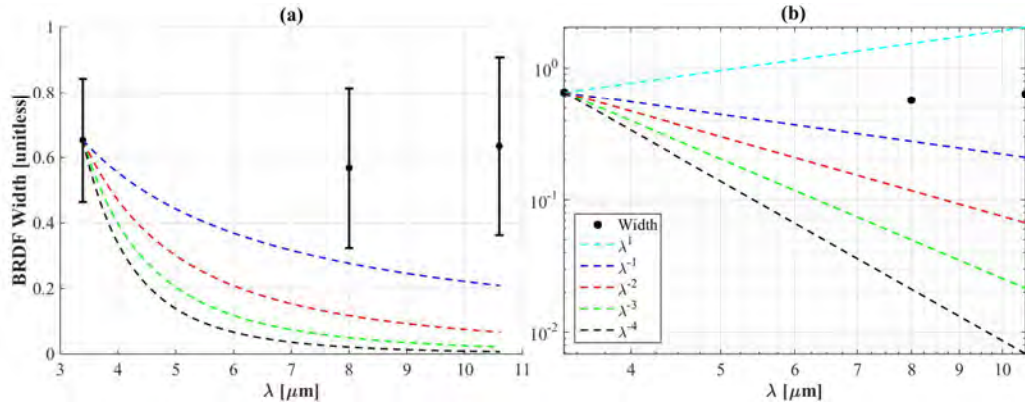


Figure 64. BRDF width versus λ for rough silver paint sample in (a) linear space (with standard deviation), and (b) log-log space.

at $3.39\ \mu m$, but it is within the standard deviation of the measurement, and thus not conclusive.) The very rough samples are also of relatively constant width, but instead of being a polished surface, these are very rough surfaces.

The same general results are present for the volume-reflecting samples. The three gray paint samples in Figures 59-61 are all varying approximately the same with wavelength. The BRDF width scaling is consistent at the wavelengths that were measured for all three samples. Consider, for example, the $\lambda = 4.4\ \mu m$ data points on these three plots, which are all close to the λ^{-2} line. Similarly, the $\lambda = 8.0\ \mu m$ data is close to the λ^{-4} line on all three plots, and the $\lambda = 10.6\ \mu m$ data is somewhat below the λ^{-4} line on all three plots. These results show consistency in the measurement and analysis, since the only difference between these samples is the DE value, which is a measure of weathering. Now consider the additional data points in Figure 60. It appears that this material is transitioning from a λ^{-2} dependence to a λ^{-4} dependence.

The black paint sample varies slowly with wavelength, and is specular at all wavelengths. The glass sample was also specular in BRDF at all wavelengths, although it was more difficult to align due to the multiple surface reflections. This difficulty in alignment, along with the significantly weak reflected signal of glass in the MWIR and LWIR, is likely the source of the large standard deviations in Figure 63 at 6.4 and $10.6\ \mu m$.

Much of this width analysis backs the intuition that the BRDF of a material becomes more specular as the wavelength increases, which is represented by a width that is inversely proportionate to wavelength. However, the analysis shows there is not a simple modification to the microfacet model to incorporate this wavelength dependence, which suggests there are fundamental flaws in the microfacet model in representing the BRDF width data. The next section illustrates from measured data what is observed in these microfacet models. Finally, the chapter ends with a

discussion of the BRDF height by analyzing the role of the cross section conversion term of the BRDF. Chapter VI then fleshes out a comparison between the microfacet model and a scalar wave optics model, forming a basis for future development of a closed-form spectral BRDF model.

Raw Wavelength-Dependent Data.

This section examines the raw unpolarized BRDF data at all wavelengths for a certain incident and scattered angle combination to determine what is happening with the raw BRDF data, particularly for samples exhibiting strong wavelength-dependent behavior.

Consider the grit-blasted Ni sample (average surface roughness $4.29 \mu m$) at $\theta_i = 40^\circ$, shown in Figure 65. In (a), the entire range of BRDF data is shown. Over this range, it appears the BRDF data is actually comprised of an overall broad base BRDF function, with a specular peak that begins to emerge from the data. In (b), the specular peak is zoomed in on, in linear space. This specular peak grows with wavelength (in general), with the exception of at $\lambda = 8.00 \mu m$ where the peak value appears to not be as large due to significant diffractive effects that can be seen near the peak. It appears that as wavelength increases, a peak emerges out of the overall broad shape of the BRDF data. This observation is consistent with Figures 32 and 33 presented at the beginning of the chapter. It is also observed in Figures 46 and 47 for the shot-blasted Ni sample, where there appeared to be a specular peak emerging from a broader underlying form in the BRDF data.

Physically, this effect can be understood by modeling the surface as a phase screen, where each element of the screen shifts the phase of the incident electromagnetic wave by a variable amount. When a surface is very rough (relative to the wavelength of light), the surface is adding a random phase offset, resulting in the relatively broad

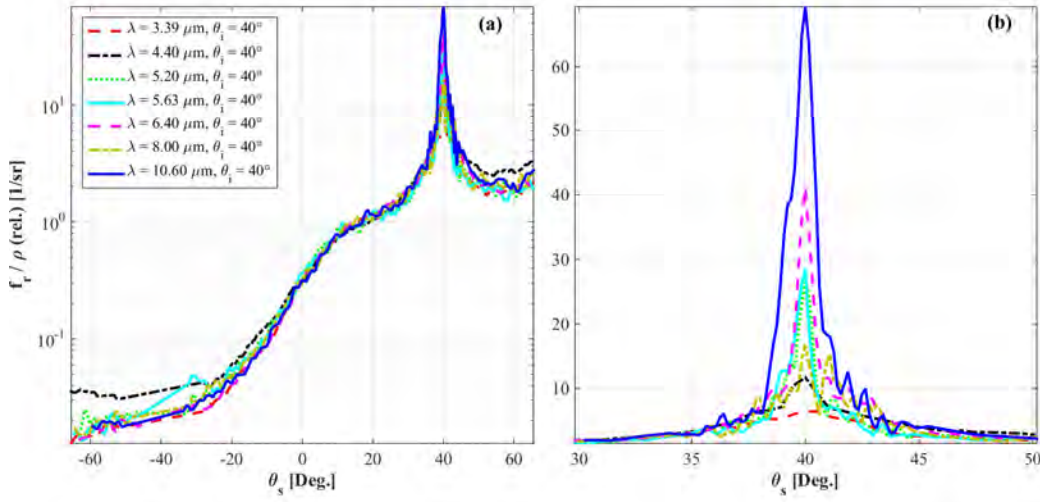


Figure 65. Raw BRDF data for grit-blasted Ni at $\theta_i = 40^\circ$ and all wavelengths, in (a) semilog space, and (b) linear space, zoomed at the peak.

structure in the BRDF data. However, as the wavelength approaches the surface roughness, the phase offset becomes less randomly distributed and diffractive effects become evident in two ways: oscillations in the BRDF data are observed due to diffraction, and a specular peak emerges due to the less randomly distributed phase offsets.

This observation suggests that the metric of BRDF width variation, shown in the previous section, may not be accurate in quantifying the BRDF width variation, simply because it emphasizes the specular peak rather than this bimodal shape that is primarily evident when viewed in log space. At some wavelengths (such as $3.39 \mu m$ in Figure 65), the BRDF width metric is measuring the width of the broad diffuse lobe. However, at higher wavelengths (such as $10.6 \mu m$ in Figure 65), the BRDF width metric is measuring the width of the narrow specular peak that has emerged from the data. Nickel is a surface-reflecting metallic sample that is resistant to oxidation, so the resulting effect is not expected to be due to volumetric scatter. Since the microfacet model does not distinguish between the overall broad shape of

the BRDF and the emergence of the specular peak, the failure of the width analysis to accurately predict the BRDF suggests a flaw in the microfacet model itself.

Considering the polished Ni sample in Figure 66, which is at $\theta_i = 40^\circ$, there is little variation in the BRDF data as a function of wavelength, as the specular peak in this sample has already emerged substantially. Diffractive features appear at all wavelengths, but the magnitude of the specular peak does not change significantly (in relative value) from one wavelength to the next, nor does the shape of the specular peak change significantly. It should be noted that the upper limit of the dynamic range of the CASI® system was reached when measuring this sample, so the specular peak of this sample may actually be higher than the reported value. A calibration scan performed during setup at each wavelength without a sample present resulted in a measured unpolarized BRDF value of around 10^6 sr^{-1} (although this value varied somewhat with wavelength). Away from the immediate peak, where instrument measurement limitation is not present, the BRDF data does appear to be declining from its peak value more slowly as wavelength increases. This is qualitatively consistent with the BRDF width analysis result, which showed a slow increase in width with wavelength overall. Furthermore, in Chapter VI, it is shown that this increase in overall width with wavelength is expected from a comparison of the microfacet BRDF model to a scalar wave optics model for a polished surface.

Note in Figure 66(b) that there is significant diffraction when the data is viewed on a logarithmic scale, although it is less pronounced with the 5.20 and 5.63 μm lasers. These diffractive peaks are expected to occur due to the machining process used to create the sample. The lack of well-defined peaks at 5.20 and 5.63 μm (which were both measured using the same QCL) suggest the BRDF data may be somewhat degraded at those wavelengths due to the quality of that particular QCL. This observation is additionally supported by Figure 55 where the width at 5.20 and

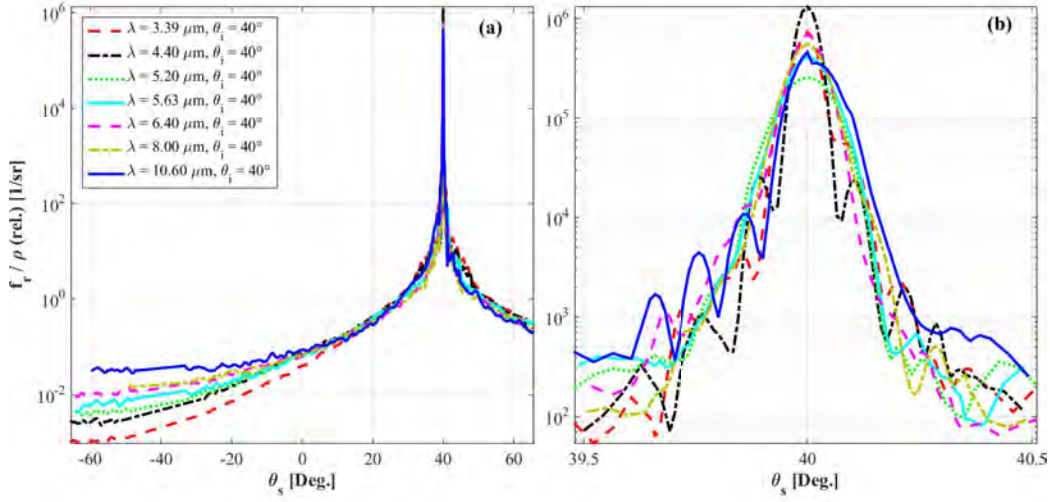


Figure 66. Raw BRDF data for polished Ni at $\theta_i = 40^\circ$ and all wavelengths, for (a) all angles, and (b) zoomed at the peak.

5.63 μm appear to be outliers.

Finally, for a rough sample, such as the AFIT Infragold® sample, the BRDF does not exhibit a significant wavelength variation; see Figure 67. Here, there is no significant specular peak, and the data is quite consistent from one wavelength to the next. Thus, the rough sample BRDF data appeared to not suffer from a deficiency in the BRDF width data analysis performed previously.

This raw data examination suggested that the BRDF width analysis performed previously to determine if there was an unknown microfacet distribution function may not be appropriate for materials where surface roughness is on the order of a wavelength, due to the bimodal nature of the BRDF data for these materials when viewed in log space. However, it does illustrate a fundamental flaw with the microfacet BRDF model, in which the microfacet distribution function is incapable of describing a BRDF peak which appears to be comprised of a sum a diffuse BRDF (due to random phasing that masks diffractive effects) and a specular peak, such as in Figure 65.

From the results in this chapter, it is observed that there are deficiencies with

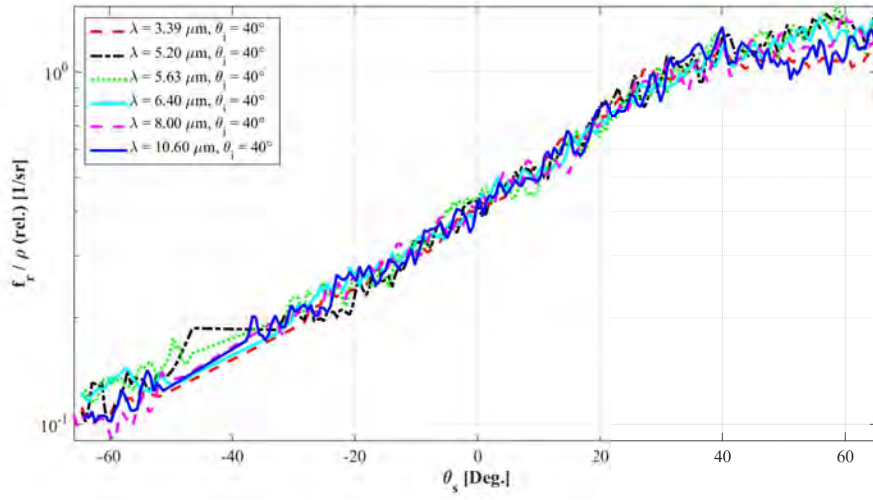


Figure 67. Raw BRDF data for Infragold® at $\theta_i = 40^\circ$ and all wavelengths.

the microfacet BRDF model. In Chapter VI, a connection between the microfacet model and scalar wave optics models is made to outline an approach to hone in on this problem, and to answer the question of when the microfacet model does work. However, prior to concluding this analysis of raw BRDF data, the role of one of the key elements of a microfacet model, the cross section conversion term, is examined using this experimental data; that subject is addressed in the next section.

5.4 BRDF Magnitude at Specular Peak

The magnitude of the BRDF at the specular peak changes with incident angle as well, as can be seen the BRDF data plots in this chapter. Moving to direction cosine space does not alter any of the BRDF magnitude data. In the microfacet model, it appears the cross section conversion term, σ , provides a scaling that captures this inherent height variation. Recall from Equation (37) that this scaling is given as $\sigma = (4 \cos \theta_i \cos \theta_s)^{-1}$. This section investigates whether the angular variation in σ provides that approximate scaling; much of this section is taken from [8].

BRDF data for a grit-blasted nickel sample at $\lambda = 3.39 \mu m$ illustrating the overall

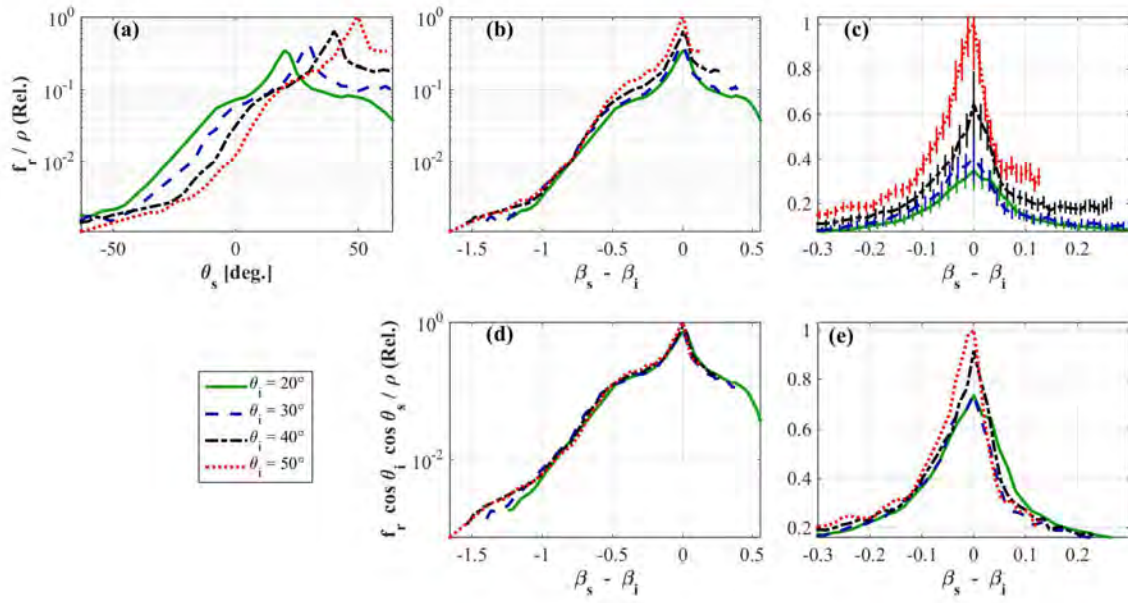


Figure 68. Grit-blasted nickel BRDF at $3.39 \mu\text{m}$ in (a) real space, (b) $\Delta\beta$ space, (c) zoomed at peak (with error bars), (d) scaled by $1/\sigma$, (e) scaled and zoomed at peak. All plots are relative to the peak at $\theta_i = 50^\circ$ and divided by DHR.[8]

process is shown in Figure 68. Unlike prior plots in this chapter, the BRDF data in this section has been scaled by the peak of the BRDF data at 50° ; *i.e.*, the peak of the BRDF data at 50° is set to 1, and all other data points are relative to that point. In Figure 68(a), the in-plane BRDF data for four different incident angles is shown in angular coordinates. Figure 68(b) is the same data transformed to direction cosine space, and (c) zooms in on the peak of the data to more clearly illustrate the scaling issue. In Figure 68(d) and (e), the direction cosine plot is scaled by $1/\sigma$, where (e) is again zoomed in on the peak. This $1/\sigma$ scaling results in a closer match for these incident angles near the peak.

Extending this analysis to other surface-reflecting materials, Figure 69 compares the peaks of the measured BRDFs at $3.39 \mu\text{m}$ for shot-blasted nickel, polished nickel, and polished aluminum, and Fig. 70 contains data for grit-blasted nickel, shot-blasted nickel, and polished nickel at $\lambda = 10.6 \mu\text{m}$. The difference in the scaling is again quite

Table 5.2. Norm of difference in BRDFs for each material measured. BRDF is scaled by weight functions w given by each column header (“Raw” indicates no scaling.)

$\lambda = 3.39 \mu m$	Raw [1/sr]	$\cos \theta_i$ [1/sr]	$\cos \theta_s$ [1/sr]	$1/\sigma$ [1/sr]
Grit-blasted Ni	0.0437	0.0214	0.0210	0.00847
Shot-blasted Ni	0.0194	0.00879	0.00873	0.00288
Polished Ni	1190	619	619	276
Polished Al	2300	1390	1390	900
$\lambda = 10.6 \mu m$				
Grit-blasted Ni	0.285	0.194	0.194	0.135
Shot-blasted Ni	0.0831	0.0551	0.0552	0.0504
Polished Ni	1110	612	612	311
Polished Al	1170	608	608	282

noticeable, particularly near the peaks.

To quantify this result, Table 5.2 lists the norm of the difference between the BRDF at all measured angles and the BRDF at $\theta_i = 40^\circ$, scaled by one of three weight functions w : $\cos \theta_i$, $\cos \theta_s$, and $1/\sigma$. The “Raw” column indicates no scaling ($w = 1$). This norm is computed as

$$\begin{aligned}
& ||w_1 f_r(\theta_{i1}, \theta_{s1}) - w_2 f_r(40^\circ, \theta_{s2})|| = \\
& \frac{1}{N} \left(\sum_{\theta_{i1}} \sum_{\theta_{s2}} [w_1 f_r(\theta_{i1}, \theta_{s1}) - w_2 f_r(40^\circ, \theta_{s2})]^2 \right)^{1/2}, \tag{140}
\end{aligned}$$

where

$$\begin{aligned}
\theta_{s1} &= \sin^{-1} [\sin 40^\circ - \sin \theta_{s2} + \sin \theta_{i1}] \\
&= \sin^{-1} [\Delta\beta(40^\circ, \theta_{s2}) + \sin \theta_{i1}],
\end{aligned}$$

chosen such that $\Delta\beta(\theta_{i1}, \theta_{s1}) = \Delta\beta(40^\circ, \theta_{s2})$, referred to below as $\Delta\beta$. $w_1 = w(\theta_{i1}, \theta_{s1})$ and $w_2 = w(40^\circ, \theta_{s2})$ are the same weighting function w evaluated at the appropriate (θ_i, θ_s) coordinates. N is the number of data points in the sum and does not depend on the weighting function. (For example, at $\lambda = 10.6 \mu m$, for grit-blasted Ni, $N = 573$; shot-blasted Ni, $N = 576$; polished Ni, $N = 988$; polished Al, $N = 951$. For

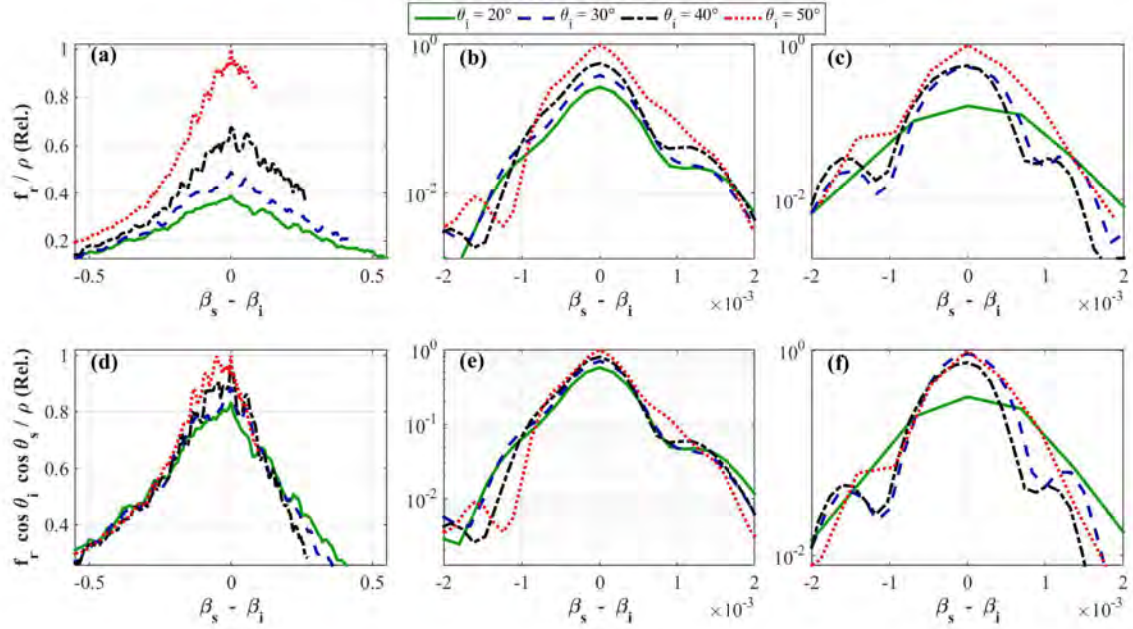


Figure 69. Comparison between peak BRDF values in (a,b,c) direction cosine space and (d,e,f) $1/\sigma$ scaled direction cosine space for: (a,d) shot-blasted nickel; (b,e) polished nickel; (c,f) polished aluminum at $\lambda = 3.39 \mu\text{m}$. All plots are relative to the peak at $\theta_i = 50^\circ$, and are divided by DHR to account for variation in reflectance.[8]

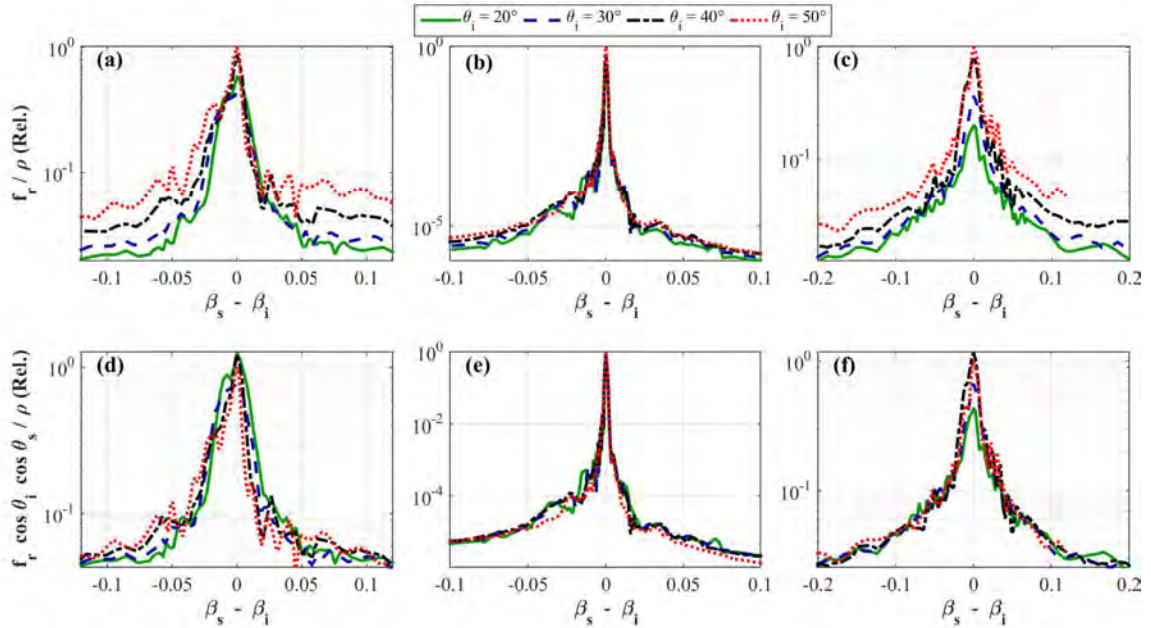


Figure 70. Comparison between peak BRDF values in (a,b,c) direction cosine space and (d,e,f) $1/\sigma$ scaled direction cosine space for: (a,d) shot-blasted nickel; (b,e) polished nickel; (c,f) grit-blasted nickel at $\lambda = 10.6 \mu\text{m}$. All plots are relative to the peak at $\theta_i = 50^\circ$, and are divided by DHR to account for variation in reflectance.[8]

$\lambda = 3.39 \mu m$, values of N are similar. The value of N is independent of weight function.) $\theta_{i1} = \{20^\circ, 30^\circ, 40^\circ, 50^\circ\}$ are the incident angles measured. For example, at specular ($\Delta\beta = 0$), the difference between the BRDF at $(\theta_{i1} = 50^\circ, \theta_{s1} = 50^\circ)$ and the BRDF at $(40^\circ, \theta_{s2} = 40^\circ)$ is computed; similarly, away from specular (e.g., $\Delta\beta = 0.2$), the difference between the BRDF at $(\theta_{i1} = 20^\circ, \theta_{s1} = 32.8^\circ)$ and the BRDF at $(40^\circ, \theta_{s2} = 57.4^\circ)$ is computed; this is done at all angles for which data was collected in the domain $|\Delta\beta| < 0.5$. All entries in Table 5.2 are in BRDF units ($1/sr$). In all cases, the norm of the difference in BRDF is lower when using the $1/\sigma$ scaling; in many cases, the improvement is substantial.

5.5 Experimental Data Conclusions

A few conclusions can be drawn from the results presented in this chapter. First, there is not likely to be a closed-form microfacet distribution function that can have its width varied by a fixed power of wavelength to provide an accurate wavelength scaling for a wide class of materials. This conclusion is supported by the difficulty of the microfacet fit process, along with the wide variety in BRDF width as a function of wavelength in the raw data analysis. Additionally, if a surface is very rough, there is not likely to be a wavelength dependence in that region. There may possibly be an approximately linear *increase* in BRDF width as a function of wavelength for a highly polished surface, as was noticed in Figure 55. Recalling what was noted when performing BRDF fits, the microfacet model was a better fit for rougher BRDF samples than it was for polished BRDF samples, suggesting there may be other changes in the BRDF of a polished surface not captured by the microfacet model.

From the magnitude comparison and the experimental results described in [8], it appears the cross section conversion term approximately accounts for the magnitude variation in the BRDF data collected. This result presented in [8] further suggests

that there is a connection between the microfacet distribution function space and direction cosine space, since data was plotted in terms of $\Delta\beta$ to align data measured at different incident angles as well as to perform the magnitude alignment. This begins to suggest a possible connection between the microfacet BRDF model and a scalar wave optics BRDF model.

Taking these results as a whole, if progress is to be made on inserting a more reliable wavelength dependence into a closed-form microfacet BRDF, it is necessary to further advance BRDF theory, and in particular to better understand the connection between microfacet BRDF models and scalar wave optics BRDF models. This connection is developed in detail in Chapter VI.

VI. Theoretical Results

In Chapter III, microfacet BRDF models that are commonly used in computer graphics, remote sensing, and scene generation are examined in detail. However, when applying BRDF models to wavelength-sensitive applications such as HSRS, the wavelength dependent behavior of the BRDF becomes of primary importance. Chapter III showed a deficiency in the wavelength dependent behavior of the BRDF observed using BRDF data from the NEF database and the MERL database. Chapter IV took a brief detour to discuss measurement approach to flesh out the rest of the background required to understand this chapter and to quantify uncertainty in the BRDF measurements. After collecting and analyzing BRDF data for even simple surface-reflecting samples such as nickel in Chapter V, it became apparent that the closed-form microfacet BRDF models do not perform well as a material transitions from highly diffuse to highly specular. Furthermore, it became clear from analysis of the raw data that the problem is not simply limited to development of a different microfacet distribution function, but rather that there is not an apparent fixed wavelength scaling in the way the microfacet model interprets the BRDF, and that up to now there is not a clear connection between microfacet BRDF models and scalar wave optics BRDF models that would facilitate the ability to address these deficiencies in a physics-based manner.

This chapter examines the microfacet model compared to scalar wave optics model to understand the flaws in the microfacet model and develop a novel connection to scalar wave optics theory. The cross section conversion term σ in the microfacet model has a flaw discussed briefly in Chapter III in that it diverges as the BRDF approaches grazing angles. This flaw is compensated for by inclusion of a shadowing and masking term G , but that term is typically developed from a geometric optics perspective, whereas the BRDF is fundamentally a physical optics scattering problem. However,

as examined at the end of Chapter V, the cross section conversion term performs an important function of scaling the BRDF magnitude in direction cosine space with incident angle.

To determine how to better accommodate for the deficiencies noted in Chapter V, and to understand from whence terms unique to microfacet BRDF models such as the cross section conversion and the $\tan \theta_h$ distribution function dependence arise, this chapter compares the microfacet model to linear systems models of the BRDF in detail. The MBK BRDF model is described briefly at the end Chapter III. From that discussion, the polished and rough surface approximations of the MBK model is compared to the microfacet model in a novel manner that has not been done in prior literature[10]. This comparison is crucial because it provides an understanding of: what the microfacet model actually represents, how to modify a microfacet BRDF to remove the cross section conversion term, how to modify the microfacet model as a surface becomes more smooth, and how to connect microfacet coordinates to linear systems coordinates. Additionally, many of the results obtained from the purely theoretical analysis to be performed in this chapter are found to have been observed in Chapter V, further validating the conclusions arrived at in this chapter. Finally, at the end of this chapter, rough surface BRDF data are fitted to a novel BRDF function in a manner that fits data better than the original microfacet BRDF models, and avoids the difficulty of a cross section conversion term, while not adding any additional fitting parameters to the computation. The substitution is generic enough to apply to any BRDF model that currently uses the Fresnel equation F .

This discussion is largely based on a paper submitted to Optics Express [10], and based in part on a conference paper in [7]. The theoretical developments in this chapter, and the observations that are tied to the experimental data collected in Chapter V, represent a novel contribution to the theoretical modeling of the BRDF.

6.1 Comparing Microfacet and Scalar Wave Optics Models

To compare the microfacet model to the MBK model, the ratio of the microfacet BRDF to the MBK BRDF is taken in both the very rough approximation and the smooth surface approximation, assuming an isotropic sample. Additionally, assume surface statistics (surface height and autocorrelation length) follow a Gaussian distribution, as this is required to arrive at a closed-form expression for the MBK model.

Recall from Chapter III that the GHS scalar wave optics BRDF model reduces to the MBK model in the limit of a polished or very rough surface. The MBK model is presented in Equation (113) in the form of an ASF, which can be multiplied by the polarization factor Q given by Equations (100)-(104) to convert it to a BRDF; this polarization factor Q is a perturbed version of the Fresnel equation for surfaces that are not infinitely smooth. In limiting cases of a polished or very rough surface, the summation can be written as a single term only.

First, consider a polished surface; $\sigma_s \ll \lambda$ and as such only the $m = 1$ term of the sum in Equation (113) is significant. Recall that g was defined in Equation (110) to be related to σ_s/λ . In [37], Krywonos defines a smooth surface as $g(\theta_i, \theta_s) < 0.025$, which results in less than 1% error compared to the infinite series summation when $\theta_i \leq 70^\circ$. Assuming Gaussian surface statistics (surface height σ_s and correlation length l_c), the polished surface MBK BRDF model is given as [37, 38]

$$f_p = \frac{4\pi^3 l_c^2 \sigma_s^2 Q (\cos \theta_i + \cos \theta_s)^2}{\lambda^4} \exp \left[- \left(\frac{\pi l_c \eta_r}{\lambda} \right)^2 \right], \quad (141)$$

where $\exp(-g) \approx 1$ since $\sigma_s \ll \lambda$ for a polished surface, and $K \approx 1$ for a polished surface, as shown in [38]. As a reminder, η_r represents the angular dependence in direction cosine space, given by Equation (99).

Similarly, the very rough surface approximation to MBK can be written as [37, 30]

$$f_{vr} = \frac{KQl_c^2}{4\pi\sigma_s^2(\cos\theta_i + \cos\theta_s)^2} \exp \left[- \left(\frac{l_c}{2\sigma_s} \right)^2 \left(\frac{\eta_r}{\cos\theta_i + \cos\theta_s} \right)^2 \right], \quad (142)$$

where again the polarization factor Q is used to convert the ASF to a BRDF, and Equations (99) and (110) are also used. In [37], Krywonos defines very rough as $g(\theta_i, \theta_s) > 800$, to result in less than 1% maximum error as compared to the infinite summation when $\theta_i \leq 70^\circ$.

In [38, 63], careful measurements of material surface statistics were made by Stover. The measured surface statistics were used to compute the Power Spectral Density (PSD) of each surface. Stover then measured the BRDF of these surfaces. The GHS BRDF model was used to compute the PSD from the BRDF data. The computed PSD using GHS theory closely matched the measured surface statistics of the surfaces. Since GHS matches MBK in the very rough or very smooth approximation, f_p and f_{vr} from MBK theory are considered to be accurate physical models in the limit of a polished or very rough surface, respectively.

Let f_μ represent the microfacet model BRDF. Since MBK theory can be used to predict accurate surface statistics, the ratios f_μ/f_p and f_μ/f_{vr} would equal 1 if the microfacet model also modeled physical truth. Differences from 1 indicate deviations in the microfacet model from the more physical MBK model, and may suggest how to alter the microfacet model to improve its accuracy while still maintaining a closed-form approximation to the BRDF. Since the scalar wave optics BRDF does not distinguish between surface reflection and volumetric scattering, this analysis is helpful in understanding the surface reflection terms of the BRDF.

Very Rough Surface Comparison.

The ratio of the microfacet BRDF f_μ to the very rough surface MBK BRDF f_{vr} is

$$\frac{f_\mu}{f_{vr}} = \left(\frac{\rho_s}{2K}\right) \left(\frac{2FG}{Q}\right) \left(\frac{(\cos \theta_i + \cos \theta_s)^2}{4 \cos \theta_i \cos \theta_s \cos^4 \theta_h}\right) \left(\frac{\sigma_s \sqrt{2}}{l_c \sigma_g}\right)^2 \times \exp \left[- \left(\frac{\tan^2 \theta_h}{2\sigma_g^2} - \frac{l_c^2}{4\sigma_s^2} \frac{\eta_r^2}{(\cos \theta_i + \cos \theta_s)^2} \right) \right]. \quad (143)$$

The exponential term is analyzed first. The angular dependence is contained in two terms: $\tan^2 \theta_h$ from the microfacet model and $\eta_r^2/(\cos \theta_i + \cos \theta_s)^2$ from MBK. Although these terms were derived with a completely different physical interpretation (geometric optics versus physical optics), these terms are shown here to be equal at all incident and scattered angles, in-plane and out-of-plane. Starting with Equation (35) and using basic trigonometry identities to rewrite $\cos \theta_h$ in terms of $\tan \theta_h$,

$$\tan^2 \theta_h = \frac{4 \cos^2 \theta_d - (\cos \theta_i + \cos \theta_s)^2}{(\cos \theta_i + \cos \theta_s)^2}. \quad (144)$$

The denominator already matches the denominator of $\eta_r^2/(\cos \theta_i + \cos \theta_s)^2$, so it is sufficient to show that the numerator equals η_r^2 as given by Equation (99). This is performed by use of the double angle formula for $\cos(2\theta_d)$ and adding zero:

$$\begin{aligned} 4 \cos^2 \theta_d - (\cos \theta_i + \cos \theta_s)^2 &= 2 + 2(2 \cos^2 \theta_d - 1) - (\cos \theta_i + \cos \theta_s)^2 \\ &= 2 + 2 \cos 2\theta_d - (\cos \theta_i + \cos \theta_s)^2 \\ &= \sin^2 \theta_i + \cos^2 \theta_i + \sin^2 \theta_s + \cos^2 \theta_s + 2 \cos 2\theta_d - (\cos \theta_i + \cos \theta_s)^2 \\ &= \sin^2 \theta_i + \sin^2 \theta_s + 2 \sin \theta_i \sin \theta_s \cos \phi_s = \eta_r^2, \end{aligned} \quad (145)$$

where in the last line, Equation (34) was used to obtain η_r^2 . Thus, linear systems

direction cosine space for a very rough surface was shown to be exactly equal to the geometric microfacet model bisector space:

$$\tan^2 \theta_h = \left(\frac{\eta_r}{\cos \theta_i + \cos \theta_s} \right)^2. \quad (146)$$

Note that this function can result in any value in the range $[0, \infty)$. This result will become important in contrast to the polished surface result.

From geometric optics σ_g is commonly thought of as the Gaussian width of the probability distribution of microsurface normals. Mathematically, the microfacet surface normals can be calculated from the surface height profile and is related to the normal to the derivative of the surface height profile; however, only the probability distribution of the surface profile is known. Instead, Equation (143) can be solved for σ_g for a very rough surface using the remaining terms in the exponential, obtaining

$$\sigma_{g, vr} = \frac{\sigma_s \sqrt{2}}{l_c}. \quad (147)$$

Recall σ_s represents the width of the Gaussian in the vertical (height) direction and l_c represents the width of the Gaussian in the horizontal (correlation length) direction. This result is identical to the result obtained in the Hyde polarized BRDF model's parameterization of the Gaussian distribution given in [33] that was derived using the Method of Moments, suggesting the methodology employed in this comparison is correct. However, Equation (147) only holds for the very rough surface approximation. A different result for the polished surface analysis is obtained later in the chapter in Equation (153), showing this interpretation of σ_g is only valid for very rough surfaces, and is not true in general. This point is discussed in more depth after comparing the polished surface approximation to the microfacet model.

Although it may be tempting to conclude that the BRDF width should have no

wavelength dependence from this result, keep in mind the very rough approximation is only valid for $g > 800$, and that $g \propto (\sigma_s/\lambda)^2$. As λ increases, the very rough approximation becomes invalid.

Equation (143) has now simplified to

$$\frac{f_\mu}{f_{vr}} = \left(\frac{\rho_s}{2K}\right) \left(\frac{2FG}{Q}\right) \left(\frac{(\cos \theta_i + \cos \theta_s)^2}{4 \cos \theta_i \cos \theta_s \cos^4 \theta_h}\right). \quad (148)$$

Direct comparisons between Q and F vary significantly in magnitude. Stover explains the s polarization, but does not suggest an approximation valid at all angles and indices of refraction for the p polarization (and thus the unpolarized term $Q = Q_s + Q_p$), although he does present approximations for a few limiting cases [62]. To improve on this understanding, the polarization factor Q is analyzed from the perspective of comparing it to not only Fresnel reflectance, but also the remaining angular terms from the microfacet model, since the microfacet model uses F instead of Q .

Reference [7] shows, for in-plane angles, there is an approximate relationship S between the unpolarized Fresnel reflectance and the polarization factor, Q , given as

$$S = \frac{4 \cos \theta_i \cos \theta_s \cos^4 \theta_h}{(\cos \theta_i + \cos \theta_s)^2} \approx \frac{2F}{Q}, \quad (149)$$

where the factor of 2 arises from $Q = Q_s + Q_p = F_s + F_p = 2F$ if $\theta_i = \theta_s$ and $\phi_s = 180^\circ$ (standard Fresnel reflection).

In [7], this relationship for S was observed to be valid when θ_i and θ_s are small; those results are discussed here. Consider the BRDF in-plane. The ratio $2F/Q$ was plotted along with the novel S approximation presented in Equation (149) in Figure 71 for $\tilde{n} = 4.0605 + 12.497i$ (Ni at $3.39 \mu m$), and in Figure 72 for $\tilde{n} = 1.4091$ (Fused Silica at $3.39 \mu m$), to illustrate two cases with significantly different indices of refraction. Each figure is a function of θ_s , with each plot representing the in-plane

slice of $2F/Q$ and S at a different incident angle in 15° increments.

In the analysis in [7] and presented above, only in-plane data was plotted, and only at two incident angles. This plot will now be extended to all angles in the hemisphere using the relative difference for out-of-plane data, where the relative difference is defined as

$$R_d = \frac{|2F/Q - S|}{2F/Q}. \quad (150)$$

Figure 73 shows results at $\theta_i = (15^\circ, 30^\circ, 45^\circ, 60^\circ)$ for five different indices of refraction. The five different indices of refraction are chosen to represent a wide range of materials: high n and high κ : $\tilde{n} = 4 + 10i$; low n and low (but nonzero) κ : $\tilde{n} = 1.5 + i$, low n and zero κ : $\tilde{n} = 1.4$, moderate n and κ : $\tilde{n} = 1.7 + 5i$, and $n < 1$: $\tilde{n} = 0.25 + 3i$. When $\theta_i = \theta_s$ and $\phi_s = 180^\circ$ (specular reflection), $R_d = 0$. In general, even out-of-plane, the error is relatively small if θ_i and θ_s are both small, but increases when either θ_i or θ_s is large. This result suggests that the cross section conversion term $\sigma(\theta_i, \theta_s)$ in Equation (37) and the microfacet distribution normalization $1/\cos^4 \theta_h$ in Equation (44) both arise from using F instead of Q , and that the deviation at large angles is due to excluding the geometric attenuation, G .

Since BRDF is fundamentally a physical optics problem and not a geometric optics problem, better approximations for G could be derived by solving $2FG/Q = S$ for G instead of from the geometric optics approach detailed in [32]; such a solution is beyond the scope of this dissertation, but is suggested for future work. Alternatively, Q does have a closed-form solution (although it is substantially more complex than F). For increased accuracy, $Q/2$ could be used in place of F using this observed relationship; this approach is explored at the end of this chapter. Although Q was derived for polished surfaces, this result suggests Q is still a better approximation than F for very rough surfaces. This novel result is used at the end of this chapter

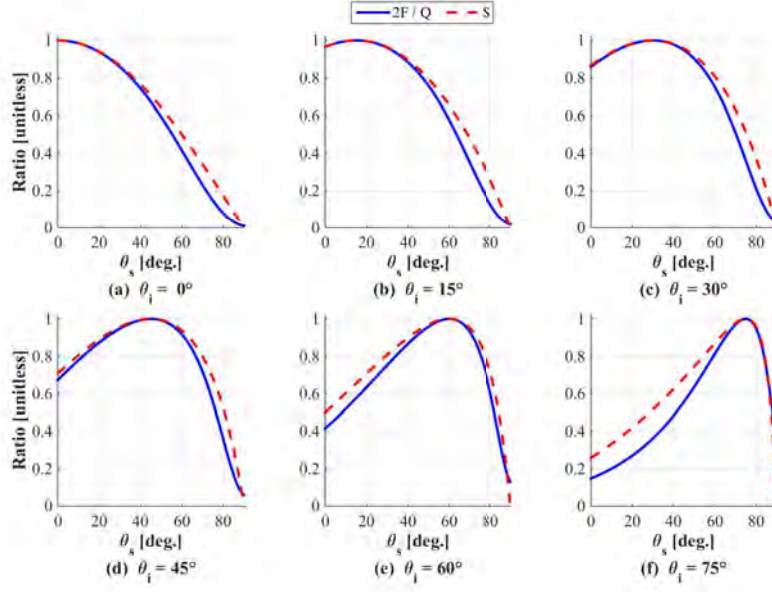


Figure 71. Comparison of the ratio of $2F(\theta_d)/Q(\theta_i, \theta_s)$ and S for Nickel at $\lambda = 3.39 \mu m$ ($\tilde{n} = 4.0605 + 12.497i$)[54] with incident angles of: (a) $\theta_i = 0^\circ$, (b) $\theta_i = 15^\circ$, (c) $\theta_i = 30^\circ$, (d) $\theta_i = 45^\circ$, (e) $\theta_i = 60^\circ$, and (f) $\theta_i = 75^\circ$. [7]

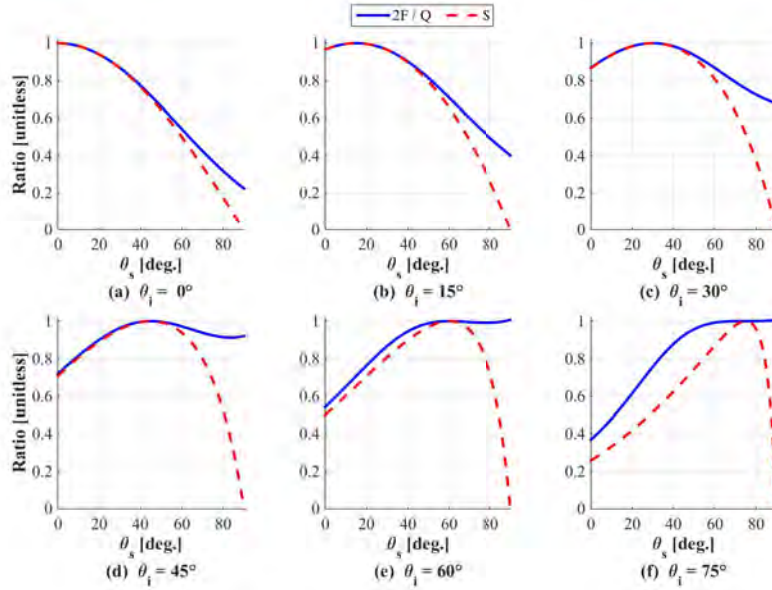


Figure 72. Comparison of the ratio of $2F(\theta_d)/Q(\theta_i, \theta_s)$ and S for fused silica at $\lambda = 3.39 \mu m$ ($\tilde{n} = 1.4091$)[40] with incident angles of: (a) $\theta_i = 0^\circ$, (b) $\theta_i = 15^\circ$, (c) $\theta_i = 30^\circ$, (d) $\theta_i = 45^\circ$, (e) $\theta_i = 60^\circ$, and (f) $\theta_i = 75^\circ$. [7]

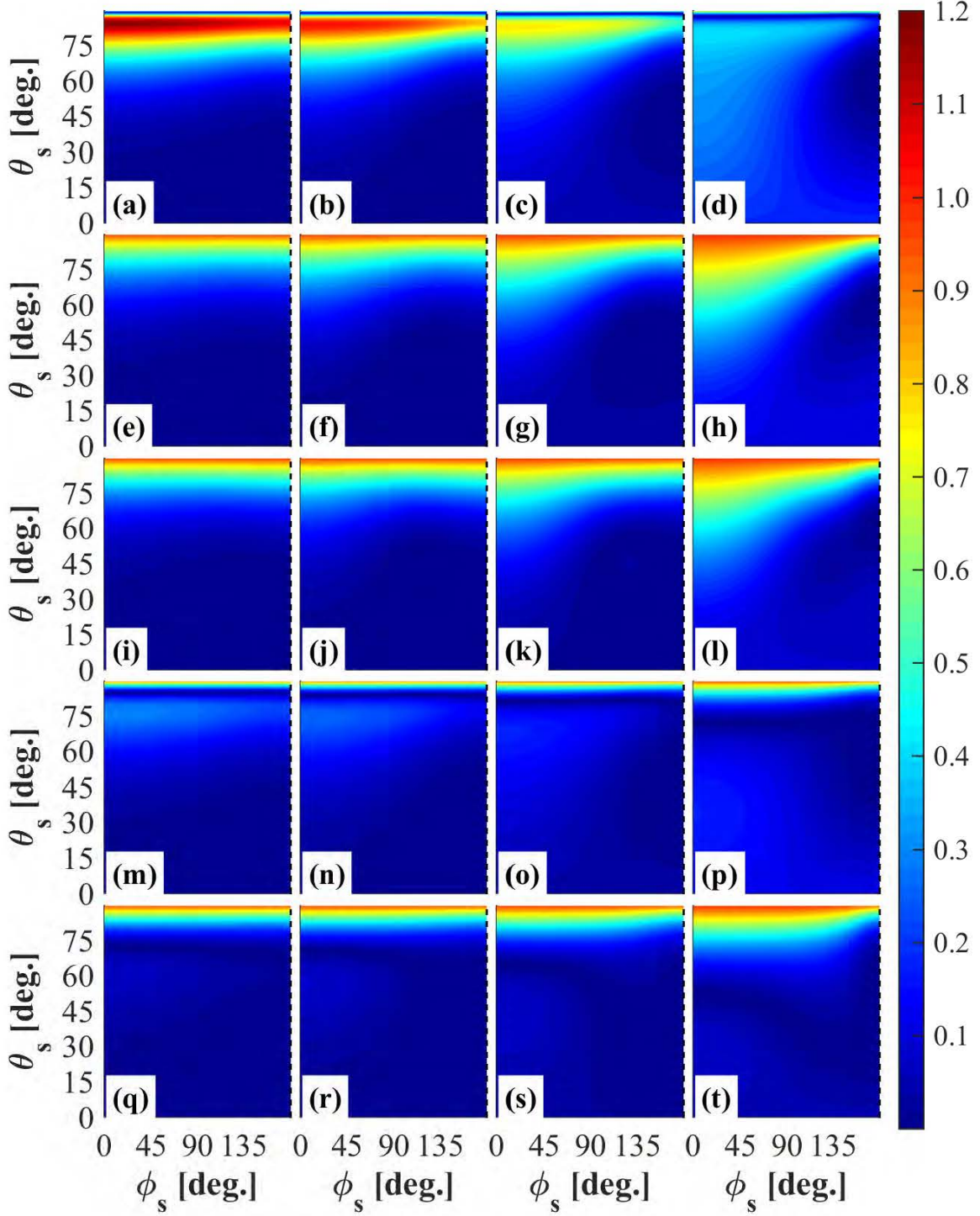


Figure 73. Surface plot of relative difference R_d for four different indices of refraction: (a-d) $\tilde{n} = 4 + 10i$, (e-h) $\tilde{n} = 1.5 + 1i$, (i-l) $\tilde{n} = 1.4$, (m-p) $\tilde{n} = 1.7 + 5i$, (q-t) $\tilde{n} = 0.25 + 3i$. For each index, four different incident angles are plotted: (a,e,i,m,q) $\theta_i = 15^\circ$; (b,f,j,n,r) $\theta_i = 30^\circ$; (c,g,k,o,s) $\theta_i = 45^\circ$; (d,h,l,p,t) $\theta_i = 60^\circ$. The plots are all symmetric about $\phi_s = 180^\circ$. The dotted black line at $\phi_s = 180^\circ$ on the right side of each plot represents in-plane scatter. In each case, $R_d = 0$ when $\theta_i = \theta_s$ and $\phi_s = 180^\circ$; R_d is generally small when θ_i and θ_s are small.

to replace the cross section conversion term, microfacet normalization, and geometric attenuation with Q , improving the fit quality of the BRDF to rough surfaces without adding any additional fitting parameters to microfacet BRDF models.

Polished Surface Comparison.

For the polished surface comparison, the analysis follows the same procedure as above, except using f_p in place of f_{vr} . This analysis is first performed in [7] for GHS, but is altered slightly to use the notation in MBK (which GHS reduces to in the polished or very rough limits) in [10]. The discussion here most closely follows the latter article.

The ratio f_μ/f_p results in

$$\frac{f_\mu}{f_p} = \frac{\rho_s \lambda^4 F G}{32 \pi^4 l_c^2 \sigma_s^2 \sigma_g^2 \cos \theta_i \cos \theta_s \cos^4 \theta_h} \times \frac{1}{(\cos \theta_i + \cos \theta_s)^2} \exp \left[- \left(\frac{\tan^2 \theta_h}{2 \sigma_g^2} - \frac{\pi^2 l_c^2 \eta_r^2}{\lambda^2} \right) \right]. \quad (151)$$

Compared to the very rough surface approximation, the angular dependence of the exponential terms has changed, so the microfacet angular dependence is no longer equal to the linear systems angular dependence. From Equation (146), note that instead of the angular dependence being simply $\tan^2 \theta_h$, the angular dependence scales as

$$\begin{aligned} \eta_r^2 &= (\tan^2 \theta_h)(\cos \theta_i + \cos \theta_s)^2 \\ &= \sin^2 \theta_i + \sin^2 \theta_s + 2 \sin \theta_i \sin \theta_s \cos \phi_s, \end{aligned} \quad (152)$$

where the last line is from Equation (99). This last line shows that the value of η_r^2 ranges between $[0, 4]$. This is in contrast to the range of $[0, \infty)$ observed in the very rough case, because in the very rough case the angular dependence was $\eta_r/(\cos \theta_i + \cos \theta_s)^2$ and not just η_r .

Additionally, a different relationship for σ_g is observed, given as

$$\sigma_{g,p} = \frac{\lambda}{\pi l_c \sqrt{2}}, \quad (153)$$

which varies with wavelength, unlike in Equation (147). This shows the microsurface normal interpretation in the microfacet model does not hold for a polished surface, since the microsurface normal distribution should not vary with wavelength. For this reason, when adding a spectral dependence to the BRDF, the physical notion of a microfacet normal distribution is not valid; instead, a surface scatter distribution function is used to take its place.

Additionally, the remaining angular terms outside the exponential are of a somewhat different form in the polished surface ratio. In particular, the $(\cos \theta_i + \cos \theta_s)$ term is now raised to the -2 power instead of the +2 power, and there is an explicit λ^4 dependence in the ratio.

Validity of Microfacet Model.

The results in this chapter show that the microfacet model is valid in the very rough approximation, but is not valid in the polished surface approximation. To physically understand this phenomenon, consider a mostly flat surface with a regular pattern, such as a reflective diffraction grating. Properly accounting for surface scatter off such a material would require including wave optics effects. Although a polished surface may not have a perfectly periodic set of features as a diffraction grating, it still is a fairly smooth surface with periodic imperfections, suggesting a more significant role for wave optics. In fact, this can be seen in the experimental results presented in Chapter V, where there are periodic humps due to diffraction that are observed; see, for example, Figure 69.

On the other hand, in the limit of a very rough surface, consider the scalar wave

optics treatment (which treats all scatter as a phase screen). Such a phase screen would be arranged in a randomized distribution, which would tend to average out the diffractive effects that would arise from a wave optics approach. Again, this effect can be seen from the data presented in Chapter V; see Figure 49.

Original Beckmann-Kirchhoff Modification.

In the original BK theory, a geometrical factor F_{bk}^2 was used instead of K , and was described as a geometrical term [2]. Although Krywonos used K in place of F_{bk}^2 in MBK, F_{bk}^2 is much simpler to compute and may be desirable in some applications of BRDF if a more complete understanding of its role were developed. That purpose is explored in this section. F_{bk}^2 was presented in Chapter III as [2]

$$F_{bk}^2 = \left(\frac{1 + (\cos \theta_i \cos \theta_s + \sin \theta_i \sin \theta_s \cos \phi_s)}{\cos \theta_i (\cos \theta_i + \cos \theta_s)} \right)^2.$$

F_{bk} is not to be confused with Fresnel reflectance; it represents a geometric term that does not depend on index of refraction. Its connection to the microfacet model was not clear from prior work on MBK in [2, 30] because it was formulated by Beckmann prior to formal definition of the BRDF; in this section, an explanation for this term is presented and a minor modification for this term is proposed to ensure the term obeys Helmholtz reciprocity of the BRDF. Rewriting F_{bk}^2 in microfacet coordinates θ_h and θ_d , it is given as

$$F_{bk}^2 = \frac{\cos^2 \theta_d}{\cos^2 \theta_i \cos^2 \theta_h}. \quad (154)$$

Using basic trigonometric manipulations to put S in microfacet coordinates, this term can be rewritten as

$$\frac{1}{S} = \frac{\cos^2 \theta_d}{\cos \theta_i \cos \theta_s \cos^2 \theta_h} \approx \frac{Q}{2F}. \quad (155)$$

These equations suggest the purpose of F_{bk}^2 is to approximate $Q/2$ so that when BK theory is multiplied by the Fresnel equation F , it scales approximately correctly. However, there is an issue with F_{bk}^2 as presented. When $\theta_i \neq \theta_s$, F_{bk}^2 does not obey Helmholtz reciprocity and differs from this approximation for $Q/2F$. For this reason, using $1/S$ is suggested rather than the original F_{bk}^2 term; using $1/S$ makes the term functionally equivalent to the cross section conversion and microfacet distribution normalization, with the modified angular term that arises from g in MBK.

BRDF Scaling by $1/\sigma$.

In [8], which was discussed in Chapter V, experimentally measured BRDF data is presented in direction cosine space, which aligns BRDF data at all incident angles, other than differing in height. Multiplying measured BRDF data by a term inspired by the microfacet cross section conversion, $\cos \theta_i \cos \theta_s$, results in an approximate height alignment. The $1/S$ term written in microfacet coordinates above explains why the scaling in direction cosine space that was observed experimentally in [8] works. When at the specular peak, $\cos \theta_h = 1$ ($\theta_h = 0$). Near the specular peak, θ_h is small and thus $\cos \theta_h \approx 1$. Thus, $S \approx \cos \theta_i \cos \theta_s$ as is observed in [8] to be the scaling term that aligned the BRDF height data in direction cosine space.

In this section, the very rough surface approximation of MBK (equivalent to the very rough surface approximation of GHS) was compared to the general form of the microfacet model. In the rough surface approximation, the angular dependence of MBK (and thus also of GHS) was shown to be exactly equal to the angular dependence in the microfacet distribution function. The remaining angular terms were compared to the ratio of the standard Fresnel term with the polarization factor Q . This led

to a novel approximation for Q , and suggested where certain terms present in the microfacet BRDF models arise. In particular, part of the microfacet distribution function normalization and the cross section conversion term were found to result from using standard unpolarized Fresnel reflectance F instead of the polarization factor Q . The approximation was found to be relatively accurate, except when θ_i or θ_s is large; in the microfacet model, this region is where there would be significant shadowing and masking. Since surface scattering is fundamentally a physical optics problem, this observation suggests that instead of attempting to derive the shadowing and masking term from geometric optics, better results may be obtained by developing a modification to the ratio $2F/Q$, particularly at large incident or scattered angles. Alternatively, it is now possible to modify the microfacet model to use Q instead of F using this relationship.

Next, key differences between the polished surface analysis that were detailed in [7] and the rough surface analysis developed in this Chapter are presented. This resulted in a modification to the angular and wavelength dependencies in the microfacet model for a polished surface, and showed the breakdown of a geometric model for BRDF.

Additionally, the original BK geometric term F_{bk}^2 was analyzed, developing an explanation for this term relative to both the microfacet and linear systems models. A modification to F_{bk}^2 in the BK model was also proposed. The physical insight developed in this Chapter is expected to lead to future development of better closed-form approximations to the BRDF that preserve the relative simplicity of the microfacet model, while increasing the fidelity of the microfacet BRDF approximation.

6.2 Experimental Validation of Results

The experimental results presented in Chapter V led to some questions that may now be answered using this comparison. Consider the angular space of the microfacet

distribution function. In the case of a very rough surface, Equation (146) shows that the angular dependence of the microfacet distribution function is equal to the angular dependence of the scalar wave optics model. This result explains why the microfacet model fits rough BRDF data well, such as was presented in Figure 49 using the Cook-Torrance BRDF model.

Additionally, with this connection of microfacet theory to scalar wave optics theory, it is now possible to directly compare all terms used in both models, representing a novel contribution of this dissertation to BRDF theory. For example, the somewhat troublesome cross section conversion term was found to arise from using F instead of Q in the microfacet model. Q is a closed form equation (although admittedly its form is far more complex than F). To avoid the problem of having a model that diverges at grazing angle, as well as improving upon the angular dependence of the model, a microfacet model such as the Cook-Torrance model can now be rewritten by solving Equation (149) for F , resulting in

$$f_r(\hat{\omega}_i, \hat{\omega}_s) = \frac{\rho_s Q(\hat{\omega}_i, \hat{\omega}_s) D_b(\theta_h) \cos^4 \theta_h}{2(\cos \theta_i + \cos \theta_s)^2}, \quad (156)$$

where the cross section conversion term is no longer present, so the shadowing and masking term is no longer required since the BRDF no longer diverges at grazing angles.

Using this novel version of the Cook-Torrance BRDF, somewhat better results were obtained for the BRDF fitting at larger θ_i and θ_s (where the error between F and Q is largest). For example, consider the rough Al sample at $6.4 \mu m$. The standard Cook-Torrance fit using the ln error metric is shown in Figure 74. Using the alternative version proposed in Equation (156) with the same ln error metric, there is little change in the best fit at small angle (as the ratio of F to Q has very little error at small angle), but the fit becomes noticeably better at large angle, particularly for

$\theta_i = 50^\circ$, without decreasing accuracy at smaller angle; see Figure 75. This process was also performed for the Infragold® sample at $5.2 \mu m$, with results plotted in Figures 76 and 77; the results are similar, although since the Infragold® sample is even more diffuse it is easier to see the impact of using Q in the microfacet model at larger values of θ_s .

The fits appear to be improving, particularly for higher incident and scattered angles, but the next question that arises in the analysis is whether the fits are both within the margin of error in the measurement. This is addressed in Figures 78 and 79 for the rough Al data at $6.4 \mu m$, and in Figures 80 and 81 for the Infragold® data at $5.2 \mu m$. For the rough Al data, the Q term improves upon the model quite clearly. For the Infragold® data, it appears there may be a region near $\theta_s = 0$ where the original term performs slightly better; however, it is within the measurement uncertainty so it is not statistically significant. Overall, there still is improvement in the fit with the modified Cook-Torrance model using Q in place of F when all scattered angles are considered, as the improvement for $\theta_s > 20^\circ$ is more significant. There also appears to be a minor improvement in the modified Cook-Torrance model using Q in place of F for $\theta_s < -20^\circ$ in this sample.

In both Figures 79 and 81, it appears the minimum value of the measured data is not fitted well to either the original Cook-Torrance model or the modified Cook-Torrance model. This is because for purposes of this comparative analysis, the Lambertian term was not used in the fitting, as can be seen in Equation (156). This choice was made for fitting because the ratios in Equations (143) and (151) did not include the diffuse term. The diffuse term would simply add an overall offset that would compensate for this offset. Physically, this would likely be due to multiple bounces off a rough surface. Note that the modified form with Q in place of F still does not make the model fit worse to the data, even in this region.

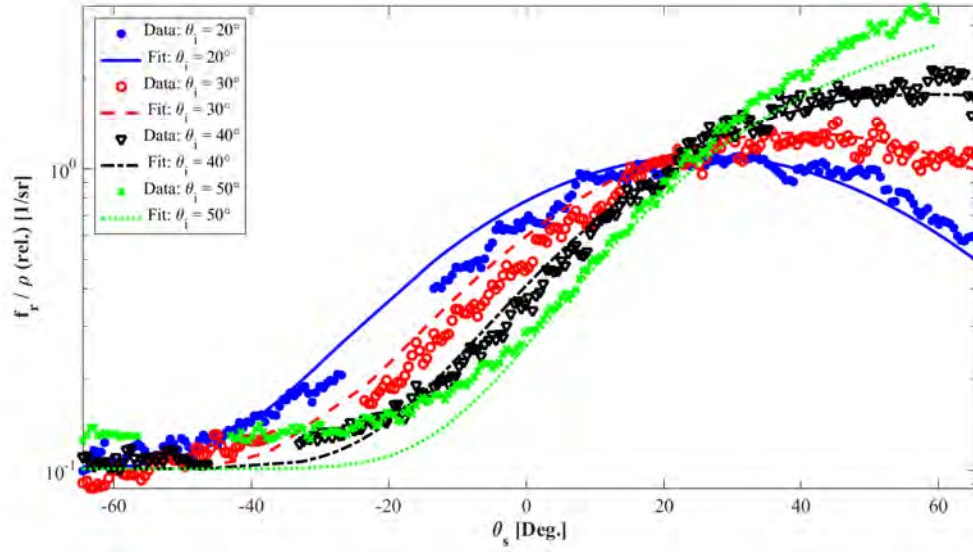


Figure 74. BRDF for rough Al at $6.4 \mu m$, fitted to Cook-Torrance BRDF, using \ln error metric, $g(x) = \ln(x)$.

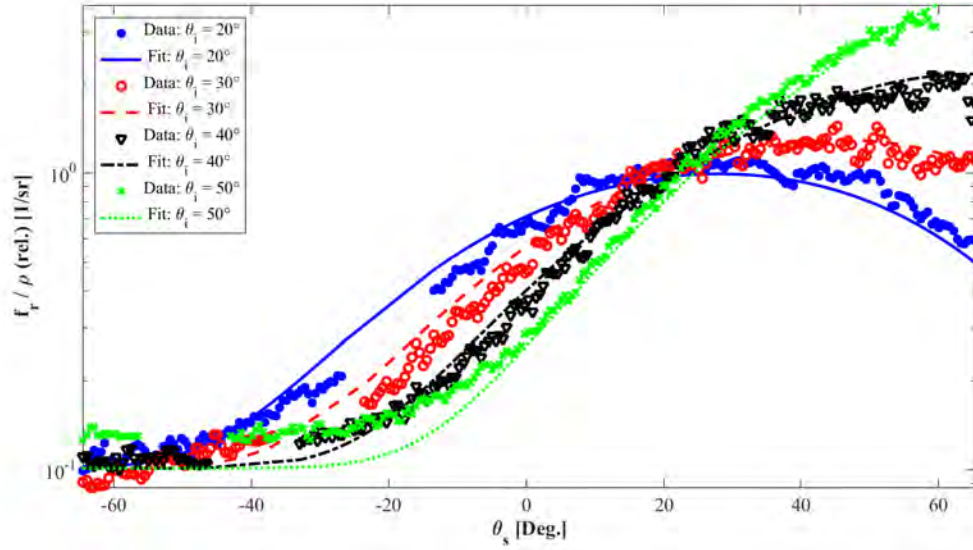


Figure 75. BRDF for rough Al at $6.4 \mu m$, fitted to modified Cook-Torrance BRDF using Q in place of F , using \ln error metric, $g(x) = \ln(x)$.

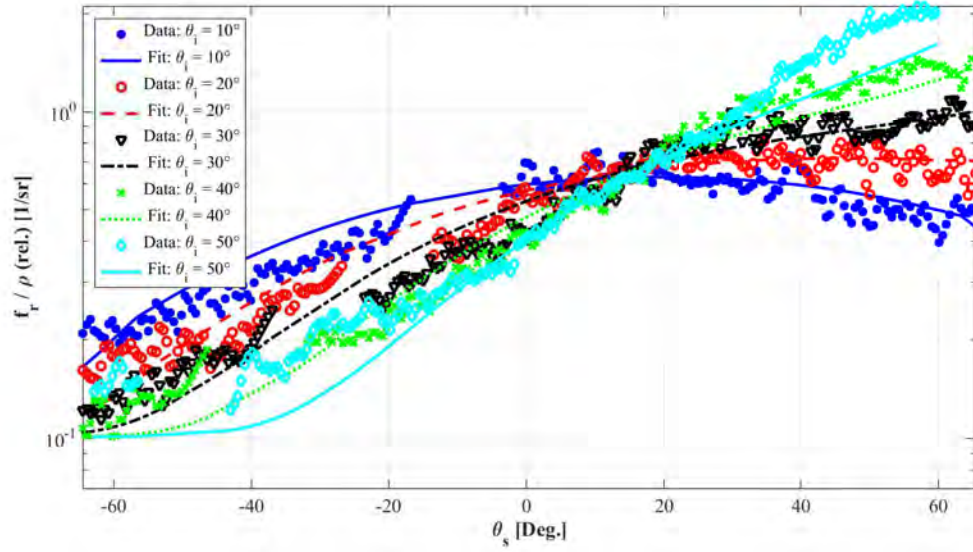


Figure 76. BRDF for AFIT Infragold® sample at 5.2 μm , fitted to Cook-Torrance BRDF, using \ln error metric, $g(x) = \ln(x)$.

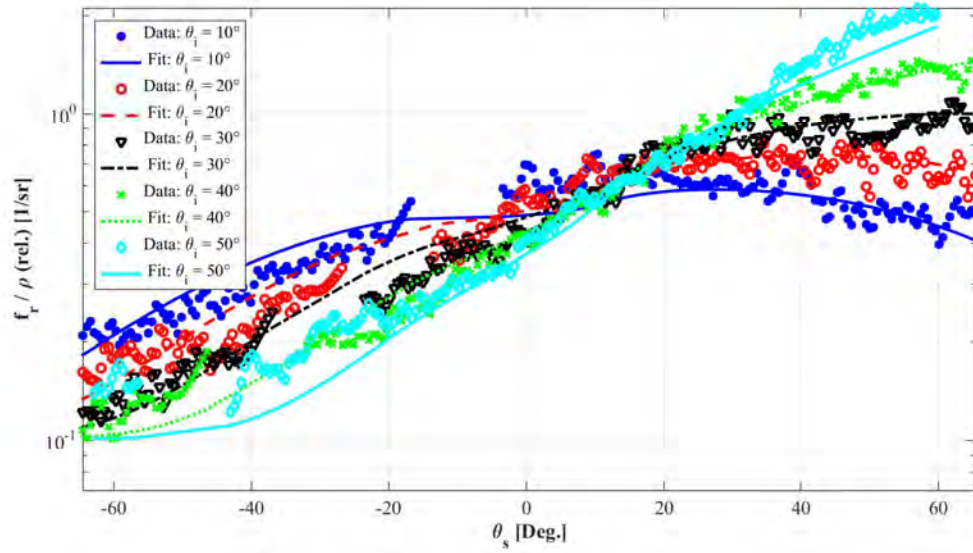


Figure 77. BRDF for AFIT Infragold® sample at 5.2 μm , fitted to modified Cook-Torrance BRDF using Q in place of F , using \ln error metric, $g(x) = \ln(x)$.

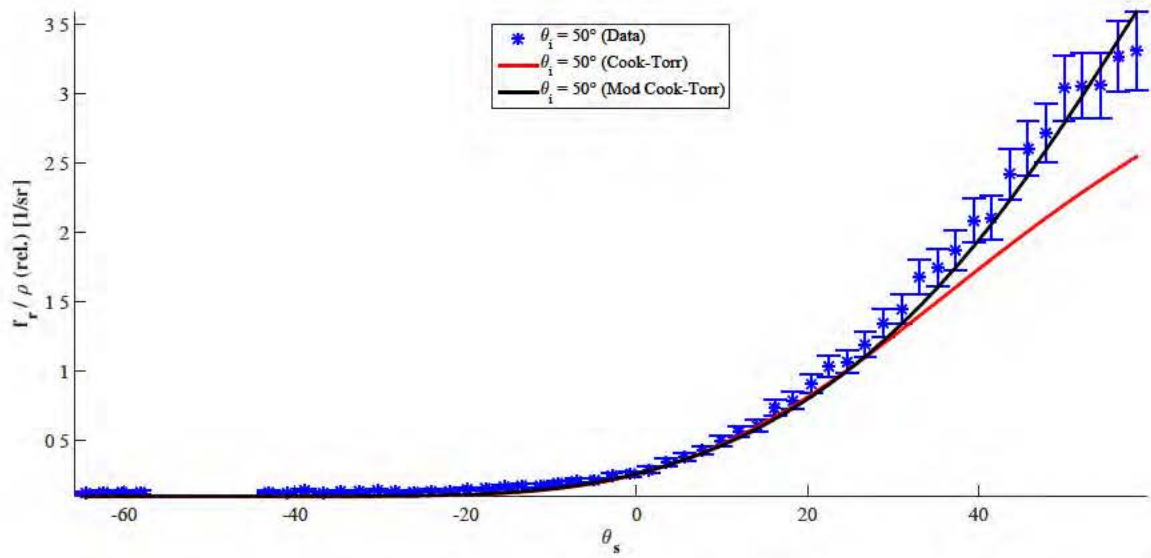


Figure 78. BRDF data, with error bars, for rough Al at $6.4 \mu m$ and $\theta_i = 50^\circ$ compared to both the original Cook-Torrance model fit and the modified Cook-Torrance model fit using Q in place of F .

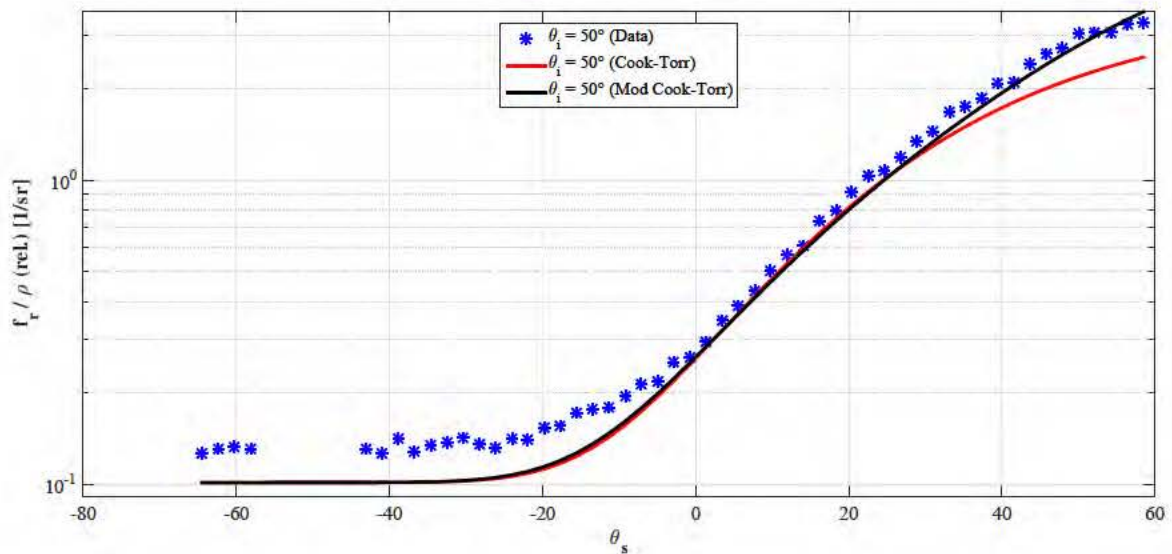


Figure 79. BRDF data for rough Al at $6.4 \mu m$ and $\theta_i = 50^\circ$ compared to both the original Cook-Torrance model fit and the modified Cook-Torrance model fit using Q in place of F , on semilog plot.

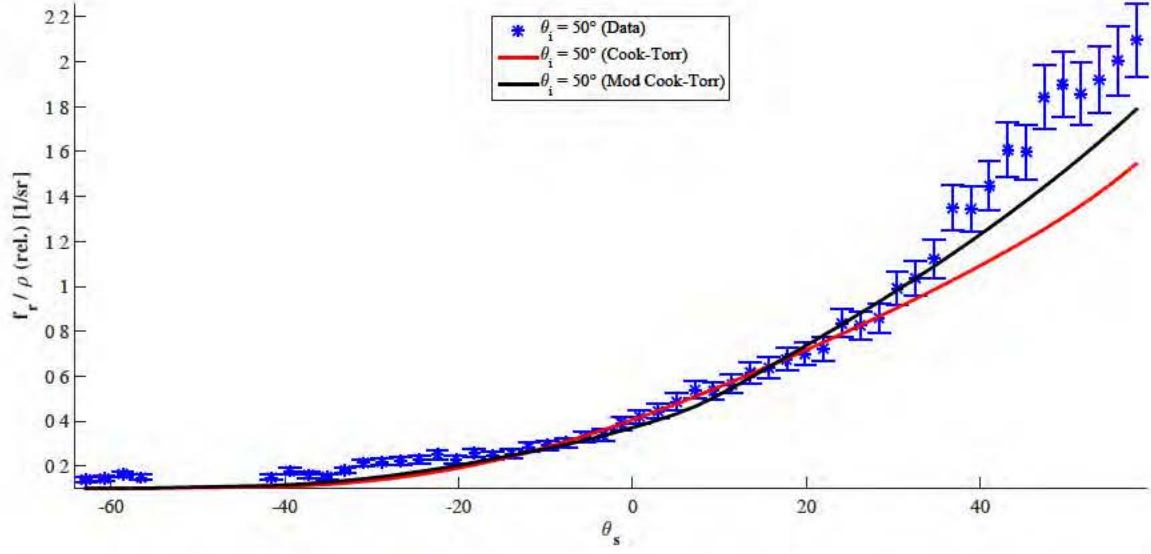


Figure 80. BRDF data, with error bars, for Infragold® at $5.2 \mu m$ and $\theta_i = 50^\circ$ compared to both the original Cook-Torrance model fit and the modified Cook-Torrance model fit using Q in place of F .

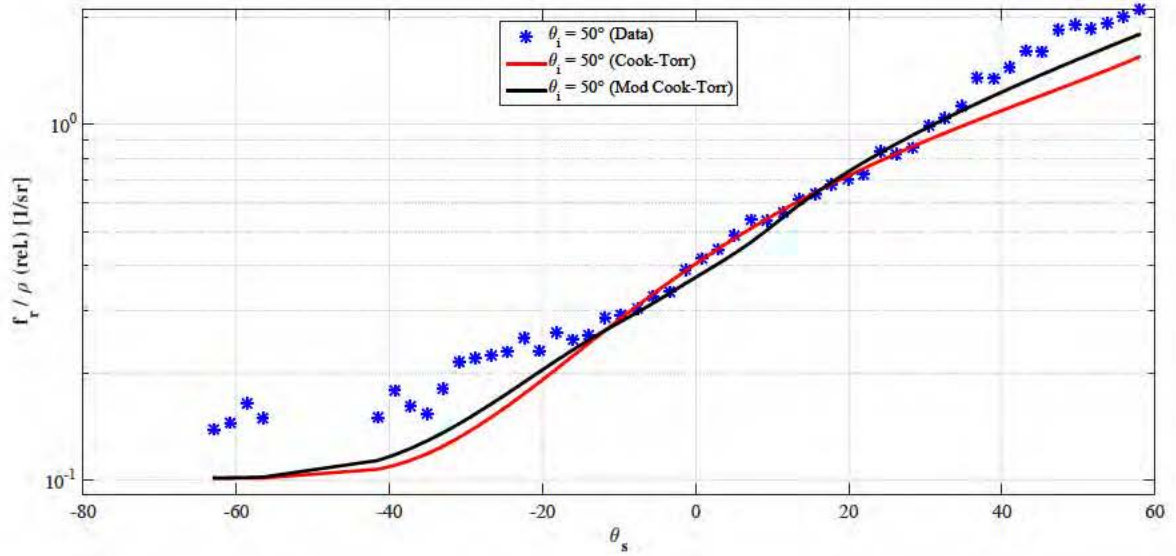


Figure 81. BRDF data, with error bars, for Infragold® at $5.2 \mu m$ and $\theta_i = 50^\circ$ compared to both the original Cook-Torrance model fit and the modified Cook-Torrance model fit using Q in place of F , on semilog plot.

Table 6.1. Comparison of the norm of the relative difference, d , when fitting BRDF data to the Cook-Torrance model using the \ln error metric, and the relative difference using the Modified Cook-Torrance model (using Q instead of F), for multiple diffuse samples, at all wavelengths measured. The largest relative uncertainty at any single data point for any incident and scattered angle is also reported.

Material	λ (μm)	Cook-Torr.	Mod. Cook-Torr.	Max. Rel. Uncertainty
Rough Al	3.39	3.23	3.10	0.138
	5.20	5.87	5.70	0.153
	5.63	5.30	5.26	0.163
	6.40	4.09	3.62	0.137
	8.00	4.37	4.08	0.160
	10.60	7.36	7.16	0.148
Infragold®	3.39	4.43	3.82	0.149
	5.20	5.32	4.57	0.137
	5.63	4.57	3.47	0.142
	6.40	4.25	3.20	0.139
	8.00	6.79	6.56	0.105
	10.60	4.80	4.09	0.149
Silver paint	3.39	6.60	4.97	0.140
	8.00	7.21	6.59	0.0899
	10.60	6.85	6.02	0.117

This method can be extended to all wavelengths by calculating the relative error between the best fit and the BRDF data at all wavelengths. The norm of the relative difference is reported as the fit error:

$$d = \left\| \frac{f_r - f_\mu}{f_r} \right\|, \quad (157)$$

where f_r represents the measured BRDF data and f_μ represents the best fit of the BRDF model to the BRDF data. The results using the best fit to the standard Cook-Torrance BRDF model compared to the modified Cook-Torrance model using Q in place of F are given in Table 6.1.

In every case measured, the BRDF fit to rough samples improved when using the modified Cook-Torrance BRDF with Q in place of F as proposed in Equation (156). The improvement in this BRDF fitting across all three rough samples that

were measured and at all wavelengths that were measured further suggests that the theoretical developments in this chapter are valid, since the microfacet model was shown in the theoretical development to model rough samples. Furthermore, these results suggest it is not necessary to use G if Q is used. Therefore, for rough materials, using the modified Cook-Torrance BRDF model presented in Equation (156) instead of the standard Cook-Torrance BRDF model is recommended to obtain a better fit.

On the other hand, as a surface becomes more highly polished, the angular dependence of the scalar wave optics model changes to a form not equal to the microfacet distribution function $\tan^2 \theta_h$ dependence, as was shown in Equation (152). This result suggests that the microfacet model would not be a good fit to the BRDF of a polished sample, which was another observation noted in Chapter V.

Furthermore, there is an issue with how the specular peak does narrow. Although the exact solution is only obtained at the very rough and polished approximations, it was noted that Equation (146) ranges over all non-negative values $[0, \infty)$, but the polished exponential only ranges $[0, 4]$. This reduction in the sampling space of the exponential would result in a more narrow specular peak, but the more narrow peak would not necessarily occur as a constant function of λ , providing some indication that the results observed in the prior section may also be valid. Although the two limiting cases for width of the specular lobe presented in this dissertation are no wavelength dependence of the specular lobe (in the very rough approximation) and linear wavelength dependence of the specular lobe (in highly polished approximation), the experimental data shows the variation is not linear in between, and is not described by scaling the specular lobe width by a constant power of λ . However, direct fitting to the polished surface BRDF data is not possible because Gaussian surface statistics were assumed for the surface height and correlation length. Despite that, a look at the raw width scaling for the polished sample is possible.

Recall that in Figure 55, and in the raw data presented in Figure 66, there appeared to be an increase in specular lobe width as λ increased in the limit of a highly polished sample (as the polished Ni sample had a NIST-traceable certificate stating its surface roughness was $0.071 \mu m$, and was the smoothest sample measured). A summary of all of the values of g for the Ni samples with NIST-traceable surface statistics are presented in Table 6.2. The table reports the value at the specular lobe, where $\theta_i = \theta_s$, but this value varies with scattered angle as well, as given by Equation (110) by approximately 50% to 150% of the reported value, depending on scattering angle. For the polished Ni surface, the polished approximation ($g < 0.025$) is reached beginning with $\lambda = 4.4 \mu m$ for certain incident angles. This region also appears to be where the width of the specular lobe is directly proportionate to λ in Figures 55 and 66. This observation suggests that the theoretical result presented in Equation (153) is valid. For the very rough samples presented in Figures 57, 58, and 64, there was no wavelength dependence observed, which is validated by the theoretical result obtained in Equation (147).

Each of these results from theory is consistent with the experimental results in the prior section. This consistency between experimental data presented in Chapter V and the novel theoretical development presented in this chapter suggests the interpretation of the microfacet model developed in this chapter is correct.

Additionally, recall from Chapter V that the BRDF width analysis was determined to be flawed because there is a second specular peak that appears to emerge from a more broad BRDF shape. This theoretical comparison suggests that it may be imprecise to directly compare the BRDF width at one incident angle with the width at another incident angle for another reason. The value of g depends on not just surface roughness and wavelength, but also on incident and scattered angle. The g term determines the number of terms required to limit the error in truncating the

Table 6.2. Values of g for Ni samples with known surface statistics. For each incident angle, the value reported is for specular scatter ($\theta_s = \theta_i$).

Material	$\lambda (\mu m)$	$\theta_i = 20^\circ$	$\theta_i = 30^\circ$	$\theta_i = 40^\circ$	$\theta_i = 50^\circ$
Pol. Ni 0.071 μm	3.39	0.0612	0.0519	0.0406	0.0286
	4.40	0.0363	0.0308	0.0241	0.0170
	5.20	0.0260	0.0221	0.0173	0.0122
	5.63	0.0222	0.0188	0.0147	0.0104
	6.40	0.0172	0.0146	0.0114	0.00803
	8.00	0.0110	0.00933	0.00730	0.00514
	10.60	0.00626	0.00531	0.00416	0.00293
Shot Ni 2.5 μm	3.39	75.8	64.4	50.4	35.5
	4.40	45.0	38.2	29.9	21.1
	5.20	32.2	27.4	21.4	15.1
	5.63	27.5	23.4	18.3	12.9
	6.40	21.3	18.1	14.1	9.96
	8.00	13.6	11.6	9.05	6.37
	10.60	7.76	6.59	5.15	3.63
Grit Ni 4.29 μm	3.39	223	190	148	104
	4.40	133	113	88.1	62.0
	5.20	94.9	80.6	63.1	44.4
	5.63	81.0	68.8	53.8	37.9
	6.40	62.7	53.2	41.6	29.3
	8.00	40.1	34.1	26.6	18.8
	10.60	22.8	19.4	15.2	10.7

infinite sum given by Equation (110), which may explain why there was variety in the BRDF width with incident angle for the same sample and wavelength.

6.3 Summary of Theoretical Results

The terms of the scalar wave optics BRDF model are now compared to the microfacet model, enabling the scalar wave optics model to be rewritten in microfacet coordinates (assuming Gaussian statistics) for a very rough surface ($g > 800$) as

$$f_{vr} = \frac{KFG}{4 \cos \theta_i \cos \theta_s} \left(\frac{l_c^2}{2\pi\sigma_s^2 \cos^4 \theta_h} \right) \exp \left[- \left(\frac{l_c}{2\sigma_s} \right)^2 \tan^2 \theta_h \right], \quad (158)$$

and for a polished surface ($g < 0.025$),

$$f_p = \frac{(2\pi)^3 FG(\cos \theta_i + \cos \theta_s)^4}{4 \cos \theta_i \cos \theta_s \cos^4 \theta_h} \left(\frac{\sigma_s^2 l_c^2}{\lambda^4} \right) \times \exp \left[- \left(\frac{\pi l_c}{\lambda} \right)^2 \tan^2 \theta_h (\cos \theta_i + \cos \theta_s)^2 \right] \quad (159)$$

The infinite summation can also be written in microfacet coordinates as:

$$f_{MBK} = \frac{\pi FG(\cos \theta_i + \cos \theta_s)^2 K l_c^2}{2\lambda^2 \cos \theta_i \cos \theta_s \cos^4 \theta_h} \exp(-g) \times \sum_{m=1}^{\infty} \frac{g^m}{m!m} \exp \left(- \frac{l_c^2}{4m\lambda^2} \tan^2 \theta_h (\cos \theta_i + \cos \theta_s)^2 \right). \quad (160)$$

Recall that g was defined in Equation (110).

The theoretical results developed in this chapter of the dissertation represent a significant step forward in understanding the microfacet model of the BRDF. For very rough surfaces, the microfacet model theory developed in this chapter showed the BRDF in a manner that does not vary significantly with wavelength. For polished surfaces, on the other hand, the microfacet model theory developed here showed considerable deficiency in the way the angular dependence is modeled, and additionally showed a wavelength-dependent relationship for the width, indicating a fundamental breakdown in the microfacet model. The theory developed in this chapter also showed from where the microfacet BRDF model terms arise as related to physical optics theory, enabling a proposed modification to the model to use the polarization factor Q rather than the standard Fresnel reflectance F . BRDF data was then presented that shows this use of Q in place of F improves the quality of fit of the BRDF to rough surface data, particularly at larger θ_i or θ_s . These observations on variation of the specular lobe width in the very rough and polished limits have been validated with the measured BRDF data. Since BRDF data and novel microfacet BRDF theory developments are both indicating similar phenomena, that leads to increased confidence in these results. Because all terms of a microfacet BRDF model are now quantita-

tively related to terms in a scalar wave optics model, a basis for further analysis to understand the spectral variation for realistic surface statistics has been developed.

VII. Conclusion

As discussed in Chapter I, the overarching problem to be solved by research in the area of spectral BRDF approximation is to develop a closed-form BRDF approximation that accounts for the wavelength-dependent properties of the BRDF, while accurately describing the BRDF properties of a wide class of materials, using a minimal number of fitting parameters. The research undertaken in this dissertation is summarized in a flow chart presented in Figure 1.

The problem was broken down into the following components:

- Determine whether BRDF may have a significant impact on HSRS using a basic scene model (Chapter II and [6])
- Catalog current closed-form, physics-based BRDF models (Chapter III and [5])
- Determine whether current models can be modified in a simple manner to insert a wavelength-dependent term (Chapter V)
- If a simple modification is not possible, determine how closed-form models relate to more accurate (but more computationally complex) physical optics BRDF models to understand how to arrive at novel closed-form approximations (Chapter VI, [7], [8], and in [10] develop the theory, relating all components of the microfacet model to scalar wave optics models)
- Test novel closed-form approximations to the BRDF (Chapter VI begins to address this by proposing a novel BRDF based on theoretical developments that fits better to rough experimental data)
- Propose a novel, physics-based, closed-form approximation to the BRDF suitable for HSRS that works at a wide range of wavelengths and for a wide class of materials (Future work)

These points will be summarized first, followed by suggestions for future work.

7.1 Summary of Key Results

This dissertation represents a significant contribution to all of the points above except the final point, although the theoretical work in Chapter VI does give the limiting boundaries of such an approximation and sets a roadmap for how this can be expanded. Initially, the approach taken was to modify the microfacet BRDF model to incorporate a simple, but nonlinear, wavelength scaling. Since materials tend to become more specular as the wavelength increases, one potential area to add this wavelength scaling was in the distribution function. To determine the form of such a wavelength scaling, experimental data was collected for 12 different samples at up to seven different wavelengths per sample, using the AFIT CASI® system that is capable of measuring BRDF data spanning approximately 10 orders of magnitude, from 10^{-4} to 10^6 $1/sr$. Initially, polarimetric BRDF data was collected for a subset of the samples; these results showed that, to obtain unpolarized BRDF data, a less cumbersome measurement approach could be taken. This approach was detailed in Chapter IV.

These experimental results were compared to the Cook-Torrance microfacet model, which was chosen because Ngan concluded it was consistently one of the best microfacet models when fitting to data in the MERL database[47]. Fitting the BRDF data to this model, even at a single wavelength, resulted in fitted values that differed from measured values by nearly an order of magnitude for a surface-reflected material with average roughness on the order of a wavelength, using either the linear or \ln fit metrics (see Figures 38 and 39). The only exception was that the fits were consistently accurate when the surface was rough (see Figure 49), but in that regime there was not an observed wavelength dependence in the width of the specular lobe (see Figure

57). This observation led to applying the Hyper-Cauchy distribution function in place of the Gaussian distribution function. When fitting BRDF functions to the MERL nickel data, the Hyper-Cauchy distribution was observed in [5] to greatly improve fit quality. In this work, the Hyper-Cauchy distribution used in Cook-Torrance did improve fit quality to the experimental data, but the fits still differed from measured results by over 100% for a surface with average roughness on the order of a wavelength (see Figure 44).

To determine if the problem was simply that the wrong model was being used, a method was developed to examine only the BRDF width of the specular lobe using the raw experimental data. The mean and standard deviation of the BRDF width at all wavelengths for all materials were calculated and plotted, showing the wavelength dependence was not straightforward. For very rough materials, there was no wavelength dependence, while some materials exhibited a very strong wavelength dependence. Typically, glossy (but not polished) materials exhibited the strongest wavelength dependence, but even then it was not a function of a constant power of λ . This result suggested there was a fundamental issue with microfacet models that had not been rigorously developed in BRDF literature.

After recognizing this difficulty with determination of the spectral dependence of the BRDF, the raw data was examined closer. For very rough samples, little wavelength variation was observed in the raw data. For the most highly polished sample measured, a gradual *increase* in the specular lobe width as a function of wavelength is observed. Between these regions, it appeared there was a specular lobe that was emerging from a broader (diffuse) base of the BRDF. This observation suggested that the BRDF width metric used may not be appropriate to describe the behavior of the BRDF, since in this transition region, the raw width analysis may be measuring either the broad, diffuse BRDF or the emerging specular lobe. This

result also suggested that the microfacet BRDF model may have inherently the wrong form, since a single microfacet distribution function does not model the emergence of a narrow specular lobe superimposed upon a more diffuse BRDF component. This observation is particularly important when applying the BRDF in the LWIR, as materials that might appear to be very rough in the visible spectrum may enter this intermediate region at the much longer LWIR wavelengths.

Then, the role of the cross section conversion term, σ , was examined, following the analysis in [8]. This term in the BRDF is simpler to compute than analogous terms in scalar wave optics theory, but has the unfortunate property of diverging at grazing angles. From [8], as discussed at the end of Chapter V, the role of this term is to align the magnitude of the BRDF in direction cosine space for various incident angle data.

These observations showed considerable room for improvement in understanding what the microfacet model represents and how it related to scalar wave optics models. This comparison was detailed in Chapter VI, [7], and in [10]. The connections between microfacet theory and scalar wave optics theory agreed with experimental results presented in Chapter V. All terms in the microfacet model are now explained in relation to scalar wave optics models. An understanding of the cross section conversion term is developed. This development makes it possible to replace certain terms in existing closed-form BRDF models with a different closed-form term called the polarization factor, Q , to eliminate the need to use the cross section conversion term that diverges at grazing angles. This connection resulted in better fits to experimental data of very rough samples at large θ_i or θ_s . Additionally, the polished expression for the scalar wave optics BRDF exhibited a different angular dependence not modeled by the microfacet BRDF, suggesting why the model does not currently fit polished BRDF data well.

Relating to a novel theoretical analysis performed in Chapter VI, the wavelength dependence, and in particular considering the potential wavelength variation of the specular lobe (which is where the error was found to be most significant in current BRDF databases such as the NEF), both the theory and the experimental results for very rough samples show that there is no wavelength dependence of the width of the specular lobe. At the other extreme, the theory and experimental results for polished Ni both showed a linear increase in specular lobe width as a function of wavelength. For materials in between these two extremes, the experimental results show there is typically an inverse relationship between wavelength and BRDF width, although this relationship is not a constant power of λ , and as mentioned above it appears from examining the BRDF data that a separate spectral lobe is apparently appearing superimposed over a more broad BRDF. Returning to the theoretical developments, and considering other terms besides the width of the specular lobe, the BRDF theory shows a λ^4 dependence is present for a polished material, but for a very rough material there is no such dependence on λ . Although a theoretical basis for this dependence has not been explicitly developed yet, the connection between microfacet and scalar wave optics BRDF models developed in this dissertation pave the way for future work to explicitly determine how this occurs by performing numerical calculations based on the GHS model in the general case, and based on the infinite summation given in Equation (113) for the simplified case of a Gaussian surface and paraxial data. The theoretical analysis also suggested the angular term $(\cos \theta_i + \cos \theta_s)$ is multiplied in both the exponential and in the surface reflection term (as compared to the very rough case). This suggests an empirical form of an angular term that may vary with wavelength, the exact dependence of which could also be fleshed out in future numerical work. Thus, the basis for a closed-form spectral BRDF model has now been developed in this work.

7.2 Summary of Contributions

Although the BRDF models in Chapter III are not novel, the task of organizing the model into the same common form presented in Table 3.1, then using that table to develop novel BRDF models by replacing the microfacet distribution function as discussed in [5] and Chapter V is novel. BRDF data in the MWIR and LWIR is typically collected at $3.39\ \mu\text{m}$ and $10.6\ \mu\text{m}$, so the collection of BRDF data at intermediate wavelengths using the CASI® also represents a novel contribution contained in this work.

The observations made in Chapter V indicated that microfacet BRDF models are primarily useful for fitting to rough surfaces. For polished surfaces, or even for glossy surfaces, the fit was not observed to be good. These results showed it is not straightforward to modify the microfacet BRDF model to include a simple wavelength scaling without further refining the closed-form approximation in the microfacet model. This negative result resulted in a shift in the approach taken by this work, to connect microfacet BRDF models with scalar wave optics BRDF models.

The relationship between the microfacet BRDF and the scalar wave optics BRDF had not been formally developed in prior literature as was performed in Chapter VI and in [10]. The relationships between direction cosine space and microfacet space are novel, as is the ability to use the polarization factor Q in place of the infinite plane wave Fresnel approximation F , which eliminates the need for a cross section conversion term σ , thereby avoiding the problem of the BRDF diverging at grazing angles. As shown at the end of Chapter VI, this development led to improved BRDF fitting even without a geometric attenuation term, G . The impact was most significant for large θ_i or θ_s .

The very rough and polished surface comparisons also represent a novel contribu-

tion resulting from this dissertation. For the very rough case, the microfacet model was found to fit measured BRDF data well; however, this fitting broke down as a surface became more highly polished. This was backed by the developed theory for these two cases. For wavelengths between these regions, when the wavelength is on order of the surface roughness, there appears to be an emerging second specular peak that is inherently different from the microfacet model form when the data is viewed on a log plot, such as in Figure 65(a). These results illustrate a fundamental issue with the microfacet BRDF model, in which the microfacet distribution function is incapable of describing a BRDF peak which appears to be comprised of the sum a diffuse BRDF (due to random phasing that masks diffractive effects) and a specular peak (which emerges as the phasing becomes less randomized relative to the wavelength of light). To enable a theoretical basis upon which this effect can be further analyzed, all terms of a scalar wave optics model have been related to the microfacet model in Chapter VI, which opens the door to quantifying this intermediate region.

7.3 Future Work

A basis is now developed to outline the form of a novel closed-form expression that captures the wavelength dependence of the BRDF. To this end, the most natural extension of this work is to perform an in-depth numerical analysis of Equation (113), representing the in-plane ASF as derived from MBK theory through use of an infinite summation. Now that the microfacet and scalar wave optics models have been connected, for different surface parameters, the summation could be evaluated numerically and compared to closed-form microfacet BRDF approximations to understand how the angular and spectral form of the BRDF varies in between the two extremes of very rough or polished surfaces. The work in Chapter VI suggests two possible bounds on how the angular scaling and wavelength dependence change, which could be com-

pared to the results from the infinite summation. After performing this analysis for the infinite summation using MBK, the task could then be extended to GHS theory, which includes an out-of-plane description of the BRDF, to determine any possible azimuthal change in the microfacet closed-form BRDF approximation as a surface becomes smoother. The results of such a task could then be evaluated against experimental data collected in this dissertation. After performing this analysis for materials following Gaussian statistics, such an analysis could be extended to other materials using numerical techniques to calculate the Fourier Transform required by scalar wave optics models. The results of such a task could then be evaluated against experimental data collected in this dissertation (since the materials measured in this work do not necessarily follow Gaussian surface statistics). This analysis would lead directly to novel closed-form models of the BRDF that could provide better spectral fitting, and may additionally lead to development of novel BRDF distribution functions.

A complementary experimental technique for future work would be to measure the surface properties of each BRDF sample. From this measurement, the correlation length, surface height, and surface probability distribution function could be calculated. This would give actual values to use for those terms in scalar wave optics models, rather than using best fit values, and may be helpful when performing the numerical analysis of the ASF.

As a separate task, the AFIT CASI® could be used to make spectral pBRDF measurements. Such a process could result in novel material identification techniques, once a more adequate closed-form approximation is developed from the future numerical work. Such a development could improve understanding on how to polarize a novel spectral BRDF model developed from the previous task.

The BRDF model background in Chapter III and contained, in part, in [5] that writes common models in a standard form, could be expanded and converted into

a review article or field guide. Additionally, based on the work in Chapter VI, it is now possible to include scalar wave optics models in such a document, thereby allowing the use of some ideas from scalar wave optics to be combined with ideas from microfacet BRDF models.

Relating to the method of using different distribution functions to fit data better, as discussed in [5] and Chapter V, an effort is underway (but as yet unfinished) to fit all materials in the MERL database to the modified Cook-Torrance BRDF model with the Hyper-Cauchy distribution as compared to using the more common Gaussian (Beckmann) distribution.

Based on the results of this dissertation, another enhancement may be possible using the Cook-Torrance BRDF model, but with the polarization factor Q in place of the Fresnel reflectance F and fitting to data in the MERL database, which contains densely measured BRDF data in red, green, and blue channels for 100 different materials. With rough samples collected in this dissertation, using Q in place of F , using Equation (149), improved the quality of fit. Since the MERL database includes densely measured BRDF data, the observed impact on in-plane and out-of-plane data could be more thoroughly analyzed using this approach, although the MERL BRDF data does not span the same dynamic range in BRDF value as the CASI® data and is broadband, visible spectrum data.

Another suggestion for future work is to perform a comprehensive analysis of the relationship between S and $2FG/Q$ presented in Equation (149) that was developed in Chapter VI, and in References [7] and [10]. Such an approximation may still be desirable even though F and Q are closed-form equations for two reasons: Q is not straightforward to compute, as can be seen in Equations (100)-(104), and there is not a consensus on the best term to use for G . Heitz has developed a geometric analysis of G in [32], but that approach ignores physical optics. Instead, developing G by

approximating Equation (149) may prove to be more promising, as suggested by the better fitting to rough surfaces shown at the end of Chapter VI.

Bibliography

1. Ashikhman, M. and P. Shirley. “An anisotropic Phong BRDF model,” *J. Graph. Tools*, 5: 25–32 (2000).
2. Beckmann, P. and A. Spizzichino. *The Scattering of Electromagnetic Waves from Rough Surfaces*. MacMillan, 1963.
3. Blinn, J. F. “Models of light reflection for computer synthesized pictures,” *Proc. 4th annual conference on computer graphics and interactive techniques* (1977).
4. Bohren, C. F. and D. R. Huffman. *Absorption and Scattering of Light by Small Particles*. Wiley-Interscience, 1983.
5. Butler, S. D. and M. A. Marciniak. “Robust categorization of microfacet BRDF models to enable flexible application-specific BRDF adaptation,” *Proc. SPIE*, 9205: 920506 (2014).
6. Butler, S. D., M. A. Marciniak, and J. Meola. “Modeling effects of the bidirectional reflectance distribution function on remote sensing in the LWIR,” *Proc. SPIE*, 9222: 92220H (2014).
7. Butler, S. D., S. E. Nauyoks, and M. A. Marciniak. “Comparison of microfacet BRDF model elements to diffraction BRDF model elements,” *Proc. SPIE*, 9472: 94720C (2015).
8. Butler, S. D., S. E. Nauyoks, and M. A. Marciniak. “Experimental analysis of bidirectional reflectance distribution function cross section conversion term in direction cosine space,” *Opt. Lett.*, 40: 2445–2448 (2015).
9. Butler, S. D., S. E. Nauyoks, and M. A. Marciniak. “Experimental measurement and analysis of wavelength-dependent properties of the BRDF,” *Proc. SPIE*, 9611 (2015).
10. Butler, S. D., S. E. Nauyoks, and M. A. Marciniak. “Comparison of microfacet BRDF model to modified Beckmann-Kirchhoff BRDF model for rough and smooth surfaces,” *Opt. Express* (Submitted 6 Jul 2015).
11. Cady, F. M., D. R. Bjork, J. Rifkin, and J. C. Stover. “BRDF error analysis,” *Proc. SPIE*, 1165: 154 (1990).
12. Chakrabarti, S., A. A. Maradudin, and E. R. Mendez. “Reconstruction of the surface-height autocorrelation function of a randomly rough dielectric surface from incoherent light scattering,” *Phys. Rev. A*, 88: 013812 (2013).
13. Conant, J. A. and F. J. Iannarilli, Jr. “Development of a combined bidirectional reflectance and directional emittance model for polarized modeling,” *Proc. SPIE*, 4481: 206–215 (2002).

14. Cook, R. L. and K. E. Torrance. "A reflectance model for computer graphics," *ACM Transactions on Graphics*, 1: 7–24 (1982).
15. Cornell Light Measurement Laboratory. "Computer graphics rendering of material surfaces," Internet, 2004. Viewed online at <http://www.graphics.cornell.edu/online/measurements/reflectance/index.html> (2014).
16. Crockett, G. "Laser Range Safety Tool (LRST) BRDF Reference," *AFRL Technical Report, AFRL-HE-BR-TR-2003-0119* (September 2003).
17. Dorsey, J., H. Rushmeier, and F. Sillion. *Digital Modeling of Material Appearance*. Morgan Kaufmann, 2007.
18. Duer, A. "An improved normalization for the Ward reflectance model," *J. Graphics, GPU, and Game Tools*, 11: 51–59 (2006).
19. Eismann, M. T. *Hyperspectral Remote Sensing*. SPIE Press, 2012.
20. Elfouhaily, T. M. and C.-A. Guerin. "A critical survey of approximate scattering wave theories from random rough surfaces," *Waves in Random Media*, 14: R1–R40 (2004).
21. Flynn, D. S. and C. Alexander. "Polarized surface scattering expressed in terms of a bidirectional reflectance distribution function matrix," *Optical Engineering*, 34: 1646–1650 (June 1995).
22. Gartley, M. G. "Polarimetric Modeling of Remotely Sensed Scenes in the Thermal Infrared," *Ph.D. Dissertation, Rochester Institute of Technology* (2007).
23. Goldstein, D. H. *Polarized Light* (Third Edition). CRC Press, 2011.
24. Goodman, J. W. *Introduction to Fourier Optics* (Third Edition). Roberts and Company Publishers, 2005.
25. Harkiss, S. I. "A Study of Bi-Directional Reflectance Distribution Functions and their Effect on Infrared Signature Models," *Masters Thesis, Air Force Institute of Technology* (2007).
26. Harvey, J. E. "Light-scattering Characteristics of Optical Surfaces," *Ph.D. Dissertation, University of Arizona* (1976).
27. Harvey, J. E. "Surface scatter phenomena: a linear, shift-invariant process," *Proc. SPIE*, 1165: 87 (1990).
28. Harvey, J. E., J. J. Goshy, and R. N. Pfisterer. "Modeling stray light from rough surfaces and subsurface scatter," *Proc. SPIE*, 9205: 92050I (2014).

29. Harvey, J. E. and A. Krywonos. “Unified Scatter Model for Rough Surfaces at Large Incident and Scatter Angles,” *Proc. SPIE*, 6672: 66720C (2007).
30. Harvey, J. E., A. Krywonos, and C. L. Vernold. “Modified Beckmann-Kirchhoff scattering model for rough surfaces with large incident and scattering angles,” *Opt. Eng.*, 46: 078002 (2007).
31. He, X. D., K. E. Torrance, F. X. Sillion, and D. P. Greenberg. “A comprehensive physical model for light reflection,” *ACM SIGGRAPH Computer Graphics*, 25: 175–186 (1991).
32. Heitz, E. “Understanding the Masking-Shadowing Function in Microfacet-Based BRDFs,” *J. Comp. Graph. Tech.*, 3: 32–91 (2014).
33. Hyde IV, M. W., J. D. Schmidt, and M. J. Havrilla. “A geometrical optics polarimetric bidirectional reflectance distribution function for dielectric and metallic surfaces,” *Opt. Express*, 17: 22138–22153 (2009).
34. Jackson, J. D. *Classical Electrodynamics* (Third Edition). John Wiley and Sons, Inc., 1999.
35. Jafolla, J. C. and W. R. Reynolds. “Bidirectional reflectance measurements for high resolution signature modeling,” *Proc. SPIE*, 5431: 184–197 (1999).
36. Kim, K., L. Mandel, and E. Wolf. “Relationship between Jones and Mueller matrices for random media,” *J. Opt. Soc. Am. A*, 4: 433–437 (1987).
37. Krywonos, A. “Predicting Surface Scatter Using a Linear Systems Formulation of Non-Paraxial Scalar Diffraction,” *Ph.D. Dissertation, University of Central Florida* (2006).
38. Krywonos, A., J. E. Harvey, and N. Choi. “Linear systems formulation of scattering theory for rough surfaces with arbitrary incident and scattering angles,” *J. Opt. Sci. Am. A*, 28: 1121–1138 (2011).
39. Lafortune, E. P., S.-C. Foo, K. E. Torrance, and D. P. Greenberg. “Non-linear approximation of reflectance functions,” *SIGGRAPH '02: Proceedings of the 29th annual conference on Computer graphics and interactive techniques*, 509–516 (1997).
40. Malitson, I. H. “Interspecimen Comparison of the Refractive Index of Fused Silica,” *J. Opt. Soc. Am.*, 55: 1205–1208 (1965).
41. Marschner, S., S. Westin, E. Lafortune, and K. Torrance. “Image-based measurement of the Bidirectional Reflection Distribution Function,” *Appl. Opt.*, 39: 2592–2600 (2000).

42. Matusik, W., H. Pfister, M. Brand, and L. McMillan. "A Data-Driven Reflectance Model," *ACM Transactions on Graphics*, 22: 759–769 (July 2003).
43. Maxwell, J. R., J. Beard, S. Weiner, D. Ladd, and S. Ladd. "Bidirectional reflectance model validation and utilization," *Environmental Research Institute of Michigan (ERIM) Technical Report AFAL-TR-73-303* (1973).
44. Montanaro, M. "NEFDS Beard-Maxwell BRDF Model Implementation in Matlab," *Rochester Institute of Technology, DIRS Technical Report 2007-83-174* (June 2007).
45. Montes, R. and C. Ureña. "An Overview of BRDF Models," *University of Grenada, Technical Report LSI-2012-001* (2012).
46. National Geospatial-Intelligence Agency. "Nonconventional Exploitation Factors Data System version 14.1", 2012.
47. Ngan, A., F. Durand, and W. Matusik. "Experimental Analysis of BRDF Models," *Proceedings of the Eurographics Symposium on Rendering*, 117–226 (2005).
48. Nicodemus, F. E., J. C. Richmond, J. J. Hsia, I. W. Ginsberg, and T. Limperis. "Geometrical considerations and nomenclature for reflectance," *National Bureau of Standards Monograph 160, Department of Commerce* (1977).
49. Nyquist, H. "Regeneration Theory," *Bell Systems Technology J.*, 11: 126–147 (1932).
50. Palmer, J. M. and B. G. Grant. *The Art of Radiometry*. SPIE Press, 2010.
51. Phong, B. T. "Illumination for computer generated pictures," *Communications of the ACM*, 18: 311–317 (June 1975).
52. Priest, R. G. and T. A. Germer. "Polarimetric BRDF in the Microfacet Model: Theory and Measurements," *Proc. 2000 Meeting of the MSS Specialty Sensors Group on Passive Sensors*, 1: 169–182 (March 2000).
53. Priest, R. G. and S. R. Meier. "Polarimetric microfacet scattering theory with applications to absorptive and reflective surfaces," *Opt. Eng.*, 41: 988–993 (May 2002).
54. Rakic, A. D., A. B. Djurisic, J. M. Elazar, and M. L. Majewski. "Optical properties of metallic films for vertical-cavity optoelectronic devices," *Appl. Opt.*, 37: 5271–5283 (1998).
55. Resnick, A., C. Persons, and G. Lindquist. "Polarized Emissivity and Kirchhoff's Law," *Appl. Opt.*, 38: 1384–1387 (Mar 1999).

56. Rusinkiewicz, S. “A New Change of Variables for Efficient BRDF Representation,” *Rendering Techniques* (1998).
57. Sandford, B. and L. Robertson. “Infrared reflectance properties of aircraft paint,” *Proc. IRIS Targets, Backgrounds, and Discrimination* (1985).
58. Schlick, C. “An Inexpensive BRDF Model for Physically-based Rendering,” *Comp. Graph. Forum*, 13: 233 (1994).
59. Schott, J. R. *Fundamentals of Polarimetric Remote Sensing*. SPIE, 2009.
60. Schroeder, S., A. Duparre, L. Coriand, A. Tuennermann, D. H. Penalver, and J. E. Harvey. “Modeling of light scattering in different regimes of surface roughness,” *Opt. Express*, 19: 9820 (2011).
61. Shell, J. R. “Polarimetric Remote Sensing in the Visible to Near Infrared,” *Ph.D. Dissertation, Rochester Institute of Technology* (2005).
62. Stover, J. C. *Optical Scattering: Measurement and Analysis* (Third Edition). SPIE Press, 2012.
63. Stover, J. C. and J. E. Harvey. “Unified Scatter Model for Rough Surfaces at Large Incident and Scatter Angles,” *Proc. SPIE*, 6672: 66720B (2007).
64. Su, P., Q. Eri, and Q. Wang. “Optical roughness BRDF model for reverse Monte Carlo simulation of real material thermal radiation transfer,” *Appl. Opt.*, 53: 2324–2330 (2014).
65. Torrance, K. E. and E. M. Sparrow. “Theory of off-specular reflection from roughened surfaces,” *J. Opt. Soc. Am.*, 57: 1105–1114 (1967).
66. Trowbridge, T. S. and K. P. Reitz. “Average irregularity representation of a rough surface for ray reflection,” *J. Opt. Soc. Am.*, 65: 531–536 (1975).
67. Vap, J. C. “Design and Characterization of Optical Metamaterials Using Tunable Polarimetric Scatterometry,” *Ph.D. Dissertation, Air Force Institute of Technology* (2012).
68. Vap, J. C., S. E. Nauyoks, T. Fitzgerald, and M. A. Marciniak. “Development of tunable polarimetric optical scattering instrument from 4.3-9.7 microns,” *Proc. SPIE*, 8154 (2011).
69. Vap, J. C., S. E. Nauyoks, and M. A. Marciniak. “Optimization of a dual-rotating-retarder,” *Meas. Sci. Technol.*, 24 (2013).
70. Ward, G. J. “Measuring and modeling anisotropic surfaces,” *ACM SIGGRAPH '92 Conference Proceedings*, 4: 255–264 (July 1992).

71. Wellem's, D., S. Ortega, D. Bowers, J. Boger, and M. Fetrow. "Long wave infrared polarimetric model: theory, measurements and parameters," *J. Optics A*, 8: 914–925 (2006).
72. Westlund, H. B., G. W. Meyer, and F. Y. Hunt. "The Role of Rendering in the Competence Project in Measurement Science for Optical Reflection and Scattering," *J. Res. Natl. Inst. Stand. Technol.*, 107: 247–259 (2002).

REPORT DOCUMENTATION PAGE

Form Approved
OMB No. 0704-0188

The public reporting burden for this collection of information is estimated to average 1 hour per response, including the time for reviewing instructions, searching existing data sources, gathering and maintaining the data needed, and completing and reviewing the collection of information. Send comments regarding this burden estimate or any other aspect of this collection of information, including suggestions for reducing this burden to Department of Defense, Washington Headquarters Services, Directorate for Information Operations and Reports (0704-0188), 1215 Jefferson Davis Highway, Suite 1204, Arlington, VA 22202-4302. Respondents should be aware that notwithstanding any other provision of law, no person shall be subject to any penalty for failing to comply with a collection of information if it does not display a currently valid OMB control number. **PLEASE DO NOT RETURN YOUR FORM TO THE ABOVE ADDRESS.**

1. REPORT DATE (DD-MM-YYYY) 17-09-2015			2. REPORT TYPE Doctoral Dissertation		3. DATES COVERED (From — To) August 2012 — September 2015	
4. TITLE AND SUBTITLE EXPERIMENTAL AND THEORETICAL BASIS FOR A CLOSED-FORM SPECTRAL BRDF MODEL					5a. CONTRACT NUMBER	
					5b. GRANT NUMBER	
					5c. PROGRAM ELEMENT NUMBER	
6. AUTHOR(S) Butler, Samuel D., Major, USAF					5d. PROJECT NUMBER	
					5e. TASK NUMBER	
					5f. WORK UNIT NUMBER	
7. PERFORMING ORGANIZATION NAME(S) AND ADDRESS(ES) Air Force Institute of Technology Graduate School of Engineering and Management (AFIT/EN) 2950 Hobson Way WPAFB OH 45433-7765					8. PERFORMING ORGANIZATION REPORT NUMBER AFIT-ENP-DS-15-S-021	
9. SPONSORING / MONITORING AGENCY NAME(S) AND ADDRESS(ES) Sensors Directorate, Air Force Research Laboratory 2241 Avionics Circle, Area B, WPAFB OH 45433 (937) 528-8200 Michael.Eismann@us.af.mil ATTN: Dr. Michael Eismann					10. SPONSOR/MONITOR'S ACRONYM(S) AFRL/RV	
					11. SPONSOR/MONITOR'S REPORT NUMBER(S)	
12. DISTRIBUTION / AVAILABILITY STATEMENT DISTRIBUTION STATEMENT A: APPROVED FOR PUBLIC RELEASE; DISTRIBUTION UNLIMITED.						
13. SUPPLEMENTARY NOTES This work is declared a work of the U.S. Government and is not subject to copyright protection in the United States.						
14. ABSTRACT The microfacet class of BRDF models is frequently used to calculate optical scatter from realistic surfaces using geometric optics, but has the disadvantage of not being able to consider wavelength dependence. This dissertation works toward development of a closed-form approximation to the BRDF that is suitable for hyperspectral remote sensing by presenting measured BRDF data of 12 different materials at four different incident angles and up to seven different wavelengths between 3.39 and 10.6 μm . The data was intended to be fit to various microfacet BRDF models to determine an appropriate form of the wavelength scaling. However, when fitting the microfacet models to measured data, the results indicated a breakdown in the microfacet model itself. To overcome this deficiency, elements of microfacet BRDF models are compared to elements of scalar wave optics BRDF models, which inherently contain a wavelength dependence. This analysis led to a theoretical understanding of how to modify microfacet BRDF models to maintain the simplicity of a closed-form model, while better approximating the underlying physics.						
15. SUBJECT TERMS BRDF, Microfacet, Infrared, LWIR, MWIR, Remote Sensing, Spectral, Hyperspectral, Measurement, Theory, Closed Form, Dissertation						
16. SECURITY CLASSIFICATION OF:			17. LIMITATION OF ABSTRACT	18. NUMBER OF PAGES	19a. NAME OF RESPONSIBLE PERSON	
a. REPORT	b. ABSTRACT	c. THIS PAGE			Dr. Michael A. Marciniak, AFIT/ENP	
U	U	U	UU	235	19b. TELEPHONE NUMBER (include area code) (937) 255-3636, x4529; mmarcini@afit.edu	